Synthesis of carbon nanotubes within porous anodic alumina templates for electronic applications

Leandro Nicolas Sacco

ÉCOLE POLYTECHNIQUE
UNIVERSITÉ PARIS-SACLAY

L2ICM

cnrs
UMR7647

Doctoral thesis in Physics

Synthesis of carbon nanotubes within porous anodic alumina templates for electronic applications

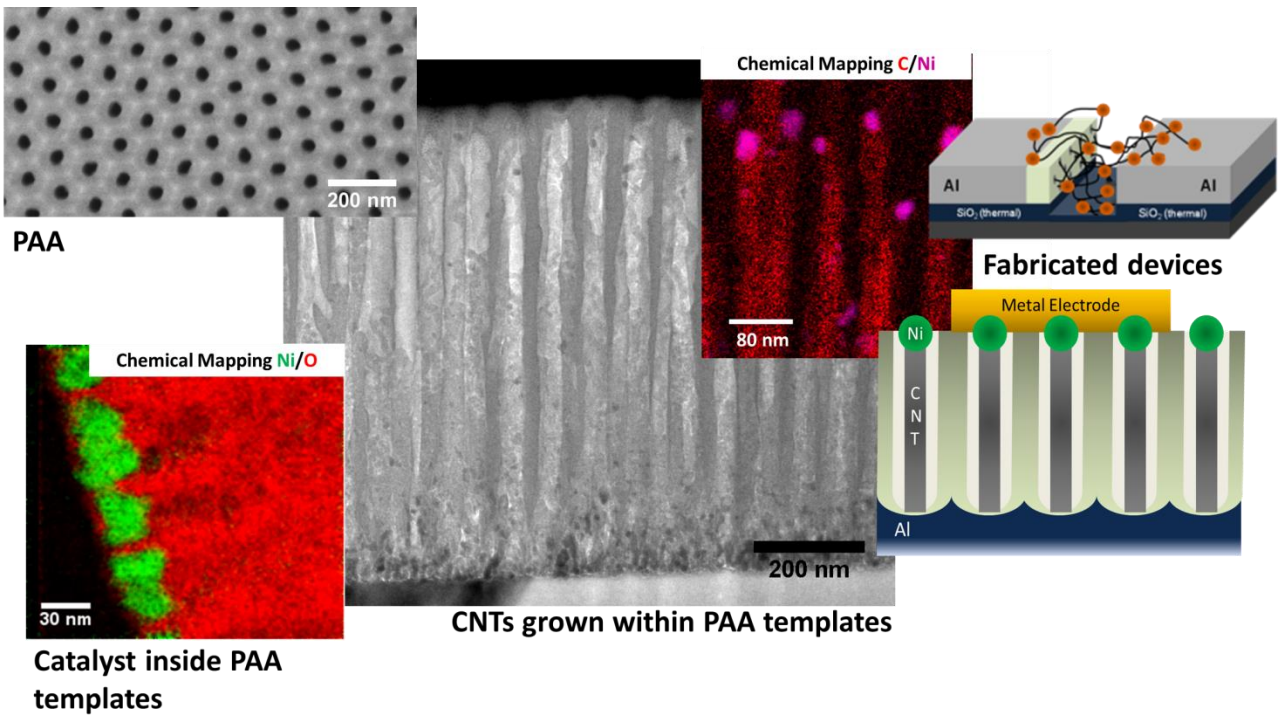

Leandro Nicolás Sacco

Thèse

Présentée pour obtenir le grade

DOCTEUR DE L'ECOLE POLYTECHNIQUE

Spécialité : Physique

Par

Leandro Nicolás SACCO

Thèse soutenue le 15 décembre 2015devant le jury composé de :

Francois LE NORMAND	**Rapporteur**
Denis BUTTARD	**Rapporteur**
Jean-Eric WEGROWE	**Examinateur**
Lucian ROIBAN	**Examinateur**
Costel-Sorin COJOCARU	**Directeur de thèse**
Marc CHATELET	**Co-Directeur**

Para Roxane,

para Léa,

y para los que vendrán…

Acknowledgements

First of all I would like to thank to Costel-Sorin Cojocaru and Bérengère Lebental for the opportunity that they gave me in order to carry out my Ph.D thesis at the Laboratoire de Physique des Interfaces et des Couches Minces (LPICM). Opportunity is something that you can never give back.

In particular, I want to thank to my thesis supervisor Costel to help me and advise me to perform the steps taken at me arrival in France. In the scientific plane, I want to highlight his open mind in order to listen my ideas and construct together new approaches to solve problems. Finally I want to express my gratitude for his encouragement in hard times.

I am also grateful to my co-supervisor Marc Châtelet for his predisposition and help, he was always present in order to invest his time and ready for the discussion, on the other hand Marc was a great allied for the writing of the present work.

Additionally, I want to be thankful with all the former and present members of the NanoMaDe team. In different stages, all of them support me and help me. Especially, I want to thank to Ki-Hwan Kim, Emmanuel Lefeuvre and Lucie Leveau which help with the first steps concerning the experimental procedures. Also I want to thanks to the support and help of Heechul Woo, Fatima Bouanis, Laurent Baraton and David Brunel. The present work it would not have been possible without the constant technical presence of Léo Caristan and Garry Rose, their help have been invaluable. Both of them, always they rescued me when technical problems appeared. Finally, I would like to express all my esteem to Ileana Florea that not only help me with the preparation of the obtained superb TEM images and their interpretation, but also was there for all discussions that have paved a friendship.

I want to express my sincere thanks to all the LPICM members that directly or indirectly help me to perform my work without any concern. In particular to Pere Roca i Cabarrocas that always was present and following my thesis. Also many members helped me in different

instance with the most diverse problems such as: Gabriela Medina, Laurence Corbel, Eric Paillassa and Cyril Jadaud.

The Ph.D results a crucial step for the professional formation of a researcher. In my case such achievement also was possible due to the previous educational formation that I forged in my native country. I want to highlight that I was form under a free university system, such educational system largely provided me the tools to carry out the Ph.D thesis. Therefore I always will recognize to the University of Buenos Aires and all the teachers that helped and formed me as scientific researcher, in especial to Silvia Goyanes who introduced me to the astonishing nanotechnology universe.

Always, I will be honored and thankful to the Ecole Polytechnique to embrace me and allows performing my thesis in such environment of excellence.

I want to thanks to my family that help me and always support me without any condition to reach all my dreams. *Especialmente, MUCHAS GRACIAS papá y mamá por toda la ayuda desde siempre y sin importar las distancias siempre estarán conmigo.*

Finally, the last person whom I want to put into words my gratitude for all the unconditional support, is to *mon amour*, *ma famille*, *mon âme sœur*, Roxane Alarcón who appeared magically the 30th March 2014 and from that time we lived amazing things and we continue for sure.

Contents

Introduction

The Nobel Prize winner in physics, Richard Feynman, asked the following question, during a talk that he has given for the annual meeting of the American Physical Society in 1959:

Why cannot we write the entire 24 volumes of the Encyclopedia Britannica on the head of a pin?

Basically the idea of manipulating the matter at the atomic scale was introduced. However we cannot manipulate atoms as easily as objects in the macroscopy world. Therefore many scientists started to fabricate and observe objects with size smaller than a 10^{-8} meters which opened a new domain in the world of science named nanotechnology.

There are a wide variety of nano-objects that can be classified based on their inherent structure: nanoparticles, nanowires, nanotubes, nanoribbons, nanosheets and so on and so forth. The common denominator of such structures is that they possess at least one characteristic length in the nanometric scale. The discovery of carbon nanotubes (CNTs) in 1991 was one of the most emblematic ones, due to the unique electrical, mechanical, thermal and optical properties. For instance CNTs have been proposed as candidate for a space elevator cable [1].

Despite the promising and astonishing properties of such nanometric structures, the critical subject of their manipulation remains as the primordial challenge. Very expensive and time consuming techniques, like e-beam lithography, have been developed in order to precisely control the growth of nanostructures, or to obtain a nano-objet from the etching of a bulk material. Such techniques are suitable as probes of concepts, however the atom-by-atom bottom-up approach is unrealistic because they are not compatible with a massive integration.

Therefore many efforts have been focused in order to fabricate devices by bottom-up approach where molecule-by-molecule follows the guidelines of supramolecular multi-component. On the other hand the miniaturization of the fabricated devices is reaching a bottleneck since the scaling-down for enhancing their performance is close to the limitation. Consequently the efforts concentrated to achieve device fabrication by continuous miniaturization leads to performances with a decline in the electrical conductivity transports values and a significantly loss of reliability. Therefore different strategies have been explored to overcome the presented problematics associated with the scaling-down process of the fabricated nanodevices. l

The control growth of the nanostructures (mainly in terms of length, growth rate and position) that form the device, plays a critical role in the further device performance. Self-organized templates provide several advantages in order to control the growth nanostructures. For instance track-etched polycarbonate [2], block copolymers [3] or DNA origami [4], and porous anodic alumina (PAA) templates have been widely studied. In particular PAA template has become a commonly used template with potential applications in a wide range of areas, owing to their easy and cheap implementation, geometry versatility, mechanically robustness, and potential application in large surfaces. Typically, PAA templates present a vertical pore structure with pore diameters of the order of nanometers and length up to millimeters; the ideal pore organization is arranged on a honeycomb pattern. The fabrication is performed by the anodization of aluminum which allows tuning of the pore structure characteristics by the variation of the parameters involved in their fabrication. Taking advantage of the well-ordered structure and the confinement imposed by the pores, these templates are utilized for the growth of carbon nanotubes and silicon nanowires. The growth of such nanostructures inside PAA paves the way to high densities of individual connection per cm^2 [5]. Several applications have been reported by the template-assisted growth of nanostructures in different domains, for instance field emitters [6], gas sensors [7], data storage media [8], solar cells fabrication [9], and for Lithium ion batteries [10].

The main constraint of the growth of nanostructures within PAA is given by the oxide barrier which remains at the bottom of the pores, such barrier could present difficulties for the

catalyst deposition required for a further synthesis of nanostructures. Different strategies have been adopted in order to overcome this problem, for instance the detachment of the PAA structure from the supporting aluminum, or by the etching of such barrier that allows an easy collective contact compatible with electronic devices fabrication since aluminum acts as a possible contact.

In the present work, we take both advantages of the PAA templates and carbon nanotubes for the device fabrications. Two different templates based approaches have been adopted, exploiting in each case their characteristic configuration. The device fabrication based on CNTs grown on conventional vertical-PAA templates doesn't require costly and complicated procedures and are compatible with large area devices, in contrast the active element for a further device application is confined inside the pores which can limit the wide range of application. On the other hand CNTs have been grown inside lateral-PAA templates, such kind of templates are compatible with the planar circuit integration, in addition the tubes are between two terminals which offers the possibility of light illumination or further CNT functionalization. For the fabrication of such devices more technological steps are involved including lithography stages. With the vertical-PAA templates humidity sensing devices are presented and also the interconnection main characteristics circuits are established. The lateral-PAA fabricated shown an unequalled photonic response under light illumination exhibiting potential application in the photodetection and photovoltaic domain. Complementary in each device step, fundamental mechanism concerning the anodization process and the synthesis of carbon nanotubes have been studied.

Regarding the device fabrication several steps have to be performed, one of the principal aims of the present work is to obtain a deep understanding on the processes involved in their fabrication, in order to improve the potentialities of the fabricated device. Consequently, the study of the anodization process and the impact of the fabrication parameters on the PAA structure have been addressed. Subsequently the interaction between the catalyst depositions inside the template is studied, taking into account that such interaction will mainly define the growth of the carbon nanostructures. Once such processes are controlled

and optimized, the second main goal of the present work is dealt with: the characterization of the fabricated devices ant the exploration of different application domain depending on the device characteristics.

The structure of the present thesis follows the road towards the device fabrication from the beginning of the template fabrication towards the proper device characterization. Firstly, the main features of the structural of PAA templates and the influence of the anodization parameters on the geometrical features are introduced in the first chapter. Their formation process and the experimental methods utilized in order to tune the template are investigated. The second chapter is devoted at the study of the electrodeposition process inside the pore structure. Moreover we utilized the nanoparticle deposition as fingerprint of the pore structure which allows the analysis of the best pore structural configuration for the synthesis of CNTs. In the third chapter the synthesis conditions are study in order to obtain the maximum number of CNTs per unit of area, a highly desire property towards the device fabrication. The performing sensing results of the fabricated devices and the mechanisms responsible of the sensing activities are summarized in the chapter four. The different fabricated devices in their two configurations, lateral and vertical, are electrically and optoelectronically analyzed, in addition for vertical devices the humidity measurements are executed. Finally, the last chapter presents the general conclusion of the work and the prospective of the potentialities of the devices fabricated using PAA templates

References

1. Edwards, B.C., *The NIAC Space Elevator Program.* Space Elevators and Tethers, 2002: p. 84-90.
2. Dauginet-De Pra, L., et al., *Fabrication of a new generation of track-etched templates and their use for the synthesis of metallic and organic nanostructures.* Nuclear Instruments and Methods in Physics Research Section B: Beam Interactions with Materials and Atoms, 2002. **196**(1–2): p. 81-88.
3. Lee, D.H., et al., *Hierarchically Organized Carbon Nanotube Arrays from Self-Assembled Block Copolymer Nanotemplates.* Advanced Materials, 2008. **20**(13): p. 2480-2485.
4. Maune, H.T., et al., *Self-assembly of carbon nanotubes into two-dimensional geometries using DNA origami templates.* Nature nanotechnology, 2010. **5**(1): p. 61-66.
5. Choi, W.B., et al., *Ultrahigh-density nanotransistors by using selectively grown vertical carbon nanotubes.* Applied Physics Letters, 2001. **79**(22): p. 3696-3698.
6. Angelucci, A., et al., *Field emission properties of carbon nanotube arrays grown in porous anodic alumina.* physica status solidi (c), 2009. **6**(10): p. 2164-2169.
7. Kolmakov, A., et al., *Detection of CO and O2 using tin oxide nanowire sensors.* Advanced Materials, 2003. **15**(12): p. 997-1000.
8. Terris, B. and T. Thomson, *Nanofabricated and self-assembled magnetic structures as data storage media.* Journal of physics D: Applied physics, 2005. **38**(12): p. R199.
9. Dang, H., et al., *Nanotube photovoltaic configuration for enhancement of carrier generation and collection.* 2015.
10. Ahn, Y.-k., et al., *Enhanced electrochemical capabilities of lithium ion batteries by structurally ideal AAO separator.* Journal of Materials Chemistry A, 2015. **3**(20): p. 10715-10719.

Chapter 1.

Porous Anodic Alumina templates

Porous Anodic Alumina (PAA) has been studied during the last century. The first studies were focused on the corrosive and mechanical resistance applications. Due to improvements in the electronic microscopy field, in 1953 Keller et. al. [1] carried out the first studies in order to characterize the nanometric features of the PAA. Nevertheless the first important work that supplied a detailed explanation of the pore growth mechanism was performed in 1970 by O'Sullivan and Wood [2], such work made a crucial step towards the understanding of the PAA formation. Until the 1990's mostly of the efforts were concentrated to obtain a detail description of the PAA and an explanation of the mechanics involved in the PAA fabrication. An important innovation was achieved by Masuda and Fukuda [3] when they proposed the two-step anodization process. This technique has improved the PAA organization leading to a template with a highly ordered close packed array. In addition, numerous progresses have been performed in terms of the template tailoring, adjusting the parameters involved in the fabrication process [4, 5], showing the great versatility of such template fabrication approach. Therefore the study of the PAA has opened new frontiers for template fabrication since the numerous advantages that provide this kind of porous structure, such as the pore ordered distribution, the wide range of possible pore aspect-ratios, the easy control of the structural parameters of the template, and the low cost of implantation of the anodization process.

This nanostructured template has triggered several applications and open new frontiers in the nanotechnology domain such as electronics [6], optoelectronics [7], photocatalytic [8],

nanophotonic [9], microfluidic and sensing devices [10], energy conversion [11] , as well as functional electrodes [12] and magnetic recording media [13].

Furthermore, in our team the lateral-PAA has been fabricated by Cojocaru et al. [14]. This sort of PAA planar structure increases the versatility of the PAA templates due to the inherent horizontal pore direction that they can be integrated in planar circuits, in particular they can be implemented in the photodetection and telecommunication domain [15] .

However some complications related with the device fabrication still remain, like the integration of the PAA with nano-objects as carbon nanotubes (CNTs) or silicon nanowires (SNWs) due to the oxide barrier layer at the bottom of the pores. The existing compact barrier layer hinders the electrochemical deposition of metals into the pores. The thickness of the barrier layer can be extremely important and determines any further applications of nanostructures formed by the anodization of aluminum. Moreover, concerning the lateral-PAA templates further studies must be performed in order to have a better understanding of the impact of the anodization parameters over the pore structure.

In this chapter the investigation of the PAA is presented in detail, providing the main characteristics of this template, the parameters involved in the fabrication and the influence over the pore structure, additionally the lateral-PAA will be introduced as well, pointing out the differences with the conventional vertical PAA templates in terms of the fabrication process and the impact of the anodization parameters over the pore structure.

1.1 The formation process of PAA

Aluminum easily reacts with oxygen at room temperature forming an alumina surface inert to oxygen, therefore such oxide layer avoids a further oxidation of the metal. The thickness of this oxide native layer is in the order of a few nanometers. When aluminum is exposed to the air, aluminum is oxidized like below:

$4\ Al + 3\ O_2 \rightarrow 2\ Al_2O_3$

Generally the anodization process is realized in an aqueous environment when a potential is applied between the aluminum and a highly inert electrode set as cathode. Therefore an electric field is established which assists the oxidize species through the metal oxide layer leading to an increment of the aluminum oxide thickness. The following reaction takes places at the aluminum surface:

$2\ Al^{3+} + 6\ HO^- \rightarrow Al_2O_3(s) + 3\ H_2O$

During the anodization process equilibrium is established between the chemical reactions at the cathode and the anode, leading to the following reactions:

$2\ Al \rightarrow 2\ Al^{3+} + 6e^-$ (at the anode)

$6\ H_2O + 6\ e- \rightarrow 6\ OH^- + 3\ H_2$ (at the anode).

Therefore the anodization evolves due to the existing electric field generated for applied anodized voltage, such electric field should be strong enough to move the ions across the metal oxide layer.

Two different types of anodic aluminum oxide can be obtained: the barrier-type anodic alumina or the porous-type anodic alumina, as is shown in figure 1-1. The structure of the resulting anodic alumina depends on the pH of the electrolyte. For basics or neutrals pH, a barrier-type anodic alumina is formed, as is shown in figure 1-1 (a). In such case, the native barrier layer is growing until it reaches a critic thickness from which the process cannot evolve anymore, because the strength of the electric field is not strong enough to transport the ions through this insulating layer. The thickness of this layer d_{BL} is proportional to the applied anodization voltage U_{Anod}, as given by the following equation:

$$d_{BL} = k * U_{Anod} \quad (1)$$

With k constant that depends on the electrolyte, the anodization temperature [2] and the duration of the anodization process [16]. This value can vary from 1-1.5 nm/V [17].

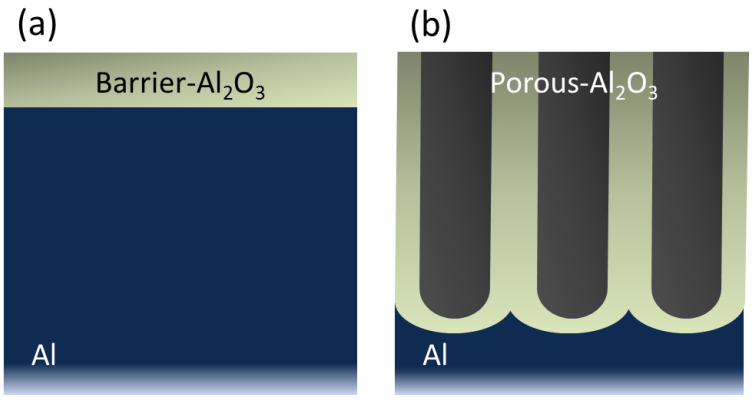

Figure 1-1. Schematic illustration of the two possible types of alumina: (a) Compact oxide barrier layer type or (b) porous alumina layer type.

On the contrary, porous anodic films as is shown in figure 1-1 (b), are generally fabricated under the anodization of aluminum in strong acids such as sulfuric, oxalic, phosphoric or chromic acid solutions. In this case, there are two concurring processes: the formation and dissolution of alumina. The following chemicals reactions take place at the aluminum surface depending on the kind of electrolyte:

$3SO_4^{2-} + 2Al^{3+} \rightarrow Al_2(SO_4)_3$ (in a sulfuric acid)

$3C_2O_4^{2-} + 2Al^{3+} \rightarrow Al_2(C_2O_4)_3$ (in a oxalic acid)

$PO_4^{3-} + Al^{3+} \rightarrow AlPO_4$ (in a phosphoric acid)

1.2.1 Species migration and the grow mechanism

The different species involved during the anodization process are well known. Those ions that have positive charges are moving towards the cathode, in contrast, the species with a global negative charge are moving to the aluminum. A schematic diagram is shown in the figure 1-2, the Al^{3+} ions generated at the alumina-electrolyte interface migrate without suffer any recombination. On the contrary, the ions with negative charges such as O_2^- and HO^- and all the

anions formed with the different acid electrolytes, moves to the alumina-electrolyte interface. Nonetheless the migration that takes place in the oxide layer is still not well understood [18]. Many efforts are focus in order to formulate a theoretical model that describes the migration that occurs within the oxide layer. Finally it is not well established if the alumina formation takes place at the alumina-electrolyte or at aluminum-alumina interphases. In the first case, the Al^{3+} ions migrate from oxide-metal zone to the oxide-electrolyte interphase and such ions react with the oxygen ions present in the electrolyte. On the other hand, if the oxide formation occurs at the alumina-aluminum interphases, the oxygen ions such as O^{2-} and HO^{-} migrate across the alumina layer reacting with the Al^{3+} ions generated in this region. The figure 1-2 takes into account the two ways.

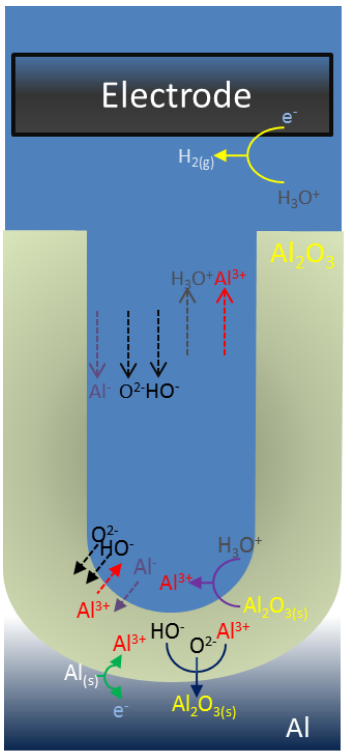

Figure 1-2. Schematic of the ion migration and the main chemicals reaction involved in the porous formation. Both alumina formations are considered in this representation, at the oxide-electrolyte interphase and at the metal-oxide interphase. The water formation and the acid-basic reactions are not represented for sake of simplicity.

Although the difficulties to well describe the oxide formation, it is important to highlight that the PAA formation is the product of the interaction of two complex processes such as the stress inside the alumina formed at the aluminum surface, and the field assisted dissolution under the application of an electric field in an acidic environment generally obtained by the electrochemically way.

The volume expansion induces the stress inside the oxide layer. The volume expansion is the relationship between the volumes of the initial aluminum and the final alumina formed layer. This value can vary between 1 and 2 depending on the anodization conditions [5]. The volume increases due to the incorporation of oxygen ions inside the aluminum. In addition depending on the acidic electrolyte, different ions can be incorporated into the pore walls, and these impurities generate an electrostatic field that imposes a local stress inside the alumina. Therefore the oxide layer acts as dielectric between the aluminum and the electrolyte, generating local charges in each interphase and leading to an electrostatic field that induces forces within the oxide layer.

1. 2. 2 Potentiostatic and Galvanostatic procedures

There are two procedures in order to perform the anodization process. The galvanostatic and potentiostatic methods, both procedures are schematized in the figure 1-3. The first technique consists in the application of a constant current between the electrodes. In the potentiostatic procedure a constant tension is applied between the anode and cathode.

Basically the pore growth formation occurs in a stationary regime. Therefore both procedures lead to similar results in this regime. However the beginning of the anodization process is not in a stationary phase, therefore there are some impacts over the pore structure due to the first moments of the anodization process [19]. For instance, as it shown in section 1.3.1 mostly of the structural parameters of the PAA depend on the applied tension, such as the pore diameter and the interpore distance. Therefore if a galvanostatic procedure is performed these parameters suffer variations until the stationary regime is reached. Taking into account

these properties, we have chosen the potentiostatic method in order to fabricate the PAA templates.

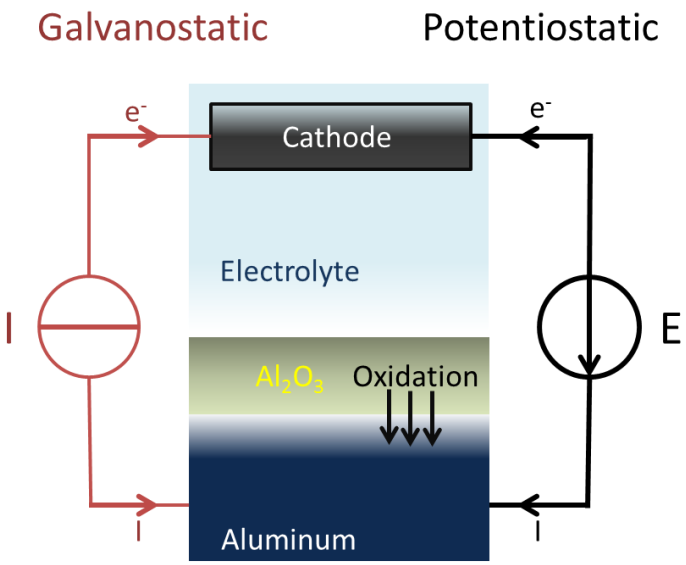

Figure 1-3. Schematic representation of the two existing procedures in order to execute the anodization process: the galvanostatic (red line) and potentiostatic (black line) procedures.

1.2.3 Stages during the pore growth formation

Different stages take place during the pore growth formation. Each phase is schematized in the Figure 1-4. Under a potentiostatic procedure, five different steps can be clearly identified as the anodization current evolves, where each step is related with a different growth pore regime.

When the process start, the aluminum has a native oxide layer of a few nanometers, thus when tension is applied the current is high because the resistance between the aluminum and the electrolyte is low. The aluminum surface suffers an abrupt oxidation, which corresponds to the second stage of the anodization process, where the thickness of the grown oxide layer leads to a current breakdown due to increment of the resistance in the system. As the

anodization evolves with time, the volume expansion of the alumina starts with a local dissolution of the oxide. The field assisted phenomenon plays a crucial role focusing in the defects of the surface, this local field concentration generates a preferentially ion transfer which induces an effective etching of the alumina. In such defecting sites, the first paths of the pores are created [2, 20] and such concentration leads to bigger alumina dissolution generating an increment in the anodization current, as shown in the stage three, the dissolution and the formation of alumina become coexisting processes . In this stage the pores are created, and the dissolution is only active at the bottom of the pores due to local field density. The oxide layer at the bottoms pores is thinner leading to a greater concentration of the field lines in these zones and it will be a bigger amount of species involved in the dissolution. This effect leads to two coexisting phenomenon: the local dissolution at the bottom of the pores and the growth of the oxide layer. Finally, when equilibrium between the dissolution and formation of alumina is established the pore growth takes place, corresponding to the stage four, the aluminum suffers an oxidation process creating the porous structure. As the anodization continues, the pores start to growth straight.

When the pores grow straight and parallel among then, the self-organization begins with a hexagonal pore array, with a period proportional to the applied tension. This is the final stage which occurs in a stationary regime where the pores length increases with the anodization time. The characteristic time in order to reach the self-organized pore growth regime depends mainly in the ion transport that takes places at the bottom of the pores, such value is determined by different anodized parameters, such as: applied voltage, electrolyte temperature, and concentration.

In conclusion, when the steady state regime is reached, the pore ordering degree highly differs at the top surface, where the pore formation begins from the bottom of the pores zone, as is schematized in the figure 1-4. This kind of porous structure is not desirable for the synthesis of nanostructures due to the irregular pathway of the pores that can block the nanostructure formation, and additionally a very low order distribution of pores are obtained at the top surface of the template. In order to avoid the described template configuration the two

step anodization process is introduced to achieve a highly ordered pore distribution with straight pores.

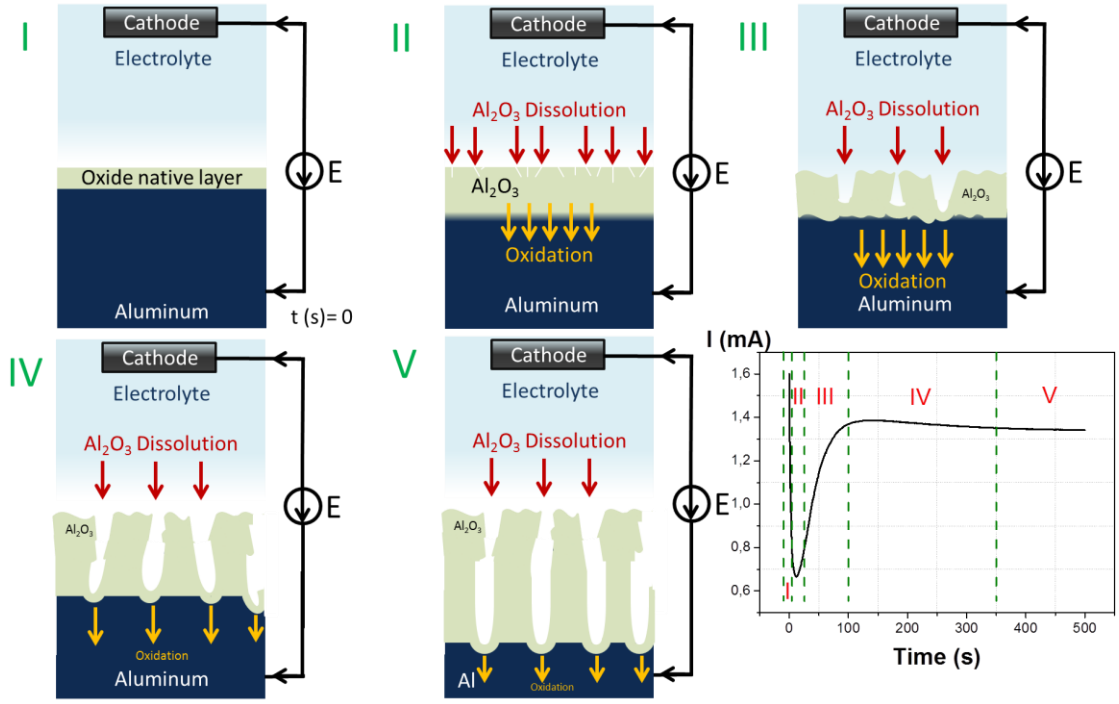

Figure 1-4. Schematic illustration of the steps involves in the pore growth during the potentiostatic procedure and their respective current time anodization curve pointing out every stage of the pore grow formation.

1.2.4 The Two Step anodization process

The pore self-organization structure is reached in the stationary regime when the equilibrium between the alumina dissolution and formation is established, and the pores grow parallel to the electric field lines generated between the cathode and the aluminum. Therefore the pore distribution at the top of the alumina surface has low ordering degree. The pore ordering degree is strictly related with the fact that the pore pathways at the beginning of the process are focused in the defects of the aluminum surface. These sites act as the seeds of the futures pores. In principle many procedures [21, 22] can be applied to obtain a smooth

aluminum surface to reduce the surface defects, anyway the pore ordering degree is not close to an ideal hexagonal array.

A significant improvement concerning the pore ordering was introduced by Masuda and Fakuda [23] when they proposed the two step anodization process. This technique exploits the fact that the initial sites of the pores are the defects of the surface. The methodology consists in the formation of PAA layer and the subsequent removal, the procedure of this technique is schematized in the figure 1-5. The first anodization process is performing until the self-organization is reached; therefore the bottom pores distribution has a higher order degree than the pore distribution at the top surface of the alumina. Then such layer is removed on etchant solution that only eliminates the alumina leaving the nano-imprints of the bottom pores in the aluminum surface. Finally a second anodization process is carried out, however in this case the field lines are focused in the nano-imprints of the previous ordered bottom pores. Therefore the pores growth formation begins straight following a hexagonal array.

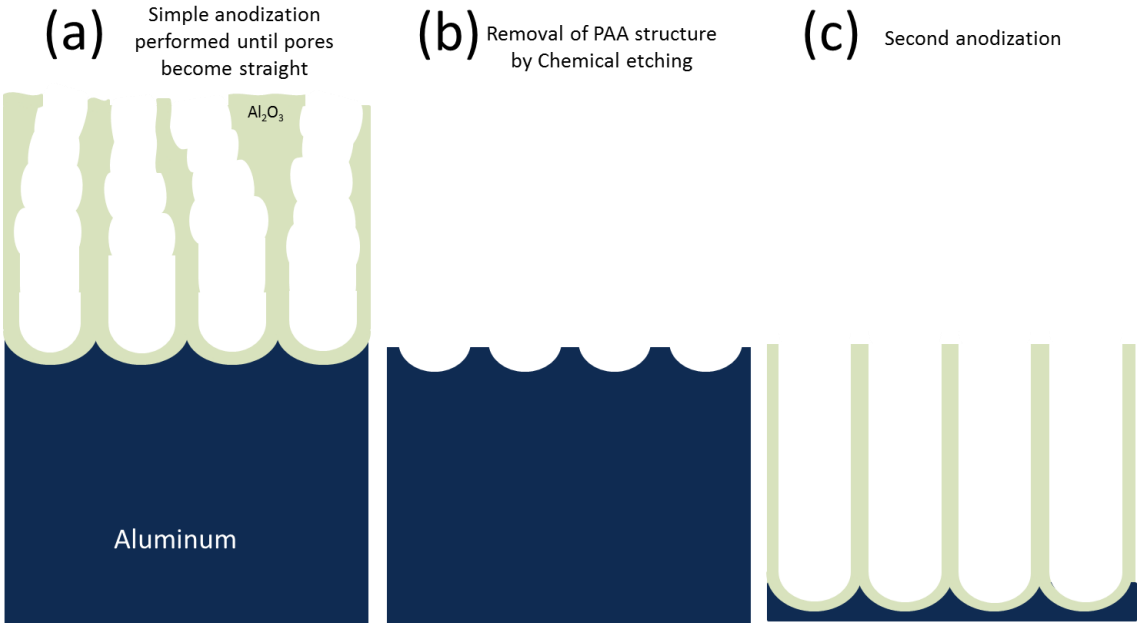

Figure 1-5. Schematic diagram representation of the PAA structure in the different fabrication steps involved in the two-step anodization process. (a) First anodization performed until the pores grow straight. (b) Removal of the porous alumina layer in a chromic acid solution. (c) Second anodization process.

The figure 1-6 shows the differences of the pore ordering degree between a PAA structures obtained via a simple anodization process, figure 1-6 (a) and a PAA structure fabricated by the two step anodization method, figure 1-6 (b). In both cases a previous electropolishing process has been applied. This procedure will be described in detail in the experimental section 1.5.3.

The main advantages of these techniques are: the low cost of implementation, the easy execution of each step concerned for the PAA fabrication, and the simple control of the pore array, thus the pore structure of the PAA can be controlled adjusting the parameters involved in the anodization process. Anyway a previous polished step is required to obtain highly ordered pore array. In contrast, the biggest limits imposed by this techniques are that, the perfect pore ordering is reached in domains of the order of μm^2 sizes [24], such constrain is caused by grain boundaries and dislocations density in the metal substrate. A drawback inherent of such technique relies on the fact that is required an initial sacrificial layer that will not be present in the final porous alumina. This is a big constraint for device fabrication on Si supports because very thick layer of aluminum has to be deposited.

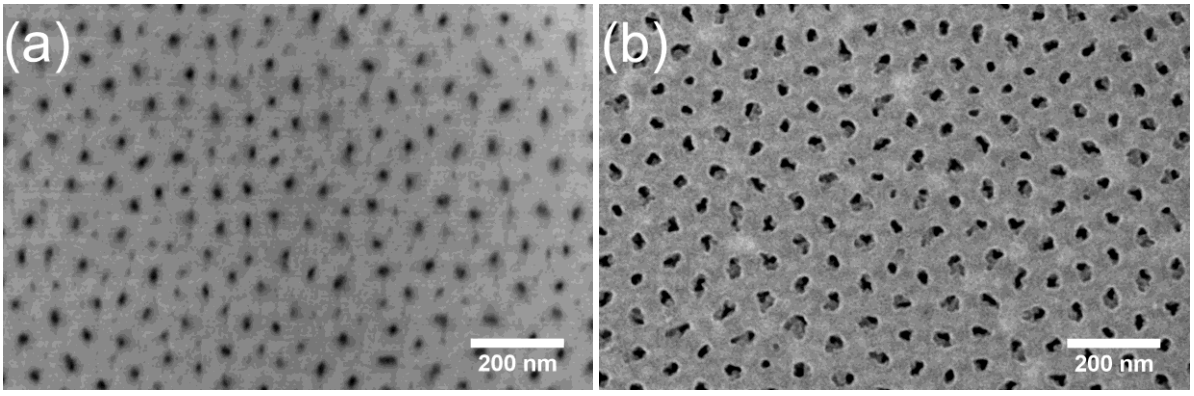

Figure 1-6. SEM top-view images of PAA fabricated by the (a) simple anodization process, the average pore diameter is (22 ± 5) nm and (b) two step anodization process, the average pore diameter is (32 ± 4) nm.

Many techniques have been developed to reach a perfect pore ordering degree. However these techniques involve: lithography steps [25, 26], plasma treatments [27-31], mask

fabrications [32-36], atomic force microscopy implantation or a combination of these techniques. Therefore these procedures have many disadvantages because there are very costly, time consuming, and all of them present scale size limitations. In addition, the procedures that involved a mask have a low versatile degree because only a few pore size cell structures can be fabricated.

In conclusion, depending on the future application a compromise among the pore ordering degree and the implementations constraints must be taken into account in order to choose the procedure to create the pre-determined sites that will lead origin to the pore formation.

1.2.5 Differences between the simple anodization and the two step anodization

There are some differences between the kinetics of the first and the second anodization performed over the same sample under identical anodization conditions. Figure 1-7 shows the current curves of the first and second anodization as function of time.

In the second anodization process, the electric field is concentrated on the nano-imprints created due to the elimination of the PAA layer (formed during the first anodization process). This phenomenon has different impacts over the kinetics of the pore formation. During the first anodization the current breakdown is higher because a thick alumina layer is created during the first moments where only the pathways are created in the defect sites; on the contrary during the second anodization, the pores are ready to grow since the nano-imprints act as the defects sites. This effect also influences over the alumina formation and dissolution, which is reached faster in the second anodization as the pores begin to grow straight leading to an easier ion transport than in the crooked pores of the first anodization.

Therefore the pore rate formation is bigger in the second anodization. Another difference is that in the stationary regime, during the second anodization current slightly

decreases as the pores become longer since the ion transport becomes more difficult. The same effect is observed for long first anodization process.

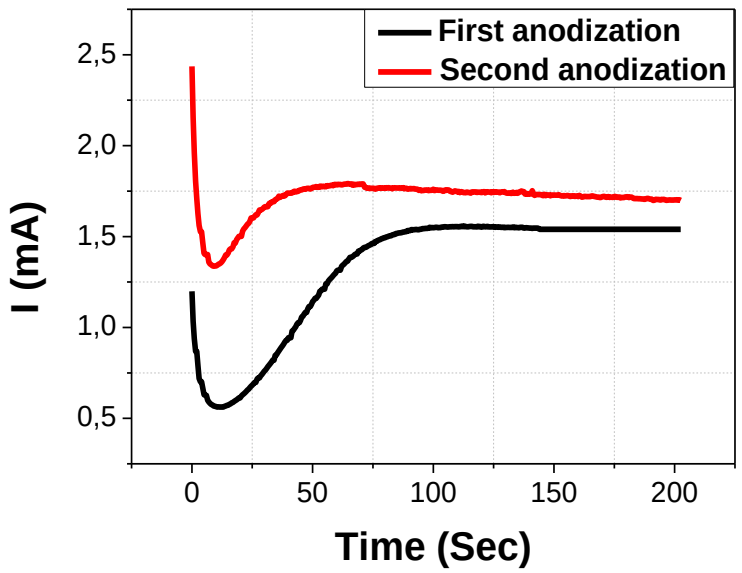

Figure 1-7. Anodization current time curves of the first anodization (black line) and second anodization (red line) processes carried out in the same sample under identical anodization conditions.

Concerning structural differences, the pores obtained by a two-step anodization process are straight from the top surface until the bottom of the pores, as contrary for the PAA fabricated by a simple anodization, where the pores are crooked close to the top surface and they begin to be straight as the process evolves. Regarding the pore diameter, the pores formed by a simple anodization method are smaller than the pores obtain by a two-step anodization process. The figure 1-6 contains the main diameter for both cases, resulting (22 ± 5) nm for the PAA obtained by the simple anodization method and (32 ± 4) nm the pore diameter formed through the two-step anodization method. PAA structures fabricated by a simple anodization step show much smaller pore diameters at the surface than those for obtained through a second anodization process, since at the beginning of the first anodization, a thick alumina layer is formed in which slowly pathways are created. This again evidences the difference of the formation rate between the first and the second anodization processes.

1.3 Factors that influence the PAA structure

Self-organized porous anodic alumina can be described as close packed array with hexagonal ordered cells with pores in each center cell. The PAA are characterized by several structural parameters such as: pore diameter, interpore distance, oxide barrier layer thickness, and pore length. Figure 1-8 schematized a typical PAA structure pointing out the main parameters. The versatility of such type of template relies in the fact that the geometrics features of the cell structure can be adjusted controlling the parameters involved in the anodization process. For instance the anodization voltage has a huge impact over the cell structure. The type of electrolyte determines the operational voltage range in which the PAA has an order hexagonal array. The anodization duration basically defines the pore length. The electrolyte concentration and the anodization temperature generally influence over the pore rate formation. However, in the present work we verify that in the lateral-PAA template has a strong impact over the pore diameter. In addition the cristanility of the aluminum substrate or the crystal orientation impacts over the pore ordering degree [37-40].

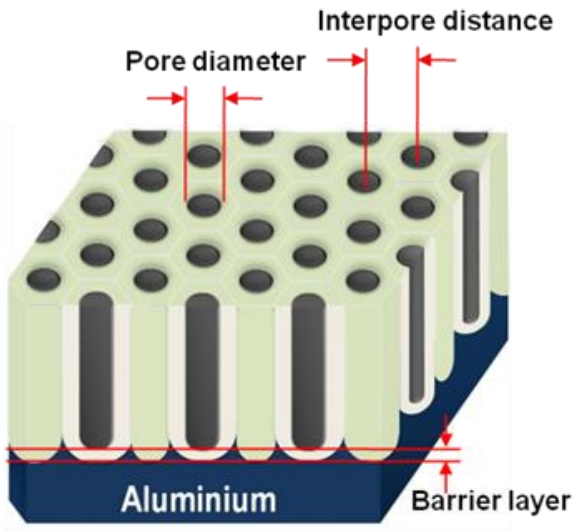

Figure 1-8. Schematic representation of the porous anodic alumina and their cell structure parameters.

1.3.1 Anodization voltage

The most influential factor during the anodization process is the applied tension. It affects most of the structural features of the PAA, such as the pore diameter, the interpore distance and the oxide barrier layer at the bottom pores.

The pore diameter of the PAA structure is linearly dependent of the applied voltage with a proportional value λ_P that can vary from 1.3 nmV^{-1}[41]. Therefore the pore diameter D_P can be expressed in terms of the anodization voltage U_{Anod} as:

$$D_P = \lambda_P * U_{Anod} \quad (2)$$

It is generally accepted that the interpore distance (D_C) of anodic porous alumina is linearly proportional to the forming potential in the stationary regime growth of anodic porous alumina with a proportionality constant λ_C of approximately 2.5nmV^{-1} [42]:

$$D_C = \lambda_C * U_{Anod} \quad (3)$$

A depth study of aluminum anodization in sulfuric and oxalic acid was performed by Ebihara et al. [43, 44]. They established the following relation depending on the applied voltage range.

H_2SO_4: $D_C = 12.1 + 1.99 * U_{Anod}$ $\quad (3 - 18V)$

$C_2H_2O_4$: $D_C = 14.5 + 2 * U_{Anod}$ $\quad (U_{Anod} \leq 20V)$

$D_C = -1.70 + 2.81 * U_{Anod}$ $\quad (U_{Anod} \geq 20V)$

In addition the anodized voltage determines the ion transport ratio, higher voltages lead to higher anodized currents. Therefore the pore rate formation is determined by the applied potential. The anodization performed at low voltages is denominated as mild process, where the pore rate formation is low, consequently long times are required to achieved a pore order at

the bottom pores. On the other hand, a hard anodization is obtained when a high field is applied. This process produces highly ordered PAA membranes with a fast film growth rate. The operational range and the optimal order of the PAA structure are determined by the anodization electrolyte.

1.3.2 Type and concentration electrolytes

The kind of electrolyte firstly determines the type of anodic alumina obtained. Depending on their pH a barrier-type or porous-type can be obtained. For the non-porous regimes, neutral pH's have to be employed. For the porous anodic alumina type pH<4 is required. In addition the concentration determines the velocity of the reaction, the rate of the species migration and the speed of the chemical reactions. However there are not concluding results on the impact of the electrolyte concentration over the pore structure [45]. Besides, the type of electrolyte influences over the global organization of the PAA. The most common acids are the oxalic, sulfuric and phosphoric acids.

The properties of the PAA formed by anodizing are also related to the electrolyte species incorporated into the oxide walls. The incorporation of anions modifies the space charge accumulation in the porous and barrier-type alumina films [46]. The duplex structure of the cell walls is described in the figure 1-9 where the cell structure contains two regions a pure alumina wall and anion incorporated layer. It was reported that the thickness of the inner layer varies depending on the electrolyte implemented in the succeeding order [47]:

$$H_2SO_4 < C_2H_2O_4 < H_3PO_4$$

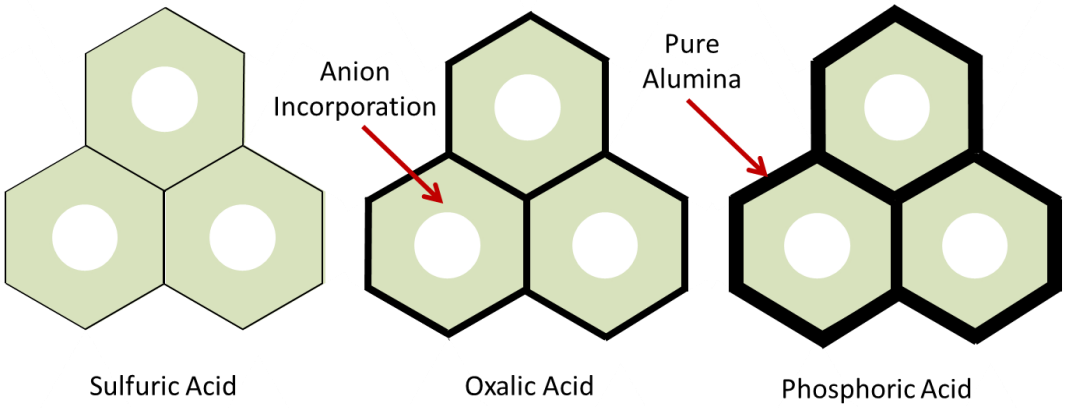

Figure 1-9. Schematic representation of the inner and outer pore cell structure depending of the anodized electrolyte: Sulfuric acid, Oxalic acid and Phosphoric acid. The thickness of the inner layer varies depending on the electrolyte implemented in the following order: H_2SO_4 < $C_2H_2O_4$ <H_3PO_4.

However, it is important to point out that the pore diameter is not directly sensitive to the nature of the electrolyte. Each electrolyte has different values in terms of ion conductivity and dissolution ratio, these factors impacts over the anodization current. Since the increment of the applied tension leads to a higher density of current, therefore the anodized solution determines the operational conditions in which the self-organized PAA structure can be obtained. There is a threshold voltage for each particular electrolyte, for lower applied tension than this value, the electric field generated is not strong enough to assisted properly the alumina dissolution and formation, thus the stress generated in the oxide layer is not balanced, leading to a disordered structure. On the other hand, high voltages lead to high currents, increasing the ion transport, thus increasing the rate of O_2 produced during the anodization. These gas bubbles generated from water electrolysis continuously emerge at the sample surface. The abundant gas bubbles hinder the ion diffusion, which will lead to the irregular arrangement of the pore cell and disrupts the self-ordering process of the pores, in spite of the process is performed under permanent stirring. Higher voltages can leads to the dielectric breakdown of the barrier layer and burned the sample. So for a given electrolyte, the upper limited voltage in self-ordering range is lower than the breakdown tension, and there is a

narrow range of anodizing voltage within which self-ordering can occur. For instance for oxalic acid the voltage range is 20-80V with an optimal order degree typically when the anodization is performed at 40V [48-50], for sulfuric acid the operational range is between 7-70V [48-50] with the best pore order structure is obtained when the anodization is carried out at 25 V and for phosphoric acid the voltage range is from 60-235V and the optimal voltage is at 195V [42, 48-50].

Finally the type of electrolyte defines the operational voltage range in which a self-organized hexagonal pore array can be obtained; such voltage range directly determines the main pore structures of the PAA templates, such as the interpore distance, pore diameter, and barrier oxide layer thickness. In conclusion the type of electrolyte not only defines the, inner and outer pore cell structure, but additionally indirectly determines the range of the characteristics length of the pore structure.

1.3.3 Anodized duration

The anodization duration determines the pores length. Basically longer anodization leads to longer alumina layers. This parameter has a huge influence over the pore order when a two-step anodization process is performed. For highly ordered close-packed hexagonal pore array, mechanical stress between neighboring pores has to be stabilized in order to distribute mechanical stress equally, so long anodization is required in order to achieve this mechanical stress equilibrium. Therefore for a longer anodization duration leads to a better pore ordering at the bottom pores. The second anodization is carried out in pre-textured surface where the nano-imprints are situated at the bottom pores location of the former PAA layer, therefore it is expected a better pore ordering degree in the final PAA structure obtained in the second anodization when the pores generated at the first anodization are longs and straight.

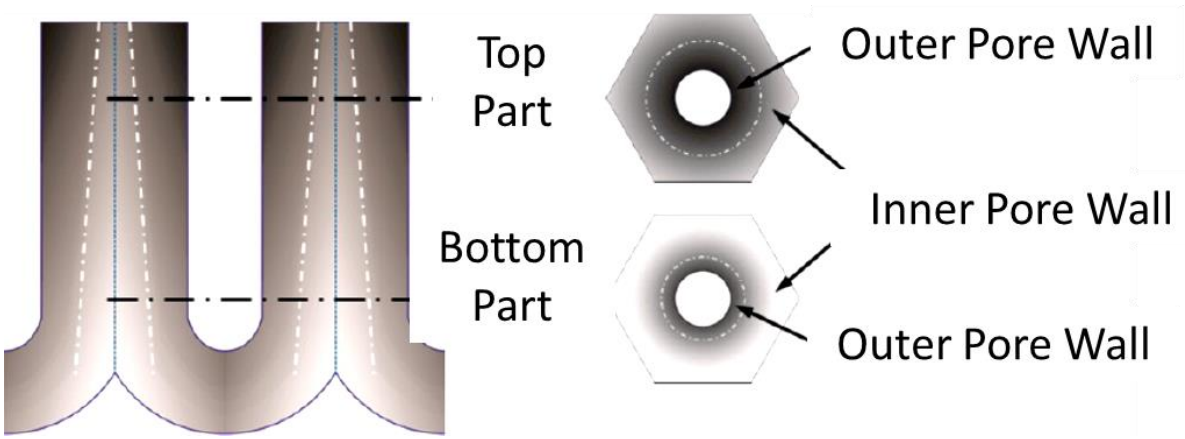

Figure 1-10. Schematics illustrating of the non-uniform distribution of anions incorporated in the outer pore wall. A different level of impurity in anodic oxide is depicted with gray scale [51].

For very long anodization process, of the order of 12 hours, the duration of the anodization also impacts over the anion incorporation to the outer walls of the cell structure, as the pores growth, the ion transport is more difficult, which leads to decrease the density of current in spite of the applied potential is the same, so the pore diameter remains the same; however a gradient of impurity concentration is established as the concentration of the solution decreases when the anodization evolves [51]. Figure 1-10 described this situation where the impurities along the grow direction vary as a function of the anodization time.

1.3.4 Electrolyte temperature

The anodization temperature determines the kinetics of the process. An increment of temperature accelerates the ion transport and the chemical reactions leading to an increment on the current density. Therefore the anodization temperature basically impacts over the pore formation rate leading to a faster self-organization of the pore array. However a very fast

anodization rate can generate O_2 bubbles which are difficult to remove from the anodized surface affecting the pore ordering degree.

Concerning the structural features of the PAA, the anodization temperature mainly impacts over the thickness of the oxide barrier layer. Higher the electrolyte temperature leads to lowers thickness of the oxide layer. This is attributed to the direct result of an enhanced field-assisted dissolution of oxide at the oxide/electrolyte interface. The oxide barrier thickness plays a critical role in the electrodeposition process of metal nanoparticles. Consequently, the control of such barrier results of particular importance for a further nanoparticle deposition within the PAA templates.

On the other hand, the anodization temperature has not great impact over the pore diameter and the interpore distance for the conventional vertical PAA templates [52, 53]. However in the present work, a detailed analysis of the influence of the anodization temperature over the pore structure of lateral-PAA and vertical-PAA templates has been performed. The results reveal that under the horizontal configuration the pore diameter is highly sensible to the electrolyte temperature.

1.3.5 Aluminum substrate

The geometric features of the formed PAA structures mainly depend on the anodization conditions. However, the kind of substrate also impacts over the formed PAA structure. The systematic utilization of the anodic alumina would require the spatial ordering of the pore channels to be controllable and homogeneous over large areas, so a very desirable characteristic of the anodic alumina is the high regularity of the pore configuration. Besides the anodization conditions, the pore order degree depends on the impurity concentrations, size of impurities, size of aluminum grains, texture and surface morphology [54, 55]. Moreover, the difference in the structure of anodic oxides films grown on various faces of single crystal substrates has been studied [37-40, 55, 56]. The best ordering of porous structure has been

observed on the grains with (1 0 0) orientation, while the structure with the worst ordering is formed on the Al grains with nearly (1 1 0) orientation Ng et. al [39] attributed the relation between the pore ordering and the crystal orientation as product of the influence elastic anisotropy over the oxide flow.

1.4 Lateral-PAA templates

The self-organized PAA templates enable the integration of collectively nanostructures arrays into functional devices. However the conventional vertical-PAA templates cannot be incorporated in planar integrated circuits. Therefore the development of PAA templates that entails a planar architecture will widely open the application domain of devices based on PAA templates. Besides, with lateral anodization directly contact of organized nanostructures can be achieved between two electrodes through the synthesis of nano-objets within lateral-PAA templates.

The lateral-PAA templates were firstly fabricated by Masuda et. al. [57], however an increase of quality and reliability concerning the template fabrication arrived several years later, when Cojocaru et. al. [58] have introduced the practical fabrication of lateral-type porous anodic alumina starting from patterned aluminum stripes. As result of such work, many studies have been focused on the fabrication of lateral-PAA templates with the goal of the fabrication PAA functional devices [59-62].

On the other hand, the fabrication process of the lateral-PAA templates is much complex than the conventional vertical type. For instance, it is necessary to encapsulate an aluminum stripe in order to just expose a certain side of the aluminum in the electrolyte bath. Otherwise, the pore formation occurs over the whole aluminum surface. The situation is schematized in the figure 1-11 (a), on the contrary when a capping layer covers the aluminum stripes, the anodization takes place only on the exposed side face of the aluminum stripes as shown in figure 1-11 (b).

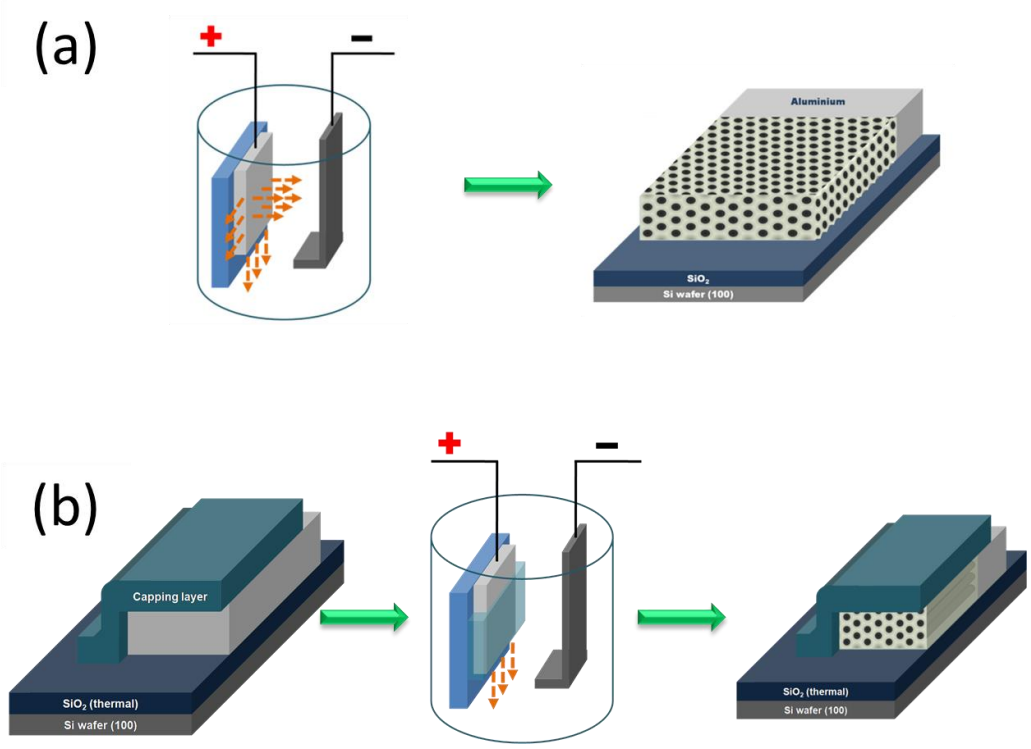

Figure 1-11. Schematic representation of anodization cell and the resulting pore structure depending on the (a) uncapped aluminum stripe and (b) capping layer configurations.

The capping layer induce constrains effects that don't exist in the case of the conventional vertical-PAA structures. Therefore a deeply study of the influence of the anodization parameter over the pore structure must be performed, since it is not possible to directly transfer the knowledge from the vertical PAA fabrication to the lateral type.

1.5 Experimental procedure

Two different classes of templates have been fabricated: the conventional vertical-PAA type and the lateral-PAA type. Concerning the anodization process, the techniques involved in

the fabrication of both kinds of templates are similar. Firstly an electropolishing process must be performing in order to flatten the aluminum surface. Afterwards, the anodization process can be carried out, where a disorder pores distribution is obtained at the top surface; on the contrary as the anodization evolves an order hexagonal array is reached at the bottom pores. For the two step anodization method, the first anodic layer is removed in a chromic acid solution and the second anodization process is executed, in this step the pores start to grow in a pre-patterned surface. Therefore, a self-ordering process is obtained from the initial moment of the anodization. In order to eliminate the oxide barrier layer at the bottom pores, at the end of the anodization process an exponential voltage decrease is applied. This method exploits the linear relation between the applied potential and the thickness of the oxide barrier. The idea consists in a gradual descent of the anodization in order to continuously thin the oxide barrier layer at the bottom of the pores. Such layer is completely removed after the application of the chemical etching. After the implementation of the mentioned processes the template is ready for nanoparticle deposition and further nanostructure growth.

1.5.1 Anodization experimental set-up

The experimental set up for the anodization process is shown in the figure 1-12. The sampler holder is made of Teflon. This device has been designed in order to perform anodization in circular surface of 0.38 cm^2, thus always the same area is anodized and exposed to the electrolyte solution. Due to the fact that during the anodization process bubbles are generated as products of chemical reactions, a constant strong stirring is required. Otherwise, the bubbles isolate certain substrate area. The current flows between graphite (this electrode that doesn't react with the electrolyte) and an aluminum foil. Additionally, the aluminum foil is in contact with a copper electrode inside the Teflon cell. In order to apply the potential and measure the anodization current, a power supply and a current meter are connected. The

applied voltage is adjusted by software. The bath temperature has been controlled trough a thermoregulator.

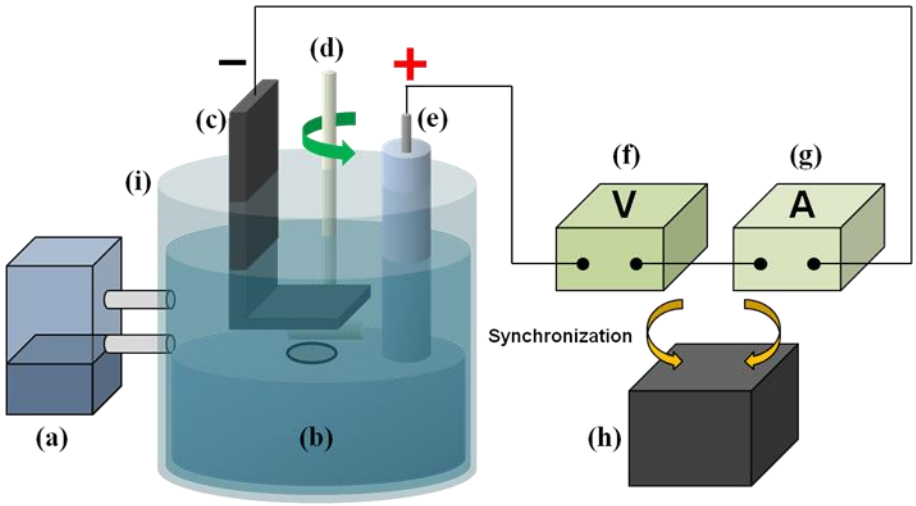

Figure 1-12. Schematic diagram of the experimental set-up used for the anodization. (a) Thermoregulator, (b) Sample holder for holding samples, (c) Graphite electrode, (d) Motor-controlled rotator for stirring solution, (e) Electrode, (f) Power supply, (g) multimeter to measure current, (h) computer to operate the potentiostat/galvanostat, (i) thermal controlling beaker with flowing oil and the beaker for putting solution and sample holder.

1.5.2 Electropolishing process

The first instants of the anodization process strongly depend on the surface topography, due to the electric field is concentrated in the defects sites [63]. In order to minimize the surface defects over the aluminum substrate an electropolishing process has been performed. For the conventional vertical-PAA templates (The electropolishing process for the later-PAA templates is explained in the section 1.5.5), the electropolishing solution consists in a mixture of 70% perchloric acid ($HClO_4$) and 95% ethanol (CH_3CH_2OH). The voltage has been set at 20V to

obtain the flattest surface. The electropolishing solution temperature has been kept at 5°C during 6 minutes. A constant stirring is applied to remove the bubbles produced during the process.

1.5.3 Two anodization process

After the application of the electropolishing process, the two anodization process can be performed. In the present work 0.3 M oxalic acid has been used as electrolyte. The range of temperature has been varied from 10 to 25°C. The voltage range has been varied from 20-60V.

During the first anodization process, a disordered pore distribution is formed at the alumina surface, after a certain anodization time the pores growth straight and a hexagonal pore array is obtained on the bottom pores. In all cases the first anodization process has been performed during two hours. Then first alumina layer is removed in a chromic acid solution, consisting in a mixture of 0.17 M chromic acid and 0.6 M phosphoric acid at 60°C. The duration of such process depends on the pore growth rate formation. Typically for anodization process performed at 40V in an oxalic acid solution, in order to completely eliminate the anodized layer it is necessary at least to dipped the sample in the chromic solution during half of the time of the first anodization duration [64]. Therefore the time duration of the first anodization process is taken as reference. Finally, the duration of the removal process has been set up as the half duration of the first anodization process for anodization voltages lowers than 40V. Therefore the PAA is dipped in the chromic acid solution during one hour. In contrast for anodization voltages higher than 40V, which correspond to a higher pore growth formation rate formation, the duration time of the alumina removal in the chromic acid solution has been set up as equal to the first anodization process time duration, is to say 2 hours. Such dipped times in the chromic acid solution guarantied the entirely elimination of the PAA layer. Subsequently, the second anodization process has been executed over an aluminum pre-textured surface where

the nano-imprints have been generated due to the removal of the former PAA layer. The second anodization duration has been varied from 90 seconds up to 1 hour.

1.5.4 Barrier thinning process

The main problem in order to utilize the PAA built electronic devices relies on the compact oxide barrier layer present at the bottom of the pores. Such layer is highly resistive and insulates the pores from the aluminum. Therefore the presence of such layer introduces many difficulties for the device fabrication, for instance for the metal nanoparticle electrodeposition it is necessary to overcome the potential induced from this layer to make an electrical contact. Additionally, the thickness of the barrier layer varies from one pore to the next one, all over the surface, so the thickness barrier for each pore is slightly different. For the multiple device applications it is mandatory to control the uniformity and the thickness of this oxide barrier layer.

Many efforts have been performed in order to reduce or eliminate the oxide barrier layer. The most common process is the wet chemical etching [65]. Typically the PAA is submerged in a H_3PO_4 solution that selectively etches the alumina. However, this solution attacks the alumina isotropically leading to a pore widening process. In addition, this process can be applied to obtain a bigger pore diameter [66]. Thus, such process constrains the minimum pore diameter for a determined cell structure. On the other hand, the dry etching is an alternative route in order to remove the oxide barrier layer. For instance, pore opening process can be performed using a dry etching with an Ar^+ ion beam [67-70], Ga^+ ion beam [71, 72] and with CF_4 ions [73]. Nevertheless, these techniques involve sophisticated and costly technologies.

An interesting approach was introduced by Furneaux et. al [74] which consists in sequentially decrease the voltage at the of the anodization process, exploiting the dependence between the thickness of the oxide barrier layer and the anodization potential applied, expressed in the equation (1). For each applied voltage a corresponding pore cell structure is determined. Subsequently, at the end of the anodic layer, the voltage is constantly decreased in order to thin the oxide barrier layer. Nonetheless, the voltage decrease has to be properly adjusted. Due to the voltage impact over the pore structure, at every potential drop, the system enters in a new equilibrium state where the alumina dissolution and formation leads to another pore cell structure. This new cell structure has a less thick oxide barrier layer, but in addition, a minor interpore distance and pore diameter than the one's obtained with the previous applied voltage. Therefore a branched structure can be obtained depending on the shape and rate of the voltage decrease [75]. For further nanostructure growth within PAA templates, such multi-branched structure is not desirable since the pores are not straight anymore which is hindering for instance a deposition of the nanoparticle that is fundamental for the growth of carbon nanostructures or silicon nanowires [76].

The voltage decrease has to be established taking into consideration that at every potential fall, the system enters into a new equilibrium state with their respective pore cell structural characteristics length which depends on the anodization parameters. Therefore, a drastic change of applied potential can stop the anodization because the system cannot be self-adjusted into the new anodization conditions, leading to an interruption of the porous formation. Under the described situation the oxide barrier layer remains at the bottom of the pores.

In conclusion the anodization voltage has to be decreased preventing a branch structure formation, which is associated with long time between every voltage drop, and on the other hand i we must avoide the interruption of the anodization process that takes places when the anodization potential changes are too fast.

As the barrier layer thickness is proportional to the applied anodization potential, the voltage decrease at any time should always be proportional to the previously applied voltage. This can be expressed by the following equation:

$$\frac{dU}{dt} = V_0 * U \quad (4)$$

Where U is the anodization voltage, t the time and V_0 a constant value. Finally, the anodization voltage results,

$$U(t) = V_0 * \exp(-\eta * t) + V' \quad (5)$$

Therefore there are three parameters to establish. In one case, V_0 and V' determine the shape of the exponential voltage decrease. On the other hand, η defines the voltage decay rate. In the present work these values were fixed taking as reference a previous work performed in our group by Marquardt et. al [76] who probed an efficient thinning barrier process. On the other hand, in the present work, we have proved that such exponential decrease parameters lead to a branched structure. Such structure at the bottom of the pores has been studied by lamella preparation and subsequently by TEM observations. In addition, by the nanoparticles deposition in chapter 2 an interesting approach is presented in order to obtain a quantitative value of the branches created per primary pore, depending on the anodization conditions. Consequently, the exponential voltage decrease parameters have to be optimized in order to obtain straight along all the PAA structure.

Finally in order to completely remove the oxide barrier layer at the bottom of the pores, in addition of the exponential decrease applied at the end of the anodization process, a wet chemical etching in a 0.3 M H_3PO_4 solution has been performed at 30°C during 25 minutes.

1.5.5 PAA-Lateral templates type fabrication

In order to fabricate the encapsulated aluminum stripes different steps are required, involving, metal evaporation, lithography, chemical wet etching, PECVD deposition and reactive

ion etching (RIE). The procedure for the lateral-PAA template fabrication is schematized in the figure 1-13 (a) pointing out the structure configuration obtained at each implemented process.

Firstly, aluminum is evaporated on p-type silicon wafer substrate in an evaporator Plassy MEB 550S. The main evaporation parameters are the evaporation rate, the evaporation current and the pressure of the chamber. In our case the evaporation rate has been set at 0,3nm/sec, the current at 20 A under a pressure of the order of $1.00xe^{-7}$ Torr. Subsequently, a photolithography has been performed. The mask pattern is also schematized in the figure 1-13 (b), indicating the channel region, that separates the aluminum electrode (zone A) with pore structure (zone B). Such mask contains 6 kinds of channel width while the channel length is fixed (5 µm), and for each channel width, there are 5 electrodes exists (same dimension), D1 to D5.

For the first photolithography step, negative resin AZ 5214 has been deposited over the sample in a spin-coating system with a rotating of 4000 rpm, subsequently the samples have been heated at 110°C during 30 seconds. The photolithography step is performed in a double-sided aligned system. The aluminum stripes have been generated through the aluminum etching at room temperature during 8 minutes, in a mixture solution of 1-5 % HNO_3 (for aluminum oxidation), 65-75 % H_3PO_4, 5-10 % CH_3COOH (for wetting and buffering) and H_2O dilution to define the etch rate at given temperature. In order to deposit the material of the capping layer the PE-CVD process has been performed. For the silicon nitride deposition (SiNx) the pressure of the chamber has been set at 1 mbar, the temperature set at 350°C, the HFSiN flow was and the plasma power at 20 sccm and 50 W. After the SiNx deposition, the second photolithography step is performed. The substrate is deposited in a spin-coating system with a rotation of 5000 rpm and a Resine Shipley S1813 is spread out onto the substrate. Then the substrate is deposited onto a hotplate during 60 seconds at 115°C. For the proper lithography step, the illumination by UV-light is performed during 180 seconds, with wavelength of 380 nm and power density of 25 mW/cm^2. Subsequently the sample is dipped in a 351 development solution during 25 seconds. The reactive ion etching steps have been executed in an Advanced Vaccum RIE system. This stage is carried out in order to remove SiNx zones where the resin is

not present. The process is performed at room temperature, under power etching of 100 W and a pressure of 0.5 mbar. The final step, is to etch the aluminum, this process is carried out with Al etch solution at 60°C during 20 seconds. After this final step, one aluminum surface exposed side is obtained.

However before the pore growth takes place, the electropolishing process is performed. For these kinds of templates a modified electropolishing solution has been prepared in order to prevent a fast consummation of the aluminum. The solution is a mixture of 70% HClO4, ethanol and Isopropan-ol (IPA) with 1:14:15 volume ratio. The process was carried out at 5°C applying 5V during 2 seconds. Such electropolishing process is compatible for lateral-PAA template fabrication, as the aluminum surface is smoothened while the aluminum surface is not placed too deeply inside capping layer. Finally the anodization process can be performed and the pore formation will occur only in the planar orientation. Concerning the barrier thinning process at the bottom of the pores, both the exponential voltage decrease parameters and the wet chemical etching in the 0.3 M H_3PO_4 solution procedure, have been chosen identically for the fabrication of the vertical-PAA templates and the lateral-ones.

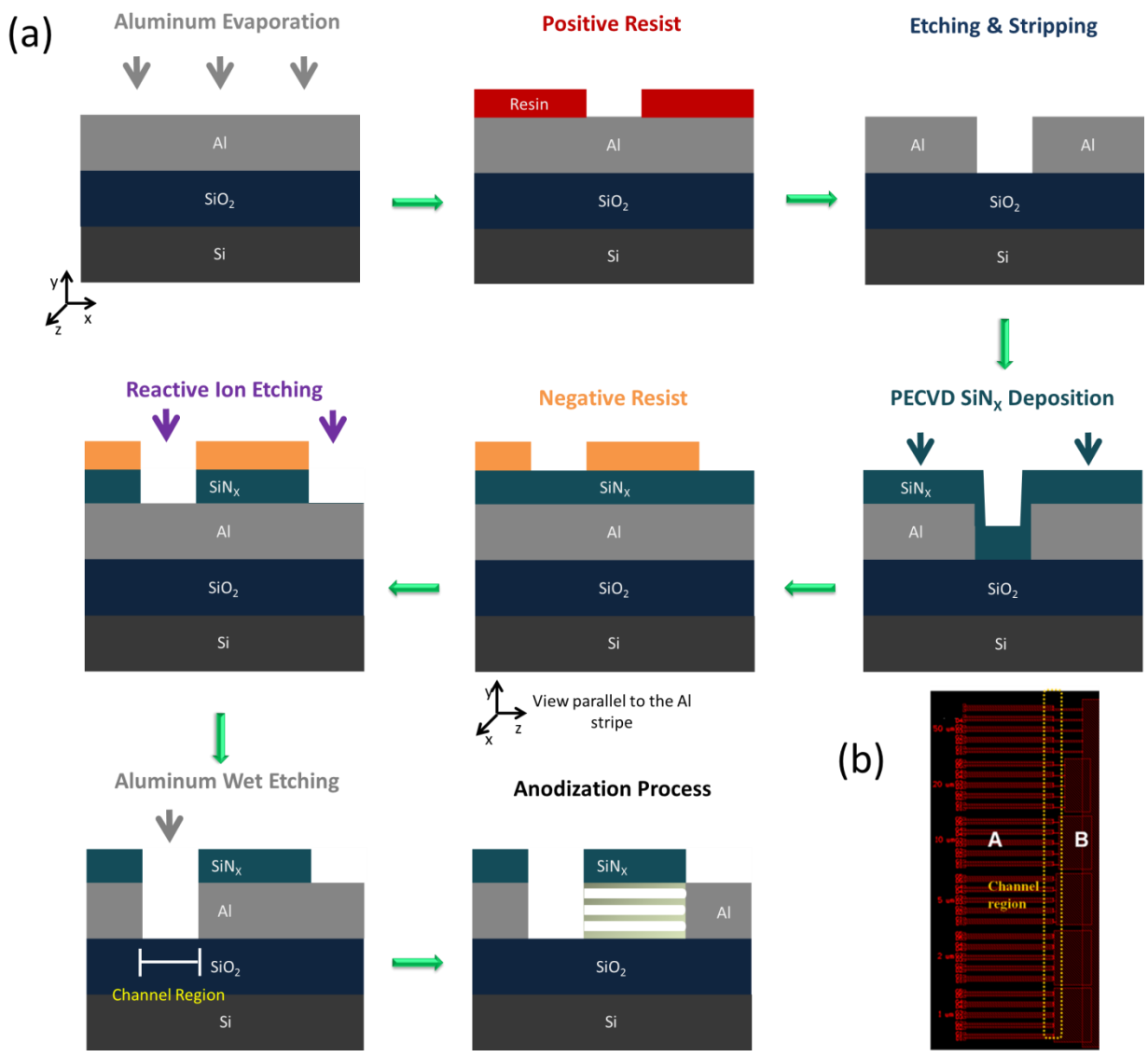

Figure 1-13. (a) Schematic diagram of the aluminum encapsulation fabrications pointing out the different steps involved: Aluminum deposition, Positive photoresist deposition for lithography step, aluminum etching for stripes generation, SiN_x layer deposition to create the capping layer, second lithography step with a negative photoresist resin, reactive ion etching to create the channel between two terminals, and the anodization process for the lateral pore formation. The mask used for the lithography steps is also included pointing out the zones A and B of the lateral template. (b) Designed mask for lateral-PAA templates indicating the channel region.

.

1.5.6 Characterization techniques of the PAA structure

The PAA templates have been characterized by Field-Emission Scanning Electronic Microscopy (FE-SEM, HITACHI S4800). Additionally, in order to obtain a high description of the pores structure cross-section Transmission Electronic Microscopy (TEM) analyses were performed using a Titan-FEI electron microscope operation at 200kV and equipped with a Cs probe corrector and a SuperX detector for EDS chemical analyses.

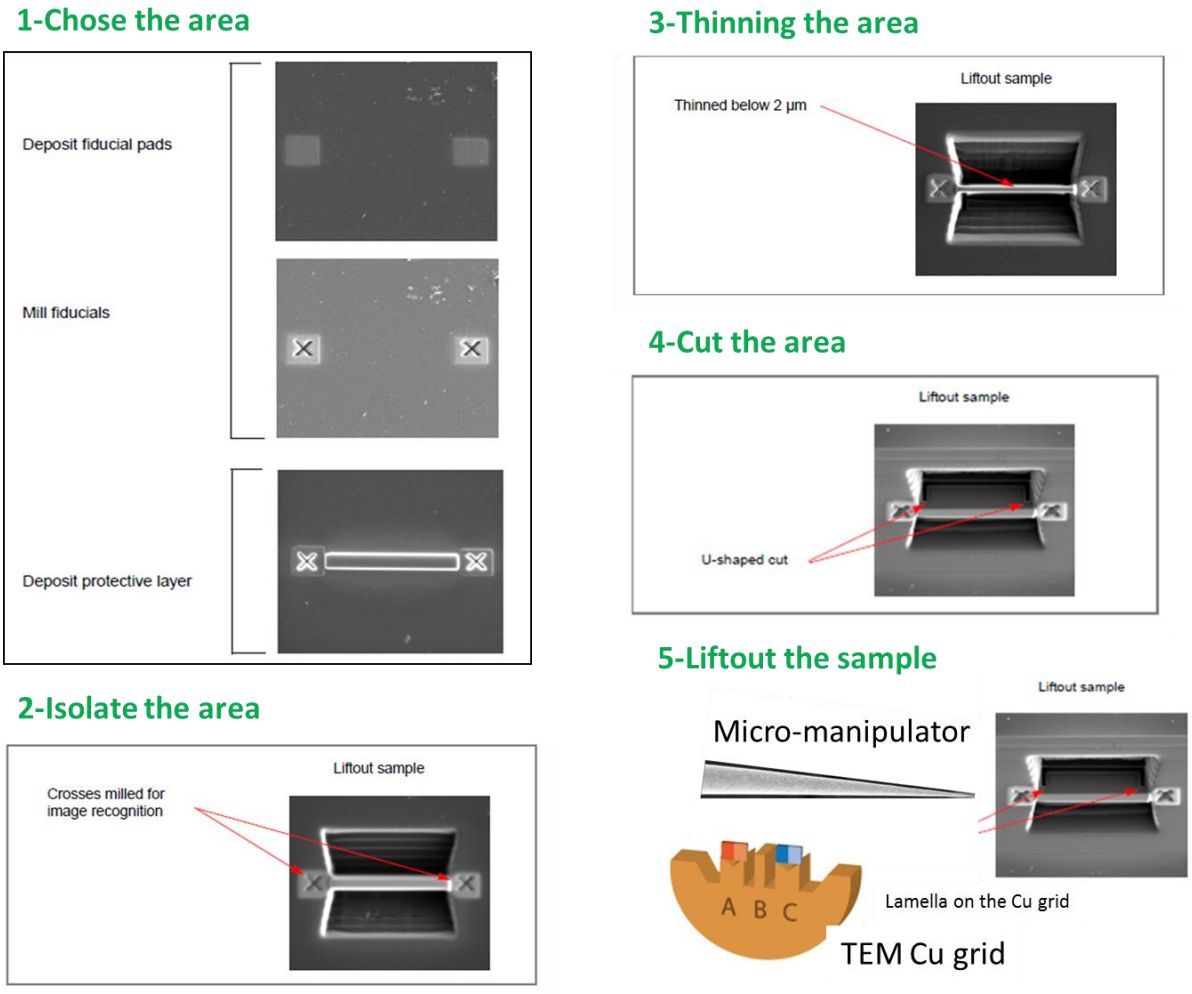

Figure 1-14. Schematic representation for obtain a PAA/Al lamella.

For the TEM analyses the preparation of the cross sections has been done using the Focus Ion Beam technique (FIB, Scios DualBeam). The procedure to obtain the PAA/Al lamella is described in the figure 1-14. At first place, the area of interest is selected and a 2/2/20 µm Platinum protective layer is deposited to protect it from excessive ion damage. Secondly, the selected area is isolated using the energetic gallium ion beam. Once the area is isolated, the milling process begins using high current ion beam and then as the lamella becomes thin 0.8 - 1µm the ion beam current is decreased. The lamella is removed from the substrate with a micro manipulator and transferred to a TEM sample grid. A second milling process using very low ion beam currents, is performed for thinning more the lamella until its thickness is about 30-50nm thick. The lamella obtained is transferred to the electron microscope chamber for the TEM observation and analyses.

1.6 Fabrication and Characterization of the PAA templates

The implementation of PAA templates for the device fabrication requires a strict control of the parameters which are involved in the anodization process and further detailed characterization of the porous structure. Such precise control of the anodization process allows achieving a desire pore configuration. For such purpose, some parameters implicated in the anodization process have been studied in order to analyze their impact over the pore structure such as: the anodization time, the anodization voltage, and the electrolyte temperature. Concerning the influence of the aluminum substrate over the resulting formed PAA, the anodization process has been performed using aluminum substrate with different single crystal orientations.

Moreover, the study of the electrolyte temperature over the pore structure on lateral-PAA templates has been carried out, as a result of such study we have been probed that it is of paramount importance to control the electrolyte temperature for the fabrication of templates

with a planar geometry which it is not the case, in the range of studied temperatures, for vertical PAA templates.

1.6.1 Measurement of the geometrical features of the PAA structures

In the present work, a deep study over the pore structure has been performed. Besides the typical parameters, such as the pore length, pore diameter and the interpore distance other important pore structural parameters have been studied as the porosity, the circularity and the pore order degree. All these parameters supply valuable information for further device fabrication and characterization.

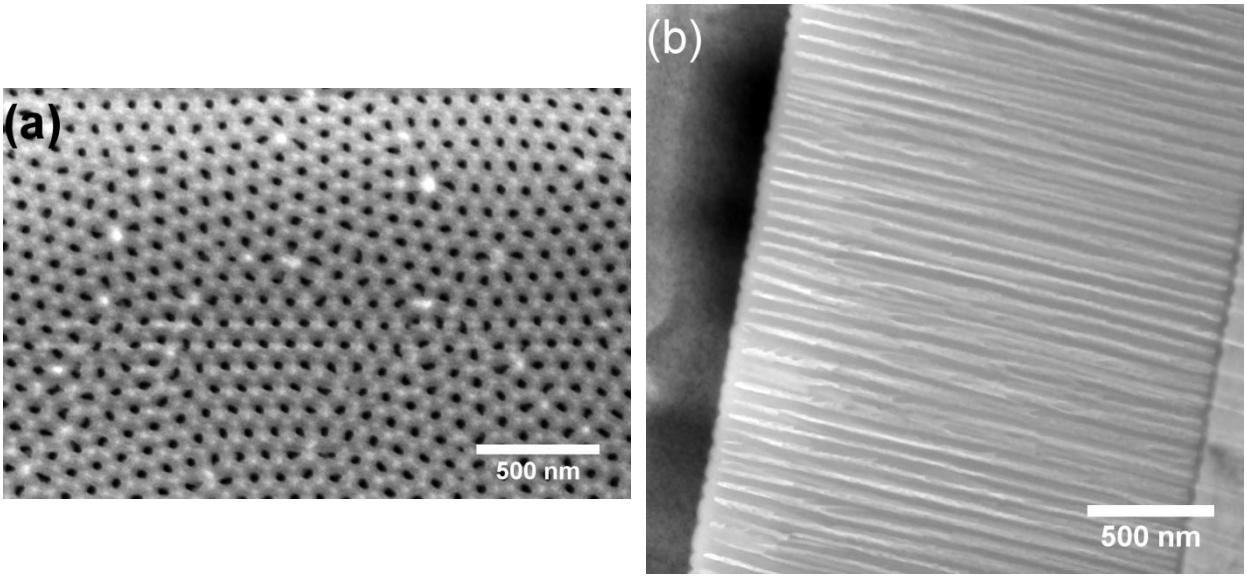

Figure 1-15. Vertical-PAA template. (a) SEM top view and (b) TEM side-view.

The figure 1-15 shows a top and side view of a vertical-PAA template. From figure 15 (a) all parameters related with the pores features can be inferred. On the other hand, figure 15 (b) shows a TEM image of a side view of the pores. In order to obtain such sample a lamella fabrication is required. These kinds of sample provide valuable information concerning the pore length, the straightness of the pores and the structure at the bottom of the pores.

1.6.1.1 Porosity

The porosity is defined as a ratio of a surface area occupied by pores to the whole surface area. For a single regular hexagon with one pore inside, the porosity formulation can be written as follows:

$$P = \frac{S_{pores}}{S} = \frac{S_P}{S_h} \quad (6)$$

Where S is the total area of the template and S_P is the pore area. Assuming that each single pore is a perfect circle, the following equations for S_P and S_h can be further evolved:

$$S_P = \pi \cdot \left(\frac{D_P}{2}\right)^2 \quad (7)$$

$$S_h = \frac{\sqrt{3} \cdot {D_I}^2}{2} \quad (8)$$

Substitution of Eqs. (7) and (8) into Eq. (6) leads to the following expression for the porosity of a nanostructure with hexagonally arranged cells:

$$P = \frac{\pi}{2 \cdot \sqrt{3}} \left(\frac{D_I}{D_P}\right)^2 \quad (9)$$

There is a great inconsistency in the literature among experimental data on the porosity of nanostructures, with the estimated porosity of anodic porous alumina varying from about 8% to 30% [77].

1.6.1.2 Circularity

A deviation of pore shape from an ideal circle can be described by circularity coefficient, defined as:

$$C = 4\pi \cdot \left(\frac{S_P}{perimeter^2}\right) \quad (10)$$

The circularity value of 1.0 indicates that the pore is ideally circular, while values close to 0.0 indicate an elongated polygon.

1.6.1.3 Pore ordering degree

The self-ordering process of the PAA can be addressed as configuration that tends to minimize the energy of perfect equilateral triangles among then. Due to the symmetry of the porous structure Mínguez-Bacho et.al [78] proposed the self-correlation function (SCF) in order to obtain a quantitative estimation of the regularity of the pores. The *SCF* is given by (11) and implanted on SEM images. This equation takes the image and the same image is shifted in a distance k_1 and k_2 in the x and y axis with respect to the center of the image. Where $F(x, y)$ is the image matrix.

$$G(k_1, k_2) = \sum_{k_1 k_2} F(x, y) \cdot F(x + k_1, y + k_2) \quad (11)$$

The resulting image, $G(k_1, k_2)$, gives a measure of the periodicity of the original image. In order to obtain a quantitative value of the degree of order of the anodized samples we

calculated the Normalized Spatial Order Parameter (*NSOP*) which is given by the following equation,

$$NSOP = \frac{1}{6} \cdot \frac{\sum_{NN=1}^{6} \frac{I_{NN}}{FWHM_{NN}}}{\frac{I_{CS}}{FWHM_{CS}}} \quad (12)$$

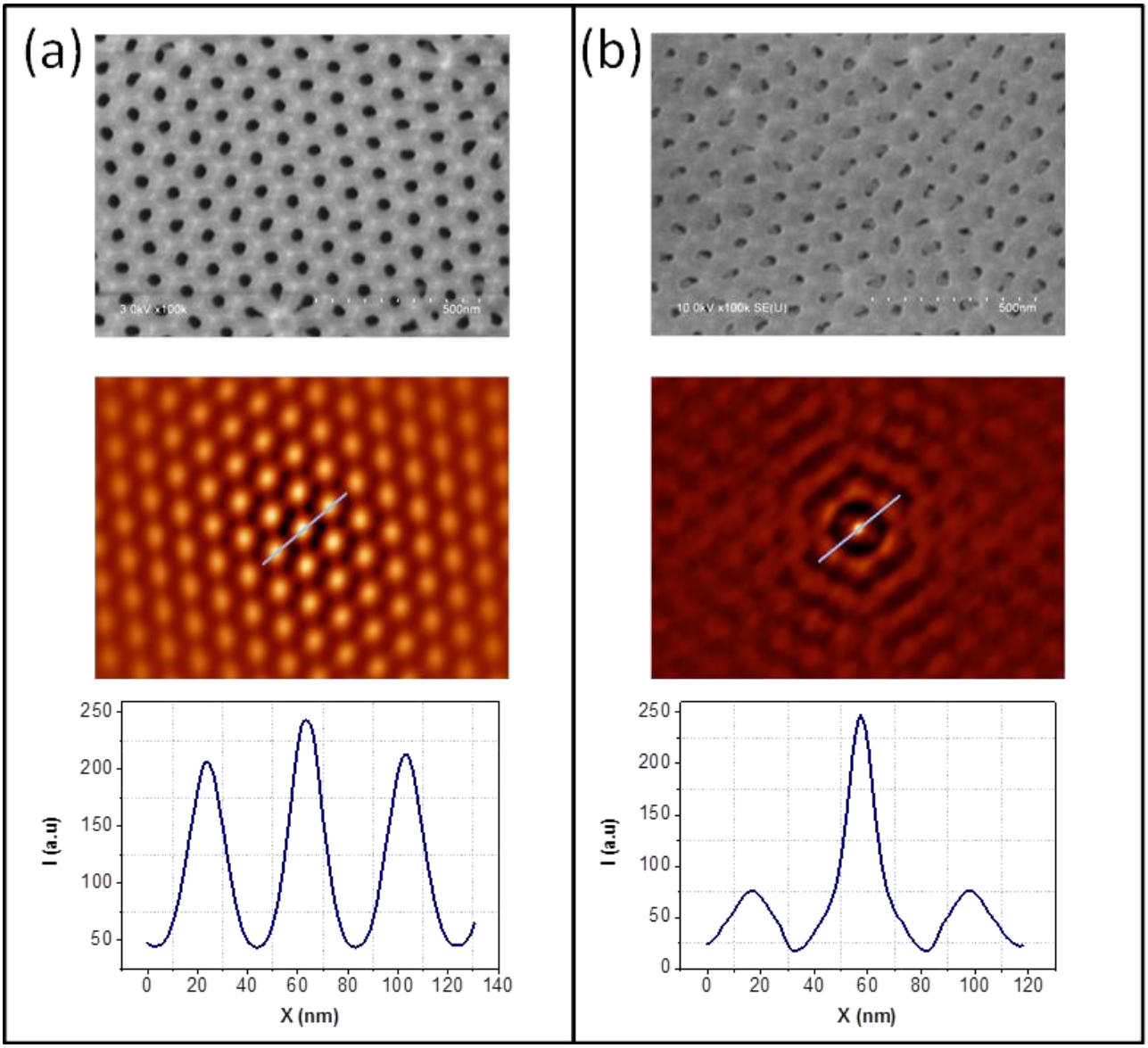

Figure 1-16. FE-SEM micrograph of PAA surfaces with their respective *SCIs* and crossing center profiles. (a) Highly ordered hexagonal pattern. (b) Low ordered pore structure.

Where the intensity (*I*) and the full width at half maximum (FWHM) of both central spot (CS) and the nearest neighbor (*NN*) of three crossing center profiles measured on the self-correlated imaged (*SCI*) provide the information of the pore ordering degree. These profiles are measured every 60° between them and the opposite vertex of a hexagon formed by the relative maxima. When the *SCF* is applied to a perfect ordered hexagonal array the resulting *SCI* is an image with a hexagonal pattern. The image starts to differ from a hexagonal since more than one pattern coexists or the degree of ordering is low, the *SCF* leads to a central spot surrounded by a ring. Therefore, when the intensity of the first neighbors of central spot is more similar in comparison with the intensity of the central spot, the *NSOP* is close to 1, which implies a highly ordered hexagonally array. On the contrary, when the central spot is surrounded by a ring, the intensity of the *NN* differs significantly with the intensity of the *CS*, which means that image has low regularity. Figure 1-16 shows two SEM micrograph, their respective *SCI* and a crossing center profile carried out on two different PAA templates. Figure 1-16 (a) shows an order pore structure that leads to a *SCI* with hexagonally array. On the other hand, figure 1-16 (b) shows a poorly ordered pore structure leading to a *SCI* with central spot is surrounded by a ring. In both cases it is possible to compare the differences of the intensities of the *CS* and the *NN*.

Conventionally, Fast Fourier Transform (FFT) is one of the most used powerful tools for SEM micrographs processing, however the implantation of the Self-correlation function is a statistical tool that leaves out the subjective factors and interpretations involved in other techniques [78].

1.6.2 Image processing

The basics parameters of the PAA structures have been measured using the ImageJ software. Such software allows performing directly measurements over different geometrical features, for instance: the pore diameter, pore area, pore perimeter. With these values is

possible to obtain the porosity, the circularity and the interpore distance. In order to obtain such characteristics length of the pores, a binarization of the SEM image is performed, as results the obtained image contains in black the surfaces which correspond to the pores and in white the zone associated with the alumina top surface of the PAA. On the other hand the pore regularity have been studied using the open software WSxM4.0 [79]. A self-correlation function (*SCF*) was performed to the SEM micrographs. The resulting self-correlated image (*SCI*) is a mathematical image that gives information of how well an image correlates with itself under discrete displacements in all possible directions. The combination of both software allows the calculation of the most relevant geometrical features of the PAA templates.

1.6.3 Influence of the anodization parameters on the PAA structure

The PAA templates present a great adaptability because their structure can be easily tailored by adjusting the parameters involved in the two-step anodization process. For the device fabrication it is of paramount importance to precisely control the cell structure. For both types of templates vertical and lateral one's, in the present work a study of the impact of the anodization parameters over the pore structure has been performed.

1.6.3.1 Anodization voltage

The PAA structure is mainly affected by the applied potential, since such anodization parameter determines the pore diameter, the interpore distance, and the thickness of the oxide barrier layer at the bottom pores. Additionally it influences the pore rate formation and the pore

ordering degree. Figure 1-17 shows top SEM images of PAA structures. These samples have been fabricated through the two anodization method using a 0.3 M oxalic acid solution at 17,5°C applying voltages in the range of 20V-60V with increment of 10V. The main pore geometrical features have been calculated, as is shown in the figure 1-19.

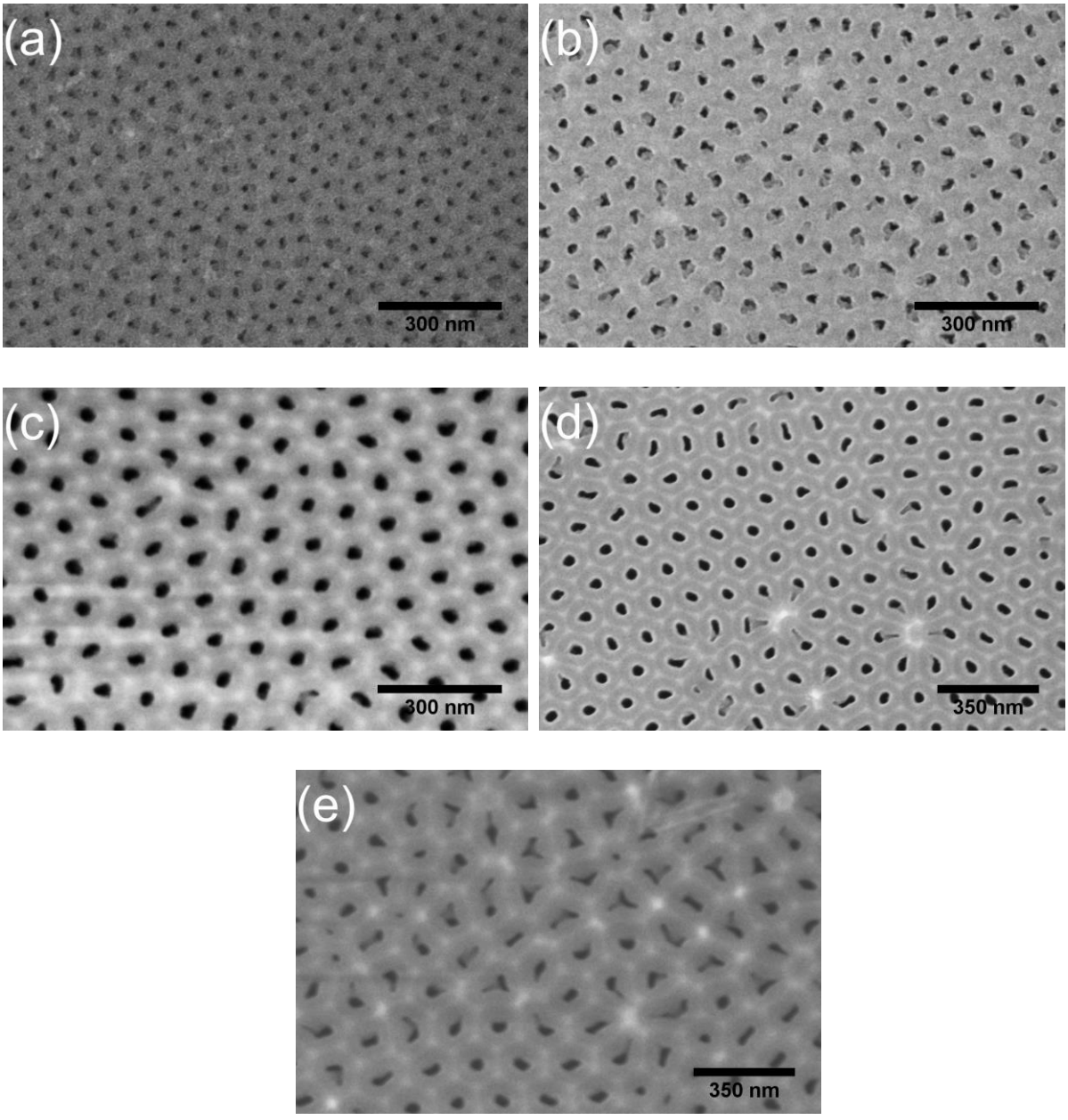

Figure 1-17. SEM images of PAA top surfaces anodized in a 0.3M oxalic acid solution at 17.5°C applying different anodized voltages in the range of 20-60V. (a) 20V, (b) 30V, (c) 40V, (d) 50V and (e) 60 V.

From the plots of the figure 18 (a) and (b) it is possible to calculate λ_P and λ_C respectively, implementing the linear relation between the applied potential, the pore diameter and the interpore distance. The obtained values are $\lambda_P = (1{,}06 \pm 0{,}07)\frac{nm}{V}$ and $\lambda_P = (3{,}47 \pm 0{,}11)\frac{nm}{V}$. Both values are of the same order of the reported one's in the literature [48].

Therefore, to obtain an order array pattern it's not only necessary to achieve the equilibrium between the dissolution and formation of the alumina at the bottom pores, figure 19 clearly indicates that all the current behaviors for all the anodization voltages follow the same trend. The internal stresses generated during the pore formation determine the pore ordering degree, thus depending on the ion transport a different volume expansion of the alumina is achieved, K. Nielsch et. Al [42] conclude that the best pore ordering is achieved when a volume expansion of alumina to aluminum is about 1.2. Therefore the anodization current highly impacts over the pore ordering degree, this fact is in accordance with previous experience that shows that the best pore order when the applied potential is 40V in an oxalic acid environment also depends on the electrolyte concentration and temperature [53, 80-82], which directly impacts over the anodization current. In addition for higher voltages than 60V the anodization current is not stable and the sample is near to the burning point, so under such conditions the pore ordering is almost non-existent.

In conclusion the characteristics of the PAA are closely related, the NSOP value provides a reference of the pore ordering array and these values are in perfect accordance with the ideal porosity values and the pore diameter and interpore distance. On the contrary, there is not any specific relation between the pore ordering degree or the quality of the pore structure and the circularity of the pores, for instance a low pore regularity is obtained when the anodization is performed applied voltage is of 60V but the pores are more circular than PAA structure anodized at 40V when the pore structure obtained is the closest to ideal hexagonal pore array.

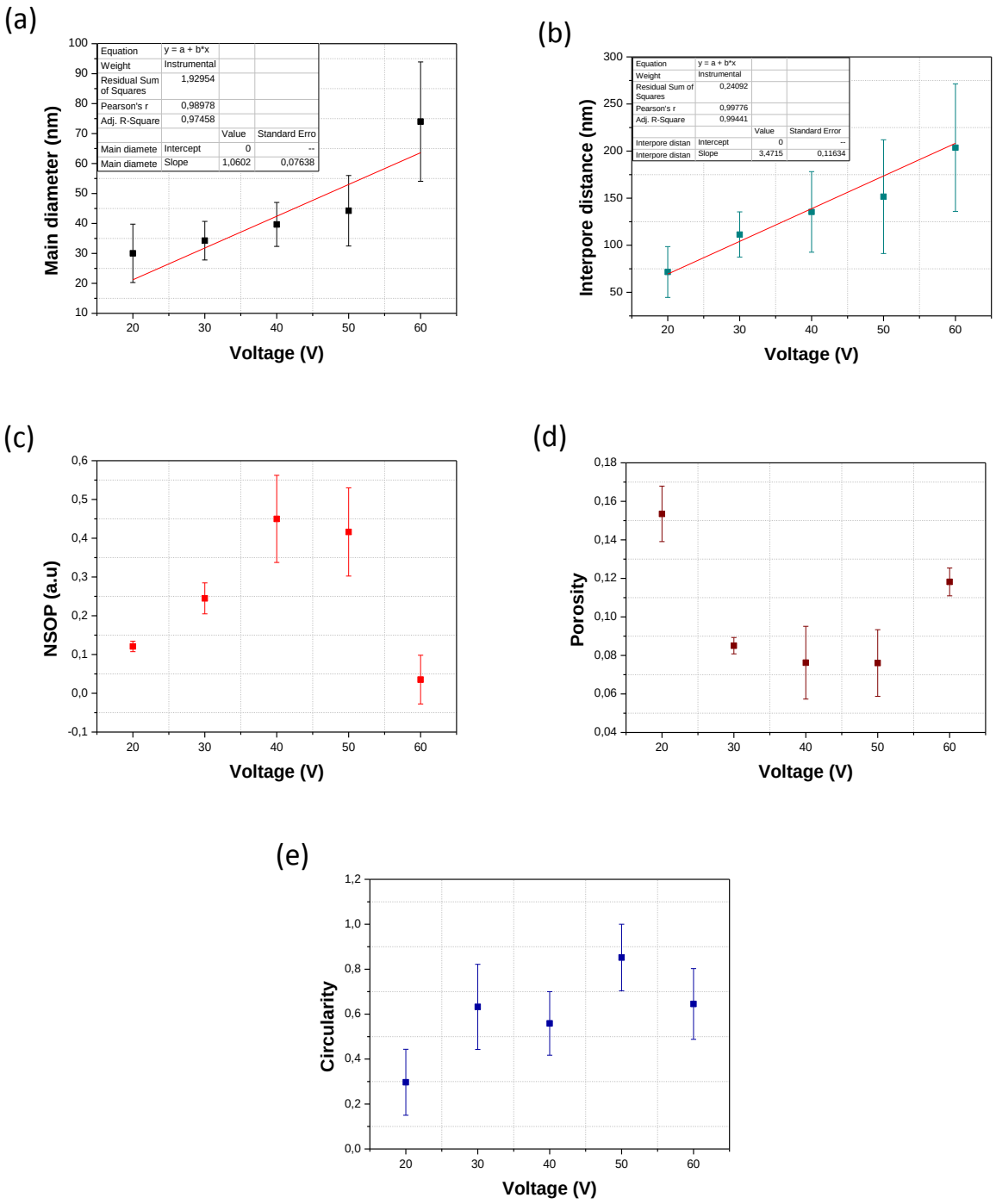

Figure 1-18. Main characteristics of the Vertical-PAA fabricated by a two anodization process in a 0.3M oxalic acid at 17,5°C. (a) Pore diameter, (b) Interpore distance, (c) NSOP value that indicates the pore ordering degree, (d) Porosity and (e) Circularity of the pores.

Concerning the porosity, as is shown in the figure 1-18 (d) the pore area over the total area varies only in a 10% between 30 and 50V anodization range voltage, but this value significant differs when the anodization voltages are lower or higher of this voltage range. This is also related with the pore ordering due to for an ideal pore hexagonal array the porosity has to be of the 10% as K. Nielsch et. al [42] proposed.

The most circular pores are obtained when the anodization applied tension is of 40V as is it shows in figure 18 (e). However it is important to point out that for high anodization as 60V the pores are quiet circular despite of the low pore ordering degree generated due to not favorable anodization conditions.

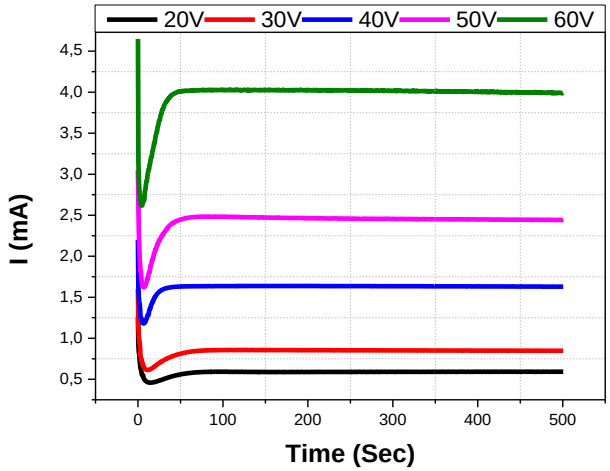

Figure 1-19. Current as function of time for all different anodization voltages applied, in the range of 20V-60V with increment of 10V.

For the further device fabrication is necessary the nanoparticle deposition is required and the consequently elimination of the oxide bottom layer. Although an exponential voltage decrease is performed at the end of the anodization process to reduce such layer, a wet etching is required for the complete alumina elimination at the bottom of the pores. However such wet etching process generates a pore widening phenomenon due to the isotropic etching. The PAA features have been measured and calculated after the pore widening process. The results are

summarized in the table 1-1. Evidently the pore diameter is increased, and the interpore distance rests without any change as the pores remain at the same position, consequently the porosity is increased. On the other hand the pore ordering degree is increased, which is related to the fact that the isotropic etching induces more circular pores, thus implicates that the pore are more similar among them. The measurement of an increment of the pore ordering degree due to an increase of the pore circularity, this phenomenon reflects the fact that the procedure in order to quantified how the pore pattern differs from an ideal hexagonal array, not only takes into account the position of the pores, but also such method considers the pore morphology as contraposition of other methods [39, 83].

Processes involved in the sample fabrication	Diameter [nm]	Interpore distance [nm]	NSOP [a.u]	Porosity [%]	Circularity
Two-anodization	40±7	135 ± 25	0,45 ± 0,15	8 ± 1	0,55 ± 0,15
Two-anodization and pore widening	52±10	135 ± 25	0,62 ± 0,10	14 ± 1	0,75 ± 0,10

Table 1-1. Differences of the cell parameters of PAA templates before and after the pore widening process.

1.6.3.2 Electrolyte temperature

The anodization temperature mainly affects the anodization current. In the present work, a detailed analysis of the influence of the electrolyte temperature over the pore structure has been performed.

The sample has been fabricated by the two anodization process in a 0.3 M oxalic acid solution applying 40V. The range of temperature studied is 15-25°C, with an increment of 2.5°C. The figure 1-20 summarizes the PAA features measured as function of the anodization temperature.

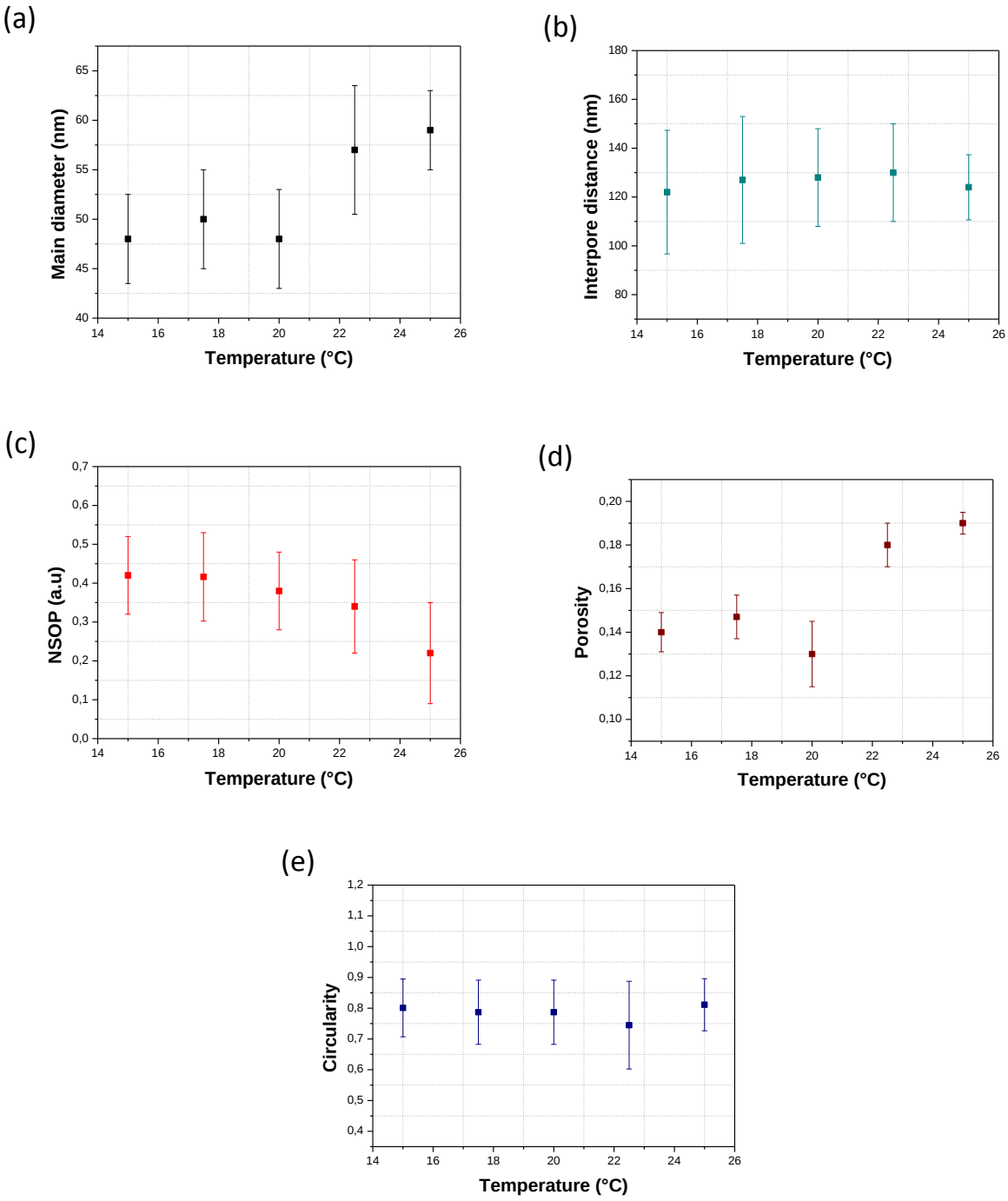

Figure 1-20. Main features of the PAA fabricated by a two anodization process in a 0.3M oxalic acid where the range of the anodization temperature has been varied in the range of 15°C to 25°C with increments of 2.5°C. (a) Pore diameter, (b) Interpore distance, (c) NSOP value that indicates the pore ordering degree, (d) Porosity and (e) Circularity of the pores.

The pore diameter as is shown in the figure 1-20 (a) does not change significantly in the studied temperature range. However two different regimes can be identified where the pore diameter remains almost constant. In the range of temperature from 15-20°C the pore diameter is approximately 50 nm and in the range of 22.5-25°C the pore diameter is of the order of 60 nm. The interpore distance does not suffer any meaningful change in the whole range studied as is shows in the figure 1-20 (b). The best pore ordering degree of the PAA structures is obtained in the 15-20°C range, for higher temperatures the pore ordering begins to decrease. As shown in figure 1-20 (c) again, the pore periodicity is mainly imposed by the volume expansion of the aluminum to alumina when the equilibrium of the alumina formation and dissolution is achieved at the metal/oxide interphase. Since the electrolyte temperature directly impacts over the anodization current, different volume expansion ratios are obtained for different temperatures or electrolytes concentrations. The porosity follows the same trend as the pore diameter, due to the fact that the interpore distance does not vary in the whole range, thus the pore remains at the same position however in the range of temperature from 22.5-25°C the pores are slightly bigger leading to a change in the porosity. The circularity of the pores shown in the figure 1-20 (e) does not suffer any change in the whole range of investigated temperatures.

1.6.3.3 Different single crystal orientation

The crystal orientation of the aluminum substrates has a huge influence over the regularity of the pores. In the present work, a comparative study of the anodization process perform over three single crystal aluminum differently oriented substrates have been investigated. Besides the pore ordering degree, a deeply analysis of the geometrical features of the resulting PAA structure have been performed. There is not any publication that analyzed the impact of the single crystal orientation of the aluminum over the final PAA characteristics such as the pore diameter, interpore distance, and porosity and circularity of the pores.

The samples have been prepared by two anodization process in a 0.3 M oxalic acid solution at 17,5°C. The anodization voltage have been varied in the range of 20-60V, with an increment of 10V.

Figure 1-21 shows the NSOP as function of the anodization voltage for the tree different single crystal orientation (1 0 0), (1 1 0) and (1 1 1). The formed PAA has better pore ordering when the crystal orientation of the aluminum is the (1 0 0), follow by the (1 1 1) crystal orientation and finally the pore configuration that most differs from the hexagonal array is obtained when the anodization process is executed in a single crystal aluminum with a (1 1 0) orientation, which is in good agreement with theory and experimental reports [37, 40].

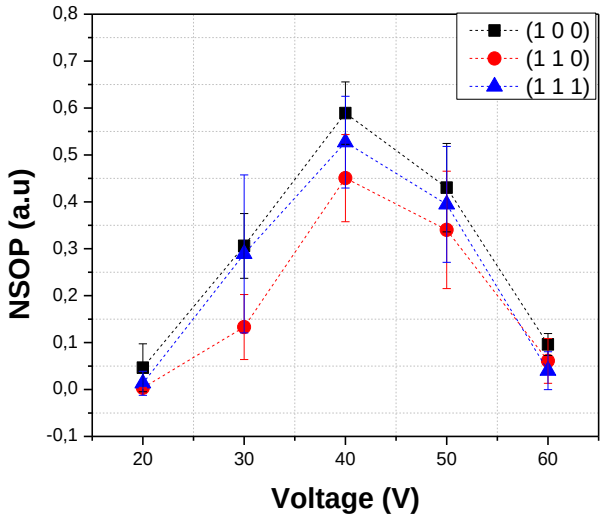

Figure 1-21. Normalized Spatial Order Parameter (*NSOP*) as function of the anodization voltage for PAA templates that have been anodized from aluminum with three different crystal orientations (1 0 0), (1 1 0) and (1 1 1).

The pore ordering degree of the resulting PAA templates using three different oriented crystals as substrates aluminum follows the same shape. For the three crystal orientations the

optimal anodization voltage is 40V. Unless for the very low voltages and the highest anodization voltage where the regularity of the pores is almost zero, the configuration closest to a hexagonal array is obtained when the anodization process is performed using (1 0 0) a single crystal aluminum, and the worst regularity always with the (1 1 0). Therefore, independently of the applied anodization voltage the Pore Ordering (PO) satisfies always the following order:

$$PO_{(1\,0\,0)} > PO_{(1\ 1\ 1)} > PO_{(1\ 1\ 0)}$$

In addition the geometrical PAA features have been measured depending on the single crystal orientation of the original aluminum substrate and the anodization voltage. Table 1-2 summarizes the proportionally constants λ_P and λ_C. From table 1-2 it is possible to conclude that the pore diameter and the interpore distance for the oriented crystal (1 1 0) and (1 1 1) are the same, but slightly change for the (1 0 0) crystal orientation.

Aluminum crystal orientation	λ_P [nm/V]	λ_C [nm/V]
[1 0 0]	1,07 ± 0,03	3,35 ± 0,15
[1 1 0]	0,94 ± 0,06	3,20 ± 0,20
[1 1 1]	0,96 ± 0,08	3,12 ± 0,13

Table 1-2. Proportionally constants λ_P and λ_C of the resulting PAA templates where the anodization process have been executed using as substrates single aluminums crystal with different orientations.

On the other hand the porosity, the circularity and the Normalized Spatial Order Parameter (*NSOP*) have been also measured in the voltage range from 20V to 60V depending on the crystal orientation of the aluminum substrate. Table 1-3 summarizes the measured and calculated PAA characteristics. The differences among the formed PAA structures are related with the pore ordering. For instance the PAA formed using (1 0 0) generally has a better pore

periodicity than the PAA fabricated from aluminum with other orientation, therefore the pores tend to be more circular and the porosity is of the order of the 10%. However, it is important to point out that for all the crystal orientation, the best pore ordering degree is always obtained when the applied potential is 40V, and for voltages lower than 20V and higher than 60V the pore ordering does not exist anymore. In conclusion the crystal orientation of the aluminum substrate strongly affects the pore ordering which is related with the 10% porosity value and pore with a high degree of circularity. Moreover, independently of the three different crystal orientations that have been studied, all of them have the same optimal operational conditions.

Finally, it is important to point out that the formed PAA template obtained through the anodization of a single crystal substrate has better pore ordering degree than the obtained through the conventional aluminum foil. Therefore, in the case of utilization of PAA templates fabricated by a two-step anodization method, in a certain application in which the periodicity of the pores has a capital importance, from the present study we can conclude that results advisable the implementation of single-crystal substrates, preferentially with a (1 0 0) orientation, instead of the highly pure aluminum foil.

In the present work, the more relevant role of the pores is the confinement of carbon nanostructures synthetized inside the PAA matrix, and the pore ordering degree takes a second place of relevance. The fabrication of the vertical-PAA templates has been done using aluminum foils with a purity of 99.995%. Such choice has been made, taking into consideration the relative high cost of the single-crystal substrate in respect from the aluminum foils, and on the other hand the regularity of the pores obtained with the aluminum foil in respect to the substrates with the (1 0 0) single crystal orientation varies in a 20%, which will not directly impact on the performance of the futures fabricated devices.

Al crystal orientation	[1 0 0]			[1 1 0]			[1 1 1]		
Voltage [V]	**Porosity[%]**	**Circularity**	**NSOP**	**Porosity[%]**	**Circularity**	**NSOP**	**Porosity[%]**	**Circularity**	**NSOP**
20	6.7 ± 1.0	0,52 ± 0,16	0,05 ± 0,04	5.5 ± 1.5	0.66 ± 0.30	0,003 ±0.001	4.4 ± 1.6	0,65 ± 0.25	0,013 ± 0.002
30	7.5 ± 1.2	0,78 ± 0,13	0,30 ± 0,07	9.0 ± 2.5	0.54 ± 0.20	0,13 ± 0.07	7.0 ± 1.5	0,68 ± 0.20	0,28 ± 0.15
40	12 ± 1.3	0,78 ± 0,12	0,58 ± 0,06	10.7 ± 3.0	0.77 ± 0.15	0,40 ± 0.10	12.0 ± 2.0	0,58 ± 0.10	0,45 ± 0.10
50	9.5 ± 1.5	0,82 ± 0,11	0,43 ± 0,09	6.4 ± 2.0	0.75 ± 0.10	0,35 ± 0.12	7.2 ± 1.2	0,80 ± 0.15	0,38 ± 0.10
60	6 ± 0.5	0,67 ± 0,20	0,10 ± 0,07	8.4 ± 3.0	0.70 ± 0.20	0,06 ± 0.04	5.2 ± 1.8	0,72 ± 0.20	0,04 ± 0.002

Table 1-3. Summarizes the porosity, circularity and the Normalized Spatial Order Parameter (*NSOP*) as function of the anodization voltage for PAA anodized in the three different single aluminum crystal.

1.6.4 Lateral-PAA fabrication

The lateral-PAA templates open the opportunity for the planar device integration. However in order to practically introduce and replace the conventional microelectronics devices it is necessary to overcome several hurdles. For instance the typical connectors between the electrodes are CNTs or SiNWs that can individually transport current of the order of some μA. Therefore in order to compete with conventional single crystalline MOSFETs hundreds or more nano-objets have to be connected per μm^2. Therefore it is crucial to improve the anodization conditions and to study the parameters involved in the lateral-PAA fabrication in order to achieve the maximum connections between the electrodes.

Nevertheless the capping layer deposit to anodize the aluminum just in the horizontal direction introduces constrained effects, introducing more mechanical stress applied to inward direction. Thus a deeply study has to be performed since it is not possible to directly transfer the knowledge of the conventional vertical PAA templates for the lateral-PAA template fabrication.

1.6.4.1 Influence of the temperature over the lateral-PAA structure

For the conventional vertical PAA templates the temperature of the acidic environment in which the anodization process is performed barely affects over the pore diameter and interpore distance. The same study has been performed in the lateral-PAA templates. Figure 1-22 shows the pore structural of three lateral-PAA templates fabricated through a simple anodization method in a 0.3M oxalic acid solution, where the anodization voltage applied was 40V, the range of temperature studied have been 10-25°C, with increment of 7,5°C. In the figure 1-22 (a), when the anodization process is performed at 25°C the resulting structure presents two rows of pores that have being merged. Thus there are no individual pores and all the pores suffer a pore merging phenomenon at the initial steps of the pore formation process. When the anodization process is carried out at 17,5°C an

intermediate configuration is obtained as is shown in the figure 1-22 (b), there are still pores merged but there are also individual pores. On the contrary when the electrolyte temperature is 10°C, as shown in the figure 1-22 (c) two rows of individual pores are obtained. In conclusion in order to adjust the pore diameter it necessary to control the electrolyte temperature since such anodization parameter has an important impact over the resulting pore structure.

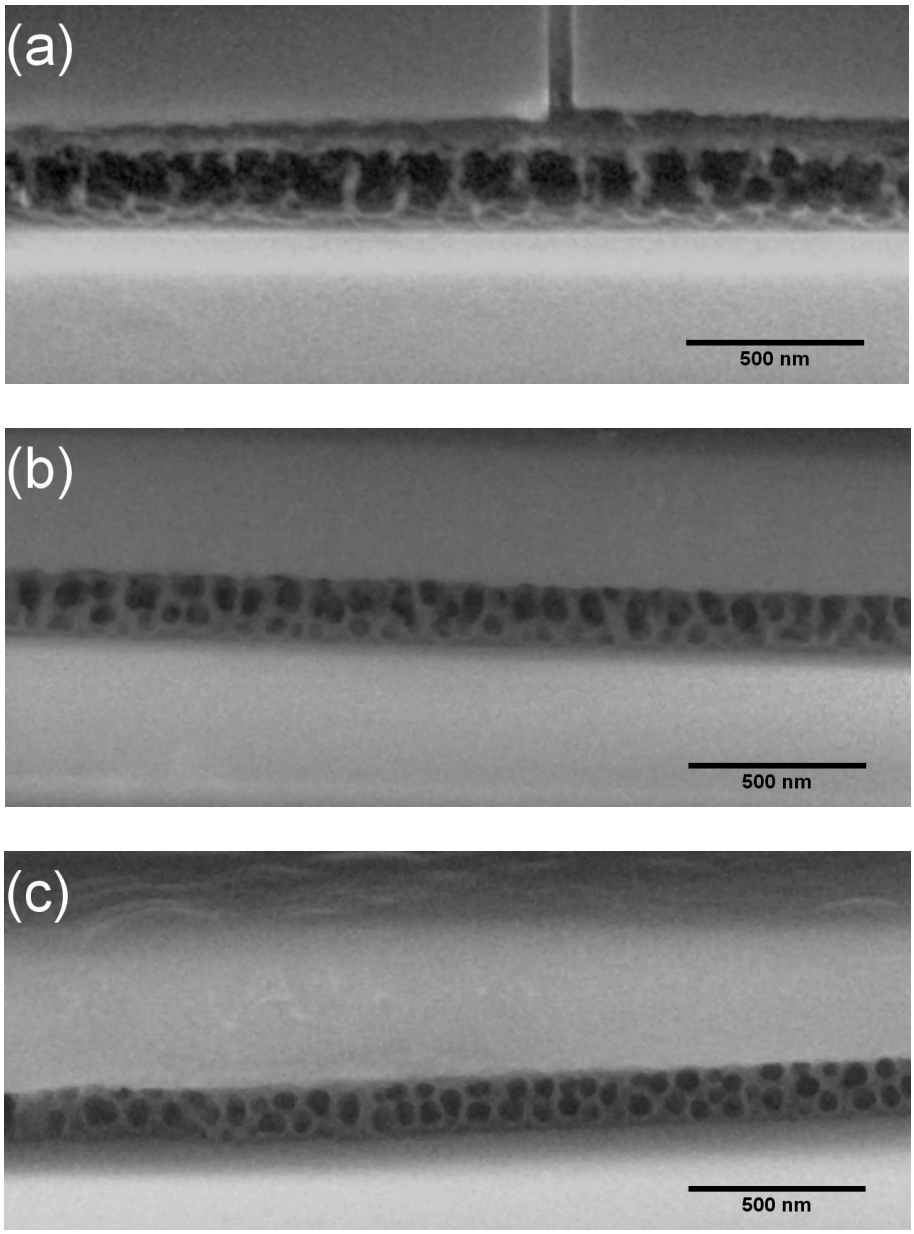

Figure 1-22. SEM images of lateral-PAA anodized at 40V in 0.3M oxalic solution for different anodization temperature. (a) 25°C, (b) 17.5°C and (c) 10°C.

The capping layer induces in addition other pore effect, as is shown in the figure 1-23: the pore diameter closer to the SiO_2 interphase has a smaller diameter than the upper pores near to SiN_x capping layer. This phenomenon is attributed to the different volume expansion of the alumina due to the constrain imposed by the different materials. The pore diameter have been measured near to the SiO_2 interphase: the pore diameter is (44 ± 16) nm and the upper pores, closer to the SiN_x have a pore diameter of (55± 20) nm. In order to achieve a symmetrical material, a SiO_2 capping layer was deposited instead of the SiN_x capping layer, however several cracks sites have been detected therefore the anodization process is not possible to be carry out in with this condition.

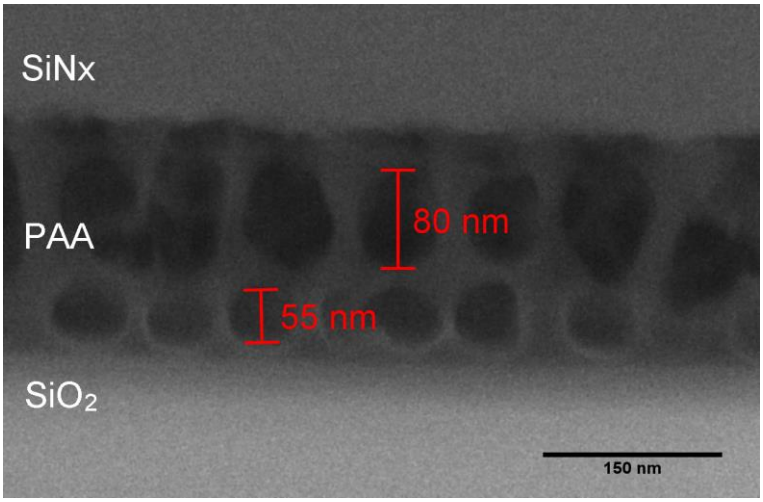

Figure 1-23. SEM images of a lateral-PAA template anodized at 10°C. The different interphases are indicating.

1.6.4.2 Thinning process in lateral-PAA templates

For the device fabrication, the electrodeposition of nanoparticles has to be performed, as it is explain in the section 1.5.4 for an effective elimination of the oxide barrier layer at the bottom of the pores: for this purpose the exponential voltage decrease process have been applied at the end of the anodization process with an operational range of

temperature between 15-25°C [76]. Therefore to obtain a pore structure with two rows of individual pores two strategies have been adopted. The first approach consists to fabricate the lateral-PAA templates at 17,5°C applying an anodization potential of 30V. Therefore, the pore diameter is smaller as the lower anodized voltage and the thinning barrier is effective as the electrolyte temperature is included in the operative range of temperature. On the other hand, the second way to fabricate a lateral-PAA template with individual pores with the oxide layer at the bottom pores partially reduced, is based on the pore fabrication at 10°C applying 40V, which guarantees the individual pores growth. Then when the barrier thinning process starts the electrolyte temperature is increased gradually until reaching the 17,5°C. The figure 1-24 shows the temperature of the electrolyte in the different stages of the anodization process.

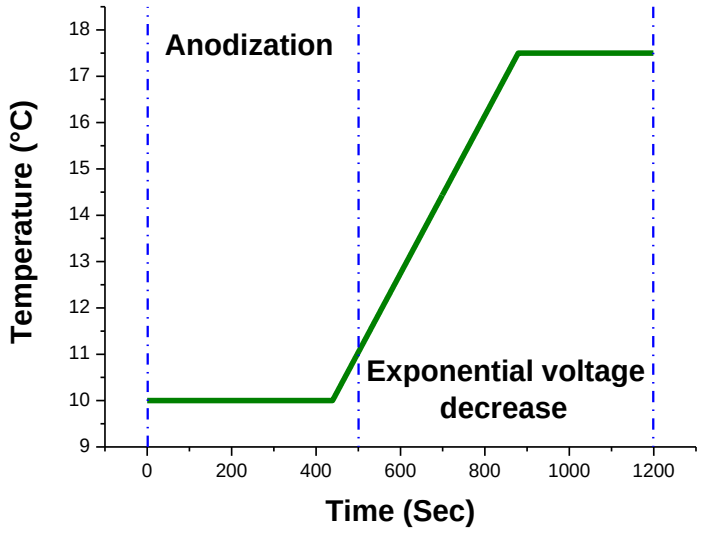

Figure 1-24. Variation of electrolyte temperature during the PAA formation in order to obtain individual pores in lateral-PAA templates and effectively to reduce the oxide barrier layer at the bottom of the pores. The anodization process has been performed during the first 500 seconds and subsequently the exponential voltage decreased is applied.

Thus the barrier thinning process is non effective until the moment in which the electrolyte temperature reaches 15°C. Figure 1-25 shows the lateral-PAA templates fabricated at 30V with an electrolyte temperature of 17.5°C, the pore diameter size is

equivalent to those obtained at 40V and with an anodization temperature of 10°C. Through the two approaches the two rows of individual pores are obtained. The evidence of the proper oxide barrier reduction has been obtained by the synthesis of CNTs inside the lateral-PAA templates. Such results are summarizes in chapter 3.

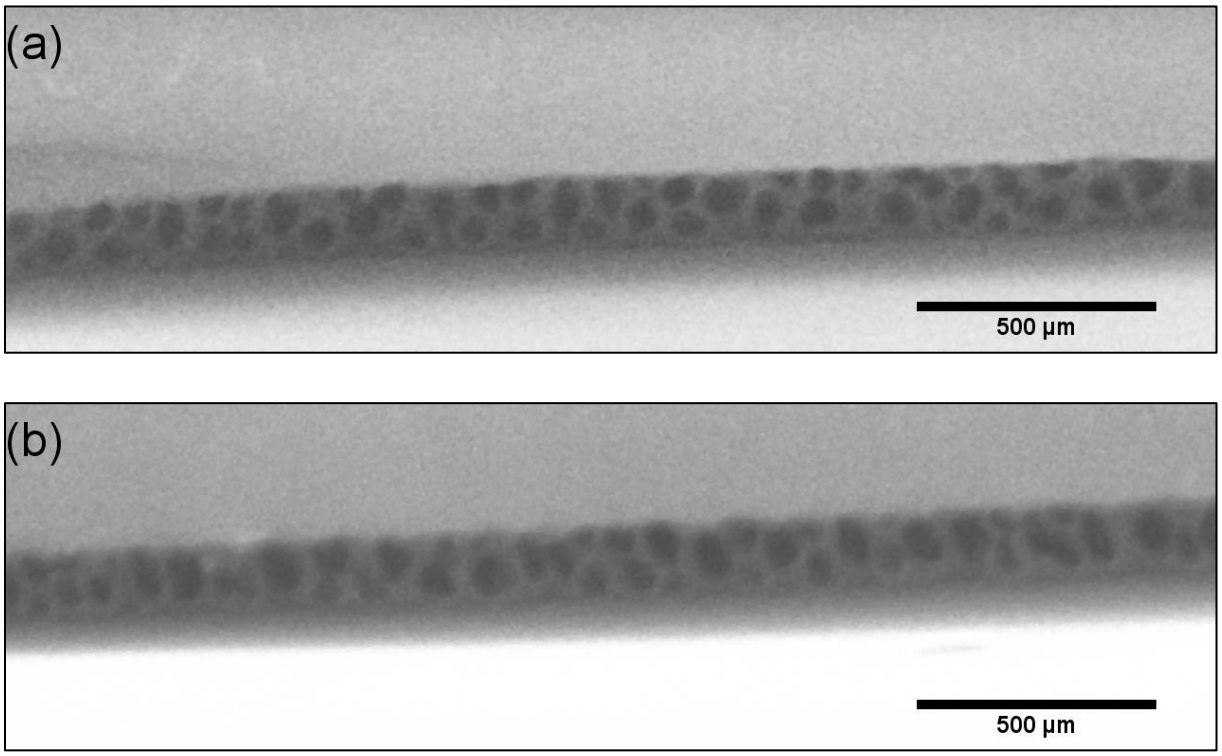

Figure 1-25. SEM images of a lateral-PAA template anodized in a 0.3M oxalic acid solution through two approaches. (a) Applying 30V with an electrolyte temperature of 17.5°C and (b) applying 40V with the electrolyte temperature varied as is shown in figure 25 from 15°C to 17.5°C.

In conclusion, the electrolyte temperature has a strong impact over the pore diameter in the fabrication of lateral-PAA templates. As difference with the conventional vertical-PAA templates, where just the anodization voltage has to be adjusting in order to control the main geometrical features of the PAA matrix, for the lateral-PAA templates fabrication both anodization parameters, electrolyte temperature and anodization voltage have to be carefully controlled.

1.7 Conclusions

The fabrication and properties of PAA have been investigated in order to implement templates for the growth of carbon nanostructures. The pore growth mechanism and the influence of the anodization parameters over the pore structure have been studied, such studies allowed to control and adjust the main geometrical features of the templates, such as the pore diameter, the interpore distance and the oxide barrier layer at the bottom pores. In particular, the impact of the anodization voltage, the electrolyte temperature and the influence of the orientation of single crystal aluminum over the pore structure has been deeply investigated. Moreover, an image processing tool was executed in order to measure the pore order degree of the templates. A quantitative notion of the regularity of the pores provides vital importance for the template fabrication and the growth of collective nanostructure.

On the other hand, the lateral-PAA templates have been fabricated. In comparison with the conventional vertical-PAA, the planar templates require patterning process in order to selectively expose the desired aluminum side face. When the anodization process is performed on such encapsulated aluminum, the capping layer imposes additional stresses that impact over the formed pore structure. In this case the anodization temperature has a huge influence over the pore diameter and the pore configuration.

The presented studies on the anodization technique and the PAA characteristics provide capital knowledge for the fabrication of versatile templates, the first step towards the device application.

References

[1] F. Keller, *et al.*, "Structural Features of Oxide Coatings on Aluminium," *J.Electrochem. Soc.,* vol. 100, p. 411, 1953.

[2] J. P. O'Sullivan and G. P. Wood, "The formation and mechanism of formation of porous anodic alumina," *Roy.Soc. Lond,* vol. 317, p. 511, 1970.

[3] H. Masuda and K. Fukuda, "Ordered Metal Nanohole Arrays Made by a Two-Step Replication of Hoenycomb Structures of Anodic Alumina," *Science,* vol. 268, p. 1466, 1995.

[4] G. Ding, *et al.*, "Fabrication of Porous Anodic Alumina with Ultrasmall Nanopores," *Nanoscale Research Letters,* vol. 5, p. 1257, 2010.

[5] A. P. Li, *et al.*, "Hexagonal pore arrays with a 50–420 nm interpore distance formed by self-organization in anodic alumina," *J. Appl. Phys,* vol. 84, p. 6023, 1998.

[6] J. Kolar, *et al.*, "Down-scaling of resistive switching to nanoscale," *Journal of,* vol. 2, p. 349, 2014.

[7] B. Dudem, *et al.*, "Broadband and wide-angle antireflective characteristics of nanoporous anodic alumina films for silicon-based optoelectronic applications," *Applied Physics B,* pp. 10.1007/s00340-015-6007-2, 2015.

[8] S. Létant , *et al.*, "Nanochannel Arrays on Silicon Platforms by Electrochemistry," *NanoLetters,* vol. 4, p. 1705, 2004.

[9] M. Kampa, *et al.*, "Semiconductor photonic crystals for optoelectronics," *Physica E: Low-dimensional Systems and Nanostructures,* vol. 21, p. 802, 2004.

[10] A. Santos, *et al.*, "Photoluminescent Enzymatic Sensor Based on Nanoporous Anodic Alumina," *ACS Appl. Mater. Interfaces,* vol. 4, p. 3584, 2012.

[11] W. Wang, *et al.*, "Three-Dimensional Ni/TiO2 Nanowire Network for High Areal Capacity Lithium Ion Microbattery Applications," *NanoLetters,* vol. 12, p. 655, 2012.

[12] J. Berrigan, *et al.*, "Conversion of porous anodic Al2O3 into freestanding,," *Journal of,* vol. 1, p. 128, 2013.

[13] K. Yasui, *et al.*, "Patterned Magnetic Recording Media Using Anodic Porous Alumina with Single Domain Hole Configurations of 63 nm Hole Interval," *Japanese Journal of Applied Physics,* vol. 44, p. 12, 2005.

[14] C.-S. Cojocaru, *et al.*, "Conformal Anodic Oxidation of Aluminum Thin Films," *Nanoletters,* vol. 5, p. 675, 2005.

[15] K.-H. Kim, *et al.*, "Cup-Stacked Carbon Nanotube Schottky Diodes for Photovoltaics and Photodetectors," *Advanced Materials,* vol. 26, p. 4363, 2014.

[16] H. Han, *et al.*, "In Situ Determination of the Pore Opening Point during Wet-Chemical Etching of the Barrier Layer of Porous Anodic Aluminum," *ACS Appl Mater Interfaces. ,* vol. 5, p. 3441, 2013.

[17] S. Wernick, *et al.*, "The Surface Treatment and Finishing of Aluminium and its Alloys," ed: ASM International, 1987, pp. 289-368

[18] T. Hoar and N. Mott, "A mechanism for the formation of porous anodic oxide films on aluminium," *J. Phys. Chem. Solids.,* vol. 9, p. 97, 1959.

[19] T. A. Renshaw, "A Study of Pore Structures on Anodized Aluminum," *Journal of the Electrochemical Society,* vol. 108, pp. 185-191, 1961.

[20] G. E. Thompson, *et al.*, "Anodic oxidation of aluminium," *Philosophical Magazine Part B,* vol. 55, pp. 651-667, 1987/06/01 1987.

[21] M. T. Wu, *et al.*, "Effect of polishing pretreatment on the fabrication of ordered nanopore arrays on aluminum foils by anodization," *Journal of Vacuum Science & Technology B,* vol. 20, pp. 776-782, 2002.

[22] D. Lo and R. A. Budiman, "Fabrication and Characterization of Porous Anodic Alumina Films from Impure Aluminum Foils," *Journal of the Electrochemical Society,* vol. 154, pp. C60-C66, January 1, 2007 2007.
[23] H. Masuda and K. Fukuda, "Ordered Metal Nanohole Arrays Made by a 2-Step Replication of Honeycomb Structures of Anodic Alumina," *Science,* vol. 268, pp. 1466-1468, Jun 9 1995.
[24] K. Lu, "Newfound capability of focused ion beam patterning guided anodization," *Electrochimica Acta,* vol. 63, pp. 256-262, Feb 29 2012.
[25] A. P. Li*, et al.*, "Polycrystalline and monocrystalline pore arrays with large interpore distance in anodic alumina," *Electrochemical and Solid State Letters,* vol. 3, pp. 131-134, Mar 2000.
[26] W. Lee*, et al.*, "Wafer-Scale Ni Imprint Stamps for Porous Alumina Membranes Based on Interference Lithography," *Small,* vol. 2, pp. 978-982, 2006.
[27] H. Oshima*, et al.*, "Detecting dynamic signals of ideally ordered nanohole patterned disk media fabricated using nanoimprint lithography," *Applied Physics Letters,* vol. 91, Jul 9 2007.
[28] H. Masuda*, et al.*, "Fabrication of highly ordered anodic porous alumina using self-organized polystyrene particle array," *Chemistry Letters,* vol. 33, pp. 584-585, May 5 2004.
[29] Y. Matsui*, et al.*, "Highly Ordered Anodic Porous Alumina with 13-nm Hole Intervals Using a 2D Array of Monodisperse Nanoparticles As a Template," *Small,* vol. 2, pp. 522-525, 2006.
[30] B. Kim*, et al.*, "Fabrication of Ordered Anodic Aluminum Oxide Using a Solvent-Induced Array of Block-Copolymer Micelles," *Small,* vol. 3, pp. 1869-1872, 2007.
[31] Z. J. Sun and H. K. Kim, "Growth of ordered, single-domain, alumina nanopore arrays with holographically patterned aluminum films," *Applied Physics Letters,* vol. 81, pp. 3458-3460, Oct 28 2002.
[32] H. Masuda*, et al.*, "Square and triangular nanohole array architectures in anodic alumina," *Advanced Materials,* vol. 13, pp. 189-192, Feb 5 2001.
[33] H. Masuda*, et al.*, "Highly ordered nanochannel-array architecture in anodic alumina," *Applied Physics Letters,* vol. 71, pp. 2770-2772, Nov 10 1997.
[34] B. Chen*, et al.*, "Novel Patterns by Focused Ion Beam Guided Anodization," *Langmuir,* vol. 27, pp. 800-808, Jan 18 2011.
[35] J. Choi*, et al.*, "Mechanism of guided self-organization producing quasi-monodomain porous alumina," *Electrochimica Acta,* vol. 50, pp. 2591-2595, 2005.
[36] T. S. Kustandi*, et al.*, "Wafer-Scale Near-Perfect Ordered Porous Alumina on Substrates by Step and Flash Imprint Lithography," *Acs Nano,* vol. 4, pp. 2561-2568, May 2010.
[37] G. Beck and R. Bretzler, "Regularity of nanopores in anodic alumina formed on orientated aluminium single-crystals," *Materials Chemistry and Physics,* vol. 128, pp. 383-387, Aug 15 2011.
[38] C. Cheng*, et al.*, "Simulation and experiment of substrate aluminum grain orientation dependent self-ordering in anodic porous alumina," *Journal of Applied Physics,* vol. 113, May 28 2013.
[39] C. K. Y. Ng and A. H. W. Ngan, "Precise Control of Nanohoneycomb Ordering over Anodic Aluminum Oxide of Square Centimeter Areas," *Chemistry of Materials,* vol. 23, pp. 5264-5268, Dec 13 2011.
[40] K. S. Napolskii*, et al.*, "Origin of long-range orientational pore ordering in anodic films on aluminium," *Journal of Materials Chemistry,* vol. 22, pp. 11922-11926, 2012.
[41] J. W. Diggle*, et al.*, "Anodic Oxide Films on Aluminum," *Chemical Reviews,* vol. 69, pp. 365-&, 1969.
[42] K. Nielsch*, et al.*, "Self-ordering regimes of porous alumina: The 10% porosity rule," *Nano Letters,* vol. 2, pp. 677-680, Jul 2002.
[43] K. Ebihara*, et al.*, "Kinzoku Hyomen Gijutsu," *J. Met. Finish. Soc. Jpn,* vol. 33, p. 156, 1982.
[44] K. Ebihara, Takahashi, H. and and M. Nagayama, "J. Met. Finish. Soc. Japan," *Kinzoku Hyomen Gijutsu,* vol. 34, pp. 548-553, 1983.
[45] M. Curioni*, et al.*, "Flow modulated ionic migration during porous oxide growth on aluminium," *Electrochimica Acta,* vol. 55, pp. 7044-7049, Sep 30 2010.

[46] A. Despić and V. Parkhutik, "Electrochemistry of Aluminum in Aqueous Solutions and Physics of Its Anodic Oxide," in *Modern Aspects of Electrochemistry No. 20*. vol. 20, J. O. M. Bockris*, et al.*, Eds., ed: Springer US, 1989, pp. 401-503.

[47] G. E. Thompson*, et al.*, "Nucleation and Growth of Porous Anodic Films on Aluminum," *Nature,* vol. 272, pp. 433-435, 1978.

[48] S. Z. Chu*, et al.*, "Large-scale fabrication of ordered nanoporous alumina films with arbitrary pore intervals by critical-potential anodization," *Journal of the Electrochemical Society,* vol. 153, pp. B384-B391, 2006.

[49] S. Ono*, et al.*, "Self-ordering of anodic porous alumina formed in organic acid electrolytes," *Electrochimica Acta,* vol. 51, pp. 827-833, Nov 10 2005.

[50] W. Lee*, et al.*, "Fast fabrication of long-range ordered porous alumina membranes by hard anodization," *Nature Materials,* vol. 5, pp. 741-747, Sep 2006.

[51] H. Han*, et al.*, "In Situ Determination of the Pore Opening Point during Wet-Chemical Etching of the Barrier Layer of Porous Anodic Aluminum Oxide: Nonuniform Impurity Distribution in Anodic Oxide," *Acs Applied Materials & Interfaces,* vol. 5, pp. 3441-3448, Apr 24 2013.

[52] L. Zaraska*, et al.*, "Analysis of nanopore arrangement and structural features of anodic alumina layers formed by two-step anodizing in oxalic acid using the dedicated executable software," *Applied Physics A,* vol. 114, pp. 571-577, 2014/02/01 2014.

[53] S. K. Hwang*, et al.*, "Fabrication of highly ordered pore array in anodic aluminum oxide," *Korean Journal of Chemical Engineering,* vol. 19, pp. 467-473, May 2002.

[54] J. M. Montero-Moreno*, et al.*, "Influence of the aluminum surface on the final results of a two-step anodizing," *Surface & Coatings Technology,* vol. 201, pp. 6352-6357, Apr 2 2007.

[55] G. Beck and K. Petrikowski, "Influence of the microstructure of the aluminum substrate on the regularity of the nanopore arrangement in an alumina layer formed by anodic oxidation," *Surface & Coatings Technology,* vol. 202, pp. 5084-5091, Jul 30 2008.

[56] I. V. Roslyakov*, et al.*, "Longitudinal pore alignment in anodic alumina films grown on polycrystalline metal substrates," *Journal of Applied Crystallography,* vol. 46, pp. 1705-1710, Dec 2013.

[57] H. Masuda*, et al.*, "Fabrication of a One-Dimensional Microhole Array by Anodic-Oxidation of Aluminum," *Applied Physics Letters,* vol. 63, pp. 3155-3157, Dec 6 1993.

[58] C. S. Cojocaru*, et al.*, "Conformal Anodic Oxidation of Aluminum Thin Films," *Nano Letters,* vol. 5, pp. 675-680, 2005/04/01 2005.

[59] H. G. Zhang*, et al.*, "A horizontally aligned one-dimensional carbon nanotube array on a Si substrate," *Journal of the Electrochemical Society,* vol. 154, pp. H124-H126, 2007.

[60] M. H. Lee*, et al.*, "Carbon Nanotubes Based on Laterally Formed Anodic Aluminum Oxide Template," *Japanese Journal of Applied Physics,* vol. 48, Apr 2009.

[61] M. Gowtham*, et al.*, "Controlled fabrication of patterned lateral porous alumina membranes," *Nanotechnology,* vol. 19, Jan 23 2008.

[62] Y. Xiang*, et al.*, "Microstructured horizontal alumina pore arrays as growth templates for large area few and single nanowire devices," *Physica Status Solidi-Rapid Research Letters,* vol. 2, pp. 59-61, Mar 2008.

[63] D. C. Leitao*, et al.*, "Nanoscale Topography: A Tool to Enhance Pore Order and Pore Size Distribution in Anodic Aluminum Oxide," *The Journal of Physical Chemistry C,* vol. 115, pp. 8567-8572, 2011/05/05 2011.

[64] P. Erdogan*, et al.*, "Effect of chemical etching on the morphology of anodic aluminum oxides in the two-step anodization process," *Applied Surface Science,* vol. 258, pp. 4544-4550, 2012.

[65] L. Zaraska*, et al.*, "Anodic alumina membranes with defined pore diameters and thicknesses obtained by adjusting the anodizing duration and pore opening/widening time," *Journal of Solid State Electrochemistry,* vol. 15, pp. 2427-2436, Dec 2011.

[66] M. M. Rahman*, et al.*, "Effect of the anodization voltage on the pore-widening rate of nanoporous anodic alumina," *Nanoscale Research Letters,* vol. 7, Aug 23 2012.

[67] L. Ba and W. S. Li, "Influence of anodizing conditions on the ordered pore formation in anodic alumina," *Journal of Physics D-Applied Physics,* vol. 33, pp. 2527-2531, Oct 21 2000.
[68] T. Xu*, et al.*, "Periodic holes with 10 nm diameter produced by grazing Ar+ milling of the barrier laver in hexagonally ordered nanoporous alumina," *Nano Letters,* vol. 2, pp. 37-41, Jan 2002.
[69] M.-N. Lin*, et al.*, "Long-range ordered nanoaperture array with uniform diameter and interpore spacing," *Applied Physics Letters,* vol. 87, p. 173116, 2005.
[70] M. N. Lin*, et al.*, "Fabrication of an ordered nanoparticle array with a nanoaperture membrane used as a contact-mask," *Nanotechnology,* vol. 17, pp. 315-319, Jan 14 2006.
[71] N.-W. Liu*, et al.*, "Focused-Ion-Beam-Based Selective Closing and Opening of Anodic Alumina Nanochannels for the Growth of Nanowire Arrays Comprising Multiple Elements," *Advanced Materials,* vol. 20, pp. 2547-2551, 2008.
[72] M. Lillo and D. Losic, "Ion-beam pore opening of porous anodic alumina: The formation of single nanopore and nanopore arrays," *Materials Letters,* vol. 63, pp. 457-460, Feb 15 2009.
[73] X. Jiang*, et al.*, "Diffusivity of sub-1,000 Da molecules in 40 nm silicon-based alumina pores," *Microfluidics and Nanofluidics,* vol. 5, pp. 695-701, 2008/11/01 2008.
[74] R. C. Furneaux*, et al.*, "The Formation of Controlled-Porosity Membranes from Anodically Oxidized Aluminum," *Nature,* vol. 337, pp. 147-149, Jan 12 1989.
[75] D. I. Petukhov*, et al.*, "Permeability of anodic alumina membranes with branched channels," *Nanotechnology,* vol. 23, Aug 24 2012.
[76] B. Marquardt*, et al.*, "Density control of electrodeposited Ni nanoparticles/nanowires inside porous anodic alumina templates by an exponential anodization voltage decrease," *Nanotechnology,* vol. 19, Oct 8 2008.
[77] A. Eftekhari, Ed., *Nanostructured Materials in Electrochemistry*. Weinheim: WILEY-VCH Verlag GmbH & Co., 2008, p.^pp. Pages.
[78] I. Minguez-Bacho*, et al.*, "Self-correlation function for determination of geometrical parameters in Nanoporous Anodic Alumina Films," *Applied Physics a-Materials Science & Processing,* vol. 106, pp. 105-112, Jan 2012.
[79] I. Horcas*, et al.*, "WSXM: A software for scanning probe microscopy and a tool for nanotechnology," *Review of Scientific Instruments,* vol. 78, p. 013705, 2007.
[80] F. Li*, et al.*, "On the Growth of Highly Ordered Pores in Anodized Aluminum Oxide," *Chemistry of Materials,* vol. 10, pp. 2470-2480, 1998/09/01 1998.
[81] S. Shingubara*, et al.*, "Ordered two-dimensional nanowire array formation using self-organized nanoholes of anodically oxidized aluminum," *Japanese Journal of Applied Physics Part 1-Regular Papers Short Notes & Review Papers,* vol. 36, pp. 7791-7795, Dec 1997.
[82] M. A. Kashi and A. Ramazani, "The effect of temperature and concentration on the self-organized pore formation in anodic alumina," *Journal of Physics D: Applied Physics,* vol. 38, p. 2396, 2005.
[83] L. Zaraska*, et al.*, "The effect of anode surface area on nanoporous oxide formation during anodizing of low purity aluminum (AA1050 alloy)," *Journal of Solid State Electrochemistry,* vol. 18, pp. 361-368, Feb 2014.

Chapter 2.

Catalyst Electrodeposition inside PAA

The present chapter introduces a description of the electrodeposition techniques and the main advantages of the Pulsed Electrodeposition (PED) process for the catalyst nanoparticle deposition within the porous anodic templates.

The impact of the oxide barrier layer at the bottom of the pores has been deeply studied. For this purpose, depending on the anodization voltage, the anodization process has been performed in different ranges of temperatures. As result, different deposition regimes have been detected depending on the anodization temperature. The influence of the pore length has also been investigated. We recall that in order to thin the oxide barrier layer, an exponential voltage decrease process is applied at the end of the anodization process; however this procedure can induce formation of a branch structure at the bottom pores. Therefore in order to have insights of the pore structure at the bottom of the pores, a comparison between the density of pores and the density of nanoparticles deposited has been carried out for deriving a value of the branches generated per pore.

The main goal is to obtain a PAA with the pores homogeneously filled with nanoparticles having a narrow distribution and appropriate size that presents good catalytic activity in the process for the carbon nanotubes growth.

2.1 Electrodeposition process

During the last two centuries the electrodeposition process has been continuously improved, this method is characterized by a relative simplicity and a low cost of

implementation. Firstly such technique was used for coating conductive materials with a metal. In the recent years this process has also been widely used for the deposition inside porous anodic alumina for templates fabrication. For instance several kind of metals or semiconducting structures could be successfully electrodeposited such as nickel [1] , cobalt [2], gold [3], zinc oxide [4], silicon [5] among others, leading to a nanostructured array of high interest for various applications such as the synthesis of silicon nanowires [6, 7] or nanotubes [8, 9].

In spite of the electrodeposition process being cost-effective compared to other deposition methods such as the chemical vapor deposition, sputtering and evaporation, the biggest constrain still relies in the difficulty to obtain a uniform layer deposition. In particular, in order to uniformly deposit metal nanoparticles inside the PAA templates it is crucial to homogeneously eliminate the oxide barrier layer at the bottom of the pores.

Different attempts such as DC, AC and pulse electrodeposition (PED) have been proposed it in order to electrodeposit mater inside the porous structure overcoming the limitation imposed by the oxide barrier layer. When the direct current (DC) method is applied either in the galvanostatic or potentiostatic mode a good control of the crystallinity of the deposited material can be achieved [10, 11]. However DC electrodeposition method results an unstable deposition process that leads to an inhomogeneous pore filling rate due to slight variations in the barrier layer thickness, which in turn induces big fluctuations on the deposition rate in each pore of the alumina template. The difficulty arises since the barrier layer at the bottom of the pores is resistive, leading to a potential drop across the oxide barrier layer that depends proportionally on the barrier thickness. Some improvements are obtained by removing the oxide barrier layer at the bottom of the pores by a chemical attack, and subsequently perform a metal deposition step through another method such as evaporation [12, 13] or sputtering [14, 15]. With such conductive layer at the bottom of the pores is possible to implement the DC electrodeposition process. However two extra steps are required; the thin metal layer deposition and the transfer of the alumina membrane [16]. Therefore finally the thickness of the PAA layer is limited, since the PAA membranes have to be relatively thick in order to avoid crack and fissures. Both processes are not desirable for the high scale devices fabrication.

The AC electrodeposition method was introduced in order to overcome these oxide barrier layer related problem [17] . In this case the alumina layer acts as a conductive layer during the cathodic half-cycles, during these cycles the metals ions are reduced at the bottom of the pores leading to the filling of material inside the nanopores, whilst the alumina layer can be treated as a dielectric of a capacitor during the anodic cycles. The rectifying behavior of the alumina and the concentration of the metal ions in the electrolyte close to the barrier layer are less unsaturated than in the DC method, considering that the capacitor can be discharged during these half-cycles. Therefore AC electrodeposition process is less prone to limitations related to the oxide barrier layer at the bottom of the pores. However, this method presents some disadvantages: part of the metal deposited is oxidized and under some conditions, there may not be enough time for the ions after the half negative potential to reach the bottom of the pores to maintain the same ion concentration, which can impede the control of the deposition [18].

The pulse electrodeposition process (PED) was introduced by Nielsch et al., in order to fill nickel nanowires within a PAA template [19]. This method can be seen as a variation of the AC electrodeposition process. Basically it consists in applying a short constant cathodic pulse in order to reduce the metallic ions followed by anodic constant pulse shorter than the cathodic one, in order to discharge the alumina barrier that acts as a capacitor. The cycle is completed by a delay time quite long to facility the recovery of the concentration close to the electrolyte and the deposited material. The PED method allows more homogeneous and uniform deposition inside the pores.

2.2 The principle of the electrodeposition process

The electrodeposition process relies on the reduction of metals ions. The metal to be deposited can be supplied by two different ways: either the solution contains the corresponding ionic form dissolved in a certain electrolyte, or the anode is made of the solid form of the material to deposit on the cathode. Al least two electrodes are required in order to carry out the process, the sample to be coated is set as cathode, where the reductions of

the metal ions take place. The metal ions (Me^{Z+}) are reduced or oxidized with the following principle reaction:

$$Me^{Z+} + Ze^{-} \leftrightarrow Me.$$

When the reaction takes place from the left to right correspond to the reduction of the metals ions leading to the metal deposition on the cathode. On the contrary when the reaction occurs from right to left an oxidation of the metal ions takes place. The ratio between the reduction and oxidation current is determined by the applied potential. The Nernst potential E_{Nernst} is established when both currents are equals, defined as,

$$E_{Nernst} = \frac{RT}{zF} ln\left(\frac{a_{M^{z+}}}{a_M}\right)$$

Where, R is the universal gas constant, T is the absolute temperature, z is the number of electrons involved in the reaction, F is the faraday constant, $a_{M^{z+}}$ is the chemical activity of the metal ions in the electrolyte and a_M is the chemical activity in the electrode.

The metal deposition over the cathode takes place only if the applied potential is higher than the Nernst potential. When the cathode is resistive, a potential drop occurs decreasing the effective applied potential for the metal ions reduction in the cathode. Therefore the potential must be sufficiently higher than the Nernst potential in order to successfully perform the electrodeposition process.

In the particular case of a metal deposition inside a PAA matrix, the applied potential must to be higher than the addition of the previously indicated Nernst potential and the potential induced by the oxide barrier layer at the bottom of the pores. Consequently the thickness of such barrier plays a critical role on the electrodeposition process.

2.2.1 The electrodeposition process within PAA templates

When electrodeposition is carried within PAA templates, a high overpotential applied during the pulsed electrodeposition process is required to guarantee the metal deposition at the bottom of the pores. The filling rate strongly depends on the oxide barrier layer between the porous structure and the aluminum. However, it is important to point out that the thickness of this barrier is not uniform, thus in each pore there is different resistance value. Therefore the equivalent resistance of the circuit formed by the electrolyte, the oxide barrier layer and the aluminum under layer is referred in figure 2-1.

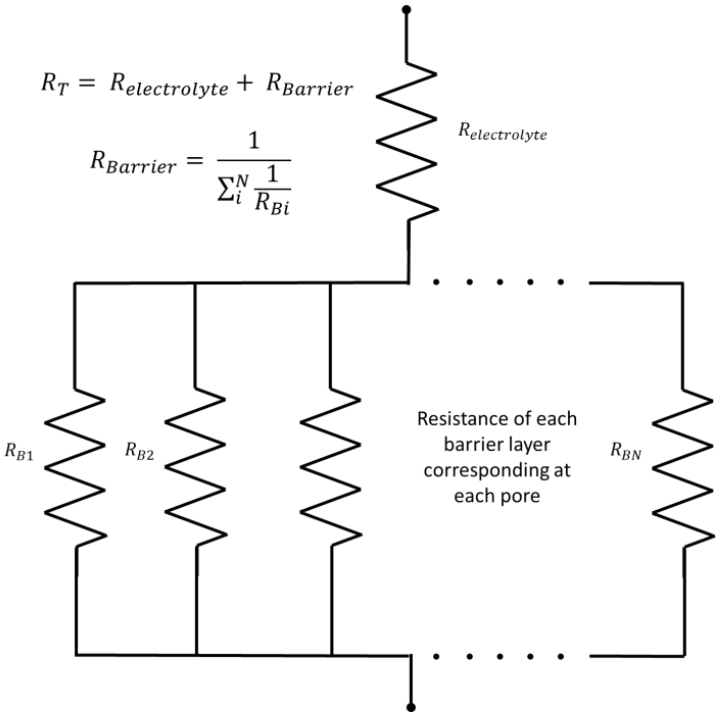

Figure 2-1. Schematic representation of the equivalent electric circuit for the electrodeposition process. The barrier layer at the pore bottom of each pore can have a different resistance value. The resistance of the barrier layer is determinated by the parallel connection. Therefore the total barrier layer resistance is equal to $R_{Total\ barrier} = \left(\sum_i \frac{1}{R_{Bi}}\right)^{-1}$.

Since the barrier layer at the bottom of each pore can have a different resistance value, the barrier layer resistance can be calculated as parallel connection. Finally the total resistance of the electrodeposition cell is the result of a serial connection between the resistance of the electrolyte and the resistance oxide barrier layer.

The total resistance of the PAA template is drastically decreased due to the parallel connection of the barrier layer. The electrodeposition current will preferentially flow through the pores with lowest resistance values. In this situation, if the potential applied is close to the reduction one, the metal deposition will take place just in the pores with the lowest resistance values. Thus only with high overpotential it becomes possible to overcome the potential drop in all the pores and achieve a uniform and homogenous deposition. In those pores with a lower resistance the initial current is higher than in the other ones, therefore the initial current extracts the ions from the electrolyte leading to an increase of the electrolyte resistance in such pores, which finally compensates the higher resistance in the pores with a thicker barrier layer. However too high overpotential can lead to a non-stable deposition process [20] due to an excessive reduction of the electrolyte which leads to an overdeposition in the pores with the lowest resistivity values. In this case, the size of the deposited nanoparticles is not homogenous and the whole process results complicated to be controled.

Therefore the overpotential is a crucial parameter in the pulsed electrodeposition process. In this case also, in order to minimize oxide barrier layer impact, a barrier thinning process is required to obtain a more uniform oxide barrier layer at the bottom pores. This procedure allows decreasing the overpotential value, and controlling the size of the nanoparticles deposited.

In the present work, the thinning barrier process consists in a combination of an exponential voltage decrease at the end of the anodization process, followed by a wet chemical etching. Both techniques have been implemented in order to uniformly reduce the oxide barrier layer at the bottom of the pores.

2.3 Experimental setup and parameters involved in the electrodeposition procedure

The electrodeposition process is generally considered to have a low-cost of implementation [21]. In the present work the metal deposition process has been performed in the same chemical cell as the anodization process. The only particularity relies in the addition of a reference electrode to obtain a more stable deposition. The most relevant parameters in the PED are the shape and the characteristics times of the applied pulse.

2.3.1 Three electrode configuration system

The deposition process is generally performed in a three electrode configuration. This system involves the two electrodes named before, where the anode acts as the counter electrode, and the cathode acts as working electrode. The third electrode introduced is a reference electrode that defines a standard potential to which the electrodeposition potential are referred. Typically reference electrode is an Ag/AgCl electrode, acting as half-cell itself, since it contains oxidants and reductants of a redox couple. The importance of such electrode relies on the fact that the potential of the counter electrode is constantly adjusting the lack or excess of charges induced by the working electrode where the deposition takes place, so either the working electrode or the counter electrode cannot be taken as a reference electrode. On the contrary, the reference electrode can adjust and measure the potential of the working electrode. Additionally, the reference electrode is connected to a very high resistive voltmeter, thus the current flowing via such electrode is negligible. Consequently all the current flow by the counter electrode providing the charges in the circuit for the reduction process.

2.3.2 Experimental setup

The electrodeposition process has been performed with the same sample-holder used for the anodization process. Thus, after the pore widening process the sample has been transferred immediately into the appropriate electrolyte for the metal deposition process.

The three electrode setup has been used, where the reference electrode is an Ag/AgCl electrode, the working electrode is PAA template and the counter electrode is a graphite electrode. The setup was supplied by a potentiostat from the company Bio-Logic and in order to set the electrodeposition parameters the EC-lab software has been employed. This software allows designing the shape of the pulsed applied on the working electrode. The potentiostatic mode has been chosen since it allows to apply the overpotential. Consequently only the ions with a reduction potential contribute to the electrodeposition current, leading to the metal deposition at the bottom pores. Under the Galvanostatic mode, the imposed current will not necessary force the overpotential required for the reduction of the ions contained in the electrolyte and can promotes hydrogen evolution [22].

The simple pulsed shape applied for the PED process is shown in figure 2-2. The pulse shape is composed by a short negative voltage of -5.5 V ms applied between the working and reference electrode during 5 ms, followed by a longer rest time of 90 ms in the open circuit potential (OCP). The OCP is the potential applied at the working electrode for which no current pass by the counter electrode. This potential corresponds to the potential that exist between both electrodes immersed in the electrolyte. Therefore the OCP establishes the zero potential with respect to the chemical cell.

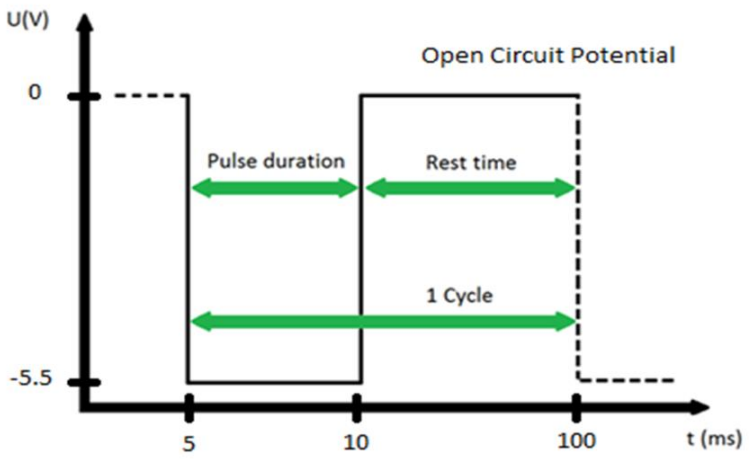

Figure 2-2. Applied pulse used for the electrodeposition process.

Nickel nanoparticles have been deposited at the bottom of the pores. In order to carried out the electrodeposition process a Watts bath has been prepared, consisting in a mixture of 330g/L $NiO_4 \cdot 6H_2O$, 45g/L $NiCl2 \cdot 6H_2O$ and 45g/L H_3BO_3. The number of sweeps has been varied between 25 and 1000 in order to deposit and adjust the size of the nanoparticles deposited.

2.4 The metal deposition at the bottom of the pores

Different studies have been performed in order to analyze the impact of the PAA structure and the template fabrication conditions on the metal deposition process. For instance, the influence of the anodization temperature, the anodized voltage and the pore length has been deeply investigated. Finally the porosity of the PAA templates has been compared with the density of nanoparticles per unit of area obtained through the deposition process. Such comparison provides useful information of the possible branch structure generated during the exponential decrease process applied in order to thin the oxide barrier layer at the bottom of the pores. The ensembles of the performed studies are of paramount importance for the device fabrication and their further characterization.

2.4.1 Influence of the barrier layer thickness over the metal electrodeposition

The impacts over the catalyst deposition of the electrolyte temperature during the second anodization process, and the exponential voltage decrease process have been investigated. Previous works reported that the thickness of the oxide barrier layer depends on the anodization temperature [23, 24]. The oxide barrier layer at the bottom of the pores is a critical parameter that can determines the distribution of the deposited nanoparticles.

The exponential voltage decrease has been applied in order to reduce the oxide barrier layer, where the exponential decay rate chosen is η =2.0·10^{-3} s^{-1}. Marquardt et. al [25] have demonstrated that such decay rate effectively reduced the oxide barrier layer and facilitate further electrodeposition procedure. However, in the present work it have been evidenced that it is necessary to also establish a proper anodization temperature in order to enhance the exponential voltage decrease process that will lead to uniform deposition of the nanoparticles within the PAA structure.

The measurements of the thickness of the oxide barrier layer are complicated to perform since a carefully cut of the PAA structure is required for avoiding any damage of the sample [26]. A recommended approach is to mill the PAA with a Focus Ion bean [27]. However such technique is time consuming, additionally as previously mentioned, the thickness of the oxide barrier layer statistically varies along all the interphase between the aluminum and the PAA structure. The approach introduced in the present work, in order to obtain information of the oxide barrier layer, consists in the deposition of the catalyst into the PAA and the subsequent elimination of the PAA structure in a 0.2 M CrO_3 and 0.6 M H_3PO_4 solution. By this procedure is obtained indirect information of the oxide barrier layer as it is possible to measure the distribution and the area occupied by the deposited material, meaning that in these zones the thickness of the oxide barrier was lower than in the regions where no material was deposited.

The second anodization process (including the exponential voltage decrease process) has been performed at different temperatures. After the electrodeposition process, the PAA

has been removed in a chromic solution. The figure 2-3 shows the nanoparticle distribution at the bottom pores of the as-removed PAA structure for the different temperatures of the electrolyte during the second anodization process. The range of temperatures studied are between 15,0°C and 17,5°C with increments of 0,5°C and the applied voltage for the anodization process is of 40V. The second anodization process lasted 500 seconds followed by the exponential voltage decrease process. Each image includes the electrodeposition current monitoring as times evolve during the deposition process. During the electrodeposition process 50 sweeps (pulse shape described above) have been applied.

The figure 2-3 (a) reveals that when the second anodization process is performed a 15,0°C there are is practically no deposition at the bottom of the pores. The electrodeposition current is positive indicating an oxidation process instead of a reduction process that could lead to metal deposition. We can infer that for these fabrication conditions of the PAA the deposition process is not achieved due to the oxide barrier layer not being efficiently reduced. By increasing the anodization temperature at 15,5°C, in the figure 2-3 (b) it becomes possible to observe the presence of nanoparticles clusters of the order of 100 nm^2. In terms of the electrodeposition current, we notice that during the first 35 pulses the current is positive leading to a reduction of the Watts bath solution. However the current decreases in absolute value, pulse by pulse, until process switch to an oxidation regime. We note that in this case, the exponential voltage decrease process was effective only in certain spots, leading to an inhomogeneous deposition. When the anodization process is carried out at 16,0°C, as is shown in figure 2-3 (c) the clusters of nanoparticles increase both in number and size becoming of the order of 500 nm^2. Concerning the electrodeposition current, we notice the redox process is achieved during the whole process in spite of the magnitude of the current still decreasing in absolute values pulse after pulse. The same trend is observed when the anodization process has been performed at 16,5°C as is shown in figure 2-3 (d), the electrodeposition current in this case becoming higher in absolutes terms and leading to a deposition of bigger nanoparticles cluster. Therefore as the anodization temperature increases the exponential voltage decrease process becomes more effective in order to thin the oxide barrier layer, due to the metal deposition process takes place in large areas. Nonetheless the fabrication conditions in this range of temperatures are not proper for a uniform deposition of individual nanoparticles. On the other hand, when

the anodization process is done at 17,0°C, in the figure 2-3 (e) we observed that the distribution of nanoparticles is composed by individual nanoparticles and smaller clusters of nanoparticles. For this anodization temperature the reduction of the oxide barrier layer is thus becoming more effective affecting larger areas and leading to an increase in the electrodeposition current. Finally for anodization processes performed at 17,5°C as shown in figure 2-3 (f), the nanoparticles are practically deposited individually and there is an uniformly filling at the bottom of the pores of the PAA. The applied anodization temperature appears very effective to homogeneously reduce the oxide barrier layer that guaranteed a uniform metal electrodeposition.

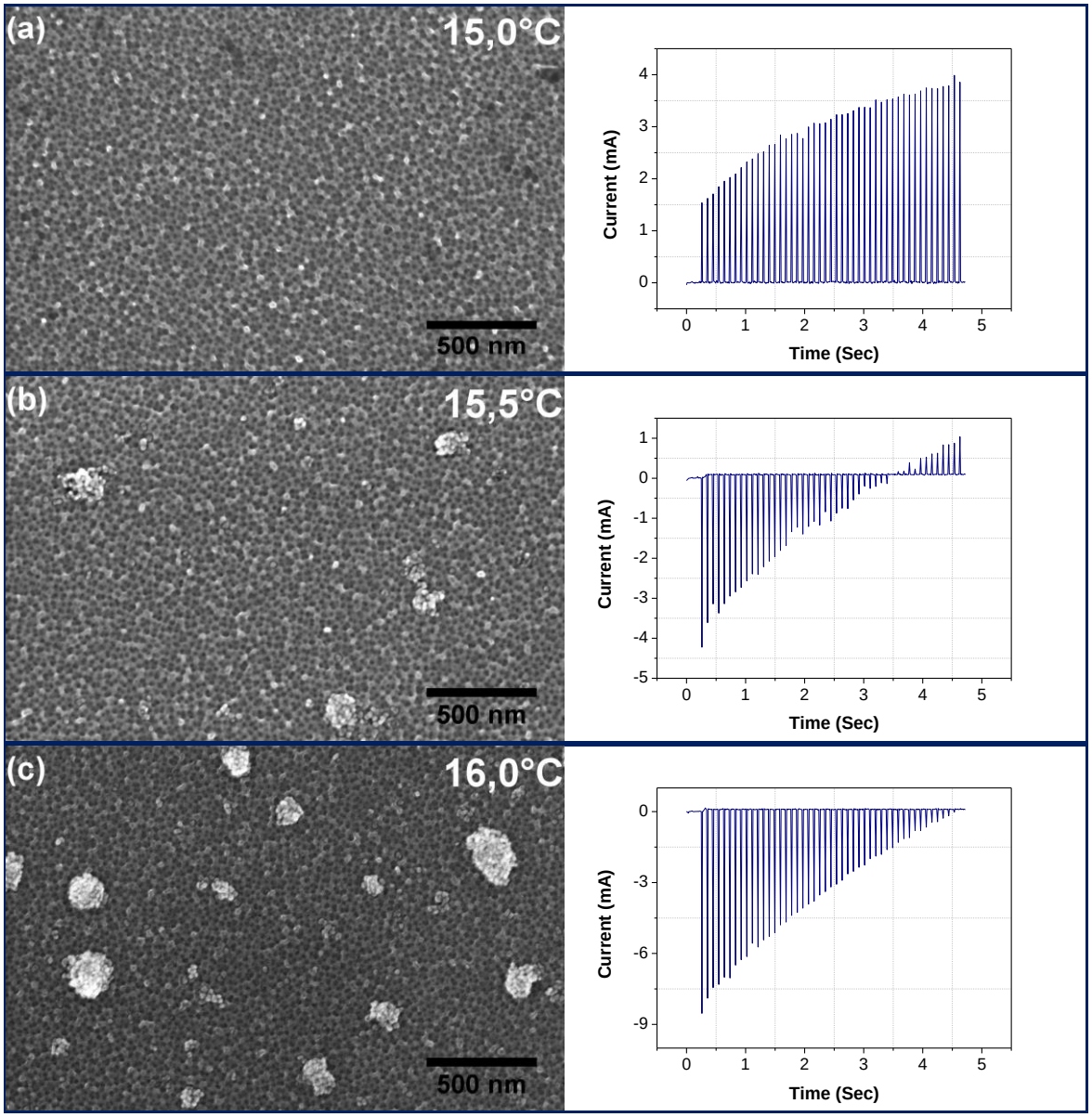

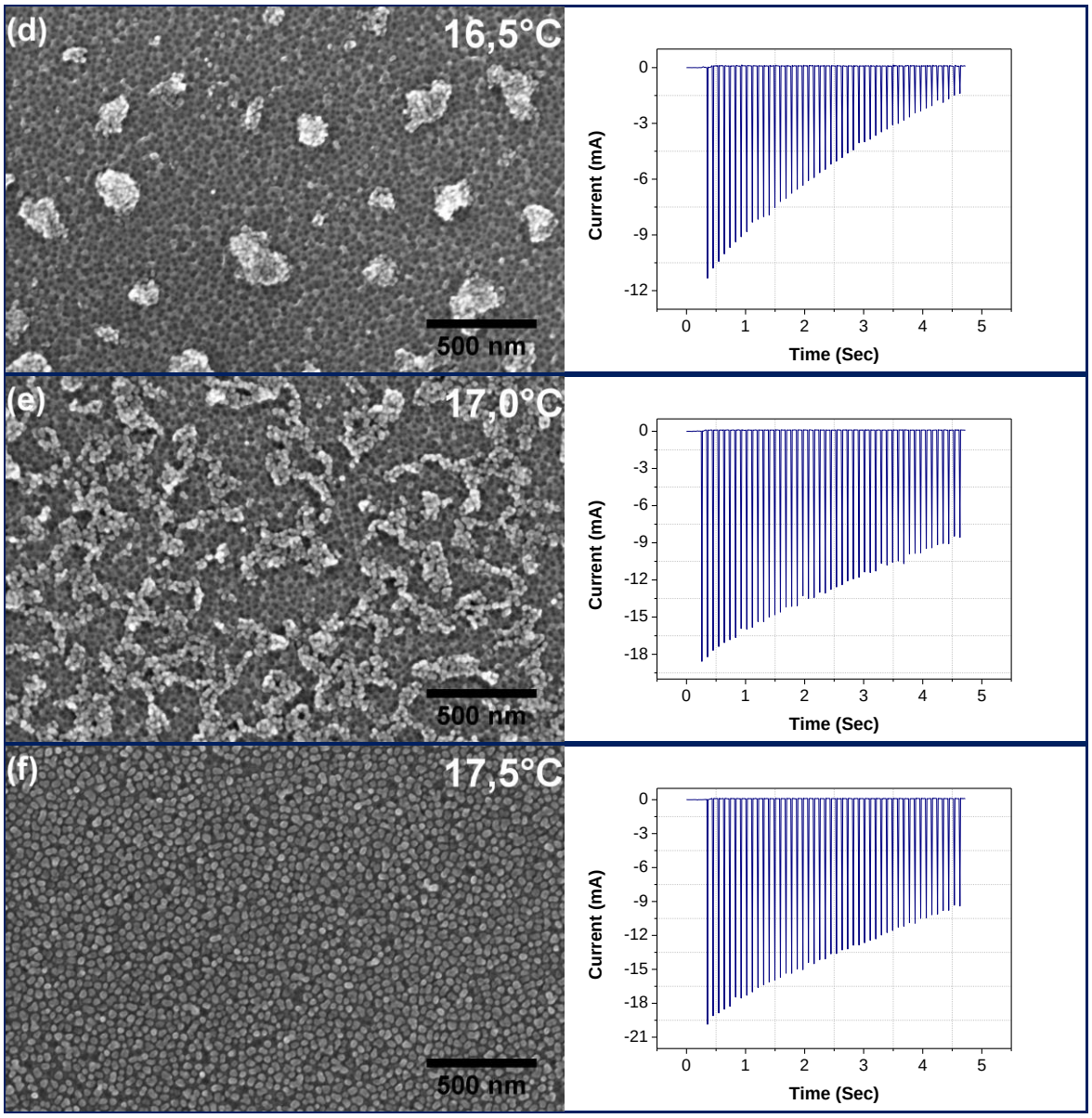

Figure 2-3. SEM images of nickel nanoparticles distribution at the bottom of the pores of removed PAA structure (the alumina is eliminated in a chromic acid solution) and their correspondent electrodeposition current as function of time. The second anodization process and the exponential voltage decrease have been performed at different temperatures. The applied potential during the anodization process is of 40V and the exponential voltage decrease constant is η =2.0·10^{-3} s^{-1}. During the electrodeposition process 50 sweeps have been applied. The different anodization temperatures are: (a) 15,0°C, (b) 15,5°C, (c) 16,0°C, (d) 16,5°C, (e) 17,0°C and (f) 17,5°C.

We evidenced that the anodization temperature has a great impact over the efficacy of the exponential voltage decrease process. Consequently, different behaviors concerning the metal deposition distribution have been observed in the range of the anodization

temperatures from 15°C to 17,5°C. For instance, at 15°C there is no deposition. Alternatively in the range of 15,5°C to 16,5°C the deposition process leads to a cluster-like distribution of the electrodeposited material. As shown in figure 2-4, as the second anodization temperature increase, the superficial nanoparticles density increases from 3% to 9% . On the other hand, in this range of anodization temperatures, the diameter of the nanoparticles remains of the order of 25 nm. When the second anodization process is performed at 17,0°C the superficial density of nanoparticles marks a significant increase, and the nanoparticles occupy (38 ± 2)% of the total surface. In addition their mean diameter increases to (33± 8)nm. When the nanoparticles are clearly individualized with no apparent cluster formation, the occupied surface is of (49 ± 2)% and the mean diameter (38 ± 10)nm.

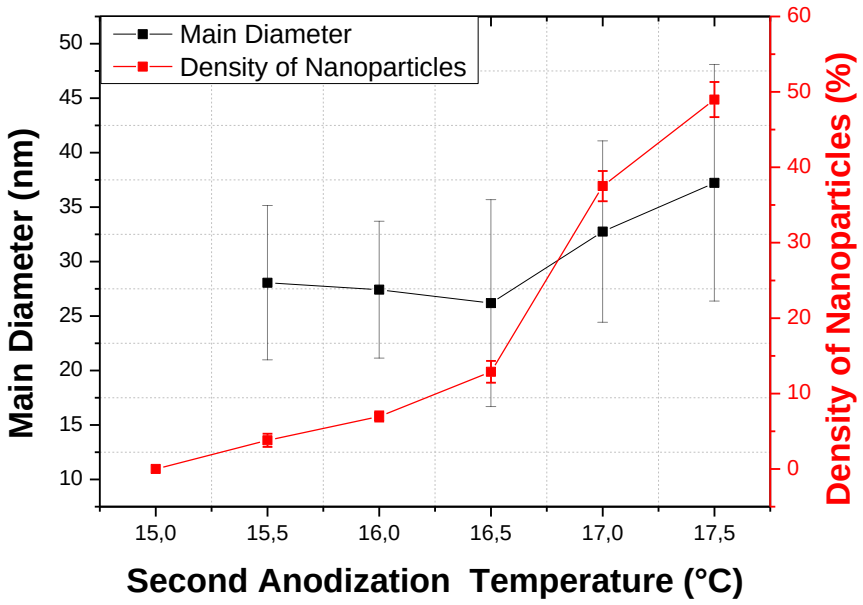

Figure 2-4. Influence of the second anodization temperature over the nanoparticle distribution and size at the bottom of the pores. The anodization voltage applied has been of 40V.

2.4.2 Operational range of the metal electrodeposition depending on the anodization voltage

The impact on the metal electrodeposition process has been studied in the range of anodization voltage from 20V to 60V with increments of 10V. For all the prepared samples the second anodization process duration has been set at 500 seconds followed by the exponential voltage decrease process with the decay rate η =2.0·10^{-3} s^{-1}. The range of temperature during second anodization process has been varied depending on the anodization voltage. During the electrodeposition process 50 sweeps have been applied for all the samples.

One of the most relevant parameter to analyze the impact of the electrodeposition process is the global charge involved in the reaction. This is a quantitative value given by the following equation:

$$Q = \int_{t_i}^{t_f} I(t)dt$$

The figure 2-5 shows the global charge as a function of the anodization temperature for different anodization potentials. For all the applied potentials, the deposition pattern follows the same trends as the sample of figure 2-4 where the applied potential is of 40V. The only difference relies on the range of temperature where the three regimes (non-deposition, inhomogeneous deposition and individual nanoparticle deposition) are obtained. The figure 2-5 indicates the non-deposition regime with a red dash lines, pointing out that for these positive global charges values it is not possible to achieve the nanoparticle deposition. Between the red dash line and the green dash line we indicated that for such global charges values an inhomogeneous deposition pattern is obtained, with clusters of nanoparticles. For higher Q values, the region delimited from the green dash line indicates that the deposition of individual nanoparticles at the bottom of the pores is achieved.

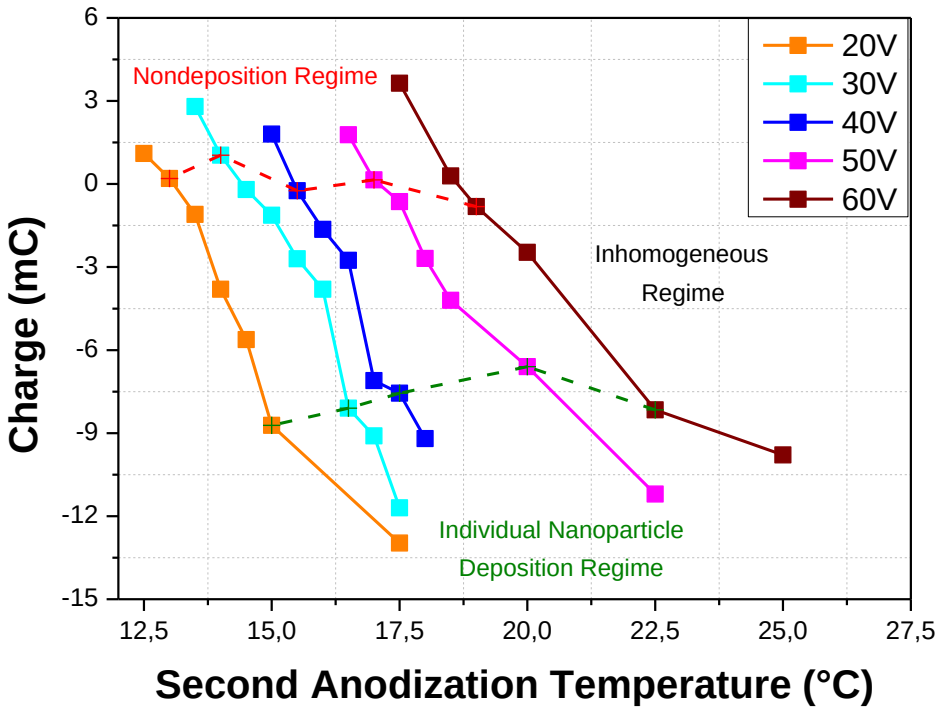

Figure 2-5. Relation between the global charge accumulated during the electrodeposition process as function of the anodization temperatures, for samples anodized in the range of 20V to 60V with increment of 10V.

Using data plotted in figure 2-5 it is possible to infer the operational range of temperature for each anodization potential, and the final deposition distribution at the bottom of the pores. For instance, if the anodization process is performed at temperatures lowers of 13°C, for an anodization potential of 20V, the electrodeposition current is always positive preventing the an effective deposition process. For temperatures up to 14.5°C, the global charge during the electrodeposition process is negative however the deposition is non-uniform, and the deposition material is cluster-type. From anodization temperature of 15.0°C individual nanoparticles are deposited. On the other hand for anodization voltages of 60V, no material is deposited for anodization temperature lower than 19.0°C, the cluster-type of distribution of nanoparticles is obtained in the range of temperatures from 19.5°C to 22.0°C, and individual nanoparticles begin to be deposited from temperatures higher than

22.5°C. In conclusion the exponential voltage decrease process is effective in different range of temperatures for each applied anodized potential.

From figure 2-5, in addition to the operational range for each anodization voltage, it is possible to conclude that higher anodization voltages require higher anodization temperatures in order to effectively reduce the oxide barrier layer that will lead to a uniform nanoparticle deposition. This phenomenon can be attributed to the fact of using the same exponential voltage decrease rate for all the anodization voltages. Evidently, the final thickness of the oxide barrier layer depends on the anodized voltage in spite of the same decay rate applied and to finish, the exponential voltage decrease process at the same step. For instance, figure 2-6 shows the exponential voltage decrease function for each anodization voltage where we highlight the same final anodization step for each case. This choice of the final voltage step should theoretically imply that the thickness of the oxide barrier (D_{BL}) should remain the same for each case, where D_{BL} is given by the following expression:

$$D_{BL} = \alpha U_{Anodization}$$

Where α is a constant and $U_{Anodization}$ is the applied potential. However as it is possible to infer from the figure 6 the final thickness of the oxide barrier layer depends on the anodization temperature and the exponential voltage decrease rate. Therefore a more exact relation between the D_{BL} and the $U_{Anodization}$ can be express as:

$$D_{BL} = \alpha(T, \eta) U_{Anodization}$$

Where $\alpha(T, \eta)$ depends on the temperature and the exponential voltage decrease rate.

We observe for each anodization voltage that it exists an associated decay rate that is effective in a certain range of temperature and consequently the thinning process depends on the anodization temperature. For higher anodization voltages, higher anodization temperatures are required since the temperature has a direct impact on the enhanced field-assisted dissolution of the oxide at the oxide/electrolyte interface.

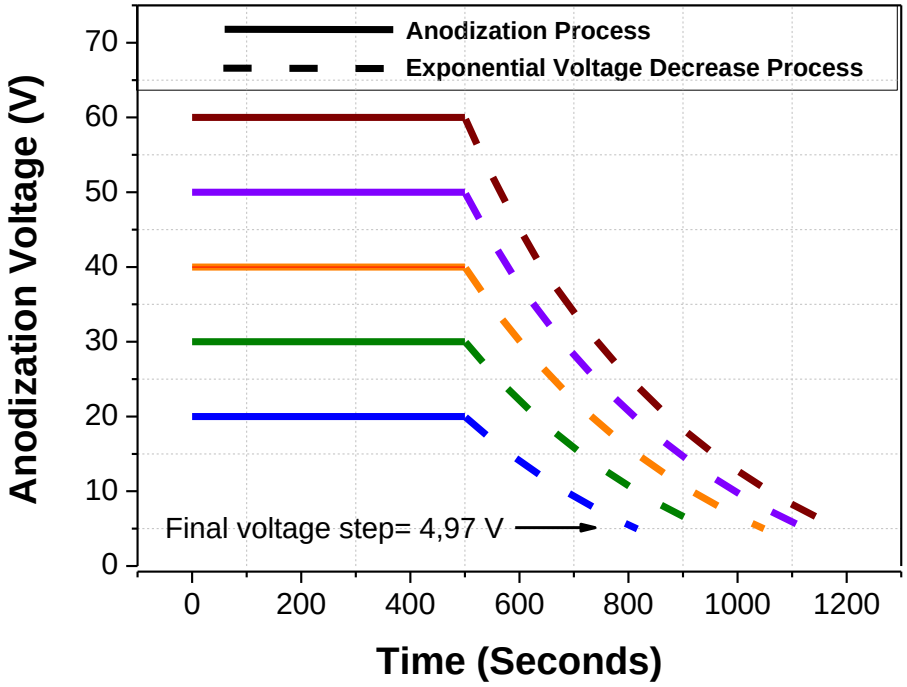

Figure 2-6. Applied voltage during the second anodization process for the PAA fabrication. In solid line the anodization potential followed in dash line by the exponential voltage decrease process. For each anodize voltage η =2.0·10^{-3} s^{-1} is the voltage decay rate and the final voltage is 4.97 V.

2.4.3 Influence of the pore length on the electrodeposition process

The anodization process duration has been the same for all the applied potentials therefore longer pores are obtained for higher anodization potential, due to higher anodization voltages which induce higher currents. In this study the anodization duration has been varied in order to establish how the pore length affects the deposition process. The first experiments were carried out with samples obtained (different anodization time) with anodization potential of 30V, an anodization temperature of 17,5°C and an exponential voltage decrease rate η =2.0·10^{-3} s^{-1}. Figure 2-7 shows the global charge accumulated as function of the pore length. Additionally to the impact of the pore length on the electrodeposition process, in the same graph we indicated the global charge accumulated

during the electrodeposition process of two samples obtained with an applied anodization potential of 60V at two different anodization temperatures, 17,5°C in which case no deposition is obtained and 25,0°C where the deposition is successfully performed. For all the samples the electrodeposition process consisted of 50 applied sweeps.

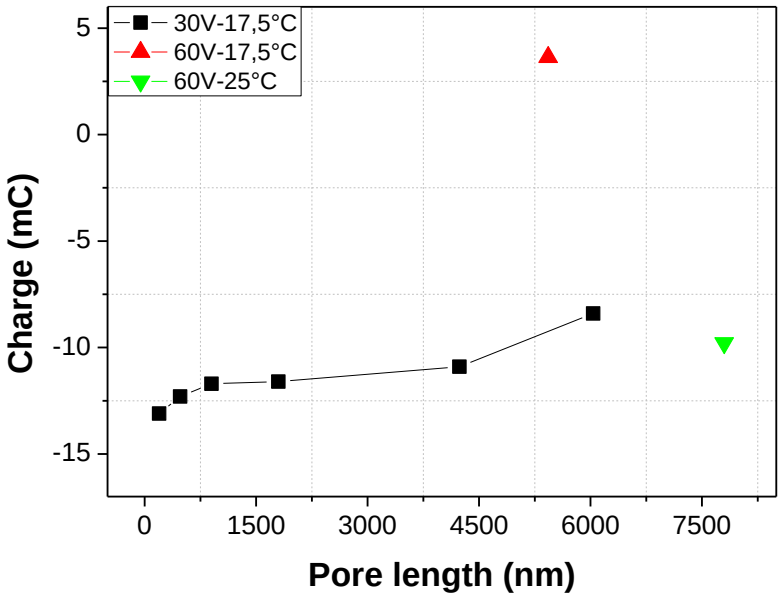

Figure 2-7. Graph of global accumulated charge during the electrodeposition process as function of the pore length. The samples have been fabricated at anodization potential of 30V, an anodization temperature of 17,5°C and with an exponential voltage decrease rate of η =2.0·10^{-3} s^{-1}. The anodization time has been varied to obtain different pore length. These samples are compared with the global charge obtained for the samples obtained with an anodization voltage of 60 V at corresponding anodization temperatures of 17,5°C and 25,0°C.

In conclusion from figure 2-7 we can observe that the pore length in the studied range does not significant affect the electrodeposition process. The nanoparticles distribution is not highly affected considering that the global charge accumulated during the electrodeposition process decrease in absolute values only 35% for a pore length variation from 6 µm. This diminution in the charge can be attributed to a more complicated ion transport inside the pores during the deposition process. It can also be related to a less

effective diffusion of the 0.3M H_3PO_4 solution during the pore widening process, in which case the thinning process is becoming less effective. On the other hand, no deposition is obtained when the sample is anodized at the same temperature but with an anodization voltage of 60V, in which case the pore length was 5,3 µm. We corroborated that the anodization temperature is more determinant than the pore length, because the electrodeposition takes place applying the same voltage but increasing the anodization temperature at 25,0°C which induces a higher anodization current that leads to a longer pore formation. Therefore as previously discussed, the anodization temperature plays a crucial role for the thinning barrier layer process that in turn will strongly impact the electrodeposition process, the pore length variation over a relatively extended range has a relatively low to negligible influence.

2.4.4 Evidence of metal nanoparticles deposited at the bottom of the pores

Previously has been showed nanoparticles could be successfully deposited at the bottom pores. Nonetheless such nanoparticles must furthermore play a catalytic role for the synthesis of carbon nanostructures. In order to verify that the chemical composition and the nature of the deposed material, chemical mapping analysis has been performed.

In the figure 2-8 is showed a chemical map carried out at the bottom pores zones using the Electron Energy Loss Spectroscopy (EELS) technique in the Energy Filtered Transmission Electron Microscopy (EFTEM) image mode. Figure 2-8 (a) shows the selected area where the chemical mapping has been performed. As result in figure 2-8 (b), is observed that the zone corresponding to the aluminum is in black revealing the absence of nickel or oxygen. On the other hand, the surface occupied by the nanoparticles is colored in green showing the presence of atomic nickel. Finally in red indicates the presence of oxygen, in this case corresponding to the PAA zone. The figure 2-8 (c) and (d) are the EELS spectra registered on the *O K* and *Ni K* ionization edges, respectively.

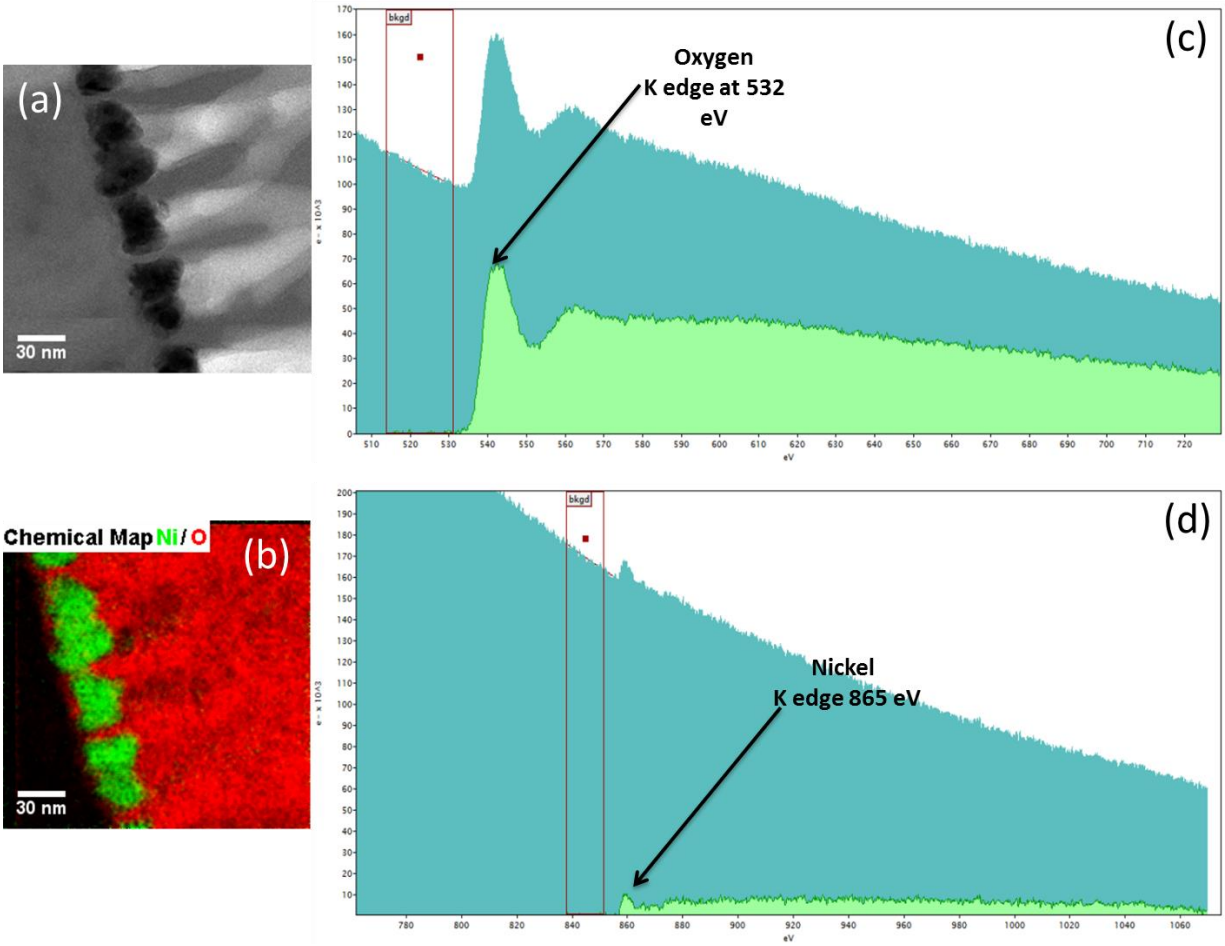

Figure 2-8. Chemical map performed at the bottom of the pores using the EELS technique in the EFTEM imaging mode. (a) Region selected to carry out the chemical map. (b) Chemical mapping indicating in red the atomic presence of oxygen and in green the atomic existence of atomic nickel. (c) EELS spectra registered on the *O K* ionization edges. (d) EELS spectra registered on the Ni K ionization edges.

We may conclude that the deposited nanoparticles within the PAA templates are promising catalysts in terms of morphology and nature for catalyzing the CVD synthesis of CNTs.

2.4.5 Number of catalytic nanoparticles electrodeposited per pore

Generally for the synthesis of CNTs the catalyst deposition plays a crucial role on the final synthetized structure. Besides the metal deposition, in the particular case of the synthesis within the PAA the pore structure the pore structure can highly affects the CVD growth carbon nanostructures. For instance a branched structure can be impacted by clogging during the growth inside the pores, since the gaseous precursors molecules lose energy due to collisions with the pore walls avoiding the carbon appropriate diffusion towards/inside the catalyst; in addition the growing CNTs can suffer mutual blocking among them when they emerge from secondary branched pores and reach the primary pore. Therefore, it is important to acquire relevant information of the bottom pore's structure before to proceed to the synthesis of carbon nanostructures within PAA templates.

Figure 2-9 shows a cross section TEM image corresponding to a PAA template with electrodeposited nanoparticles at the bottom pores. The PAA was fabricated with an anodization potential of 30V at 17,5°C. In figure 2-9 (a) are indicated the different zones of the template as the PAA structure and the aluminum. At the bottom of the pores the nickel nanoparticles are pointed as well as the presence of a branched pore structure near to the interphase between the PAA and the aluminum. This structure reflects that the pore formation evolves straight until the exponential voltage decrease process begins. In figure 10 (b) under a higher magnification it is possible to clearly identify the branched structure, however in order to properly assess the number branches for each pore a tomography study must be performed. The most important fact to highlight is that the nanoparticles electrodeposition is successfully achieved in spite of a branch structure at the bottom of the pores. However it is necessary to analyses the branch multiplication phenomenon regarding the synthesis of carbon of nanostructures. In the present work we have introduce an interesting approach that involves the nanoparticle deposition at the bottom of the pores in order to count the number of branches created per primary pore during the exponential voltage decrease process.

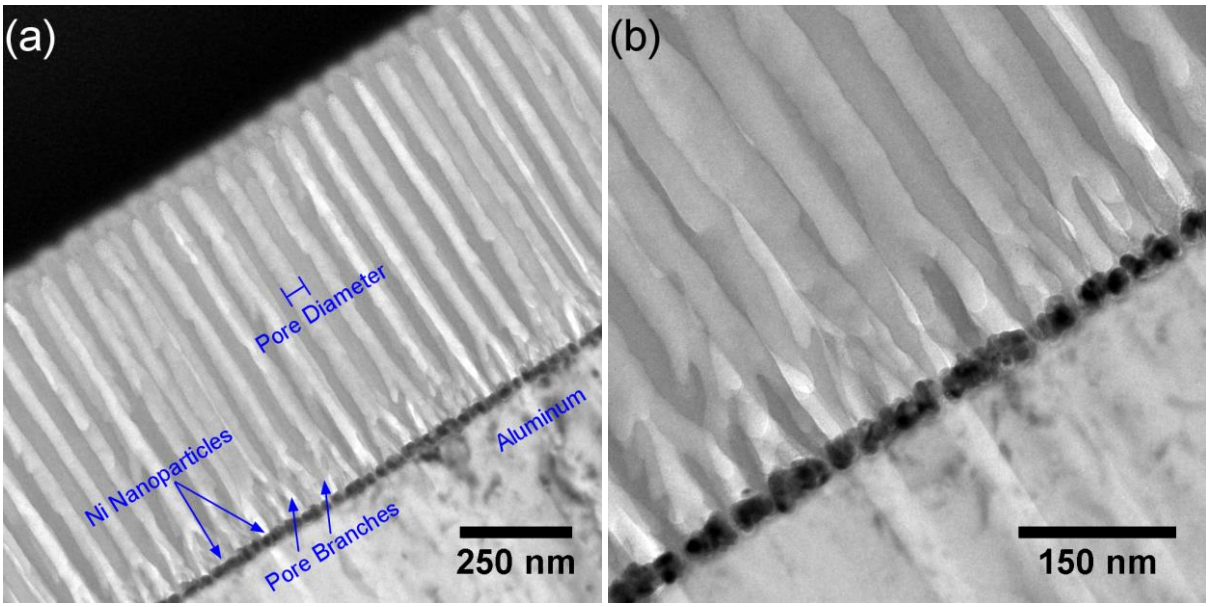

Figure 2-9. TEM cross-section of a PAA template anodized at 30V with anodization temperature of 17,5°C. The lamella has been obtained by FIB fabrication/manipulation. (a) PAA structure with nanoparticles deposited at the bottom of the pores. (b) Zone of the bottom of the bottom of the pores.

The adopted strategy to calculate the number of secondary pores generated per each primary pore, consists in the comparison of the pore top surface with the pore distribution at the bottom of the pores. The pore shape at the bottom of the PAA can be easily performed measuring the density of the electrodeposited nanoparticles. From figure 2-6 is possible to obtain the required electrodeposition conditions in order to achieved filling rate of the pores close to 100%. Under these conditions, after the deposition process, the nickel nanoparticles should cover completely the related “hole” left by the bottom pore. Avoiding an over deposition state, the metal electrodeposition will than reflect the fingerprint of the previous shape/state of the bottom of the pores. Figure 2-10 shows a schematic representation of the procedure implemented to obtain the number of branches generated by pore. Therefore properly adjusting the deposition conditions and by the subsequent elimination of the PAA structure via selective chemical attack, it become possible to obtain the bottom pores distribution that reflects the number of secondary branched pores generated by primary pore. Afterwards, in order to have a notion of the number of branches created for each primary pore, it is necessary to compare the number of nanoparticles per

cm^2 with the number of the pores of the PAA per cm^2. This correlation directly yield the number of nanoparticles deposited in each primary pore. This approach provides a quantitative notion of the number of branches generated during the exponential decrease process.

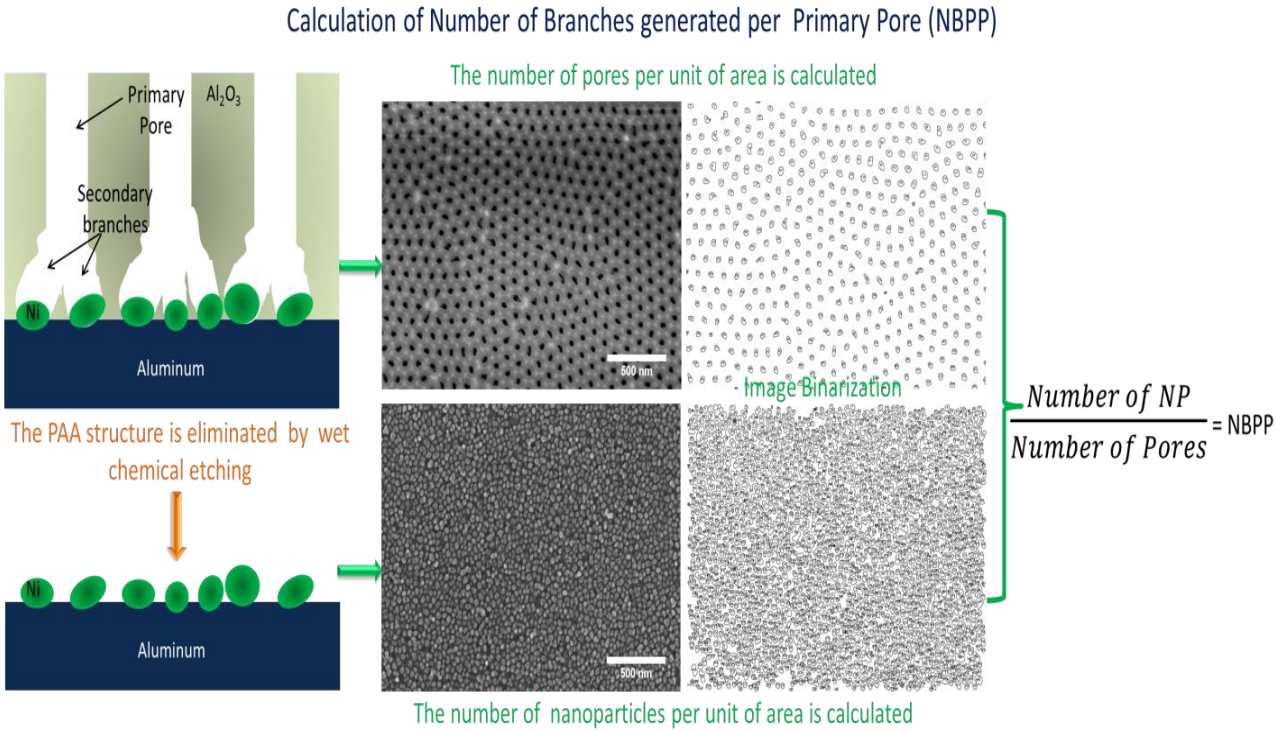

Figure 2-10. Schematic representation of the procedure in order to deduce the distribution of the bottom pores after the exponential voltage decrease process.

The figure 2-11 is shown the nanoparticles deposited at the bottom of the pores with filling rate close to 100% while avoiding the overdeposition of nanoparticles into primary pores. Correlating figure 2-11 and figure 2-4 (f), which satisfices the same requirements previously mentioned, it is possible to estimate the bottom pores distribution before the electrodeposition process, when anodization process is carried on in the voltage range of 20V to 60V with increments of 10V. Applying the same procedure implemented to calculate the porosity of the PAA (section 1.6.2), the number of nanoparticles per unit of area can be deduced.

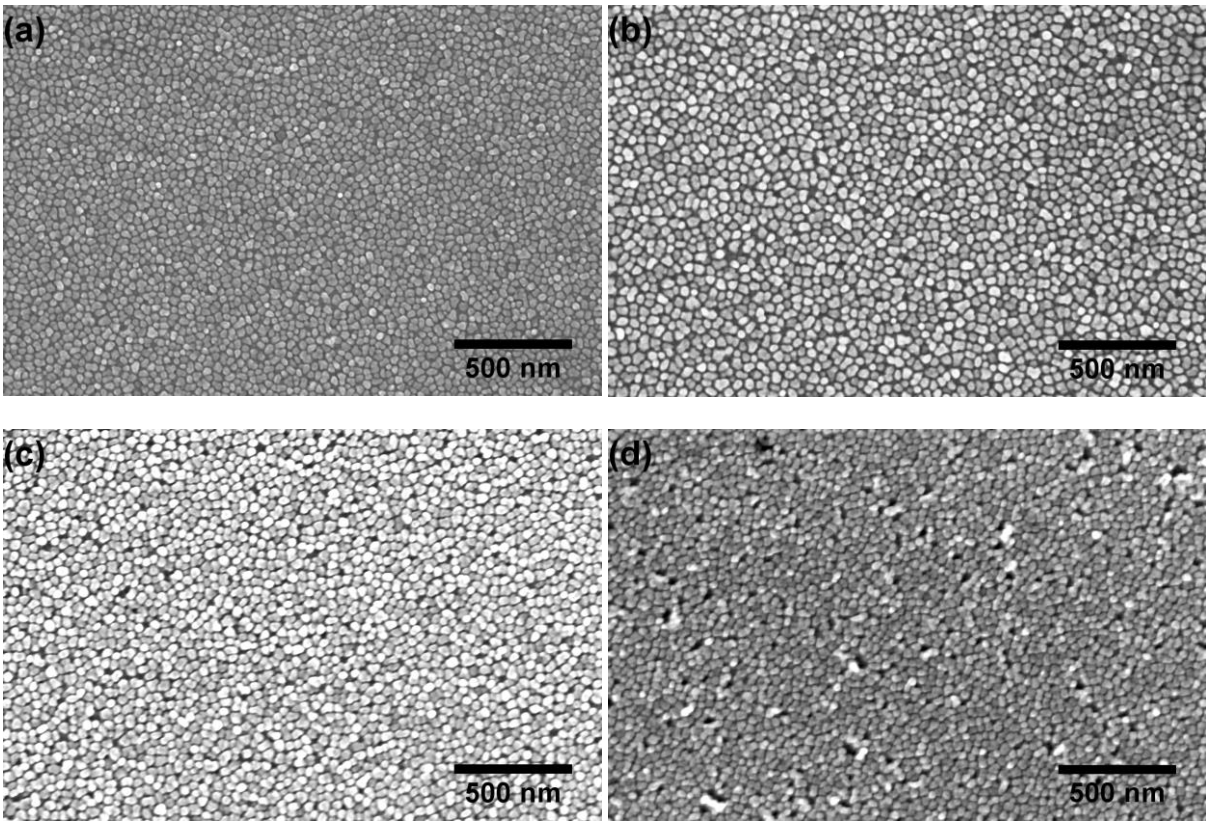

Figure 2-11. Metal nanoparticles deposited at the bottom of the pore after the PAA selective etching. The electrodeposition conditions applied are chosen in order to achieve a 100% branched pores filling rate while avoiding the overdeposition of the nanoparticles into the primary pores. (a) anodization voltage of 20V and electrolyte temperature of 16,5°C, (b) anodization voltage of 30V and electrolyte temperature of 17,5°C, (c) anodization voltage of 50V and electrolyte temperature of 22,5°C and (d) anodization voltage of 60V and electrolyte temperature of 25,0°C. The electrodeposition conditions have been the same for all the samples and 50 sweeps have applied for each sample, whilst the exponential voltage decrease has been of $\eta = 2.0 \cdot 10^{-3}\ s^{-1}$.

The figure 2-12 (a) provides the information (above discussed) in order to calculate the number of branches generated for each pore. The figure 2-12 (a) is the graph of the density of pores and nanoparticles per unit of area in the logarithmic scale as function of the anodization voltage. We can remark that the density of the pores decreases as the anodization voltage increases. On the other hand the density of nanoparticles per unit area fluctuates between 4.9×10^{-4} and $8{,}3 \times 10^{-4}$. From the relation between the density of nanoparticles and the density of the pores, we derived as is shows the plot in figure 14 (b) the estimated number of nanoparticles deposited in each primary pore, for anodization

process in the voltage range of 20V to 60V. As the anodization voltage increases, the number of nanoparticles deposited in each pore significantly increases. For instance for an anodization voltage of 20V just two nanoparticles are deposited per pore, on the other hand for the anodization voltage of 60V an averaged 10 nanoparticles are deposited in each pore. Assuming that every bottom branched pore has been filled with one nanoparticle during the electrodeposition process it is possible to consider that the number of nanoparticles deposited for each primary pore is equal to the number of branches generated per pore during the exponential voltage decrease process.

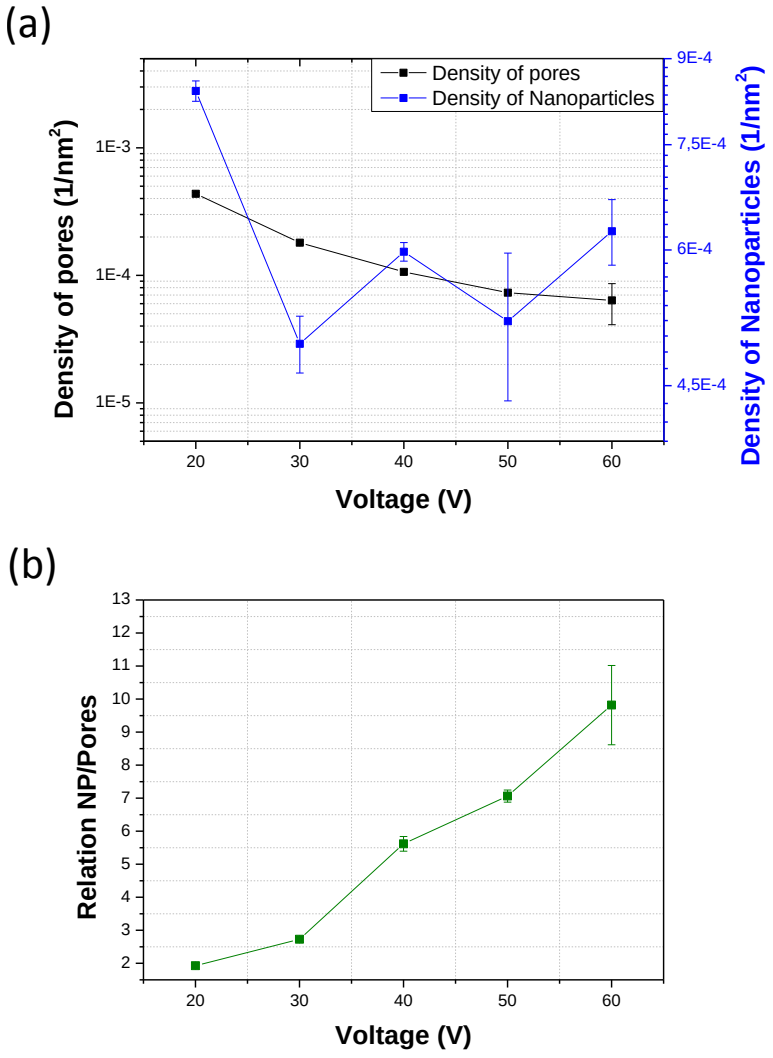

Figure 2-12. (a) Measure of the density of pores per unit of area and density of nanoparticles per unit of area in as function of the anodized voltage. (b) Calculated relation between the numbers of

nanoparticles deposited in each pore during the electrodeposition process as a function of the anodization voltage.

We remark that when implementing the same exponential voltage decrease rate for higher applied voltages the number of branches created for each pore is higher. Such phenomenon of branch multiplication can be related to the fact of imposing the same exponential voltage decrease regardless of the chosen anodization voltages. As the voltage drop and the final applied voltage are the same for all the cases, the boundary conditions for the exponential decrease process implies that the higher anodization voltages will require more time to finalize the thinning process. Consequently longer exponential voltage decrease process promotes the branches multiplication.

Anyway in order to obtain a more detailed analysis of the impact on the exponential voltage decrease rate on the pore structure it is necessary to perform tomography studies, thus a fully reconstruction of the pore structure can be obtained and subsequently also an assessment of the number of branches per pore. Nevertheless it is important to highlight that with the approach carried out in the present work it is possible to obtain a quantitative result of a three dimensions structure (branch structure) from the analysis of a two dimension distribution (electrodeposition of nanoparticles at the bottom of the pores), providing precious information for both the synthesis of CNTs and from a more general perspective for the further devices fabrication.

Under these PAA fabrication conditions, only the templates fabricated in the range of 20V to 30V are promising candidates for the synthesis of carbon nanotubes. The other type of templates exhibits too numerous branch structure that can induce “clogging” side-effect during the carbon nanostructure growth.

2.6 Conclusions

The electrodeposition process has been successfully carried out at the bottom of the pores of the PAA templates. The influence of several anodization conditions has been studied, such as the anodization temperature, the anodization voltage and the pore length. The results obtained shows that the anodization temperature has a huge impact on the oxide barrier layer formation at the bottom pores that in turn strongly impact the electrodeposition process in terms of size, distribution and density of nanoparticles. For higher anodization voltages, higher anodization process temperatures are require in order to obtain a homogeneous distribution of nanoparticles. On the other hand, in the range of pores length studied, from 100 nm to 6 μm, the pore length does not seem to have a significant impact over the deposition process.

Through a chemical mapping analysis performed at the bottom of the pores by the Electron Energy Loss Spectroscopy (EELS) technique in the Energy Filtered Transmission Electron Microscopy EFTEM image mode, it has been evidenced that the material deposited at the bottom of the pores are nickel nanoparticles.

A branched pore structure at the bottom of the pores has been observed from the lamella preparation of the PAA templates and the further observation by TEM microscopy. Nanoparticles have been electrodeposited at the bottom of the branched secondary pores with a filling rate close to 100%. Subsequently by comparing the number of nanoparticles deposited and the number of primary pores per unit of area, we obtained a relation of the number of branches generated per pore for a range of anodization voltages. In the range of anodization voltage from 20V to 60V we evidenced that for same value of the constant of the exponential voltage decrease process, as the anodization voltage increase the number of branches created per pore is increasing.

The results obtained provide valuable information for the further development of the synthesis of carbon nanotubes within PAA templates in order to obtain the maximum density of tubes per unit of area, a desirable characteristic for the device fabrication in the present work.

References

[1] M. Zemanová*, et al.*, "Nickel electrolytic colouring of anodic alumina for selective solar absorbing films," *Renewable Energy,* vol. 33, pp. 2303-2310, 2008.

[2] Z. Shaterabadi*, et al.*, "Modification of microstructure and magnetic properties of electrodeposited Co nanowire arrays: A study of the effect of external magnetic field, electrolyte acidity and annealing process," *Materials Chemistry and Physics,* vol. 160, pp. 389-397, 2015.

[3] H.-N. Umh*, et al.*, "Fabrication of gold nanowires (GNW) using aluminum anodic oxide (AAO) as a metal-ion sensor," *Korean Journal of Chemical Engineering,* vol. 32, pp. 299-302, 2015/02/01 2015.

[4] L. Li*, et al.*, "Direct Electrodeposition of ZnO Nanotube Arrays in Anodic Alumina Membranes," *The Journal of Physical Chemistry C,* vol. 111, pp. 7288-7291, 2007/05/01 2007.

[5] J. Mallet*, et al.*, "Growth of Silicon Nanowires of Controlled Diameters by Electrodeposition in Ionic Liquid at Room Temperature," *Nano Letters,* vol. 8, pp. 3468-3474, 2008/10/08 2008.

[6] A. P. Leontiev*, et al.*, "Arrays of rhodium nanowires based on anodic alumina: Preparation and electrocatalytic activity for nitrate reduction," *Electrochimica Acta,* vol. 155, pp. 466-473, 2015.

[7] H. Liu*, et al.*, "Optical properties of porous anodic alumina embedded Cu nanocomposite films," *Optical Materials,* vol. 44, pp. 9-12, 2015.

[8] N. Ke*, et al.*, "Carbon nanotube diameter control via catalytic Co nanoparticles electrodeposited in porous alumina membranes," *Rsc Advances,* vol. 5, pp. 25747-25754, 2015.

[9] Y. Pang and R. Chandrasekar, "Cylindrical and Spherical Membranes of Anodic Aluminum Oxide with Highly Ordered Conical Nanohole Arrays," *Natural Science,* vol. 7, p. 232, 2015.

[10] B. S. Simpkins*, et al.*, "Controlling the Crystallinity of Electrochemically Deposited CdS Nanowires," *The Journal of Physical Chemistry C,* vol. 117, pp. 11843-11849, 2013/06/06 2013.

[11] T. Gao*, et al.*, "Template synthesis of single-crystal Cu nanowire arrays by electrodeposition," *Applied Physics A,* vol. 73, pp. 251-254, 2001/08/01 2001.

[12] D. Xu*, et al.*, "Preparation and characterization of CdS nanowire arrays by dc electrodeposit in porous anodic aluminum oxide templates," *Chemical Physics Letters,* vol. 325, pp. 340-344, 2000.

[13] S. Dellis*, et al.*, "Electrochemical synthesis of large diameter monocrystalline nickel nanowires in porous alumina membranes," *Journal of Applied Physics,* vol. 114, p. 164308, 2013.

[14] N. Zafar*, et al.*, "Effects of pH on the crystallographic structure and magnetic properties of electrodeposited cobalt nanowires," *Journal of Magnetism and Magnetic Materials,* vol. 377, pp. 215-219, 2015.

[15] N. Adeela*, et al.*, "Fabrication and temperature dependent magnetic properties of nickel nanowires embedded in alumina templates," *Ceramics International,* vol. 41, pp. 12081-12086, 2015.

[16] A. Brudzisz*, et al.*, "Effect of processing parameters on pore opening and mechanism of voltage pulse detachment of nanoporous anodic alumina," *Electrochimica Acta,* vol. 178, pp. 374-384, 2015.

[17] V. Caboni, "Italian Patent 339 232," 1936.

[18] N. J. Gerein and J. A. Haber, "Effect of ac Electrodeposition Conditions on the Growth of High Aspect Ratio Copper Nanowires in Porous Aluminum Oxide Templates," *The Journal of Physical Chemistry B,* vol. 109, pp. 17372-17385, 2005/09/01 2005.

[19] K. Nielsch*, et al.*, "Uniform nickel deposition into ordered alumina pores by pulsed electrodeposition," *Advanced Materials,* vol. 12, pp. 582-586, 2000.
[20] M. P. Proenca*, et al.*, "Ni growth inside ordered arrays of alumina nanopores: Enhancing the deposition rate," *Electrochimica Acta,* vol. 72, pp. 215-221, 2012.
[21] U. S. Mohanty, "Electrodeposition: a versatile and inexpensive tool for the synthesis of nanoparticles, nanorods, nanowires, and nanoclusters of metals," *Journal of Applied Electrochemistry,* vol. 41, pp. 257-270, 2011/03/01 2011.
[22] C. Frantz*, et al.*, "Pulse electrodeposition of adherent nickel coatings onto anodized aluminium surfaces," *Applied Surface Science,* vol. 330, pp. 39-47, 2015.
[23] L. Zaraska*, et al.*, "Analysis of nanopore arrangement and structural features of anodic alumina layers formed by two-step anodizing in oxalic acid using the dedicated executable software," *Applied Physics A,* vol. 114, pp. 571-577, 2014/02/01 2014.
[24] R. Pinner*, et al.*, "Factors Affecting the Formation of Anodic Oxide Coatings," *Journal of the Electrochemical Society,* vol. 102, pp. 359-360, 1955.
[25] B. Marquardt*, et al.*, "Density control of electrodeposited Ni nanoparticles/nanowires inside porous anodic alumina templates by an exponential anodization voltage decrease," *Nanotechnology,* vol. 19, Oct 8 2008.
[26] S. Lee*, et al.*, "Anodized pore structural evolution of focused ion beam patterned Al: direct analysis of branched nanopores and nanosacks," *Physical Chemistry Chemical Physics,* vol. 15, pp. 10659-10665, 2013.
[27] B. Chen and K. Lu, "Influence of Patterned Concave Depth and Surface Curvature on Anodization of Titania Nanotubes and Alumina Nanopores," *Langmuir,* vol. 27, pp. 12179-12185, 2011/10/04 2011.

Chapter 3.

Synthesis of carbon nanotubes within PAA templates

Since the first observation of the MultiWall-Carbon NanoTubes (MWCNT) reported by Ijima in 1991 [1], CNTs have been in the focus of many research studies due to the behaviors of their quasi one dimension structure. As a result of such studies until nowadays it has been proven that the CNTs present unique and exceptional thermal, mechanical and electronic properties and remarkable chemical stability [2-5]. Consequently the CNTs have expanded the limits for a wide range of applications. However even if individual CNTs present excellent properties, there are still several challenges to overcome in order to fabricate devices based on CNTs. The main difficulties rely on the alignment of the tubes [6], the contacting [7] and the control of the electrical characteristics in terms of the chirality of the tubes [8].

Collectively CNTs organization via the synthesis inside PAA templates is a quite promising method to improve the main problems related with the synthesis of self-organized CNTs. In addition due to the PAA versatility the CNTs can be synthetized with a wide range of diameters, lengths and densities.

In the present chapter after the presentation of the main properties and applications of the CNTs, the different synthesis methods in order to growth the CNTs are addressed. In particularly the hot filament chemical vapor deposition (HF-CVD) technique and their corresponding experimental set-up are introduced and discussed. Finally the main results obtained of the synthesis of CNTs within PAA templates are presented pointing out the

properties of collectively organized device. The impact of the synthesis parameters and boundaries conditions imposed by the template on the CNTs structures is investigated. The obtained results in the present studies provide the accurate procedure in order to satisfy one of the main objectives of the present work: the growth of aligned and collectively ordered CNTs compatible with the device fabrication.

3.1 Characteristics and physical properties of carbon nanotubes

The CNTs can be represented as graphene sheets rolled into cylinders. The number of rolled up graphene sheets determines the type of tube, such as single-walled or multi-walled as shown in figure 3-1. In a graphene sheet the carbon is sp^2 hybridized forming a honey-comb lattice.

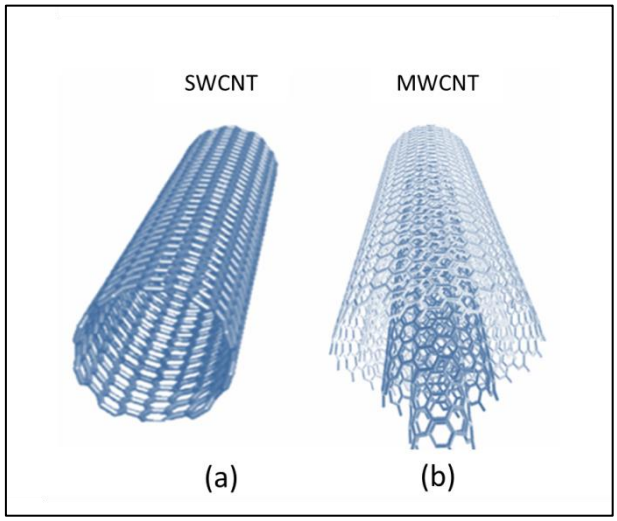

Figure 3-1. Schematic representation of SWCNTs and MWCNTs.

The circumference of a SingleWall-Carbon NanoTube (SWCNT) is established by the chiral vector which connects two different crystallographic sites. Therefore the structure of

two-dimensional graphene sheet is described by a unit cell as shown in figure 3-2 (a), such unit cell which connects two different crystallographic sites. It is defined by the chiral vector described in the following expression:

$$\vec{C} = n\overrightarrow{a_1} + m\overrightarrow{a_2}$$

Where $\overrightarrow{a_1}$ and $\overrightarrow{a_2}$ are the unit cell vectors of the two-dimensional lattice which formed by the graphene sheet, and n and m are integrals numbers [9]. The chiral angle θ represents the angle between the $\vec{C}$ and $\overrightarrow{a_1}$ vectors. Therefore θ is given by:

$$\theta = \tan^{-1}\left(\frac{\sqrt[3]{3}n}{2m+n}\right)$$

The diameter d of the carbon nanotube is given by the circumferential length L as is shown in the following expression:

$$d = \frac{L}{\pi} = \frac{\left|\vec{C}\cdot\vec{C}\right|}{\pi} = \frac{a\sqrt{n^2+m^2+n\cdot m}}{\pi}$$

Where $a = 2.49\ \dot{A}$ is the constant lattice.

Finally, SWCNTs can be described by the chiral vector $\vec{C}$, or by their diameter d and the θ angle. However, since the graphene sheet is the sum of the unit vectors, the cell is usually described just with two integer numbers (n, m) that determines the chiral vector. Such integer values define three different types of CNTs. For instance, the armchair type satisfies that $n = m$ and in terms of the chiral angle $\theta = 30°$. The zig-zag mode of CNT verifies that $m = 0$ meaning that chiral angle $\theta = 0°$. The named chirals CNTs have integers numbers (n, m) with $n \neq m \neq 0$ which imply CNTs with chiral angles $0 < \theta < 30°$. The figure 3-2 highlights the distinct CNTs types depending on the integers values n and m . The most important aspect to highlight is that the electronic, optical and mechanical properties of the SWCNTs depend on their chirality.

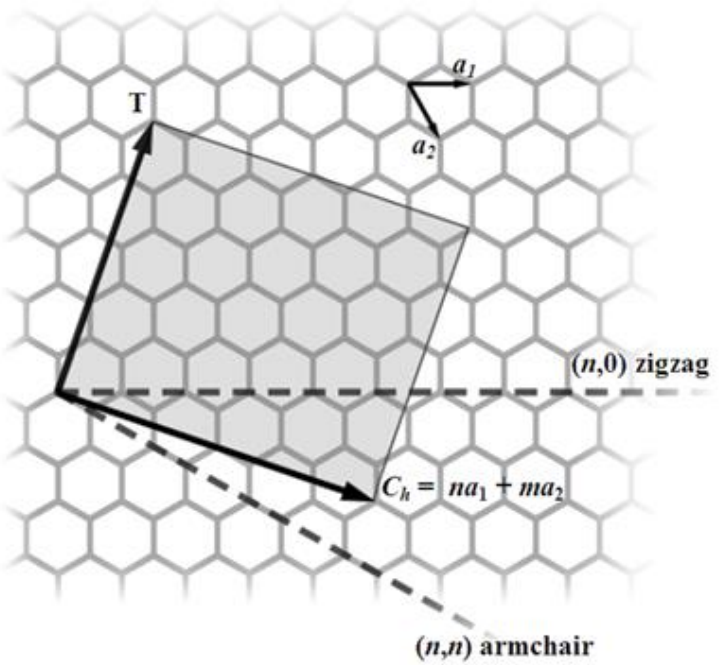

Figure 3-2. The crystal lattice structure of a graphene sheet. The chiral vector $\vec{C}$ is defined by the unit vectors $\overrightarrow{a_1}$ and $\overrightarrow{a_2}$ with integers values n and m. These integers values determines how the tube is rolled up, therefore the chirality of the tube depends on the combination of such values. The three different chiral possibilities of the SWCNT,armchair, zig-zag and chiral, are pointed out depending on the chiral vectors.

3.1.1 Electronic properties

The most important aspects to point out concerning the electronic properties of the CNTs are that the reduced phase space for scattering of the carriers leads to a ballistic or quasi-ballistic transport. Consequently, power dissipation is low. The strong covalent bonds of the carbon atoms provide a high mechanical and thermal stability, additionally a high resistance to electromigration. For instance the current densities measured in carbon nanotubes are high as 10^9 A/cm^2 [10].

On the other hand the electronic behavior for the SWCNTs is determined by the rolled up of the graphene sheets. As mentioned previously, the chirality of the SWCNTs is

defined by the integers numbers (n, m), such numbers establish the electronic properties of the tubes. For instance, the tubes that satisfy the relation $|n - m| = 3i$ behave as metallic conductors, in contrast when $|n - m| = 3i \pm 1$ the SWCNTs have semiconducting properties, where i is an integer number. Conversely, the conducting behavior of the MWCNT results more complicated to describe since every graphene sheet can be rolled up differently leading to distinct conducting behaviors. Anyway CNTs with large diameters are conductive at room temperature, therefore the chirality in this case is not critical [11] but the diameter plays a crucial role. This is due to the fact that for semiconducting SWCNT the energy gap E_G depends on the nanotube diameter d, the nearest neighbor carbon bond length a and the $V_0 = -2.7\ eV$ nearest-neighboring tight-binding parameter [12]. The energy gap E_G of semiconducing SWCNT is given by:

$$E_G = \frac{aV_0}{d}$$

At room temperature $k_B T \approx 0.0258\ eV$, consequently, for diameters larger than 15 nm the energy gap becomes smaller than $0.0258\ eV$ which implies that all the shells of the MWCNT including the semiconducting ones have a metallic conducting behavior. On the other hand the transport in the MWCNTs strongly depends on the electrical contact, where the transport can be dominated by just the outer-shells [13-16], on the contrary when a perfect contact is achieved between the probe and the tube, all the rolled graphene sheets contribute to the electron conduction [11]. Therefore the MWCNTs present 1-D or 2-D transport characteristics depending on their structure and the contact with an electrode.

In conclusion in order to use the CNTs as building block for further electronic device fabrication, it will be crucial the control of the tube structure, in particularly the chirality and the tube diameter.

3.1.2 Optical properties

The low dimensionality of carbon nanotubes provides a quantum confinement for electrons which impacts over the optical properties. Such confinement implies a typical feature of one-dimensional crystal that relies in the formation of Van Hove singularities [17]

which are characterized of electronic transitions with energy levels related with a certain density of states [18] that descends gradually and then increase in a discontinuous spike. On the contrary three-dimension materials have a continuous density of states (DOS), the figure 3-3 shows the typical dependence of the electronic DOS for different dimensionalities.

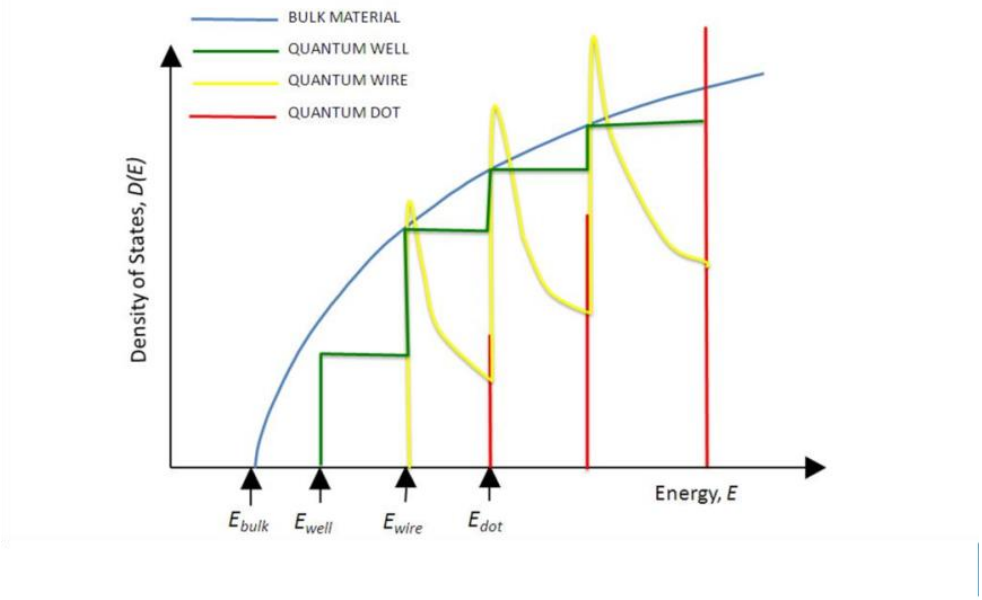

Figure 3-3. Characteristic electronic density of state for different dimensionalities.

The Van Hove singularities are associated with remarkable optical properties, since in agreement with the Fermi's Golden Rule for any optical transition that is resonant with the Van Hove singularities they are expected to be greatly enhanced [19]. Figure 3-4 shows the electronic density of states (DOS) related to a single-walled nanotube.

Additionally the energies between the Van Hove singularities depend on the CNT structure. Besides the optical transitions are sharp, therefore result relatively easy to detect optical signals from individual CNTs with certain (n, m) indices. Consequently, varying the structure of individuals CNTs it is possible to obtain and detect different optoelectronic properties [20-22]. It is important to point out that such optical results have been obtained in SWCNTs [23] and MWCNTs [19]. However, in the case of the MWCNTs the tubes have to satisfy certain structural conditions associated with their diameter and purity in order to

mask the fact that MWCNTs contain a mixture of tubes with small and larger diameters and tubes presenting different chiralities that are coupled by Van der Waals interactions.

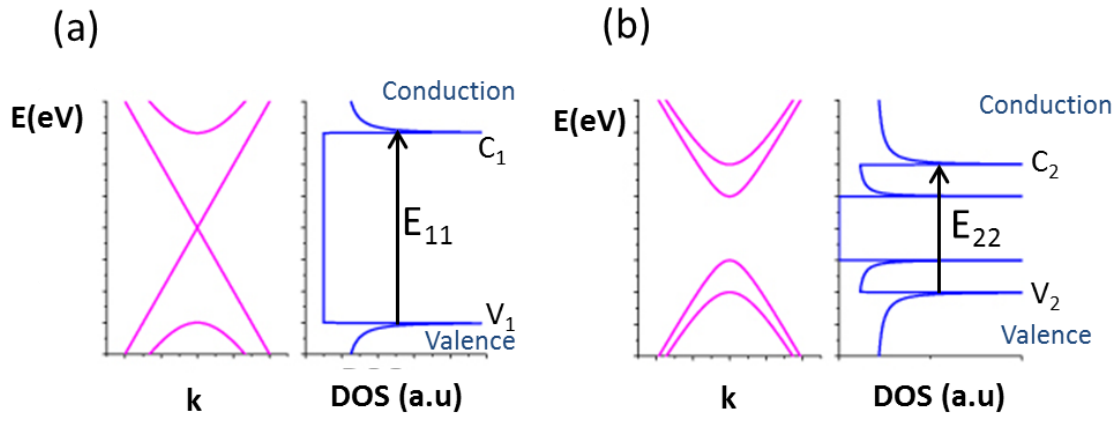

Figure 3-4. Band diagram and their corresponding one-dimensional density of state for (a) metallic single-walled nanotubes and (b) semi-conductive single-walled nanotubes. The $V_1 \rightarrow C_1$ correspond the first Van Hobe optical transition and $V_2 \rightarrow C_2$ the second Van Hobe optical transition.

Consequently it is preferable to perform Raman spectroscopy, photoluminescence and optical absorption in order to fully characterized the structural of the CNTs. Besides the optical response can be implemented for the separation of CNTs depending on their structure [24] and a further device fabrication [25, 26].

3.1.3 Mechanical properties

Carbon covalent bond in the basal plane of graphite is the strongest of all chemical bonds in nature; therefore carbon nanotubes have exceptional mechanical properties. For instance theoretical calculations show that the Young's modulus of an isolated SWCNT does not depend on their chirality or their aspect ratio and has a value of the order of TPa [27].

Furthermore it has been reported through *in-situ* measurements that the experimental value of an individual MWCNTs is 1.8 TPa [28], nevertheless this value decrease with the increasing value of the nanotube diameter [29]. However the stiffness of the CNTs is subject to different types of defects [30].

In spite of the very high Young's modulus, by using atomic force microscopy it has been proven that nanotubes can be bend into loops without any crack [31], revealing that the CNTs are flexible, tough and possess a great capacity for reversible deformation. In addition it has been reported that SWCNTs with small diameters can be elongated by a 30% before breaking [32], and concerning the breaking strength value of 55 GPa has been obtained [33]. On the other hand the tensile strength performed on MWCNTs reveals that is lower in comparison with SWCNTs since the inner shells starts to pulled out breaking the outermost layer [34].

In summary the CNTs have a high Young's modulus value, a great capacity of deformation and a high strength tensile value, besides a great aspect ratio can be obtained since is possible to obtained ultra-long CNTs with heights of the order of tens of centimeter [35]. Therefore due to their exceptional and unique mechanical properties CNTs are highly used in diverse applications on mechanical devices and as reinforce for composite fabrication.

3.1.4 Thermal properties

The CNTs are expected to be good thermal conductors along the tube axis due to the ballistic conduction, and good insulators lateral to the tube axis. However the thermal properties have not been so widely studied as the electronic, optical or mechanical one's. Such studies are still in development. The difficulty relies heavily on the difficult manipulation of individuals tubes. From a theoretical approach, simulation has suggested that the lattice thermal conductivity of a SWCNT with lattice indices of (10,10), reaches the maximum value of approximately 37000 $\frac{K}{W \cdot m}$ at 100 K and decreases to approximately 6600

$\frac{K}{W \cdot m}$ at 300 K [36]. Nevertheless, due to the diverse methods of measuring and the different sample qualities, the experimentally measured thermal conductivity value κ strongly varies from 200–25 000 W $\frac{K}{W \cdot m}$ [37-39]. Recently it has been reported that the intrinsic thermal conductivity of perfects crystalline SWCNTs is approximately 4000 $\frac{K}{W \cdot m}$. In addition depending on the CNT structure and chirality it has been measured that κ tends to grow with the increase on the SWCNT diameter [40]. Anyway further studies must be performed in order to exploit all the thermal properties of the CNTs for the device fabrication.

3.2 Carbon nanotubes based devices

Since their discovery diverse investigations have been focused in the implementation of CNTs for the device fabrication due to the exceptional mechanical, electronic, optical, and thermal properties. The versatility of the CNTs and their uniqueness excellent properties open the frontiers of the applications in widely different fields. In figure 3-5 a summary of the implementation of CNT by major industry sector is given [41].

For instance due to their strong carbon covalent bond the CNTs have been used as reinforcement for the fabrication composites [42, 43]. Basically the properties improved of the composites are due to the reinforcement CNTs which includes: tensile strength and tensile modulus toughness, glass transition temperature, thermal conductivity, electrical conductivity and, solvent resistance [44]. Therefore this kind of material can be used in a wide range applications such as the aerospace industry [45, 46], bike construction or tennis racquets [47]. However the biggest challenge to overcome for the composite fabrication is the homogeneous dispersion of CNTs which is complicated due to the Van der Waals interaction among then [48].

Besides the excellent mechanical properties due to their high electronic conductivity the CNTs have been chosen for various tip applications [49-52], in particular for the tip of atomic force microscopy [53-55] and scanning tunneling microscopy [56, 57].

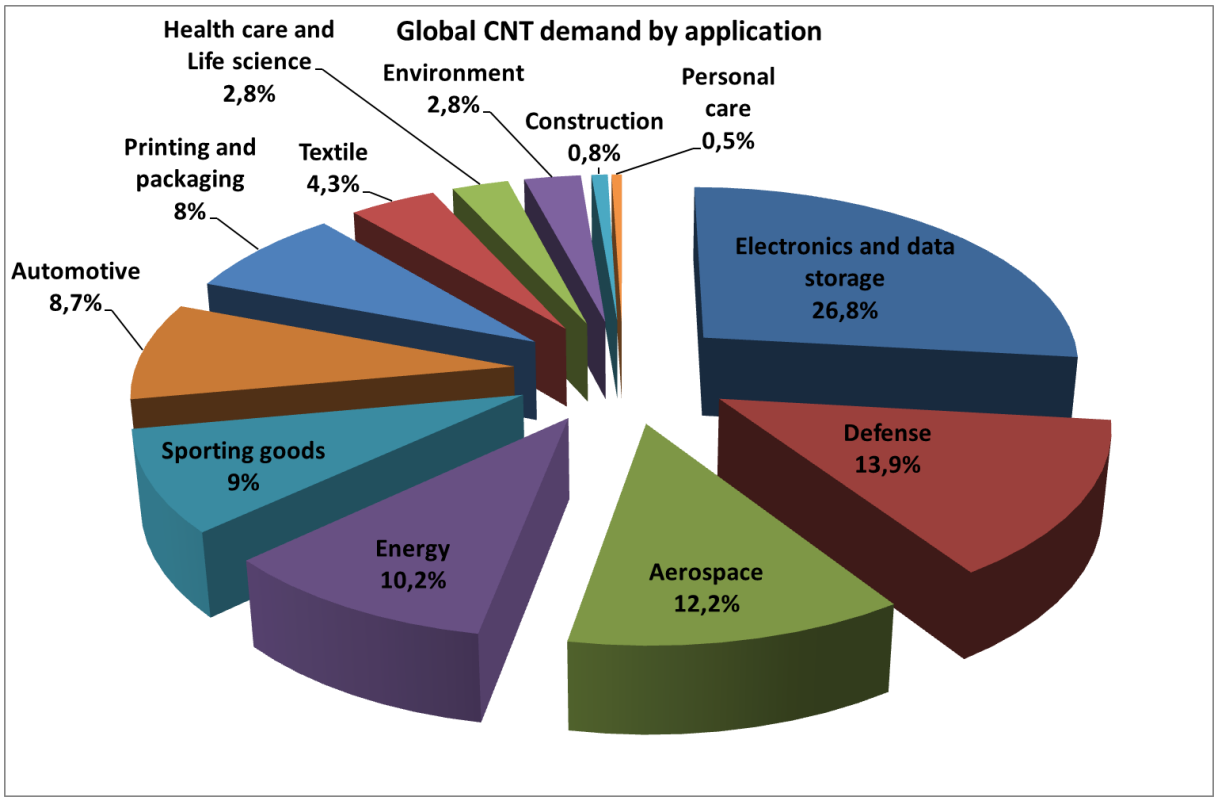

Figure 3-5. Global CNT demand by different field of application [41].

On the other hand CNTs are used as building block for the energy conversion and storage devices [58-60], in particular, as electrodes for lithium-ion batteries due to their high cyclic stability, however they are limited by a low capacity [60, 61]. On the contrary, silicon has been extensively used as anode material due to the high gravimetric capacity. Consequently, many efforts have been devoted to synthesizing CNT/Si composite materials, which are expected to provide their individual advantages to guaranteed both requires characteristics for the lithium-ion electrodes high specific capacity and cyclic stability. In the same way, exploiting their unique tubular structures and superior electrical properties, which leads to a fast ions and electrons transportation, vertically aligned densely packed CNTs have been used as supercapacitors [62-64].

The CNTs are additionally used in order to fight against the environmental pollution caused by toxic metals (heavy metals, radioactive metals) by the removal of toxic metals from contaminated water. The CNTs have been used among diverse developed adsorbents,

because they present an exceptional effect on the fast adsorption and rapid removal of toxic impurities from the aqueous source [65, 66].

In the following section it will highlight the implementation of CNTs with applications that exploit the electronic and optoelectronics properties of such carbon nanostructures, in particular the application associated with the synthesis of CNTs which have been grown collectively organized.

3.2.1 CNTs-Based sensors

Their unique electrochemical, electronic and optical properties of CNTs provide a unique platform for the fabrication of sensors based on electrochemical [67], electrical [68] or optical signal outputs [69]. Moreover the high surface-to-volume ratio is a very attractive characteristic in order to enhance the sensitivity of the CNTs-based sensors. In some cases the CNTs have not the intrinsic recognition ability for sensing a certain entity. Therefore CNTs can be hybridized with a component having specific recognition in order to perform the proper sensing process [70, 71]. Due to development technique of the CNTs functionalization, nowadays the diversity of sensors fabricated based on CNTs is extensive, for instance there are sensors devoted for drug detection [72, 73], for the flow measurement [74], as well for the detection of different gas species such as $NH_3, NO_2, CO_2, O_2, H_2, Ar$ among others [75-77]. Moreover there are a great diversity of biosensors [75, 76], in particular this sort of sensor results very attractive because the effective detection area can be made into the size of a single biomolecules or virus, thus the characteristics lengths of the detector are from the same scale of the specific kind of molecular to distinguish.

In conclusion a great variety of CNTs based sensors has been developed, the main challenge relies in the CNT manipulation and the acquisition of the signal responsible of the sensing performance. In our particular work the synthesis of CNTs within PAA templates

provides a platform for a collective organization of the CNTs and a simple method to perform electrical [78] or optical measurements [79] toward a sensing device fabrication.

3.2.2 CNTs-based interconnects

The continuous device miniaturization using copper as wiring material causes undesirable size effects in the interconnected systems. For instance there is a considerable difference of thermal expansion of copper (17.5 ppm/k) with the thermal expansion of the silicon (2.5ppm/k), this can induces a huge stress between both interphases. Besides the maximal current density of copper is 10^7 A/cm^2. These phenomena can lead to stress migration and electro migration effects. Therefore alternatives technologies have to be developed in order to overcome the continuous down scaling devices guarantying a low resistivity and a high reliability. The International Technology Roadmap for Semiconductors (ITRS) proposed several emerging technologies to replace copper in future interconnect schemes [80] and projected carbon nanotubes as a very promising candidate due to their extraordinary already mentioned thermal, electrical and mechanical properties.

The approach in order to resolve and improve the characteristics of metal-based interconnects integrated circuit technology is called three dimensional integration. This methodology will allow a decrease in the total length of the wiring in a given circuit, stacking chips to make use of the vertical direction to integrate more components and functions in the same device. The implementation requires simultaneously a high CNT quality and a large CNT density. Many efforts have been addressed in order to develop this technique, however performance advantage of three-dimensional integration cannot achieved the values of the theoretical predictions for the CNTs [81, 82]. For instance Fiedler et. al measured the resistance of a MWCNT with 20 shells, the resulting resistance of such nanotube is of 38 kΩ/CNT, two order of magnitudes higher than the theoretical value of 6.5 kΩ/CNT [83]. The biggest obstacle to overcome is the CNT's synthesis temperature, which on one hand impacts on the CNT quality and on the other hand affects the electrical contact through the interfacial oxide layers created during the CNT growth [81]. Recently Xu et.al [84] have

developed a procedure to avoid the constrains imposed by the temperature fabrication, however they have not performed any electrical characterization of the device.

3.2.3 Field emission devices

Electrons are generally confined to the surface of bulk material by an energy barrier roughly equivalent to the work function ϕ. The electrons can be emitted from such bulk material under thermal excitation leading to a named thermionic emission mechanism. On the other hand the field emission process can take place by quantum mechanical tunneling. Under the application of a sufficiently strong electric field, electrons near to the Fermi level tunnel to the energy barrier and escape to the vacuum level. The emitted current depends on the local electric field at the emitting surface E, and on its work function ϕ. Figure 3-6 shows a schematic diagram of field emission process from a metal at absolute zero temperature. Under the presence of a strong field the barrier formed along the line AB is deformed promoting the electron tunneling phenomenon.

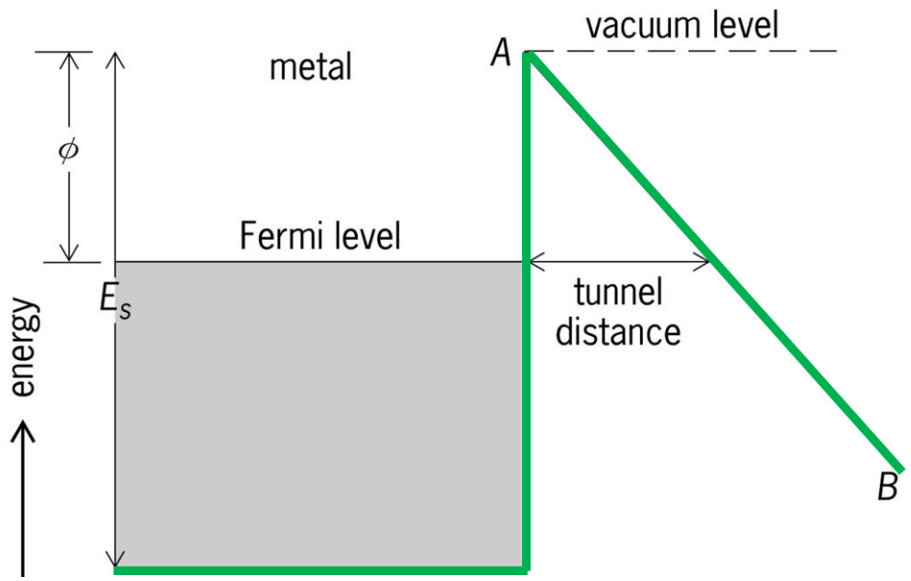

Figure 3-6. Diagram of the energy-level scheme for field emission from a metal at absolute zero temperature.

The Fowler-Nordheim equation determines the behavior of a field emitting system current which is given by the following expression,

$$I = \frac{a \cdot (\beta \cdot E)^2}{\varphi} exp\left(-\frac{b \cdot \varphi^{-3/2}}{\beta \cdot E}\right)$$

where *I* is the field emission current density, φ is the work function, *E* is applied pontential, the constants a and b are 1.54×10^{-6} A(eV)$V^{-2}$and 6.83×10^{9} $(eV)^{-3/2}$ Vm^{-1} respectively [85], finally β is named as the field enhancement factor which is equal to the aspect ratio of the material which is affected by the applied field.

The current emission density equation implies that the current can increase by several ways: decreasing the work function, increasing the applied electric field, increasing the enhancement factor and a combination of all the mentioned factors.

Since the enhancement factor depends strongly on the aspect ratio of the emitter, one of the simplest ways to generate a high enhancement is the utilization of a sharp object. Carbon nanotubes satisfy many requirements to act as field emission tip due to the strength, chemical stability, electronic conductivity and mainly due to the high aspect ratio.

The first reports have been made by Heer et al. [86] and Rinzer et al. [87] on the field emission from films and individual multiwall carbon nanotubes respectively, such works triggered the fabrication of field emitter devices on different substrates [88-90] and by different techniques [91-93] .

The field emission process using CNTs as emitters are highly affected by two factors: the morphology of the CNT and the density of CNTs. For instance the SWCNTs present a higher enhancement factor value than the MWCNTs, however the MWCNTs have a lower degradation rate. In addition the performance are also affected by the presence or not of the catalyst at the tip of the CNT and if the tip is close-type or open type [94]. Concerning the CNTs density, the field emission properties are affected by the distance between the field emitter objects [95, 96]. A dense CNT structure suffers an electrostatic screening effect generated by the neighboring proximity leading to a limitation field emission performance. A pillar array of aligned CNT bundles has shown better field emission performance [97].

Despite the progresses achieved in the field emission domain there are still many efforts to perform. For instance, reliability and reproducibility are the main factors. The electrical breakdown and current degradation are the two biggest limiting causes of the reliability of CNT based field emitters. In order to address such restrictions a new generation of field emission devices are recently constructed based on the hybridization of CNTs and graphene sheets [98-100], and carbon nanotubes supported nanowires [101, 102].

3.3 Synthesis of carbon nanotubes

Basically there are three types of methods that can be considered for synthetizing synthetized CNTs. Arc discharge and laser ablation have been the first techniques used to produce high quality CNTs but nowadays these methods have been mainly replaced by chemical vapor deposition (CVD) techniques. The figure 3-7 illustrates the schematic representation of the basic different CNT growth techniques.

The discovery of CNTs has been realized by Ijima and the production method implemented was the arc-discharge [1]. The most common methods use DC arc discharge between two graphite water-cooled electrodes as is indicated in figure 3-7 (a). The carbon nanotube formation is generated due to the sublimation of the carbon-contained in the negative electrode product under the high temperature arc discharge. Generally the synthesis is performed at temperatures above 1700°C which leads to the production of CNTs with a few amounts of defects. Both kinds of tubes can be synthetized, for the synthesis of SWCNTs the anode is composed of graphite and a metal, such as Ni, Fe or Co. On the other hand for the production of MWCNTs the absence of catalyst is required.

The laser ablation method has been introduced by Smalley group [103]. Typically such technique is used to synthetized different fullerenes. Similar to the arc-discharge technique as is shown in figure 3-8 (b), the CNTs are obtained due to laser vaporization of graphite at temperatures of the order of 1200°C. The characteristics of the CNTs synthetized depend on many parameters such as: the laser properties (energy fluence, peak power,

repetition rate and oscillation wavelength), the structural and chemical composition of the target material, the chamber pressure and the chemical composition, flow and pressure of the buffer gas, the substrate, and the distance between the target and the substrates. Both types of CNTs can be synthetized by the laser ablation method, with highly pure graphite electrode are obtained SWCNTs. For the synthesis of MWCNTs is necessary to used MWCNTs targets as electrodes [104]. Anyway such technique is mostly executed in order to obtain high pure SWCNTs.

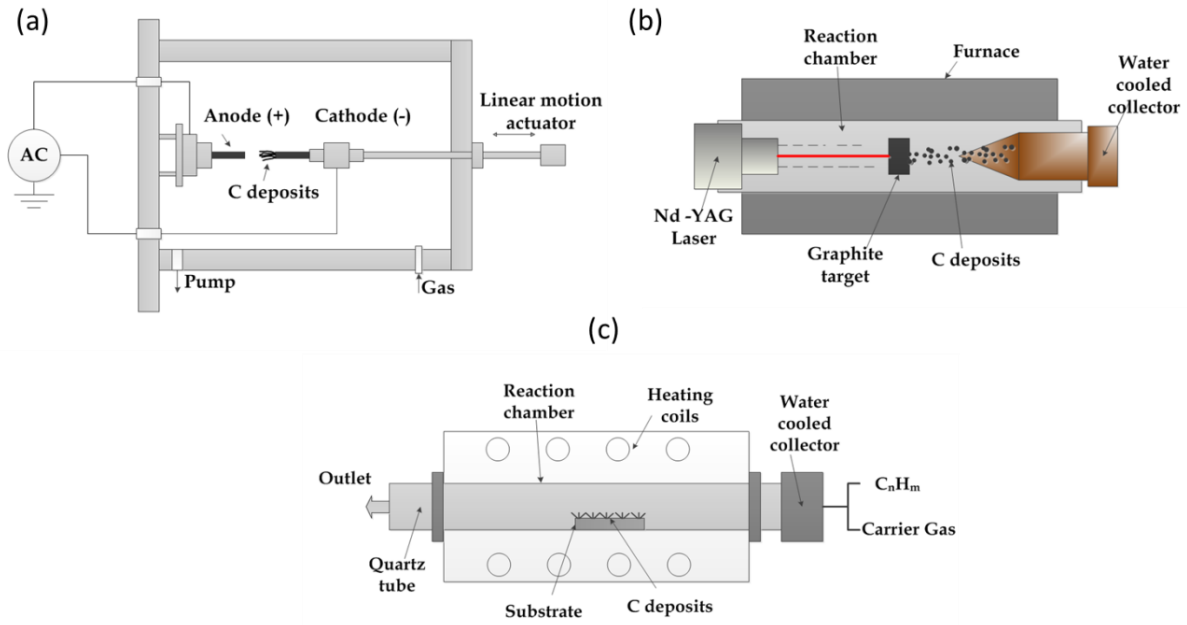

Figure 3-7. Different methods in order to synthetize CNTs. (a) Arc-discharge, (b) laser ablation and (c) chemichal vapor deposition (CVD).

The main problem of the arc-discharge and laser ablation procedures is the production of carbon sub-products. Therefore a purification process must be carrying out in order to separate the CNTs from the residual carbon. In addition the high temperatures constrain the range of substrates that can be used. For these reasons the chemical vapor deposition (CVD) technique has been widely implemented because the operational ranges of temperatures are between 500-1000°C. Although a worse crystallinity of the tubes is obtained, the carbon sub-products created during the synthesis are highly reduced. Besides

the CVD technique allows to control orientation, alignment, nanotube length, diameter, purity and density of the synthetized CNTs.

3.3.1 Chemical Vapor Deposition (CVD) method

The prevailing method for the synthesis of CNTs is the chemical vapor deposition method. In addition of the already mentioned benefits the CVD method is a low-cost implemented technique. However the main advantages rely in the easy control of the CNTs characteristics by varying the factors involved in their synthesis. Therefore a good understanding of the synthesis parameters is required in order to obtain the desire carbon nanostructure.

The synthesis of CNTs takes place when a carbon containing gas precursor is injected into a reactor as is show in figure 3-7 (c). The process can be performed with or without catalyst [105], however in presence of a catalytic nanoparticle the growth control is more predictable, since the growth behavior and the final CNTs structure is highly determines by the catalyst. The hydrocarbon used as gas precursor can be decomposed either thermally or by enhanced plasma. The growth model of CNT is still discussed nowadays [106, 107]. Two different growth mechanisms are proposed: the vapor-liquid-solid (VLS) and the vapor-solid-solid mechanism (VSS). In the VLS case the catalytic nanoparticle form a liquid alloy between the carbon and the metal, subsequently carbon atoms start to diffuse through the nanoparticle and eventually precipitate at the nanoparticle surface forming the tube structure [108]. In contrast, in the VSS mechanism the carbon atoms just diffuse through the catalytic surface and the diffuse carbon precipitates leading the formation of CNT without the formation of a liquid alloy between the carbon atoms and the nanoparticle [109].

The main CVD parameters that impacts over the CNT structures are: the process temperature, the precursor gas and the vapor pressure. For instance the graphitization quality of the CNTs is affected by the temperature process. In order to obtain less defective carbon nanostructures higher synthesis temperatures are required. The range of

temperature to successfully growth CNTs are determined mainly by the carbon precursor and catalyst type. For the synthesis of SWCNTs the nanoparticles impose a biggest constrain [110, 111], however temperatures higher than 700°C are required in order to synthesized SWCNTs with a low degree of impurities. Generally lowers process temperatures are required for the synthesis of MWCNTs [112]. The gas precursor is another factor that has a great impact on the final carbon structure generating sub-products due to a carbon excess feedstock. Basically the only condition that has to satisfy the feedstock gas is the presence of carbon in their molecular composition. Thus a great variety of precursors have been used for the synthesis of CNTs, from waste chicken fat [113], coconut oil [114] to camphor [115]. However one of the most used gas precursor is acetylene (C_2H_2) since their easy decomposition at relatively low temperatures. Nevertheless the high carbon content can lead to the deposition of amorphous carbon on the sidewalls of the CNTs. Methane (CH_4) results an alternatively in order to avoid an over carbon deposition, however higher process temperatures are required. The growth control and the carbon supply are also determined by the vapor pressure. The total vapor pressure is given by the contribution of the gas pressure of the carbon feedstock precursor, reductive gas and a carrier gas. Therefore a proper balance among each gas has to be achieved, because a too low vapor pressure of the gas precursor CNTs will not be created and on the contrary too high vapor pressure will lead to the deposition of parasitic amorphous carbon that decreases the CNT quality an even can clog the growth. Furthermore the growth dynamics it will be affected by the pretreatment conditions [116, 117] and an eventual assistance energy source applied to decompose the carbon feedstock such as: microwave plasma [118], DC plasma [119], RF plasma [120] or hot filament [121].

3.3.2 Catalyst for the synthesis of CNTs

Conventionally the synthesis of CNTs is performed using catalyst nanoparticles since the particle can defines and determines quality and characteristics of CNT. Various catalyst types have been used for the CNT synthesis like Al, Mg, Sn, Cr, Mo and Mn [122]. However

transition metals such as Iron (Fe), Cobalt (Co) and Nickel (Ni) result to be result the most effective catalyst to grow CNT [123]. Such metals have high carbon solubility and diffusion rate at high temperature. Furthermore, they have stronger adhesion with the CNT produced at the end of the process and potential in forming high curvature of CNT. Every catalyst metal leads to different synthesis results, for instance, the catalytic activity of metal species towards carbon deposition was found to decrease in the following order Nickel > Cobalt > Iron [124]. In terms of the graphite structure the best results are obtained with cobalt nanoparticles [125]. In the same group of transition metals, Pt, Ag, Cu, and Pd have been also used for the CNT growth.

Despite the inherent characteristics of the catalytic nanoparticle, the interaction between the catalyst and the substrate plays a crucial role. There are two different growth behaviors as indicated in figure 3-8. When the catalyst is strongly attached to the support layer, the CNT formation is product of the base-growth mode, as is shown in figure 3-8 (a). In contrast, when the interaction between the catalyst and the support layer is weak the tip-mode growth takes place, as is schematized in figure 3-8 (b).

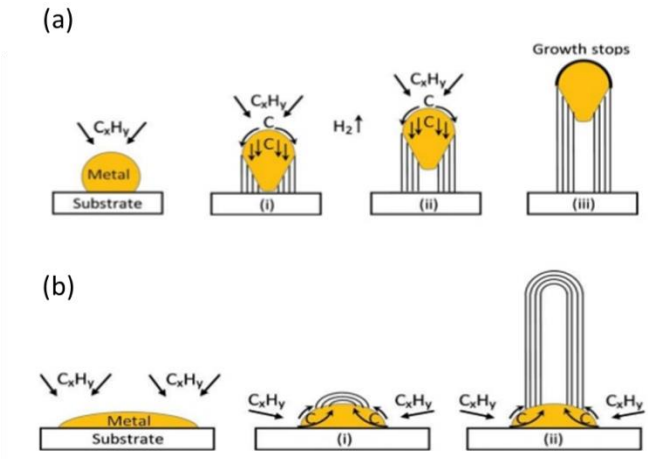

Figure 3-8. The different growth mode depending on the interaction between the catalyst and the support layer. (a) Tip-growth mode and (b) Base-growth mode.

It is important to note that under the ideal situation where one tube growths per each pore of the PAA, and assuming that the tube is confined by the pores walls, the growth

mode inside the PAA structure which can only takes place is the tip-growth mode, otherwise the grown CNT will clog the tube formation. Then it would be impossible forthe hydrocarbon to reach the catalyst due to the boundary conditions imposed by the pore walls. The base-growth mode can occur when the formed carbon structure is not confined by the pore walls. Regarding towards an electrical device application, the tip-mode results a highly desirable contact mode, because in such case the contact between CNT and certain electrode is governed by the nanoparticle. An consequently, it opens the possibility to the creation of Schottky Barrier [139]. Therefore the chemical nature of the nanoparticle at the CNT tip can determine the electrical behavior of the fabricated device.

3.3.2 Organized growth of carbon nanotubes

Different kinds of approaches have been developed in order to control the collective order of the CNTs. There are three possible ways to obtain an organized distribution of CNT over a substrate: after the synthesis of CNTs, during the growth of the CNTs and before the synthesis.

For instance, the organization after the CNTs synthesis consists in the dispersion of already synthetized CNTs over a substrate by spin coating [126] or printed circuits [126]. This kind of strategy is compatible with flexible substrates, however all the characteristics of the CNTs are not controllable and consequently it results very difficult to obtain aligned CNTs with difficulties to get an electrode contact.

On the other hand aligned CNTs can be obtained controlling the synthesis parameters without any pretreatment over the substrate [127, 128]. During the catalyst dissociation, the nanoparticle reaches an optimal size for carbon nucleation, and the surrounding carbon transforms into a graphite tube. There exists an optimal inter-particle distance that leads to continue aligned nanotube formation perpendicular to the substrate direction [129]. Nevertheless this kind of approach limits mainly the CNTs density.

The most generalized adopted strategy in order to growth CNTs in predetermine sites consist in the fabrication of patterned substrates. The catalyst is patterned by different approach as laser writing, multiphoton lithography and focused ion beam milling [130]. These sorts of techniques can design arbitrary forms however there are serial methods which imply a lower surface throughput. On the other hand locally directed actions that interacts with a certain template by mechanical stresses, capillary forces or electromagnetic fields, allows the creation of novel self-organized designs without throughput limitations [131]. The major difficulty is that many of the mentioned processes require further development to achieve high production rates and uniformity over large areas.

The synthesis of CNT within PAA templates results a solution in order to address the problem of the collectively self-organized growth. The PAA structure provides an ordered structure without the requirements of lithography steps. Besides, the catalyst can be easily deposited at the bottom of the pores by a reliable and low cost process as the electrodeposition process. In addition the anodization process offers the opportunity to control the PAA structural characteristics. As the pore diameters present the same size as the grown CNTs the pore can serve as guide for the future tube grown. Therefore the CNTs grown inside growth parallels among then isolated with a given inter-tube distance. The whole processes are compatible with large-scale production which attracts the interest of many research groups [132-137].

3.4 Experimental set-up

In the present work the synthesis of CNTs has been carried out by the hot-filament assisted chemical vapor deposition (HF-CVD) technique. This technique allows the local thermal decomposition of the molecules involved in the synthesis at certain distance of the sample with the catalyst nanoparticles. The implementation of the HF-CVD technique enables the synthesis of CNTs at relatively lower temperatures than the conventional thermal CVD process [138]. The figure 3-9 schematized the HF-CVD system pointing out the

two hot filaments. The filament can be powered independently in order to increase the temperature locally leading to the molecule decomposition.

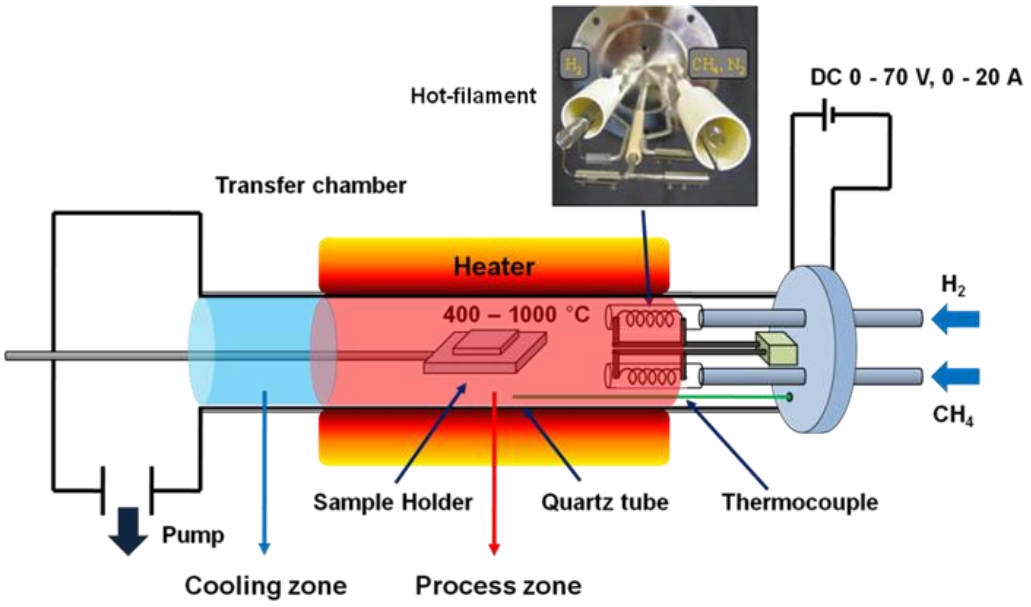

Figure 3-9. Schematic design of the hot filament chemical vapor deposition (HFCVD) system.

Methane has been chosen as the precursor gas and molecular hydrogen (H_2) in order to perform a pretreatment before the growth of the CNTs and to etch continuously the parasitic amorphous carbon deposited in the sidewalls during the CNTs synthesis. Tungsten filaments of 0.38 μm thick are placed at each gas inlet. Subsequently the hydrocarbon feedstock can be regulated by varying the hot filaments power. Different amount of hydrocarbon and carbon atom can be created. The filament power for the molecular hydrogen determines the energy of the hydrogen atoms which attack the parasitic amorphous carbon.

In order to study the impact of the hot filament power (HFP) over the CNT structure different ranges of power have been chosen. Additionally different pretreatment conditions have been executed to study the impact of such treatment over the deposited nanoparticles.

The HF-CVD system has two different zones as indicated in the figure 3-9. This configuration allows the exposition of the sample at high temperatures just for the desired

processes to be performed. The figure 3-10 shows the whole procedure for the synthesis of CNTs with the respective position of the sample in each step. For instance during the heating stage, the sample is located at the cooling zone. Subsequently when the set conditions of the pretreatment process are achieved, the sample is translated in the process zone. When the pretreatment is finished, the synthesis of the CNTs immediately begins. Finally when the synthesis of CNTs is stopped the sample is moved again to the cooling zone while in the process zone the temperature is decreasing.

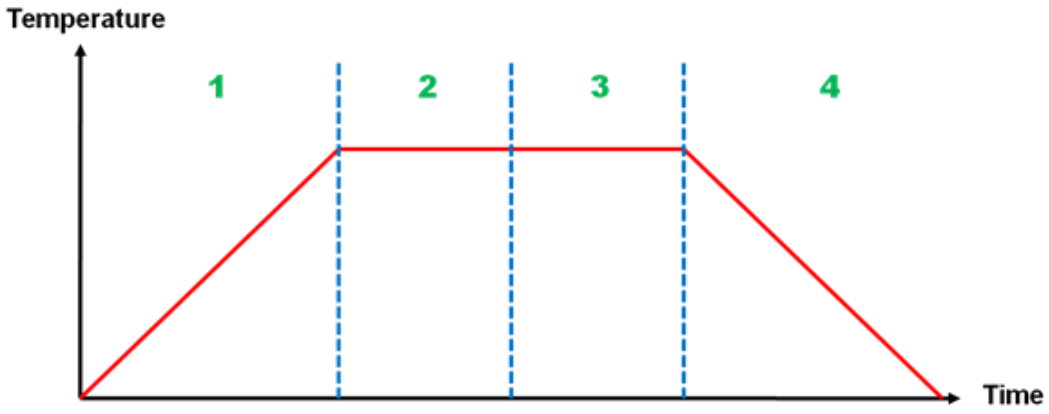

Regime	Sample position	Process stage
1	Cooling zone	Heating
2	Process zone	Pretreatment (Catalyst reduction & formation)
3	Process zone	CNT growth
4	Cooling zone	Cooling

Figure 3-10. Procedure to synthesized CNTs by the HF-CVD technique indicating the position of the sample during the different processes stages.

The parameters values applied during the pretreatment and synthesis process are summarized in table 3-1. The pressure, gas flow, HFP and temperature have been taken as reference from previous works [138, 139]. On the other hand the synthesis duration has been adjusted in order to control the nanotube length.

Process	Pressure [mbar]	H_2 flow [sccm]	CH_4 flow [sccm]	HFP H_2 [W]	HFP CH_4 [W]	Temperature [°C]	Duration [s]
Pretreatment	50	100	-	0-200	-	500-600	0-300
Synthesis	50	50	50	0-200	0-200	500-600	45-900

Table 3-1. Parameters values applied during the pretreatment and synthesis process for the synthesis of CNTs by the HF-CVD technique.

3.5 Results of the synthesis of carbon nanotubes within vertical-PAA templates

There are two main aspects that will determine the device behavior: the density of CNTs per unit of area and the contact mode between the CNT and the electrode that collect charges carriers. In the present work different studies have been executed in order to maximize these two desirable characteristics for the further device fabrication based on CNT grown inside vertical-PAA templates. The resulting CNTs growth is basically govern by the geometrical characteristics of the PAA structure and the synthesis conditions. First we have analyzed the interaction between catalyst and the supporting aluminum at different temperature conditions. On the other hand the influence of the hot-filament power on the CNT structure has been studied via Raman spectroscopy. In addition the influence of the anodization voltage on the CNT growth behavior has been studied. As we have already proved under the introduced template fabrication process, each anodization voltage is associated with a different branched structure at the bottom of the pores. The impacts of the structure at the bottom of the pores have been analyzed by electron microscopy studies carried out on cross-sections samples prepared by FIB milling. Finally the influence of the pore length over the density of CNTs synthesized inside the PAA template has been study in order to maximize the number of contacts of the future fabricated devices.

3.5.1 Nanoparticles pretreatment

Conventionally, before the synthesis of CNTs a pretreatment under H_2 atmosphere is performed in order to improve the catalytic activity of the nanoparticles [140, 141]. However these pretreatments can modify the interface between the catalyst and the support. Therefore, it results of paramount importance to investigate the interaction between the catalyst nanoparticles and the support, and the absence of any catalyst diffusion inside the support material, and to block the catalytic activity of the nanoparticle by contamination from substrate.

Different pretreatment conditions have been applied; subsequently the PAA layer has been selectively removed in order to observe the nanoparticles at the bottom of the pores. Figure 3-11 shows the nanoparticles distribution after applying three different pretreatment conditions. For the sample preparation the two step anodization procedure has been performed at 17,5°C with an anodization voltage of 30V. For the nanoparticles deposition 50 sweeps have been applied during the electrodeposition process. Concerning the pretreatment conditions as shown in table 3-1, the samples have been pre-treated at 500°C keeping the pressure at 50 mbar under molecular hydrogen. The introduced variations have been the time duration process and the activation of the H_2 hot filament power.

The figure 3-11 (a) shows the nanoparticles at the bottom of the pores for sample that has been exposed at 500°C during 2 minutes. There are not any meaningful differences with the same sample before the pretreatment but after the electrodeposition process as are shown in chapter 2. When the pretreatment duration is increased up to 15 minutes, as is shows in figure 3-11 (b) the sample starts to suffer the exposure to high temperatures creating irregularities on topography of the bottom of the pores. As it is pointed out in figure 3-11 (c), this effect is even more pronounced when the hot filament is activated during two minutes with a power of 200 W. Under these conditions the catalyst starts to diffuse into the aluminum foil.

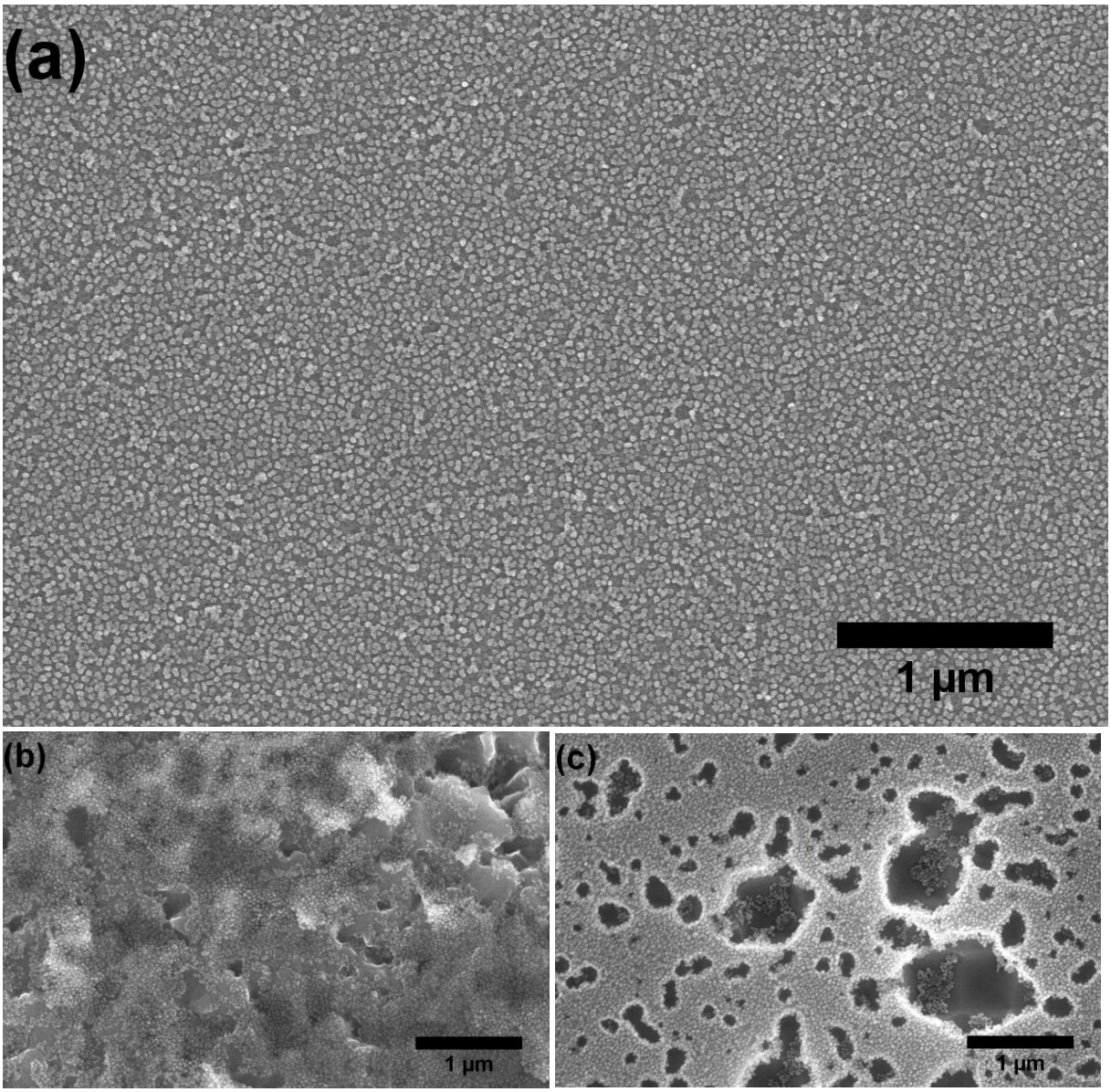

Figure 3-11. SEM analyses on the distribution of the nanoparticles at the bottom of the pores after different pretreatment conditions. (a) 500°C in H_2 atmosphere during 2 minutes, (b) 500°C in H_2 atmosphere during 15 minutes and (c) 500°C in H_2 atmosphere during 15 minutes and the hot filament activated with a power of 200W.

These analyses allowed us to conclude on the fact that the pretreatment conditions that do not affects the interaction between the nanoparticles and the substrates are those applied to sample exposed in the 500°C in H_2 atmosphere during 2 minutes. Such conditions have been taken as reference and have been used for the fabrication of all the samples.

Besides, we have realized that these conditions provide information for the further synthesis of CNTs evidencing that long time exposure of the sample at 500°C has to be avoided, in order to not damage the structure of the future device

3.5.2 Influence of the hot filament power on the CNTs

Compared with the conventional thermal CVD process the hot-filament assisted CVD process allows to dissociate locally the molecules involved in the synthesis of CNT when they pass along the hot-filament. Therefore the energy of the dissolved molecules will impact over the CNT formation inside the PAA template.

Both hot-filament powers have been varied in order to analysis the impact over the CNT quality. The template preparation has been performed using the two-step anodization process with an anodization voltage of 30V and an electrolyte temperature of 17,5°C. For the catalyst deposition, 50 sweeps have been applied. Concerning the growth of CNTs, the temperature process has been set at 500°C, the total pressure 50 mbar and the gas flow has been set to 50 sccm for both gases involved during the synthesis. The ranges of powers studied have been 0W to 200W for both filaments. The synthesis duration has been of 600 seconds in order to obtain a spaghetti-like structure at the top of the PAA template.

Typical Raman spectra were carried out in order to obtain a quantitative value of the CNT quality. The amount of defects present in the formed CNT is determined by the D-band which indicates the disordering level and the G-band which evidence the graphitization level of the synthesized carbon nanostructure. Finally the intensity ratio between the D-band and G-band provides the information of the structural quality of the CNT, where lowers values of I_D/I_G imply better quality of the synthesized CNT.

Figure 3-12 shows the Raman spectra obtained for the CNTs synthesized with different hot filament power.

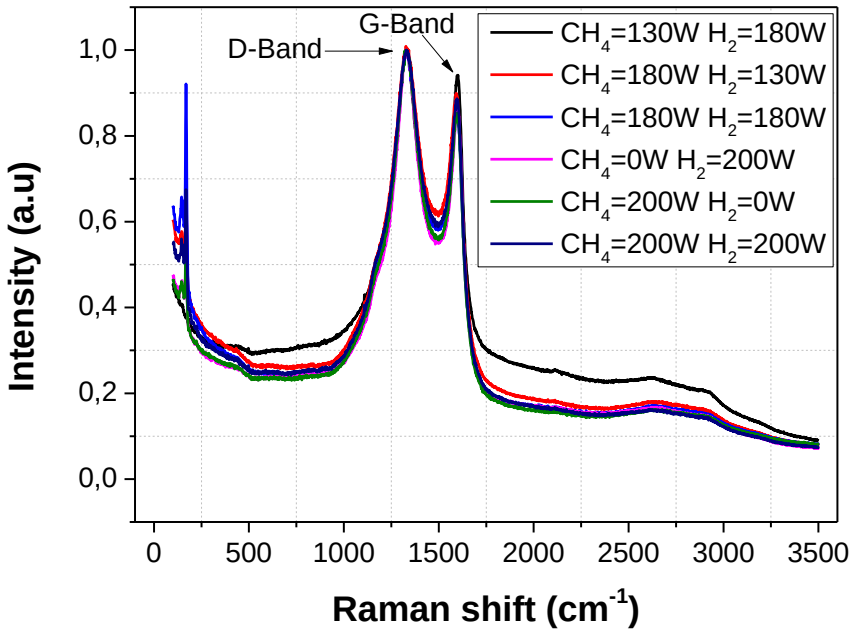

Figure 3-12. Raman spectra of grown CNTs using different hot filament powers of CH_4 and H_2.

Table 3-2 summarizes the I_D/I_G values obtained for the different ranges of hot-filament powers applied during the growth of CNTs. The obtained results reveal that the hot-filament powers in the studied range do not significant affects the quality of the CNTs. On the other hand the activation of one of the filament is required for the successful synthesis of the CNTs.

$HF - P_{CH_4}\ [W]$	$HF - P_{H_2}\ [W]$	I_D/I_G
0	0	No CNTs obtained
130	180	1,08
180	130	1,11
200	0	1,17
0	200	1,15
200	200	1,13

Table 3-2. I_D/I_G ratio obtained for different values of hot-filament powers applied during the synthesis of CNTs.

As the hot filament power does not significantly affects the CNTs quality, the power values has been adjusted in each case considering the technical aspect as the variability from the set it values in each synthesis. In spite of the HFP values have not influence on the final CNT structure, the activation of at least one filament is vital for the successful synthesis of CNTs for the applied temperatures, flow gases and pressures.

3.5.3 Influence of the branch structure over the synthesis of CNTs

The PAA fabrication entails an exponential voltage decrease process, then a branched structure is created at the bottom of the pores, as it is evidenced from the comparison between the number of pores and the number of deposited nanoparticles. Due to the porous structure, the growth of CNTs inside the PAA is completely different compared with the growth on conventional plane substrates. In the porous configuration, the hydrocarbons have more difficulty to reach the catalyst nanoparticles. The scenario is aggravated with the presence of a branch structure at the bottom of the pores. Such structure leads to energy losses of the hydrocarbon due to collisions with the pore walls complicating the carbon diffusion into the catalytic nanoparticle. Even if the tubes are formed they can be clogged among then when they reach the main pore. From figure 2-14 it is proved that when the anodization process is performed with an exponential voltage decrease of $\eta = 2.0 \cdot 10^{-3}\ s^{-1}$ the number of branches generated during the barrier thinning process for each pore depends on the anodization voltage. In the range of 20V to 30V between two and three deposition sites are created per pore, as the anodization voltage increases the number of branches also increases, for instance when the anodization voltage is 40V in average 5,6 secondary pores are produced by pore, for 50V in average 7 secondary pores and for anodization voltage of 60V, 10 secondary pores are created for each primary pore.

Figure 3-13 displays the obtained CNTs grown in PAA templates anodized in the range of 20V to 50V. The anodization conditions implemented have been adjusted in order to successfully deposit the nanoparticles at the bottom of the pores. The same synthesis

conditions have been used for all the samples. Both filaments have been activated during the CNT synthesis at a power of 180W and 130W for the H_2 and CH_4 filaments, respectively. The synthesis temperature has been set at 500°C and 10 minutes duration process has been considered.

For anodization voltages of 20V and 30 V, as shown in figures 3-13 (a) and (b) the synthesis of CNTs is successfully carried out. In both samples the CNTs cover all the PAA templates with a typical spaghetti-type distribution [142]. Under this kind of CNTs distribution it is not possible to identify the amount of CNTs grown for each pore, however it is possible to conclude that a high CNTs yield is obtained. In contrast when the anodization process is performed applying 40V the amount of CNTs drastically decreases as shown in figure 3-13 (c). When the anodized voltage is of 50V there are not any CNTs that reach the top surface of the PAA structure as is indicated in figure 3-13 (d).

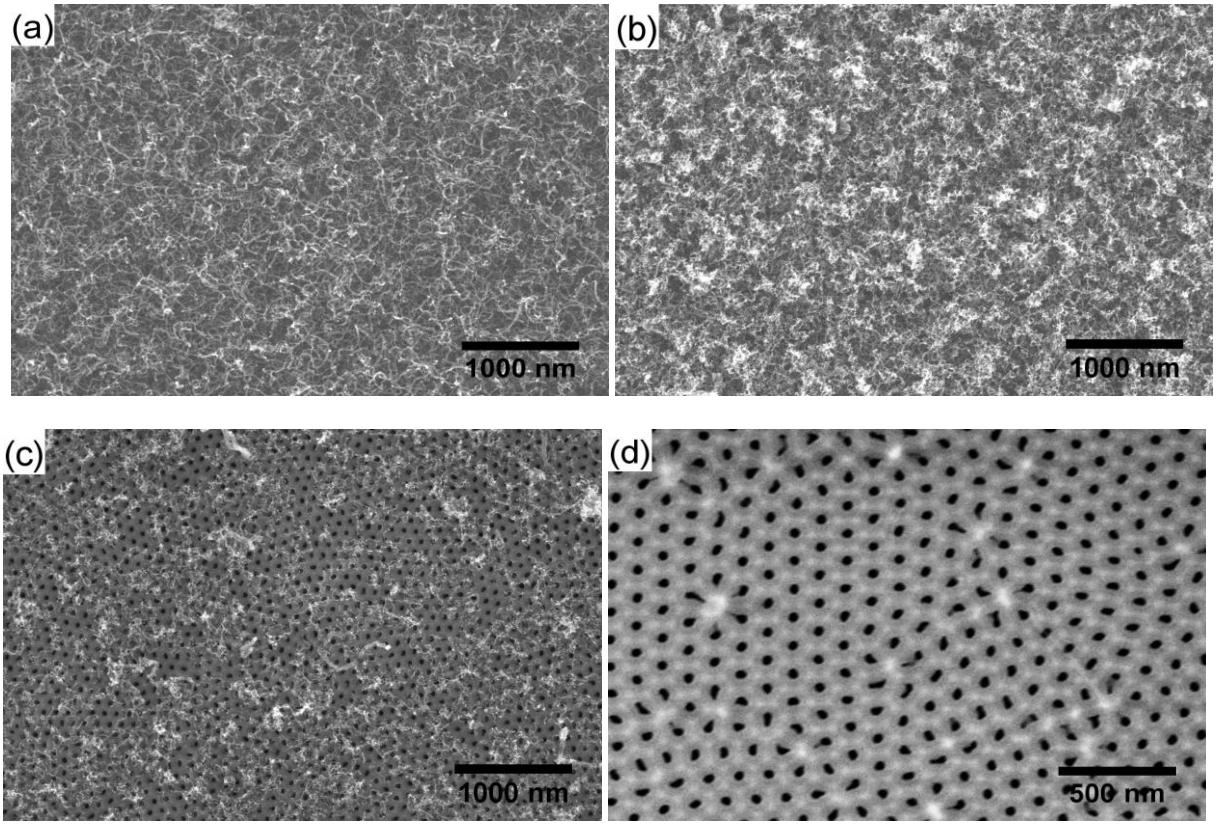

Figure 3-13. SEM analyses on CNTs synthetized within the PAA templates for different anodization voltages (a) 20V, (b) 30 V, (c) 40V and (d) 50V. For the template fabrication a two anodization step has been performed with 50 sweeps during the electrodeposition process in order to fill the pores with nanoparticles. The differences for each sample rely on the anodization voltage with their associated optimal anodization temperature for the electrodeposition process.

The obtained results are in complete agreement with the mentioned model introduced in chapter 2 which predicts that the branched structure at the bottom of the pores created during the exponential voltage decrease process makes significantly difficult the CNTs growth. Therefore the anodization conditions highly affect the CNT formation. In order to directly verify the effect imposed by the geometrical features of the PAA template fabricated with an anodization voltage of 40 V, different cross-section of PAA lamella have been prepared by FIB milling. Figure 3-14 contains TEM images of the cross-section of the PAA template in which the synthesis of CNTs has been carried out. As it can be observed most of the metal nanoparticles remain at the bottom of the pores zone, despite carbon nanostructures have been formed, most of such structures cannot successfully evolves outside the branched pore region. We attributed this phenomenon to the mentioned branched structure at the bottom of the pores that hinders the CNTs formation.

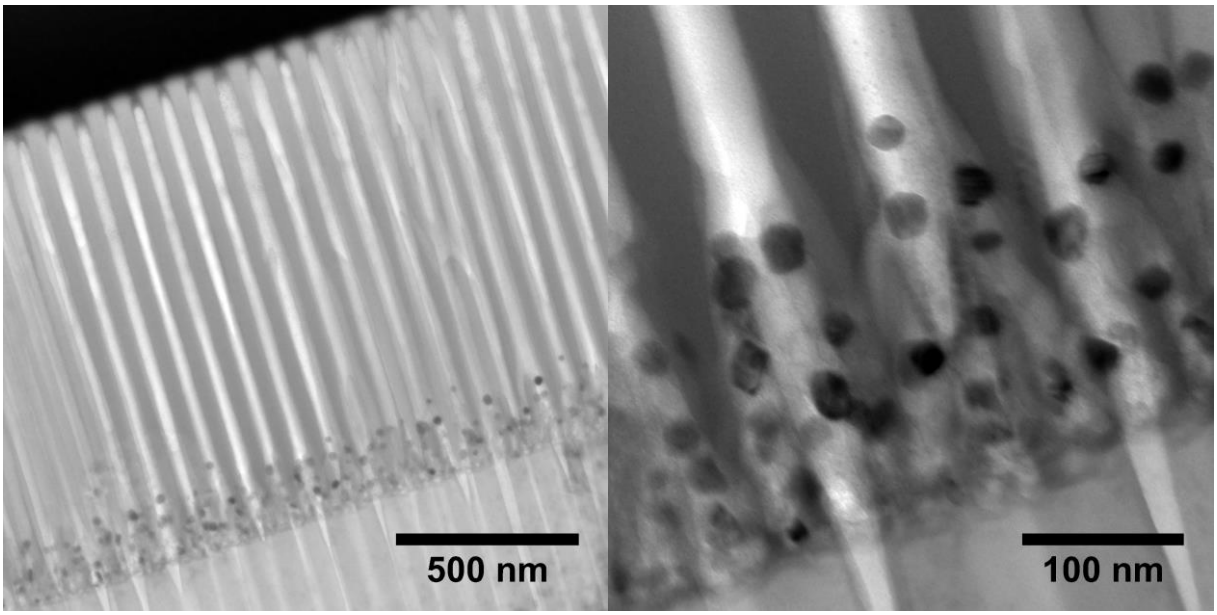

Figure 3-14. Cross-sectional TEM images obtained through FIB milling of the PAA template. PAA template fabricated with an anodization voltage of 40V, after catalyst deposition the CNTs synthesis has been performed. The right of the image shows a magnification over the bottom of the pores.

From the obtained results we have chosen to perform the anodization with voltages in the ranges of 20V to 30V. These anodization voltages lead to a PAA matrix with a more disorder pore structures but guaranteed the growth of CNTs with higher yields.

3.5.4 Evolution of CNTs inside the PAA templates

For the fabrication of devices based on vertical templates it is crucial to control the CNTs length. In order to connect individually each CNTs with an electrode the CNTs lengths must be ideally the same as the pore length. Therefore, the synthesis of CNTs has to be stopped when the CNTs reach the top of the PAA surface, otherwise when the tubes emerge from the pores, they lost the confinement and a disorder CNTs distribution is obtained with undesirable contacts among the carbon nanostructures.

Figure 3-15 shows SEM micrographs of CNTs growth inside PAA where the synthesis duration has been varied for each sample.

The PAA templates have been fabricated by the two step anodization procedure, with a second anodization duration time of 500 seconds, the anodization voltage of 30 V and the electrolyte temperature of 17.5°C. The deposit the catalyst nanoparticles have been made with 50 sweeps. For the synthesis of CNTs both filaments have been activated with a power of 200W and 130W for the H_2 and CH_4 filaments, respectively. The synthesis temperature has been fixed at 500°C and the duration process has been varied for each sample. For the sample shown in figure 3-14 (a) the synthesis duration is of 180 seconds; we can clearly observe the tips of the CNTs reaching the PAA top surface. When the synthesis process least 195 seconds as is shown in figure 3-14 (b) that the CNTs begin to come out from the pores, this is the initial configuration that leads to the spaghetti-like structure. This kind of distribution is obtained when the synthesis duration takes 225 seconds as indicated in figure 3-14 (c). The spaghetti-like structure results in an unwanted type of distribution since the collective organization of the CNTs is lost outside the PAA structure. The time

duration process is a key parameter for the pore length which finally determines the CNTs distribution.

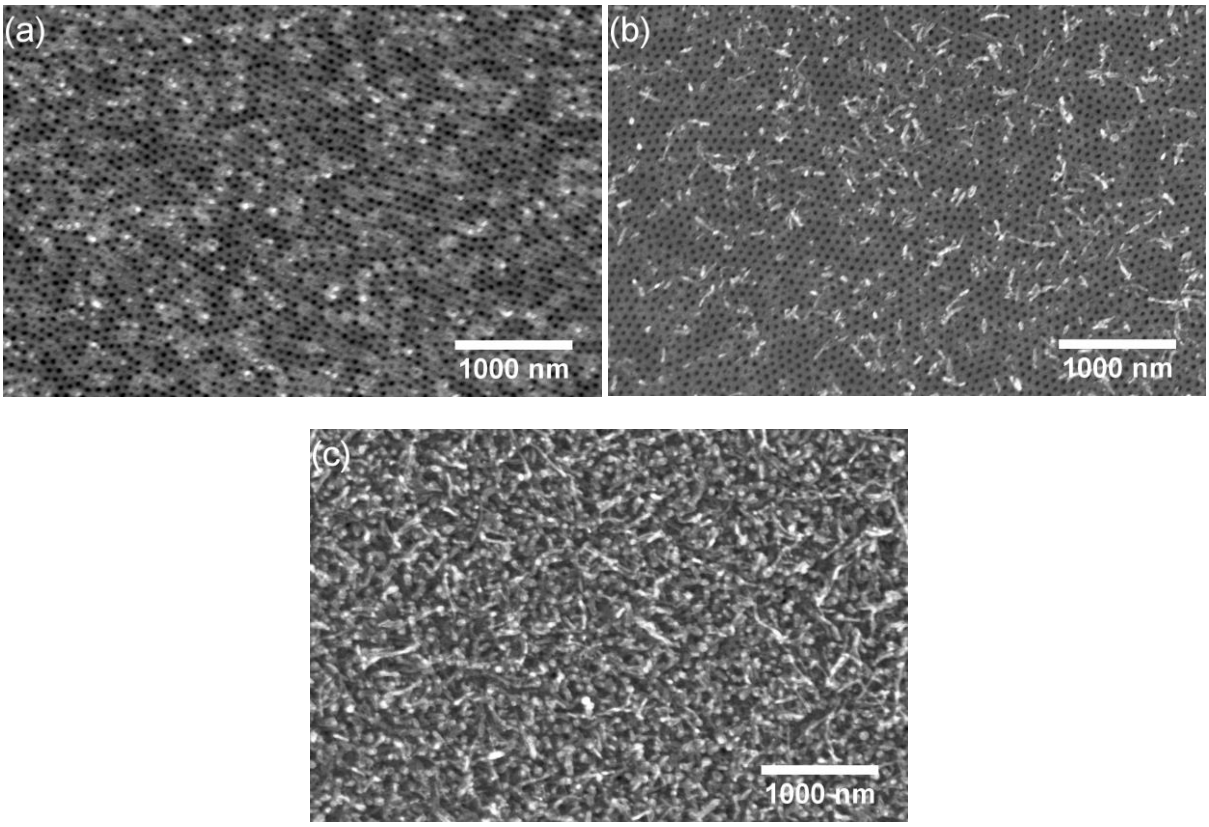

Figure 3-15. SEM analyses of CNTs grown inside PAA templates fabricated following the two-step anodization process for different durations of the CNTs synthesis: (a) 3 minutes, (b) 3.25 minutes and (c) 3.75 minutes. The template fabrication is identical for the three samples.

On the other hand from figures 3-15 (a) and (b) we can estimate the number of CNTs grown per pore. Under the described conditions 30% of nanotubes are grown from the total number of pores.

In order to identify the evolution of the CNTs inside of the PAA templates a cross section observation of the porous structure has been performed through the lamella preparation using the FIB and further TEM observation. This procedure shed light over the growth behavior inside the PAA structure as summarized in figure 3-16. The synthesis duration has been stopped at three different times. For instance figures 3-16 (a) and (b)

shows the CNTs inside the PAA structure synthesized with a duration process of 60 seconds , the figure 3-16 (c) and (d) the process duration has been least 120 seconds and 180 seconds for figures 3-16 (e) and (f). The common denominator in the three prepared samples is the presence of Ni catalyst at the bottom of the pores. This fact can indicate that there is an excess of deposited catalyst in order to growth the carbon nanostructures, but additionally it can indicate the possible growth modes that can take place at the bottom of the pores. From the SEM top views of figures 3-15 and 3-19 we can infer that the tip-grow mode occurs for the CNTs that reach the PAA top surface, however it is important to point out that in such cases the diameter of the CNTs and pore diameter are the same, therefore the tip-growth mode is the only the one that can take place because the tubes are confined and carbon feedstock can diffuse only through the catalyst. On the other hand, the presence of catalyst at the bottom of the pores, and the fact that from figure 3-16 is not always possible to identify the catalyst at the tip of each carbon nanostructures reflect that the base-growth mode cannot be discarded when the synthetized CNTs are not confined by the pore walls.

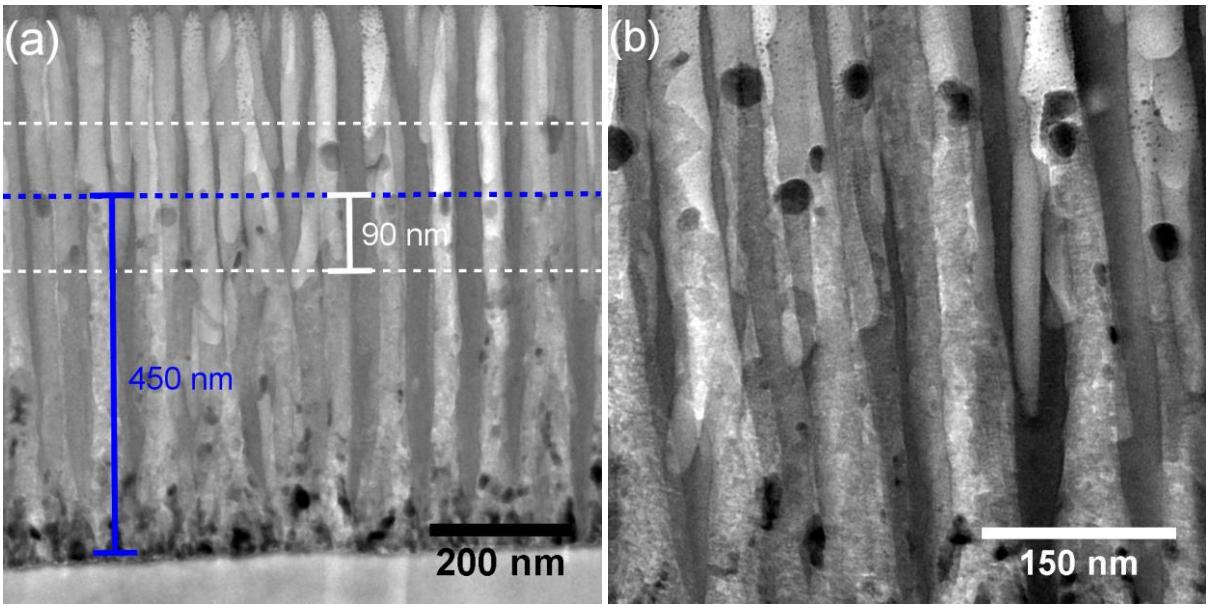

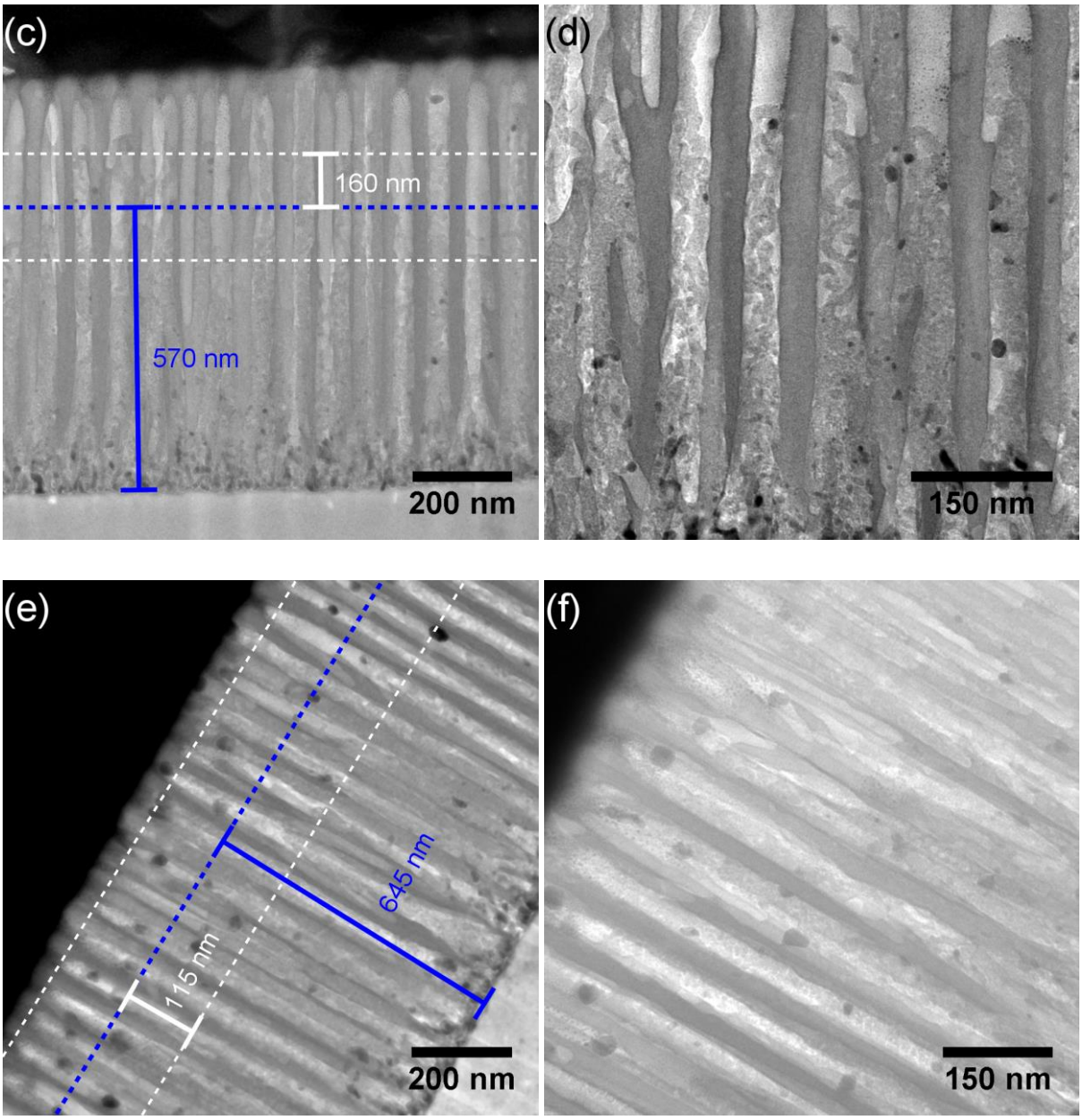

Figure 3-16. FIB cross sections TEM analyses on samples for different durations of CNTs synthesis. The syntheses of CNTs have been performed in three identical PAA templates. The synthesis duration has been the only varied parameter. The synthesis processes have been: (a) and (b) 60 seconds, (c) and (d) 120 seconds and (e) and (f) 180 seconds. The blue dashes lines indicate the average height that CNTs reach inside the pores. The white dashes lines point out the standard deviation with respect the mean height value

A comparison among the average height that the CNTs reach inside the PAA structure has been performed. The dash blue line in figures 3-16 (a), (c) and (e) indicates the mean height

that the CNTs reach inside the PAA structure for different synthesis duration. The white dash lines indicate the standard deviation of the height reached by the CNTs from the mean value. It is important to point out that the height reached by the CNTs can highly differs from the CNTs length since more than one CNT can grow in each pore, therefore the CNT is not totally confined by the pore walls as it is clearly show in figure 3-15 (d). For a synthesis time of 60 seconds the CNTs reach an average position from the aluminum of (450 ± 90) nm, in this case, no CNT tip has been detected on the top surface of the PAA structure. When the synthesis duration lasted 120 seconds the CNTs achieved an average height of (570 ± 160) nm, under such conditions just a few CNTs reach the top surface. When the synthesis takes place during 180 seconds the average height reach for the CNTs is (645 ± 110) nm, in this case in 30% of the pores one CNT tip reaches the PAA top surface. The growth rate outside the PAA structure results more complicated to quantify because as we have already mentioned, without the pore wall confinement as the CNTs synthesis evolves with time the distribution of formed carbon nanostructures leads to a spaghetti-like distribution on top of the PAA template. Consequently it is very complicated to measure the length of individuals CNTs.

Chemical analyses using energy dispersive X-ray spectroscopy (EDX) technique have been performed for the identification of the CNTs and catalyst within the porous structure. This type of analyses have been performed on a Titan-Themis TEM/STEM electron microscope operating at 200kV accelerating voltage equipped with a Cs probe corrector and SuperX detector. We have taken the K edge of carbon and Ni. Figure 3-17 and figure 3-18 summarize the EDX chemical analyses performed in two different areas, close to the bottom of the pores (figure 3-17) and near the top surface of the PAA structure (figure 3-18) on the sample for which we have considered two minutes for the tubes growth. The STEM-HAADF images performed in the scanning imaging mode of the electron microscope give us a primary information on the localization of the tubes and catalyst within the PAA structure. The poor contrast between the tubes and the PAA structure makes difficult their identification. Contrary the EDX elemental maps obtained for carbon and nickel revealed us their exact localization. Moreover from the catalyst elemental map information concerning their size could also be revealed.

Zone closer to the bottom of the pores

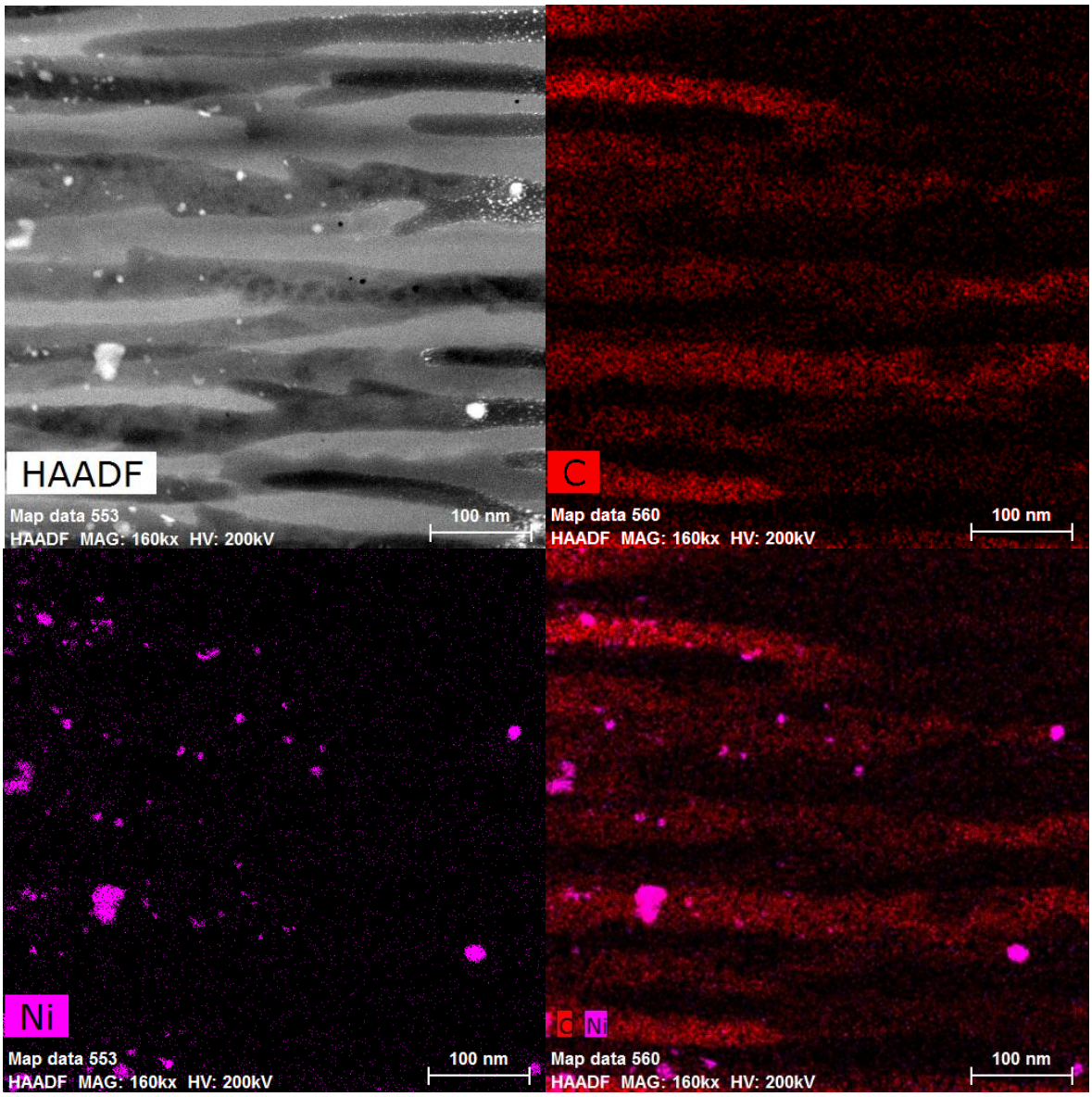

Figure 3-17. EDX chemical analysis on an area chosen close to the bottom pores for the sample for which the tubes synthesis has been carried out for 120 seconds. Up-Left:HAADF-STEM image for the chosen area where the CNTs are difficult to identify within the PAA porous structure; Up-Right: EDX Carbon elemental map and Down-Left: Ni elemental map , after background extraction Down-Right :Relative map of carbon in red and nickel in pink .

Zone closer to the PAA top surface

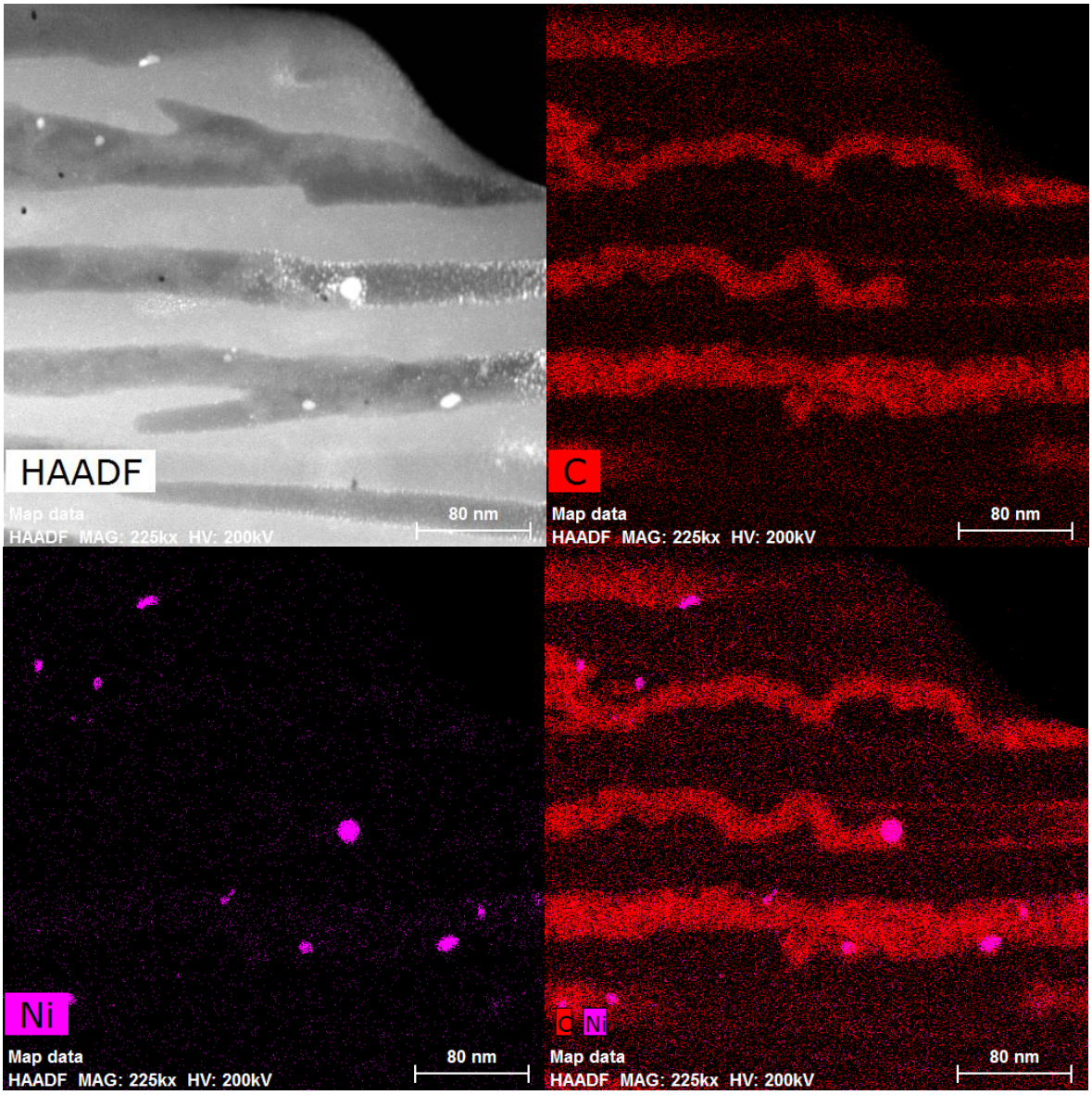

Figure 3-18. EDX chemical analysis on an area chosen close to the PAA surface for the sample for which the tubes synthesis has been carried out for 120 seconds. Up-Left:HAADF-STEM image for the chosen area where the CNTs are difficult to identify within the PAA porous structure; Up-Right: EDX Carbon elemental map and Down-Left: Ni elemental map , after background extraction Down-Right :Relative map of carbon in red and nickel in pink.

From the figures 3-16, 3-17 and 3-18 we concluded that only a fraction of the deposited metal nanoparticle leads origin for the formation of CNTs, such catalyst excess induces that part of the nickel which is contained within the nanotubes [143]. On the other

hand, the PAA structure limits only the maximum possible CNT diameter that can be grown but we can have more than one tube that can be grown for each pore. However, we have observed that just one CNT arises at the surface of the PAA structure as shown previously in figures 3-14 (a) and 3-14 (b). These results indicate that the tubes that reach the PAA top surface mainly have the same diameter as the host pore. On the contrary, it is not detected more than one nanotube tip coming from one pore. This fact is attributed to a competition established inside the pore when more than one tube per pore is formed, subsequently these tubes can be blocked among them trying to emerge from the pore. Alternatively, if there are not blocks, inside the pore, these CNTs need more time to reach the PAA top surface because a greater length is required with a more entangled growth, as is clearly shown in figure 3-16 (b).

The nanotube diameter is mainly determines by the catalyst size. In the present work, we propose that the morphology of the nanoparticle determines the carbon nanostructure behavior inside the vertical-PAA templates. From figure 2-11 we verify that one nanoparticle is deposited at the bottom of each secondary pore. In some pores just one carbon nanostructure growths with the same diameter as the host pore as it has been previously mentioned. However there are pores as confirmed on figure 3-16, where more than one tube growth inside with smaller diameter than the host pore. In these cases we can explain such growth behavior due to the morphology of the catalyst nanoparticle. Assuming that during the electrodeposition process the same mass of catalyst has been deposited in each pore, we propose a model which takes into account the superficial area of the catalyst nanoparticle. Basically, when the deposited catalyst differ from a nanoparticle with a spherical geometry , more than one active site for the synthesis of CNTs can be created during the pretreatment applied in a H_2O atmosphere. Figure 3-19 schematized the proposed growth behavior of CNTs inside the PAA depending on the catalyst morphology which is governed by the bottom pore shape. For sake of simplicity we consider the growth of CNTs without the presence of a branched structure. Figure 3-19 (a) shows two different pore shapes. After the catalyst electrodeposition we assume that the catalyst follows the bottom pore shape and in both cases the same amount of catalyst has been deposited, as shown figure 3-19 (b). In the case where there is a higher superficial area, after the pretreatment in H_2O, the nanoparticles affected with these geometries can lead to more

than one catalytic nanoparticle as it is pointed out on figure 3-19 (c). Finally depending on the nanoparticle morphology as is indicated in figure 3-19 (d), one tube or more than one can be formed during the synthesis of CNTs. The introduced model is in agreement with the fact that it exists an excess of catalyst at the bottom of the pores after the synthesis.

Concerning the CNT growth mode, we conclude that just one tube growths per pore when the tip-mode takes place. However, when there is more than one tube it is not possible to fully confirm such growth mode, because we cannot identify all their corresponding CNTs tips with their respective catalyst.

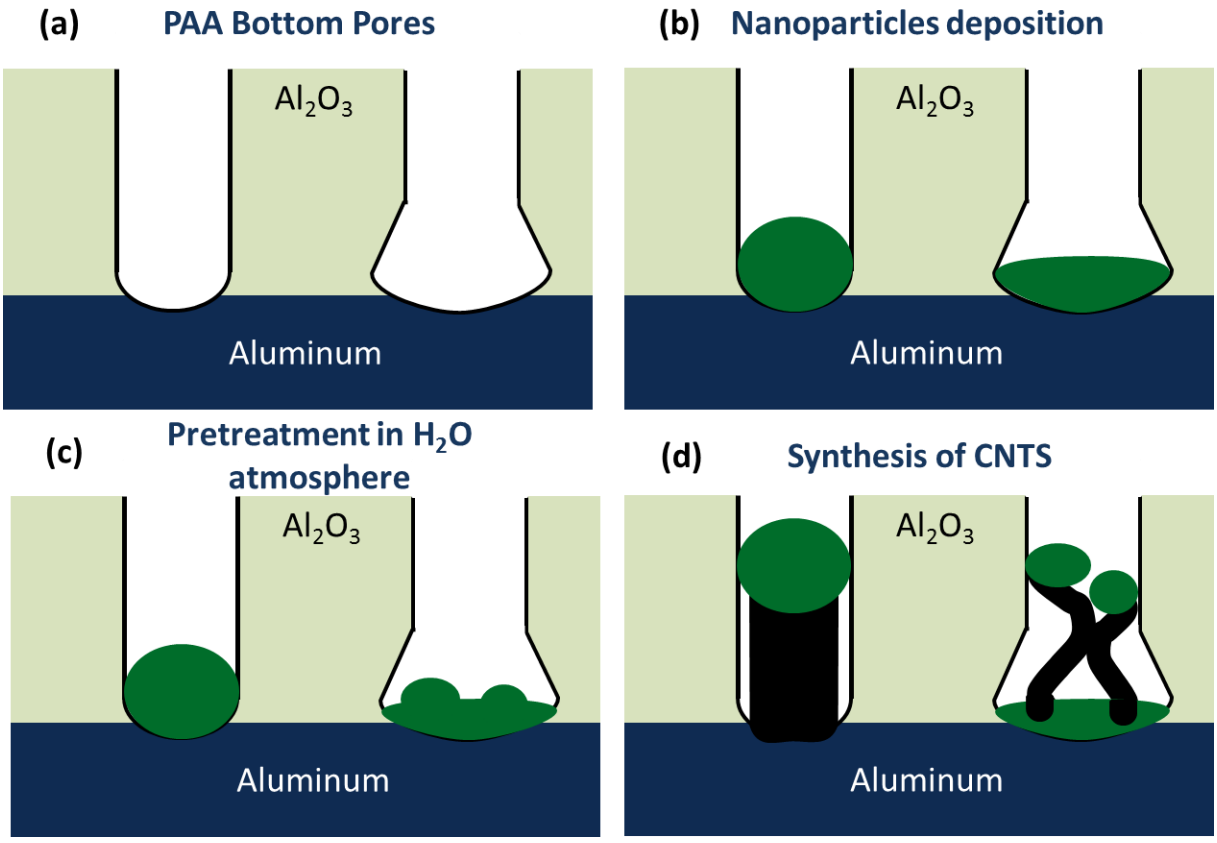

Figure 3-19. Schematic representation of the carbon nanotubes growth proposed model in order to explain the carbon nanostructure inside the PAA templates. For sake of simplicity we considered the growth in a primary pore. (a) Bottom of the pores with different shapes. (b) Catalyst electrodeposited at the bottom of the pores with different morphologies assuming that the same amount of mass have been deposited. (c) Catalyst morphology after the pretreatment in a H_2O atmosphere. (d) Growth of carbon nanostructures.

In conclusion, the different growth behavior from pore to pore is not only determined by the branched structure, but additionally by the nanoparticle morphology. When the nanoparticle size that leads to the tube formation matches with the pore diameter, as the synthesis takes place, just one tube grows per pore, without any competition, and reachs the top PAA surface. On the other hand, we deduce that the carbon nanotube cannot emerge from the pores for two reasons: a branched structure can block the growth when the carbon nanostructures reach the primary pore. This growth behavior has been verified for PAA templates fabricated with anodization voltage of 40V, where 5.5 branches are created per primary pore. In the range of anodized voltage of 20-30V between 2 and 3 pores are created, therefore such phenomenon can also occur. The second reason that can induced to a reduction in the pore filling of CNTs, can be the formation of more than one CNT per pore which established a competition among then, impeding that these carbon nanostructures can emerge from the pores. However, further studies have to be performed in order to directly corroborate the influence of the catalyst morphology on the growth of CNTs inside the PAA templates.

3.5.5 Effect of the pore length

The higher density of contacts is a desired characteristic in order to fabricate devices based on CNTs growth inside PAA structures. In previous section it has been demonstrated that the porous structures highly affect the growth within the PAA templates and the number of CNTs that emerge from the pores. In order to obtain a major density of CNTs, the influence of the pore length has been studied. Besides the geometrical characteristics at the bottom of the pores, the pore walls influence the CNTs growth since the hydrocarbon molecules can lose energy due to collisions which lead to difficulty for further carbon diffusion into the catalyst nanoparticle.

The PAA structure has been fabricated with an anodization voltage of 20V, the anodization time has been varied between 60 seconds and 2000 seconds in order to obtain PAA structure with various pore length. Figure 3-20 shows the SEM top images of the CNTs

grown inside the PAA templates. The synthesis duration in each case has been adjusted in order to stop the CNT growth when the first tips are coming out from the PAA template. From figure 3-20, we can verify that the pore length affects the growth of CNTs. Besides, from figure 3-20 (a), (b) and (c) it is corroborated again that generally just one CNT tip arises from each pore. For long pore length, no carbon nanostructures reach the top surfaceas demonstrated in figure 3-19 (d).

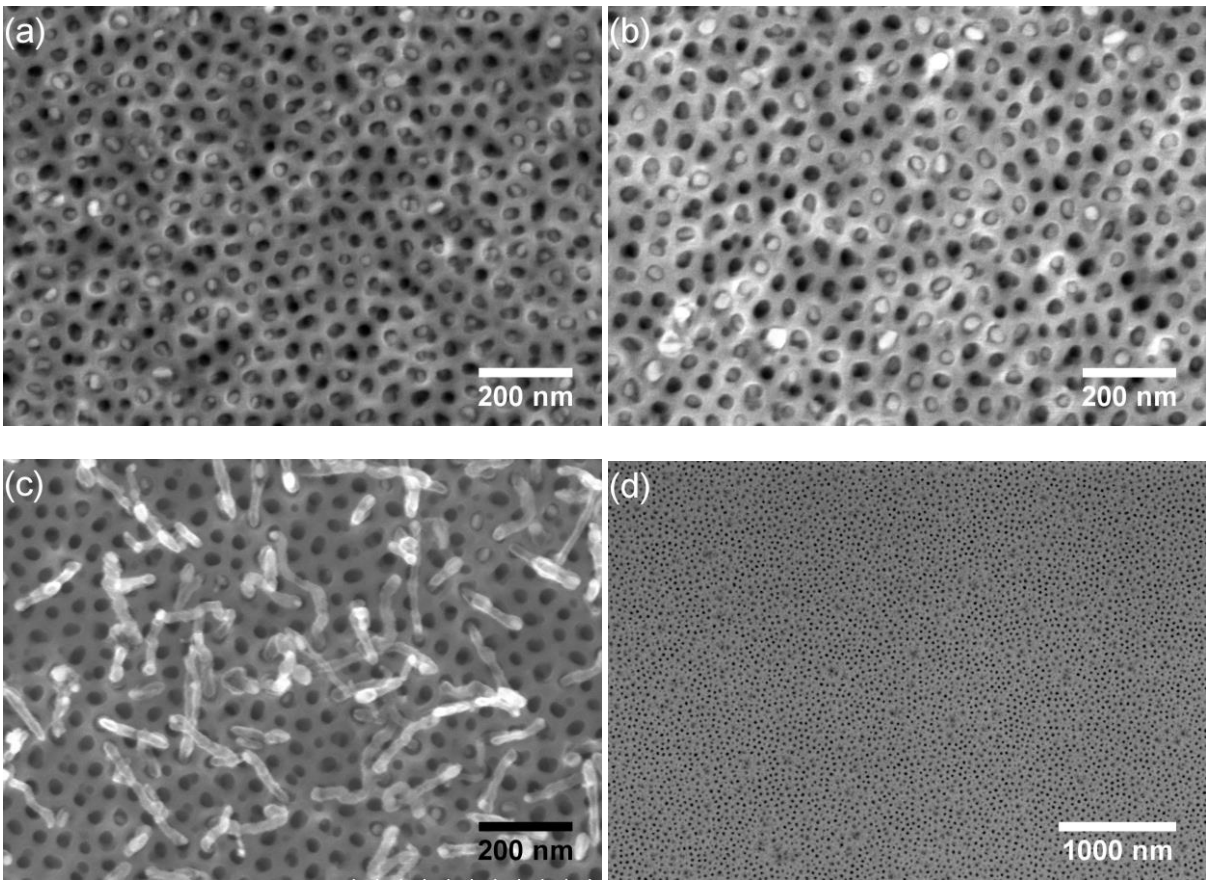

Figure 3-20. SEM analyses on sample for which the CNTs have been synthetized within PAA templates presenting different pore length: (a) 160 nm, (b) 340 nm, (c) 710 nm and (d) 1200 nm.

In figure 3-21 is plotted the percentage of CNT that arises from the pores as function of the pore length . This value does not significantly change in the range of 120 nm to 400 nm pore length, with a CNT filling rate of the order of 50%. For longer pore length, this value drastically decreases down to 35%, however the density of CNT is increased in a 5% in comparison with the samples prepared with an anodization voltage of 30V and similar

length, this results is in agreement with the fact that a lower number of branches is created at the bottom pores for lower anodization voltages, as a counterpart a lower pore order degree is obtained. Finally for too long pore length CNT synthesis does not take place.

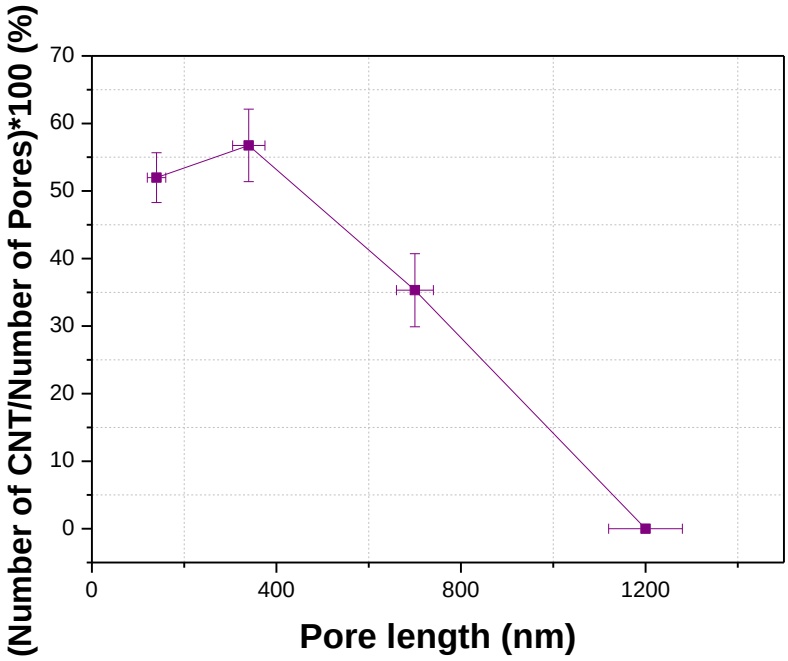

Figure 3-21. Percentage relation of the total CNTs grown within the PAA pores as function of the pore length.

Therefore in order to increase the number of CNTs that reach the PAA top surface it is necessary to considered the influence of the PAA height. The pore length range which favors the CNTs growth is between 140nm and 400 nm, on the contrary pore length longer than 800 nm drastically decreases the number of carbon nanostructures that can reach the PAA top surface. This range has been taken as reference for the further device fabrication based on CNTs grown within vertical-PAA templates.

3.6 Synthesis of CNTs inside lateral-PAA templates

Devices based on the lateral-PAA structures are useful and required for the integration in planar electronic circuits, however their fabrication processes are more complicated due to the capping layer required in order to perform just the anodization process in the horizontal direction. Bolger et al. have demonstrated that pores created in the planar direction have dendritic morphology [144], this kind of structure give difficulties for the catalyst deposition and consequently further CNTs synthesis. Therefore, it is not possible to directly transfer all the knowledge of the conventional vertical-PAA templates for the fabrication of lateral-PAA templates, rather the fabrication parameters must be taken as reference and subsequently a parametric study must be performed to optimize the lateral-PAA fabrication.

3.6.1 Synthesis of CNTs into lateral PAA templates fabricated with different thinning process conditions

In chapter 1 we have shown that the electrolyte temperature has a great impact on the lateral pore structure. For instance for anodization voltage of 40V and an electrolyte temperature of 17,5°C, the obtained structure presents a pore merge phenomenon. In order to avoid such pore structure and successfully perform the thinning barrier process (which is effective in the range of 15,0°C to 25,0°C), two different strategies have been adopted:

i-The anodization voltage has been set at 30V keeping the electrolyte temperature at 17,5°C.

ii-The anodization voltage applied has been set at 40V and the electrolyte temperature has been set at 10,0°C and 1 minute before the beginning of the exponential voltage decrease process the temperature has been increased with a rate of 1,0°C/min until reach 17,5°C.

The catalyst deposition in the case of the vertical PAA templates can be verify removing the PAA layer; in contrast due to the capping layer in the lateral-PAA templates the nanoparticles deposition at the bottom of the pores is complicated to measure. Therefore the synthesis of carbon nanostructures has been carried out without corroborating the catalyst deposition process. In order to deposit the catalyst, 100 sweeps have been applied during the electrodeposition process. Concerning the synthesis of carbon nanostructures both filaments have been activated with a power of 200W and 130W for the H_2 and CH_4 filaments, respectively. The synthesis temperature has been at 500°C, the total gas pressure has been set at 50 mbar and each gas flow at 50 sccm, the process duration has been of 10 minutes. Figure 3-22 shows the CNTs grown inside lateral-PAA templates fabricated by the two approaches that guaranteed the individual pore formation, the successfully oxide barrier thinning and subsequently catalyst deposition.

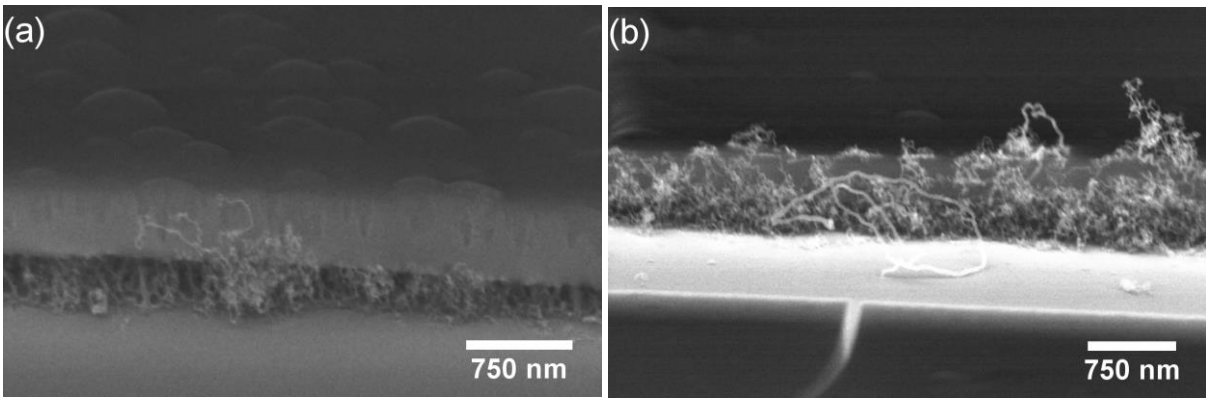

Figure 3-22. SEM analyses of CNTs grown inside lateral-PAA templates for two different templates fabrication approaches. (a) The anodization voltage has been set at 30V keeping the electrolyte temperature at 17,5°C. (b) The anodized voltage applied has been set at 40V and the electrolyte temperature has been set at 10,0°C and 1 minute before the starting to decrease the exponential voltage process the temperature has been increased with a rate of 1,0°C/min until reach 17,5°C.

Figures 3-22 (a) and (b) reveal that synthesis of CNTs has been successfully performed in both kinds of templates. Anyway a significantly bigger amount of CNTs is obtained in the templated anodized at 40V.

3.6.2 Temperature influence on the CNTs growth

The contact mode between the carbon nanostructure tip and the metal electrode plays a crucial role in the device behavior. The contacting mode and the particular election of the metal electrode can leads to a Schottky contact [145]. The ideal lateral-PAA device is schematized in figure 3-23, where a tip contact mode between the catalyst nanoparticle and the electrode is pointed out.

Figure 3-23. Schematic figure of an ideal lateral-PAA device based on CNTs grown inside horizontal pores, where the nanoparticle directly contacts the electrode establishing a tip-contact mode.

The synthesis of CNTs inside the lateral-PAA templates has been performed at two different temperatures in order to obtain straighter CNTs that will lead to a tip-contact mode between the carbon nanostructure and the electrode. Figure 3-24 shows two lateral-PAA templates fabricated under identical conditions. The lateral-PAA structures have been obtained by the single-step anodization process applying a potential of 40V, the electrolyte temperature has been varied between the anodization process and the exponential voltage decrease process from 10,0°C and 17,5°C with a rate of 1,0°C/min. For the catalyst deposition 100 sweeps has been applied. The HF-CVD with both activated filaments has been carried out for the synthesis of CNTs with a power of 200W and 130W for the H_2 and CH_4 filaments, respectively. The total gas pressure has been set at 50 mbar and each gas flow at 50 sccm, the synthesis temperature has been the only varied parameter. In the case of figure 3-24 (a) the process temperature has been set at 550°C, as results the CNTs mainly start to grow in the vertical direction, therefore the collectively organization is highly reduced, besides a further tip-mode contact seems impossible to achieve. When the

synthesis temperature is set at 600°C as shown in figure 3-24 (b) the amount of CNTs increases significantly, but it is not possible to identify the lateral-PAA structure. Under these synthesis conditions the collectively order and the horizontal direction of the synthesized CNTs are completely lost. Therefore as shown in figure 3-24 the synthesis performed at 500°C leads to a smaller amount of CNTs. But this is more important for the further device fabrication, since the CNTs are straighter in comparison with those synthetized at higher temperatures.

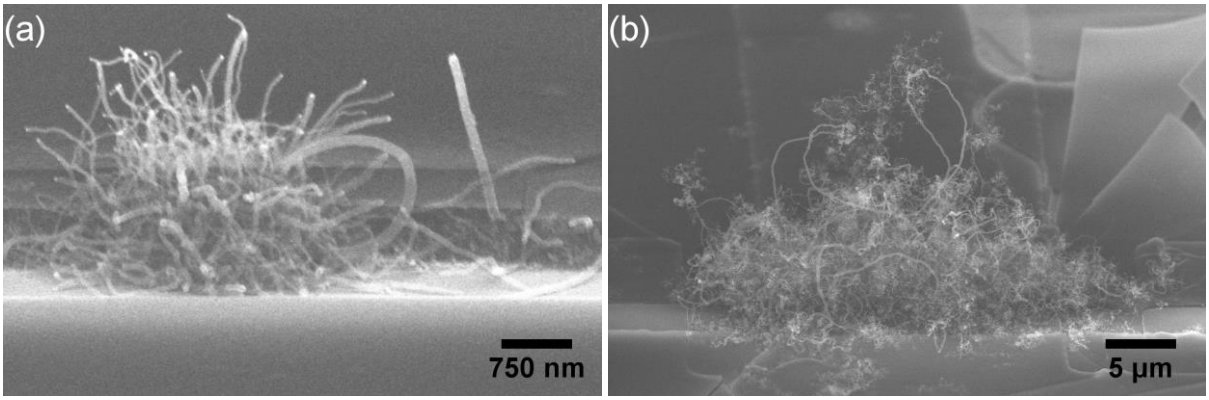

Figure 3-24. SEM images of CNTs grown inside lateral-PAA templates at different synthesis temperatures: (a) 550°C and (b) 600°C.

3.7 Conclusions

The syntheses of CNTs have been successfully performed in both types of PAA templates. In order to obtain a collective organization of CNTs several influencing parameters have to be controlled. Firstly the geometrical constrains imposed by the porous structure must to be taken into account. In the vertical PAA templates it has been proven that higher anodization voltages create more branches at the bottom pores. Although the catalyst can be effectually deposited in all pores and their respective branches, the CNTs are highly reduced, as the branched structure is predominant at the bottom of the pores. This fact has been directly evidenced by FIB lamella preparation and further TEM/STEM analyses. In addition the CNT growth evolution has been measured for the very first time for different

synthesis times inside the PAA structure. Such study provides useful information of the growth rate and the growth dynamics. For instance despite the fact that generally just one CNT tip reaches the top PAA surface, more than one CNT can grow in each pore and a competition is established inside the pore that can even block the CNT formation. Besides it has been verified that the pore length has a huge impact on the CNT yield. Concerning the synthesis parameter, the hot-filament powers have been varied and it has been shown that in the range of the studied powers there is no significant variation in terms of the CNTs quality.

On the other hand the syntheses of CNTs have been studied in lateral-PAA templates. Firstly trough the synthesis of CNTs, it has been shown two different procedures in order to reduce the oxide barrier layer at the bottom pores without suffering a pore merging phenomenon. Subsequently the synthesis temperature has been investigated in order to obtain the straightest synthetized CNTs that will preserve a collective organization and additionally will favor the tip-contact mode with the electrode that will collect the hole carriers under a potential application.

Besides the important results obtained concerning the evolution and the dynamic growth of the CNTs inside PAA structure, the present studies provide some parametric values for the synthesis of CNTs inside PAA structures that will maximized two desired characteristics for the future device fabrication: the number of contact between the CNTs and the electrodes is maximized and secondly the tip-contact mode between the CNTs and the metal electrode is highly promoted. Therefore all the fabrication conditions are established for further device characterization.

References

[1] S. Iijima, "Helical microtubules of graphitic carbon," *Nature,* vol. 354, pp. 56-58, 1991.

[2] S. Xie*, et al.*, "Mechanical and physical properties on carbon nanotube," *Journal of Physics and Chemistry of Solids,* vol. 61, pp. 1153-1158, 2000.

[3] A. A. Balandin, "Thermal properties of graphene and nanostructured carbon materials," *Nature Materials,* vol. 10, pp. 569-581, 2011.

[4] Q. Cao*, et al.*, "Arrays of single-walled carbon nanotubes with full surface coverage for high-performance electronics," *Nat Nano,* vol. 8, pp. 180-186, 2013.

[5] S. Niyogi*, et al.*, "Chemistry of Single-Walled Carbon Nanotubes," *Accounts of Chemical Research,* vol. 35, pp. 1105-1113, 2002/12/01 2002.

[6] M. F. L. De Volder*, et al.*, "Carbon Nanotubes: Present and Future Commercial Applications," *Science,* vol. 339, pp. 535-539, Feb 1 2013.

[7] G. S. Tulevski*, et al.*, "Toward High-Performance Digital Logic Technology with Carbon Nanotubes," *Acs Nano,* vol. 8, pp. 8730-8745, 2014/09/23 2014.

[8] E. J. G. Santos*, et al.*, "Toward Controlled Growth of Helicity-Specific Carbon Nanotubes," *The Journal of Physical Chemistry Letters,* vol. 6, pp. 2232-2237, 2015/06/18 2015.

[9] M. S. Dresselhaus*, et al.*, "Physics of carbon nanotubes," *Carbon,* vol. 33, pp. 883-891, 1995.

[10] R. H. Baughman*, et al.*, "Carbon Nanotubes--the Route Toward Applications," *Science,* vol. 297, pp. 787-792, 2002.

[11] H. J. Li*, et al.*, "Multichannel Ballistic Transport in Multiwall Carbon Nanotubes," *Physical Review Letters,* vol. 95, p. 086601, 2005.

[12] J. W. G. Wilder*, et al.*, "Electronic structure of atomically resolved carbon nanotubes," *Nature,* vol. 391, pp. 59-62, 1998.

[13] S. Frank*, et al.*, "Carbon Nanotube Quantum Resistors," *Science,* vol. 280, pp. 1744-1746, June 12, 1998 1998.

[14] A. Bachtold*, et al.*, "Aharonov-Bohm oscillations in carbon nanotubes," *Nature,* vol. 397, pp. 673-675, 1999.

[15] P. G. Collins*, et al.*, "Engineering Carbon Nanotubes and Nanotube Circuits Using Electrical Breakdown," *Science,* vol. 292, pp. 706-709, April 27, 2001 2001.

[16] C. Berger*, et al.*, "Multiwalled carbon nanotubes are ballistic conductors at room temperature," *Applied Physics A,* vol. 74, pp. 363-365, 2002/03/01 2002.

[17] L. Van Hove, "The Occurrence of Singularities in the Elastic Frequency Distribution of a Crystal," *Physical Review,* vol. 89, pp. 1189-1193, 1953.

[18] C. T. White and J. W. Mintmire, "Density of states reflects diameter in nanotubes," *Nature,* vol. 394, pp. 29-30, 1998.

[19] M. E. Brennan*, et al.*, "Nonlinear photoluminescence from van Hove singularities in multiwalled carbon nanotubes," *Optics letters,* vol. 28, pp. 266-268, 2003.

[20] J. J. Crochet*, et al.*, "Photoluminescence imaging of electronic-impurity-induced exciton quenching in single-walled carbon nanotubes," *Nat Nano,* vol. 7, pp. 126-132, 2012.

[21] K. Iakoubovskii*, et al.*, "Midgap luminescence centers in single-wall carbon nanotubes created by ultraviolet illumination," *Applied Physics Letters,* vol. 89, p. 173108, 2006.

[22] D. Bouilly*, et al.*, "Graft-Induced Midgap States in Functionalized Carbon Nanotubes," *Acs Nano,* vol. 9, pp. 2626-2634, 2015/03/24 2015.

[23] F. Wang*, et al.*, "The Optical Resonances in Carbon Nanotubes Arise from Excitons," *Science,* vol. 308, pp. 838-841, May 6, 2005 2005.

[24] S. M. Bachilo*, et al.*, "Structure-Assigned Optical Spectra of Single-Walled Carbon Nanotubes," *Science,* vol. 298, pp. 2361-2366, December 20, 2002 2002.

[25] M. Engel*, et al.*, "Hot Spot Dynamics in Carbon Nanotube Array Devices," *Nano Letters,* vol. 15, pp. 2127-2131, 2015/03/11 2015.

[26] J. A. Misewich, *et al.*, "Electrically Induced Optical Emission from a Carbon Nanotube FET," *Science,* vol. 300, pp. 783-786, May 2, 2003 2003.
[27] G. Overney, *et al.*, "Structural rigidity and low frequency vibrational modes of long carbon tubules," *Zeitschrift für Physik D Atoms, Molecules and Clusters,* vol. 27, pp. 93-96, 1993/03/01 1993.
[28] M. M. J. Treacy, *et al.*, "Exceptionally high Young's modulus observed for individual carbon nanotubes," *Nature,* vol. 381, pp. 678-680, 1996.
[29] M. S. Dresselhaus, *et al.*, "UNUSUAL PROPERTIES AND STRUCTURE OF CARBON NANOTUBES," *Annual Review of Materials Research,* vol. 34, pp. 247-278, 2004.
[30] M. Sammalkorpi, *et al.*, "Mechanical properties of carbon nanotubes with vacancies and related defects," *Physical Review B,* vol. 70, p. 245416, 2004.
[31] M. R. Falvo, *et al.*, "Bending and buckling of carbon nanotubes under large strain," *Nature,* vol. 389, pp. 582-584, 1997.
[32] B. I. Yakobson, "Mechanical relaxation and “intramolecular plasticity” in carbon nanotubes," *Applied Physics Letters,* vol. 72, pp. 918-920, 1998.
[33] M.-F. Yu, *et al.*, "Tensile Loading of Ropes of Single Wall Carbon Nanotubes and their Mechanical Properties," *Physical Review Letters,* vol. 84, pp. 5552-5555, 2000.
[34] M.-F. Yu, *et al.*, "Strength and Breaking Mechanism of Multiwalled Carbon Nanotubes Under Tensile Load," *Science,* vol. 287, pp. 637-640, January 28, 2000 2000.
[35] R. Zhang, *et al.*, "Growth of Half-Meter Long Carbon Nanotubes Based on Schulz–Flory Distribution," *Acs Nano,* vol. 7, pp. 6156-6161, 2013/07/23 2013.
[36] S. Berber, *et al.*, "Unusually High Thermal Conductivity of Carbon Nanotubes," *Physical Review Letters,* vol. 84, pp. 4613-4616, 2000.
[37] P. Kim, *et al.*, "Thermal Transport Measurements of Individual Multiwalled Nanotubes," *Physical Review Letters,* vol. 87, p. 215502, 2001.
[38] D. J. Yang, *et al.*, "Thermal conductivity of multiwalled carbon nanotubes," *Physical Review B,* vol. 66, p. 165440, 2002.
[39] E. Brown, *et al.*, "Ballistic thermal and electrical conductance measurements on individual multiwall carbon nanotubes," *Applied Physics Letters,* vol. 87, p. 023107, 2005.
[40] X. Zhang, *et al.*, "Optical visualization and polarized light absorption of the single-wall carbon nanotube to verify intrinsic thermal applications," *Light Sci Appl,* vol. 4, p. e318, 2015.
[41] marketsandmarkets.com, "Carbon Nanotubes (CNTs) Market by Type (SWCNTS & MWCNTS), Application (Electronics & Semiconductors, Chemical & Polymers, Batteries & Capacitors, Energy, Medical, Composites, & Aerospace & Defense) & Geography - Global Trends & Forecasts To 2018," 2013.
[42] J. Guo, *et al.*, "Aspect ratio effects of multi-walled carbon nanotubes on electrical, mechanical, and thermal properties of polycarbonate/MWCNT composites," *Journal of Polymer Science Part B: Polymer Physics,* vol. 52, pp. 73-83, 2014.
[43] K. Jiang, *et al.*, "Nanotechnology: Spinning continuous carbon nanotube yarns," *Nature,* vol. 419, pp. 801-801, 2002.
[44] N. G. Sahoo, *et al.*, "Polymer nanocomposites based on functionalized carbon nanotubes," *Progress in Polymer Science,* vol. 35, pp. 837-867, 2010.
[45] P. M. Ajayan and J. M. Tour, "Materials Science: Nanotube composites," *Nature,* vol. 447, pp. 1066-1068, 2007.
[46] M. B. Jakubinek, *et al.*, "Single-walled carbon nanotube–epoxy composites for structural and conductive aerospace adhesives," *Composites Part B: Engineering,* vol. 69, pp. 87-93, 2015.
[47] C. Kingston, *et al.*, "Release characteristics of selected carbon nanotube polymer composites," *Carbon,* vol. 68, pp. 33-57, 2014.
[48] X. Chen, *et al.*, "Quantitative nanomechanical characterization of the van der Waals interfaces between carbon nanotubes and epoxy," *Carbon,* vol. 82, pp. 214-228, 2015.
[49] Z. Wu, *et al.*, "Imaging of soft material with carbon nanotube tip using near-field scanning microwave microscopy," *Ultramicroscopy,* vol. 148, pp. 75-80, 2015.

[50] S. S. Wong*, et al.*, "Single-walled carbon nanotube probes for high-resolution nanostructure imaging," *Applied Physics Letters,* vol. 73, pp. 3465-3467, 1998.
[51] H. Yan*, et al.*, "Fabrication and Characterization of CNT-Based Smart Tips for Synchrotron Assisted STM," *Journal of Nanomaterials,* vol. 2015, p. 7, 2015.
[52] J. M. Larson*, et al.*, "Scanning MWCNT-Nanopipette and Probe Microscopy: Li Patterning and Transport Studies," *Small,* pp. n/a-n/a, 2015.
[53] M. Kristoffer*, et al.*, "Quantification of tip-broadening in non-contact atomic force microscopy with carbon nanotube tips," *Nanotechnology,* vol. 23, p. 405705, 2012.
[54] D. S. Engstrom*, et al.*, "High Throughput Nanofabrication of Silicon Nanowire and Carbon Nanotube Tips on AFM Probes by Stencil-Deposited Catalysts," *Nano Letters,* vol. 11, pp. 1568-1574, 2011/04/13 2011.
[55] Y. Lisunova*, et al.*, "Ultrahigh Currents in Dielectric-Coated Carbon Nanotube Probes," *Nano Letters,* vol. 13, pp. 4527-4531, 2013/09/11 2013.
[56] M. Irita*, et al.*, "Application of Single-Walled Carbon Nanotube to the Probe of Scanning Tunneling Microscopy," *e-Journal of Surface Science and Nanotechnology,* vol. 11, pp. 105-108, 2013.
[57] S. Hasegawa*, et al.*, "Nanometer-Scale Four-Point Probe Resistance Measurements of Individual Nanowires by Four-Tip STM," in *Atomic Scale Interconnection Machines*, C. Joachim, Ed., ed: Springer Berlin Heidelberg, 2012, pp. 153-165.
[58] Y. Qiu*, et al.*, "Vertically Aligned Carbon Nanotubes on Carbon Nanofibers: A Hierarchical Three-Dimensional Carbon Nanostructure for High-Energy Flexible Supercapacitors," *Chemistry of Materials,* vol. 27, pp. 1194-1200, 2015/02/24 2015.
[59] F. A. Hill*, et al.*, "Storing energy and powering small systems with mechanical springs made of carbon nanotube yarn," *Energy,* vol. 76, pp. 318-325, 2014.
[60] E. Frackowiak and F. Béguin, "Electrochemical storage of energy in carbon nanotubes and nanostructured carbons," *Carbon,* vol. 40, pp. 1775-1787, 2002.
[61] J. Ren*, et al.*, "Twisting Carbon Nanotube Fibers for Both Wire-Shaped Micro-Supercapacitor and Micro-Battery," *Advanced Materials,* vol. 25, pp. 1155-1159, 2013.
[62] H. Ben*, et al.*, "Highly flexible, all solid-state micro-supercapacitors from vertically aligned carbon nanotubes," *Nanotechnology,* vol. 25, p. 055401, 2014.
[63] H. Zanin*, et al.*, "Reduced graphene oxide and vertically aligned carbon nanotubes superhydrophilic films for supercapacitors devices," *Materials Research Bulletin,* vol. 49, pp. 487-493, 2014.
[64] X. Fan*, et al.*, "Growth of carbon composites by grafting on pregrown vertically aligned single-walled carbon nanotube arrays and their use in high power supercapacitors," *Rsc Advances,* vol. 5, pp. 45484-45491, 2015.
[65] J.-G. Yu*, et al.*, "Removal, recovery and enrichment of metals from aqueous solutions using carbon nanotubes," *Journal of Radioanalytical and Nuclear Chemistry,* vol. 299, pp. 1155-1163, 2014/03/01 2014.
[66] V. Gupta*, et al.*, "Study on the removal of heavy metal ions from industry waste by carbon nanotubes: effect of the surface modification-A review," *Critical Reviews in Environmental Science and Technology,* pp. 00-00, 2015.
[67] M. M. Barsan*, et al.*, "Electrochemical sensors and biosensors based on redox polymer/carbon nanotube modified electrodes: A review," *Analytica Chimica Acta,* vol. 881, pp. 1-23, 2015.
[68] K. Besteman*, et al.*, "Enzyme-coated carbon nanotubes as single-molecule biosensors," *Nano Letters,* vol. 3, pp. 727-730, 2003.
[69] Y. C. Tan*, et al.*, "Continuous refractive index sensing based on carbon-nanotube-deposited photonic crystal fibers," *Sensors and Actuators B: Chemical,* vol. 202, pp. 1097-1102, 2014.
[70] M. L. Yola and N. Atar, "A novel voltammetric sensor based on gold nanoparticles involved in p-aminothiophenol functionalized multi-walled carbon nanotubes: Application to the

simultaneous determination of quercetin and rutin," *Electrochimica Acta,* vol. 119, pp. 24-31, 2014.
[71] J. Kong*, et al.*, "Functionalized carbon nanotubes for molecular hydrogen sensors," *Advanced Materials,* vol. 13, pp. 1384-1386, 2001.
[72] A. L. Sanati*, et al.*, "A voltammetric sensor based on NiO/CNTs ionic liquid carbon paste electrode for determination of morphine in the presence of diclofenac," *Materials Science and Engineering: C,* vol. 35, pp. 379-385, 2014.
[73] B. Sanghavi*, et al.*, "Nanomaterial-based electrochemical sensing of neurological drugs and neurotransmitters," *Microchimica Acta,* vol. 182, pp. 1-41, 2015/01/01 2015.
[74] S. Ghosh*, et al.*, "Carbon Nanotube Flow Sensors," *Science,* vol. 299, pp. 1042-1044, February 14, 2003 2003.
[75] K. G. Ong*, et al.*, "A wireless, passive carbon nanotube-based gas sensor," *Sensors Journal, IEEE,* vol. 2, pp. 82-88, 2002.
[76] S. Baldo*, et al.*, "Defects and gas sensing properties of carbon nanotube-based devices," 2015.
[77] A. Star*, et al.*, "Gas sensor array based on metal-decorated carbon nanotubes," *The Journal of Physical Chemistry B,* vol. 110, pp. 21014-21020, 2006.
[78] D. Ding*, et al.*, "Hydrogen sensors based on aligned carbon nanotubes in an anodic aluminum oxide template with palladium as a top electrode," *Sensors and Actuators B: Chemical,* vol. 124, pp. 12-17, 2007.
[79] L. Wang*, et al.*, "Engineering optical properties of metal/porous anodic alumina films for refractometric sensing," *Applied Surface Science,* vol. 355, pp. 139-144, 2015.
[80] http://cseweb.ucsd.edu/classes/fa12/cse291-c/roadmap/2011InterconnectRoadmap.pdf. (2011). *INTERNATIONAL TECHNOLOGY ROADMAP FOR SEMICONDUCTORS*.
[81] H. Fiedler*, et al.*, "Carbon nanotube based via interconnects: Performance estimation based on the resistance of individual carbon nanotubes," *Microelectronic Engineering,* vol. 120, pp. 210-215, 2014.
[82] J. Liu*, et al.*, "Chemically vapor deposited carbon nanotubes for vertical electronics interconnect in packaging applications," in *Solid-State and Integrated Circuit Technology (ICSICT), 2014 12th IEEE International Conference on*, 2014, pp. 1-6.
[83] K. Masayuki*, et al.*, "Improvement in Electrical Properties of Carbon Nanotube Via Interconnects," *Japanese Journal of Applied Physics,* vol. 50, p. 05EF01, 2011.
[84] D. Xu and Z. Wang, "Structure design of through silicon via interconnects and growth of carbon nanotubes," in *Electronic Packaging Technology (ICEPT), 2015 16th International Conference on*, 2015, pp. 1105-1109.
[85] R. H. Fowler and L. Nordheim, "Electron emission in intense electric fields," in *Proceedings of the Royal Society of London A: Mathematical, Physical and Engineering Sciences*, 1928, pp. 173-181.
[86] W. A. de Heer*, et al.*, "A Carbon Nanotube Field-Emission Electron Source," *Science,* vol. 270, pp. 1179-1180, November 17, 1995 1995.
[87] A. G. Rinzler*, et al.*, "Unraveling Nanotubes: Field Emission from an Atomic Wire," *Science,* vol. 269, pp. 1550-1553, 1995.
[88] S. Sridhar*, et al.*, "Enhanced Field Emission Properties from CNT Arrays Synthesized on Inconel Superalloy," *Acs Applied Materials & Interfaces,* vol. 6, pp. 1986-1991, 2014.
[89] S. Berhanu*, et al.*, "Microscopic analysis of performance variations in carbon nanotube field emission cathodes: Implications for device optimization," *physica status solidi (a),* vol. 209, pp. 2114-2125, 2012.
[90] J. Su*, et al.*, "Improved field emission properties of MgO-nanoparticle-doped carbon nanotube films and their application in miniature vacuum gauges," *physica status solidi (a),* vol. 210, pp. 349-355, 2013.
[91] X. Xia*, et al.*, "Patterned growth of carbon nanotube array for field emission application," in *Vacuum Nanoelectronics Conference (IVNC), 2015 28th International*, 2015, pp. 140-141.

[92] J. Lee, *et al.*, "High-performance field emission from a carbon nanotube carpet," *Carbon,* vol. 50, pp. 3889-3896, 2012.
[93] A. Pandey, *et al.*, "Very stable electron field emission from strontium titanate coated carbon nanotube matrices with low emission thresholds," *Acs Nano,* vol. 7, pp. 117-125, 2012.
[94] J. M. Bonard, *et al.*, "Field emission from carbon nanotubes: perspectives for applications and clues to the emission mechanism," *Applied Physics A,* vol. 69, pp. 245-254, 1999/09/01 1999.
[95] J.-M. Bonard, *et al.*, "Tuning the field emission properties of patterned carbon nanotube films," *Advanced Materials,* vol. 13, pp. 184-188, 2001.
[96] M. O. S. Dantas, *et al.*, "Field emission enhancement achieved by selective multi-walled carbon nanotubes deposition over silicon microstructures," in *Microelectronics Technology and Devices (SBMicro), 2014 29th Symposium on*, 2014, pp. 1-4.
[97] M. Katayama, *et al.*, "Ultra-low-threshold field electron emission from pillar array of aligned carbon nanotube bundles," *Japanese Journal of Applied Physics,* vol. 43, p. L774, 2004.
[98] J.-H. Deng, *et al.*, "Improved field emission of few-layer graphene–carbon nanotube composites by high-temperature processing," *Materials Letters,* vol. 124, pp. 15-17, 2014.
[99] H. Zanin, *et al.*, "Field emission properties of the graphenated carbon nanotube electrode," *Applied Surface Science,* vol. 324, pp. 174-178, 2015.
[100] P. Nayak, *et al.*, "Enhanced Electron Field Emission of One-Dimensional Highly Protruded Graphene Wrapped Carbon Nanotube Composites," *The Journal of Physical Chemistry C,* vol. 118, pp. 5172-5179, 2014.
[101] Y.-J. Hung, *et al.*, "Patterned growth of carbon nanotubes over vertically aligned silicon nanowire bundles for achieving uniform field emission," *Nanoscale Research Letters,* vol. 9, pp. 1-7, 2014.
[102] H. Hu, *et al.*, "Highly enhanced field emission from CuO nanowire arrays by coating of carbon nanotube network films," *Vacuum,* vol. 115, pp. 70-74, 2015.
[103] T. Guo, *et al.*, "Catalytic growth of single-walled manotubes by laser vaporization," *Chemical Physics Letters,* vol. 243, pp. 49-54, 1995.
[104] A. A. Stramel, *et al.*, "Pulsed laser deposition of carbon nanotube and polystyrene–carbon nanotube composite thin films," *Optics and Lasers in Engineering,* vol. 48, pp. 1291-1295, 2010.
[105] M. Rummeli, *et al.*, "Synthesis of carbon nanotubes with and without catalyst particles," *Nanoscale Research Letters,* vol. 6, p. 303, 2011.
[106] J. Li, *et al.*, "Carbon nanotube growth: First-principles-based kinetic Monte Carlo model," *Journal of Catalysis,* vol. 326, pp. 15-25, 2015.
[107] Y. Zhang, *et al.*, "A new understanding of carbon nanotube growth: Different functions of carbon species," *Applied Surface Science,* vol. 332, pp. 756-760, 2015.
[108] E. Kukovitsky, *et al.*, "VLS-growth of carbon nanotubes from the vapor," *Chemical Physics Letters,* vol. 317, pp. 65-70, 2000.
[109] D. Takagi, *et al.*, "Carbon Nanotube Growth from Diamond," *Journal of the American Chemical Society,* vol. 131, pp. 6922-6923, 2009/05/27 2009.
[110] S. Sakurai, *et al.*, "Diameter and Density Control of Single-Walled Carbon Nanotube Forests by Modulating Ostwald Ripening through Decoupling the Catalyst Formation and Growth Processes," *Small,* vol. 9, pp. 3584-3592, 2013.
[111] M.-F. Fiawoo, *et al.*, "Evidence of correlation between catalyst particles and the single-wall carbon nanotube diameter: a first step towards chirality control," *Physical Review Letters,* vol. 108, p. 195503, 2012.
[112] J. Prasek, *et al.*, "Methods for carbon nanotubes synthesis—review," *Journal of Materials Chemistry,* vol. 21, pp. 15872-15884, 2011.
[113] A. B. Suriani, *et al.*, "Vertically aligned carbon nanotubes synthesized from waste chicken fat," *Materials Letters,* vol. 101, pp. 61-64, 2013.
[114] S. Paul and S. K. Samdarshi, "A green precursor for carbon nanotube synthesis," *New Carbon Materials,* vol. 26, pp. 85-88, 2011.

[115] M. Kumar and Y. Ando, "Camphor–a botanical precursor producing garden of carbon nanotubes," *Diamond and Related Materials,* vol. 12, pp. 998-1002, 2003.
[116] G. D. Nessim*, et al.*, "Precursor gas chemistry determines the crystallinity of carbon nanotubes synthesized at low temperature," *Carbon,* vol. 49, pp. 804-810, 2011.
[117] E. C. Neyts, "The role of ions in plasma catalytic carbon nanotube growth: A review," *Frontiers of Chemical Science and Engineering,* vol. 9, pp. 154-162, 2015.
[118] Y. C. Choi*, et al.*, "Controlling the diameter, growth rate, and density of vertically aligned carbon nanotubes synthesized by microwave plasma-enhanced chemical vapor deposition," *Applied Physics Letters,* vol. 76, pp. 2367-2369, 2000.
[119] M. Chhowalla*, et al.*, "Growth process conditions of vertically aligned carbon nanotubes using plasma enhanced chemical vapor deposition," *Journal of Applied Physics,* vol. 90, pp. 5308-5317, 2001.
[120] J. Wang*, et al.*, "Synthesis of carbon nanosheets by inductively coupled radio-frequency plasma enhanced chemical vapor deposition," *Carbon,* vol. 42, pp. 2867-2872, 2004.
[121] X. Chen*, et al.*, "TEM investigation on the growth mechanism of carbon nanotubes synthesized by hot-filament chemical vapor deposition," *Micron,* vol. 35, pp. 455-460, 2004.
[122] S. Esconjauregui*, et al.*, "The reasons why metals catalyze the nucleation and growth of carbon nanotubes and other carbon nanomorphologies," *Carbon,* vol. 47, pp. 659-669, 2009.
[123] M. Kumar and Y. Ando, "Chemical vapor deposition of carbon nanotubes: a review on growth mechanism and mass production," *Journal of Nanoscience and Nanotechnology,* vol. 10, pp. 3739-3758, 2010.
[124] U. Narkiewicz*, et al.*, "Catalytic decomposition of hydrocarbons on cobalt, nickel and iron catalysts to obtain carbon nanomaterials," *Applied Catalysis A: General,* vol. 384, pp. 27-35, 2010.
[125] M. Azam*, et al.*, "Systematic review of catalyst nanoparticles synthesized by solution process: towards efficient carbon nanotube growth," *Journal of Sol-Gel Science and Technology,* vol. 73, pp. 484-500, 2015/02/01 2015.
[126] M. C. LeMieux*, et al.*, "Solution Assembly of Organized Carbon Nanotube Networks for Thin-Film Transistors," *Acs Nano,* vol. 3, pp. 4089-4097, 2009/12/22 2009.
[127] D. Yu*, et al.*, "Vertically Aligned Carbon Nanotube Arrays Co-doped with Phosphorus and Nitrogen as Efficient Metal-Free Electrocatalysts for Oxygen Reduction," *The Journal of Physical Chemistry Letters,* vol. 3, pp. 2863-2870, 2012/10/04 2012.
[128] V. Bajpai*, et al.*, "Large-Scale Synthesis of Perpendicularly Aligned Helical Carbon Nanotubes," *Journal of the American Chemical Society,* vol. 126, pp. 5070-5071, 2004/04/01 2004.
[129] M. Bedewy*, et al.*, "Collective mechanism for the evolution and self-termination of vertically aligned carbon nanotube growth," *The Journal of Physical Chemistry C,* vol. 113, pp. 20576-20582, 2009.
[130] M. De Volder*, et al.*, "Strain-engineered manufacturing of freeform carbon nanotube microstructures," *Nature communications,* vol. 5, 2014.
[131] S. Tawfick*, et al.*, "Engineering of Micro-and Nanostructured Surfaces with Anisotropic Geometries and Properties," *Advanced Materials,* vol. 24, pp. 1628-1674, 2012.
[132] Y. Sui*, et al.*, "Synthesis of multi branched carbon nanotubes in porous anodic aluminum oxide template," *Carbon,* vol. 39, pp. 1709-1715, 2001.
[133] T. Kyotani*, et al.*, "Preparation of Ultrafine Carbon Tubes in Nanochannels of an Anodic Aluminum Oxide Film," *Chemistry of Materials,* vol. 8, pp. 2109-2113, 1996/01/01 1996.
[134] R. M. Matthew*, et al.*, "Vertical single- and double-walled carbon nanotubes grown from modified porous anodic alumina templates," *Nanotechnology,* vol. 17, p. 3925, 2006.
[135] S.-H. Jeong*, et al.*, "Carbon nanotubes based on anodic aluminum oxide nano-template," *Carbon,* vol. 42, pp. 2073-2080, 2004.
[136] N. Ke*, et al.*, "Carbon nanotube diameter control via catalytic Co nanoparticles electrodeposited in porous alumina membranes," *Rsc Advances,* vol. 5, pp. 25747-25754, 2015.

[137] C. Rochford*, et al.*, "Planarized arrays of aligned, untangled multiwall carbon nanotubes with Ohmic back contacts," *Journal of Materials Research,* vol. 30, pp. 315-322, 2015.
[138] K.-H. Kim*, et al.*, "The role of catalytic nanoparticle pretreatment on the growth of vertically aligned carbon nanotubes by hot-filament chemical vapor deposition," *Thin Solid Films,* vol. 575, pp. 84-91, 2015.
[139] A. Gohier*, et al.*, "High-Rate Capability Silicon Decorated Vertically Aligned Carbon Nanotubes for Li-Ion Batteries," *Advanced Materials,* vol. 24, pp. 2592-2597, 2012.
[140] G. D. Nessim*, et al.*, "Tuning of vertically-aligned carbon nanotube diameter and areal density through catalyst pre-treatment," *Nano Letters,* vol. 8, pp. 3587-3593, 2008.
[141] R. Chetty*, et al.*, "Effect of reduction temperature on the preparation and characterization of Pt− Ru nanoparticles on multiwalled carbon nanotubes," *Langmuir,* vol. 25, pp. 3853-3860, 2009.
[142] C. Dekker, "Carbon nanotubes as molecular quantum wires," *Physics today,* vol. 52, pp. 22-30, 1999.
[143] S. W. Pattinson*, et al.*, "The life and death of carbon nanotubes," *RSC Advances,* vol. 2, pp. 2909-2913, 2012.
[144] C. T. Bolger*, et al.*, "Mechanical constraint and release generates long, ordered horizontal pores in anodic alumina templates," *Nanotechnology,* vol. 23, p. 175602, 2012.
[145] K. H. Kim*, et al.*, "Cup-Stacked Carbon Nanotube Schottky Diodes for Photovoltaics and Photodetectors," *Advanced Materials,* vol. 26, pp. 4363-4369, 2014.

Chapter 4.

The applications of devices based on CNTs growth inside PAA templates

Devices based on CNTs grown inside PAA templates have been characterized. Two different templates approaches have been adopted for the device fabrication: the lateral-PAA procedure which requires lithography steps and has a characteristic length device in the micrometers scale and on the other hand, the conventional vertical-PAA templates which are obtained by the simple anodization process of an aluminum foil, with a characteristic device area in the millimeter scale.

For the lateral-PAA devices two different approaches have been implemented in order to asymmetrically contact the arrays of nanotubes. This asymmetry arises from the smart use of the aluminum as a Schottky contact for holes carriers and the metal as nanoscale electronic contacts obtained by the promotion of a tip-contact mode or a metal decoration of the side-wall of the CNTs. The resulting characterized devices present outstanding photonic response under light illumination. By rough comparison with solar cell devices fill factor has been calculated. Additionally exploring further potential applications in telecommunications, time responsivity measurements have been performed in the infrared band.

On the other hand, vertical-PAA devices have been electrically and optoelectronically characterized. The same contact mode and work function configuration have been preserved, however different behavior had been measured due to the inherent geometry of each device that affects the active element for the sensing devices. In addition humidity

sensing measurements has been performed, such measurements exhibits potential interest for further applications in the gas sensing domain.

4.1 Devices fabrication and characterization

Over the previous chapters we have discussed the main processes involved for the fabrication of devices based on CNTs grown inside PAA templates. The impact of the anodization parameters on the resulting vertical-PAA templates has been deeply studied. By the extensive analysis of the exponential voltage decrease process and catalyst electrodeposition, the branched structure at the bottom of the pores has been deduced. The template fabrication has been adjusted in order to obtain the maximum density of CNTs. Therefore a set of optimized fabrications conditions have been established in order to allow one to start their electrical characterization.

For the fabrication procedure of the lateral-PAA templates previous work has been taken as reference [1]. In the present work, concerning the fabrication process the main contribution relies on the studies of the effect of the anodization temperature on the pore structure.

The conditions for fabrication of both kinds of devices are analyzed for further device characterization performance. In addition we will introduce in detail the experimental set-up used for the study of the electrical, photonic and humidity sensing performance of the fabricated devices.

4.1.1 Lateral-PAA devices preparation

As it has been previously introduced for the lateral-PAA device fabrication 200 nm thick aluminum have been evaporated on 500 nm thick thermally grown SiO_2 on a p-doped Si wafer. By photholitography steps aluminum stripes are obtained, ready to perform the

anodization process. In order to favor the optimum pore formation an electropolishing process is carried out in a mixture solution of 70% perchloric acid, ethanol and isopropanol, with a volume ratio of 1:14:35 at 5°C during 2 seconds. Such mixture solution provides a lower etching rate than the conventional electropolishing solution based on perchloric acid and ethanol. The pore formation have been carried out by a simple anodization step in a 0.3 M Oxalic acid solution at 10°C applying 40 V during 60 minutes followed by the exponential voltage decrease process with a decay rate of 2.0×10^{-3} sec^{-1}. Subsequently a pore widening process is performed in a 0.3 M H_3PO_4 solution in order to completely remove the oxide barrier layer at the bottom of the pores, this process allows the successfully deposition of the catalyst. The nanoparticles have been deposited by the electrodeposition process in Watts baths solution using a square function, where the electrodeposition pulse has been set at -5.5 V during 5 ms and the rest time in the open circuit voltage during 90 ms. The total number of pulses has been set at 100.

Two different types of lateral-PAA devices have been used in order to perform the optoelectronic device characterization. In one case the capping layer that prevents the pore formation in the vertical direction has been removed after the anodization process by reactive ion etching and further metal decoration of the grown CNTs has been done. For the second kind of devices the SiNx layer has been kept in order to promote the tip-contact mode between CNTs and the counter electrode.

The same CVD synthesis conditions have been implemented in both sorts of devices. Before the CVD synthesis a pretreatment stage has been done in a H_2 at 50 mbar, with gas flow of 100 sccm at 500°C during 5 minutes. After the pretreatment step, both filaments are activated with a power of 200W and 130W for the H_2 and CH_4, respectively. The flow has been fixed at 50 sccm for both gases. The CNT synthesis duration has been set at 15 minutes.

Concerning the metal decoration process of the as-grown CNTs various metals has been electrodeposited using the same chemical cell as for the catalyst deposition. The prepared salts and pulses applied voltage for each solution are summarized in table 4-1. The same numbers of sweeps, pulse and rest times have been used for all the prepared solution.

Decorated metal	Solution	Applied pulse value [V]
Nickel	330 g/L $NiSO_4 \cdot 6H_2O$, 45 g/L $NiCl_2 \cdot 6H_2O$, and 30 g/L H_3BO_3	-5.5 V
Palladium	2 g/L $Pd(NH_3)_4Cl_2$ and 20 g/LNH_4Cl	-5.75 V
Iron	120 g/L $CoSO_4 \cdot 7H_2O$, 30 g/L H_3BO_3 and 0,6 g/L $C_6H_8O_6$	-5.4 V
Copper	1.0 M $CuSO_4 \cdot 5H_2O$ and 1.0 M H_3BO_3	-4.3 V

Table 4-1. Mixture solution of the decorated metal on the side-walls of the carbon nanotubes grown in lateral devices without the insulating capping layer.

4.1.2 Vertical-PAA devices preparation

The vertical-PAA templates have been fabricated by the two-step anodization process. In order to obtain a flat surface an electropolishing process is performed in a solution of 70% perchloric acid and ethanol in a proportion of 1:4 applying 20V during 7 minutes at 5°C. The first anodization process has been performed in a 0.3 M oxalic acid solution at 17,5°C with an anodization voltage of 20V during 2 hours. The PAA layer has been removed in a 0.2 M CrO_3 and 0.6 M H_3PO_4 at 60°C during 1 hour. The second anodization process is carried out under the same conditions as the first anodization step during 240 seconds followed by an exponential voltage decrease with a decay rate 2.0 x 10^{-3} sec^{-1}. To completely remove the oxide barrier the PAA structure is dipped in a 0.3M H_3PO_4 at 30°C during 25minutes. Nickel nanoparticles have been deposited by the pulse electrodeposition process in a Watt bath solution. A total of 50 sweeps has been applied. Each sweep is formed by a pulse of -5,5 V applied during 5 ms and the rest time of 90 ms in the open circuit potential. Concerning the synthesis of CNTs, a pretreatment has been performed during 5 minutes in a H_2 atmosphere at 500°C, with a gas flow of 100 sccm at a pressure of 50 mbar. During the CNTs growth both filament are activated with a power of 130 W for the CH_4 and 180 W for the H_2. The synthesis temperature has been fixed at 500°C during 90 seconds.

Such template fabrication leads to an average interpore distance of 75 nm, a pore diameter of 30 nm and a pore length of 350 nm. The fabrication conditions lead to a 50% rate of successful growth of CNTs to respect the total number of pores, that is to say for half of the total number of nanopores, a nanotube tip reach the top surface of the PAA. Precisely the synthesis time duration has been adjusted in order to stop the synthesis when the first nanotubes tips emerge from the pores. The mentioned devices fabrication condition leads to an average CNTs density of 200 CNTs/μm^2.

The counter electrode for vertical devices has been deposited differently than for lateral templates.. The metal deposition has been performed in a Plassys Evaporator in a pressure of 1.00 x 10^{-7} Torr, with a current of 0.2 A and deposition rate of 0.3 nm/ sec. Four different electrode materials have been deposited: nickel, aluminum, palladium and gold. The thickness of the electrode has been set at 10 nm. A simple shadow mask has been mounted on top of the PAA structure. The resulting deposited counter electrodes are squares of approximately 62500 μm^2. The resulting vertical-PAA devices are schematized in figure 4-1 where all the structural properties are indicated.

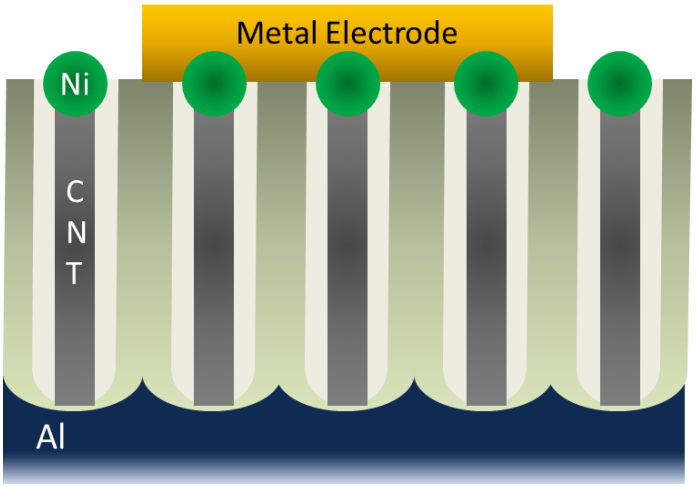

Figure 4-1. Schematic figure of the devices based on CNTs grown within vertical-PAA templates.

4.1.3 Electrical, photonic and humidity characterization set-up

Electrical measurements have been realized using a Keithley 4200 SCS apparatus. The measurement set-up possesses four micro-probes in order to carry out the electrical measurements. In the present work the classical two probe measurement have been implemented. Each probe is located in positional micrometers. The sample temperature can be regulated through a Peltier mounted sample holder. The chamber is connected to two pipe lines, in one case N_2 can be introduced and in the second water vapor. Water vapors is generating by circulating N_2 in a heated bottle of water. The chamber is connected to a high vaccum pumping system, with base pressure of the order of 1.00×10^{-5} mbar.

For the photonic characterization, the optical experimental setup consists of an Olympus BX51 microscope capable of accommodating objectives of various magnifications and NA values; the one used in this study was a 100× objective with a numerical aperture NA = 0.9. A tunable argon ion laser (458, 514 nm wavelengths) from Melles Griot and a He-Ne laser operating at 633 nm are focused on the sample in a normal incidence configuration. Several neutral filters with the optical densities 0.3, 0.6, 1, 2, 3 or 4 are used to equally attenuate the intensity of the laser beam over the wavelength range used in this study. For infrared wavelengths, Thor Labs unfocused laser diodes (850 nm – L850P010 and 1550 nm – ML925B45F) have been mounted on a temperature controlled laser diode mount (TCLDM9). Optical chopper system and chopper wheels have been used for generating the 5 kHz laser pulse in order to carry out time response measurements.

4.2 Devices based on CNTs grown in Lateral-PAA templates

Lateral devices based on CNTs have been optoelectronically characterized regarding for further for photovoltaic and photodetectors applications. These devices are based on

asymmetrical contacted arrays of nanotubes leading to Schottky photodiodes. Two different strategies have been implemented in order to engineer the contact between the CNTs and the counter electrode.

4.2.1 Impact of the Contact mode of CNTs on the electrical behavior

One of the properties that characterized the presented lateral devices based on CNTs is that the contacting process of the CNTs with a counter electrode is achieved during the CNTs synthesis. The contact mode between the CNTs and such terminal strongly affects the current behavior of the fabricated devices. Basically two different contact modes can take place during the CNTs growth as is indicated in figure 4-2, the side-wall contact mode and the tip-contact mode. In the side-wall contact mode, the carbon material of the CNTs walls is connected between the two terminal leading to a symmetrically connection with a configuration of aluminum-CNT-aluminum. This symmetry is broken when the nanoparticle present in the CNT tip directly contact to the counter electrode. Therefore the asymmetrically contact is characterized by the aluminum-CNT-catalyst-aluminum configuration. First the contact mode directly impacts on the electrical current considering that the electric conduction of CNTs in the radial direction is much lower than in the axial direction. On the other hand considering the tip-contact mode, the contact resistance by the direct connection of the CNT with the counter electrode can be highly dependent on the junction between the CNT and metal electrode. The adopted strategy to decrease the contact resistance relies in the proper election of a metal electrode with a higher work function than the work function of the CNTs. The work function of CNTs depends mainly on their structural characteristics, the previously reported values are in the range of 4.5 eV to 5 eV [2-4]. The metals used as contacts electrodes are usually palladium (5.22 - 5.6 eV), platinum (5.12 – 5.93 eV) and gold (5.1 - 5.47 eV) [5-7]. The lateral-PAA side contact electrode is not readily available for modifying its contact interface with the CNTs. Moreover, aluminum is not a metal with a well matched work function with the CNT work

function [8], since their value is in the range of (4.06 – 4.26 eV). In summary the side-wall contact mode has to be avoided for two main reasons:

i-Withthe symmetrical contact and under such configuration an electrical resistor is obtained.

ii- Under the fabricated device configuration it is not possible to choose the electrode material, therefore since work function values of the components of the device (Aluminum electrodes and the CNTs) are not well matched, it is impossible to create a Schottky contact that can allow the application of the devices in the photonic domain.

On the other hand, the asymmetrically connection configuration offers the possibility to create a Schottky contact, this kind of contact requires a well matched work function among the device components.

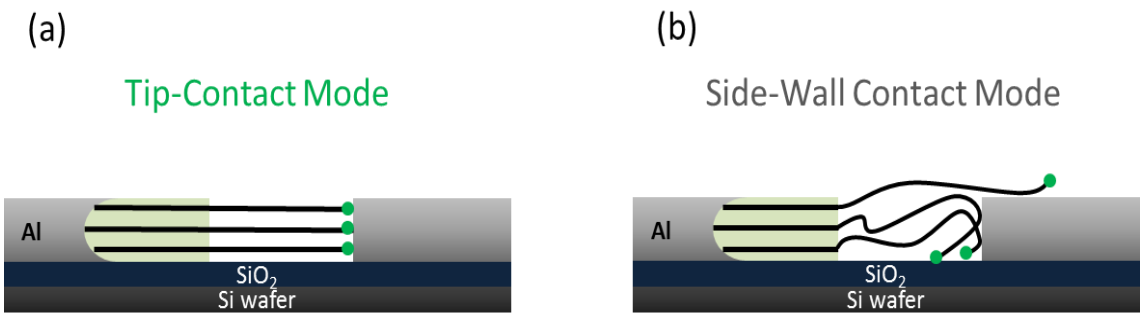

Figure 4-2. Schematic images of the possible contact modes between the CNTs and the counter electrodes.

In order to promote such asymmetrical contact mode two different approaches have been adopted. The resulting devices are schematized in figure 4-3. In one case an insulating capping layer has been deposited on top of the counter electrodes to eliminates as maximum as possible the side-wall contact mode as is shown in figure 4-3 (a). The principle consists in only exposing the surface in the same direction in which the growing CNTs emerge from the pores. The procedure has to be complemented with the growth of the

straightest CNTs as possible. Under such fabrication conditions the tip-contact mode is highly promoted.

On the other hand a metal decoration process has been carried out in a chemical cell through an electrodeposition process, in devices where the insulating capping layer is removed after the catalyst nanoparticle process is performed. The idea consists in modifying the nature of the side-wall contact mode by adding an interfacial metal between the carbon nanotube wall and the counter electrode. Therefore after the decoration process the symmetrical connection dominated by the side-wall contact mode is broken through the incorporation of a metal as it is shown in figure 4-3 (b). This technique also allows a wider range of metal work functions as non-catalytic metals for CNTs grown can now be utilized in order to obtain an asymmetrical contact eliminating the dependence of the tip-contact mode.

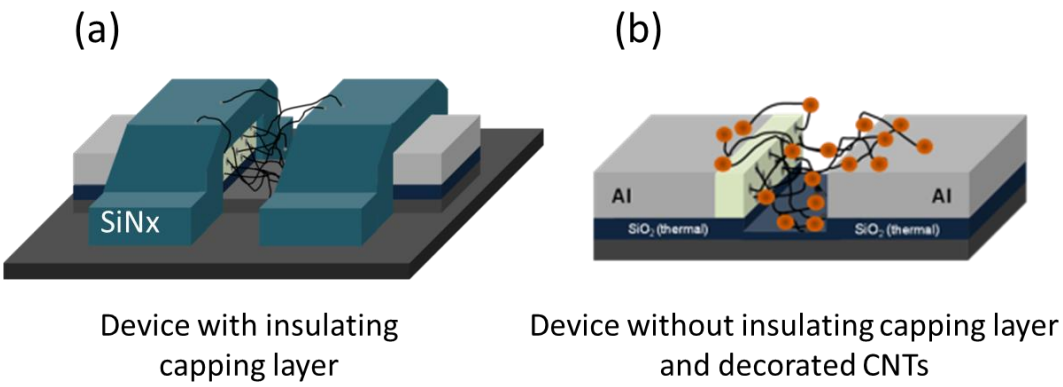

Figure 4-3. Two different implemented approaches in order to promote asymmetrically contacted devices. The work functions values of the metal nanoparticles have been matched in order to obtain a Schottky contact at the counter electrode. (a) Deposition of a capping layer to maximizes the tip-contact mode between the CNTs and the counter electrode. The resulting contact between the two terminal is dominated by the Aluminum-CNT-Metal catalyst-Aluminum. (b) Metal decoration of CNTs performed in order to modify the nature of the side-wall contact mode that's break the symmetry configuration between the two terminals. The contacted configuration results Aluminum-CNT-Decorated metal-Aluminum.

4.2.2 Devices with capping layer

In the devices fabricated with a capping layer the nickel catalysts located at the nanotube tips are used as nanoscale electronic contacts. The desired device architecture is schematized in figure 4-3 (a), the present configuration takes mainly the advantage of, on one side, the physical contacts of the left aluminum electrode with the as-grown CNTs within the lateral-PAA, and simultaneously, the contact between the Ni catalyst-ended CNTs tips with a counter electrode.

The electrical characterization has been performed by applying a voltage bias V_B to the counter electrode connecting CNT's catalyst-terminated tip, whilst the lateral-PAA side contact electrode is grounded. The current-voltage curve is displayed in figure 4-4 in black line, it is clearly detected an efficient rectifying behavior in the reverse bias regime ($V_B < 0$) whereas current can flow in the forward bias regime ($V_B > 0$).

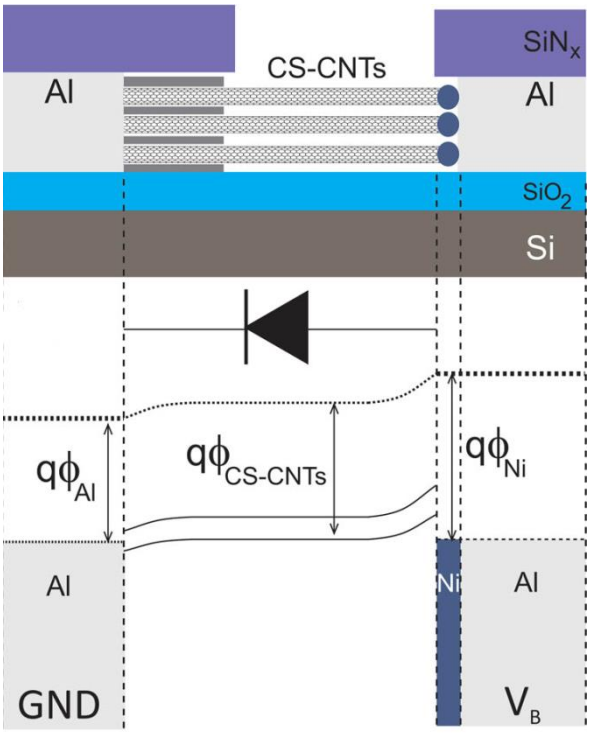

Figure 4-4. Schematic band diagram of CNT Schottky diode at V_B=0 following the device configuration.

Previously we mentioned that MWCNTs with diameters greater than 15 nm, at room temperature have an electrical conducting behavior. In the present work the tubes have diameters of the order of 30 nm which is twice larger; therefore a classical resistor behavior could be expected. However as it is evidenced in figure 4-4 the obtained rectifier effect can only take places if the CNTs have a semiconducting behavior. The only types of carbon nanotubes reported in the literature with semiconducting behavior at room temperature and independently of the diameter, are the cup-stacked carbon nanotubes (CS-CNTs) [9]. From a morphological approach, CS-CNTs consist on many truncated conical graphene layers, different from conventional CNTs made up of multi-seamless cylinders of hexagonal carbon networks. The figure 4-5 (a) shows a schematic representation of the named CS-CNT. This kind of carbon structure are synthetized in a wide range of temperatures between 250°C and 1500°C [10, 11]. The growth mechanism is still under debate. Therefore in order to explain the semiconducting behavior of the CNTs we assume that the resulting grown carbon nanostructures within the lateral-PAA templates are CS-CNTs type. In order to obtain information of the wall orientation of the synthetized carbon nanostructures inside the lateral-PAA devices, TEM observation have been performed. The figure 4-5 (b) presents the carbon nanostructures grown inside a lateral-PAA template. Concerning the grid preparation, the lateral-PAA device has been scratched in the channel zone between the two electrodes, and then the powder has been deposited on a TEM grid. From figure 4-5 (b) we can observed that the corresponding carbon structure has an irregular channel that we can attributed due to the product of the stacked truncated conical stacked graphene layer with a graphitic edge. Anyway, besides the performed TEM observations, deeper structural studies must been performed in order to obtain a complete characterization of the CNTs structures grown inside the lateral-PAA templates.

On the other hand, concerning the carrier type involved in the conduction, a hole transport is here assumed as CS-CNTs are grown on top of a SiO_2 insulating layer. Indeed, as generally observed for all carbon nanostructures based devices fabricated on SiO_2 insulating layer and measured in air, O_2 /H_2O redox couple species lead to the suppression of the n-type conduction. Considering the difference work functions on each contact interface and the p-type conduction and the observed rectifying behavior, a Schottky barrier model is by far preferable to the tunnel contacts model proposed in the literature [12]. The left

aluminum electrode is a low work function metal that acts as a Schottky contact for p-type carriers while the right nickel, present in the CS-CNTs that act as electrode is a high work function metal contact for p-type carriers. Concerning the CS-CNTs work function it has been previously calculated by tight binding theory at 4,6 eV [13] and experimentally measured at 4,7 eV [14]. Considering work functions of $q\varphi_{Al} = 4{,}26\, eV$ for aluminum and $q\varphi_{Ni} = 5{,}35\, eV$ for nickel, a Schottky barrier $q\Delta\varphi = q(\varphi_{Metal} - \varphi_{CS-CNT})$ is calculated for both interfaces. The work function $q\varphi_{CS-CNT}$ will be arbitrary taken and assumed at 4.7 eV for CSCNTs and measured from the Fermi level for a p-type semiconductor. The Al/CS-CNTs interface leads to a negative Schottky barrier around –0.34 eV (rectifier contact with p-doped semiconductor) whereas the CS-CNTs/Ni interface leads to a positive one around +0.75 eV (ohmic contact with a p-doped semiconductor). The Schottky diode is then schematized in figure 4-4 following the device structure with the Fermi level pinning at each interface.

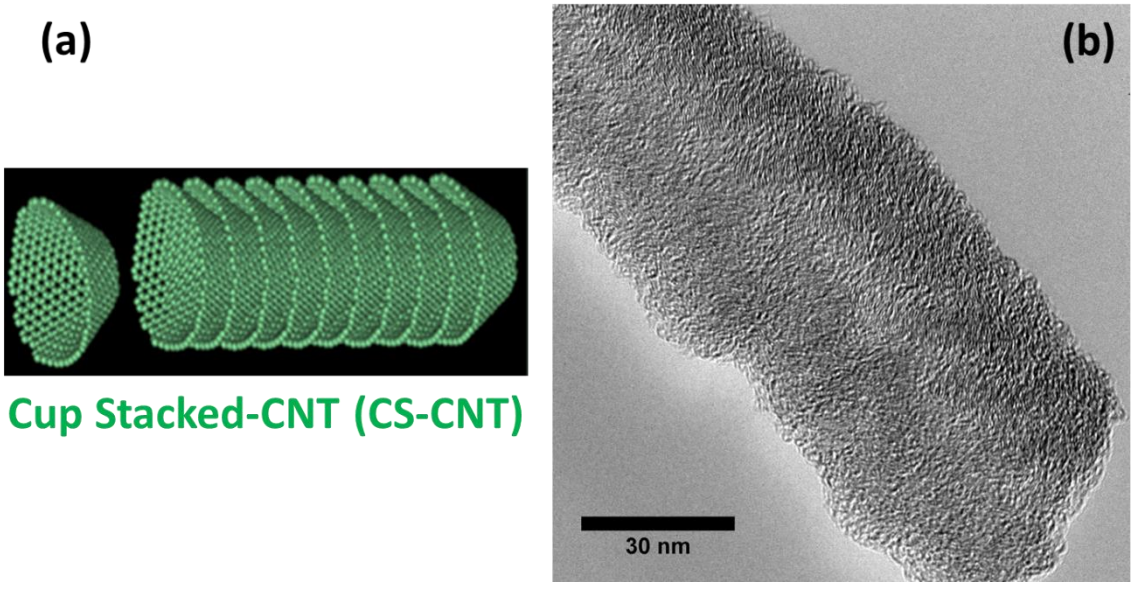

Figure 4-5. Cup-Stacked carbon nanotubes (CS-CNTs). (a) Schematic diagram of many truncated conical graphene layers which form the CS-CNT. (b) TEM images of the carbon nanostructure synthetized inside the lateral-PAA templates, from their structural morphology and the electrical device response we can assume that such structures correspond to CS-CNTs.

In order to evaluate the photonic response of the lateral device with a capping layer, the channel where the CS-CNTs are located has been illuminated using infrared light with a wavelength of $\lambda = 850\ nm$ and a density power of $\rho = 2.22\ mW/cm^2$. In figure 4-6 (a) it is shown that under light illumination a large photocurrent (red line) is then added to the dark current in the reverse bias regime. An equivalent photoresponse has been measured with a $\rho = 0.5\ mW/cm^2$ as is shown in figure 4-6 (b). In this plot, values around the origin are enlightened and clearly show an open circuit and a short $V_{OC} = 0,17\ V$ circuit current $I_{SC} = -3,71\ \mu A$. When a forward bias is equal to the band gap, the photocurrent is cancelled at the open circuit voltage. In a first approximation, the open circuit voltage measured here would give the bandgap energy of the CS-CNTs in this device at $E_G \sim qV_0 = 0,17\ eV$ [15].

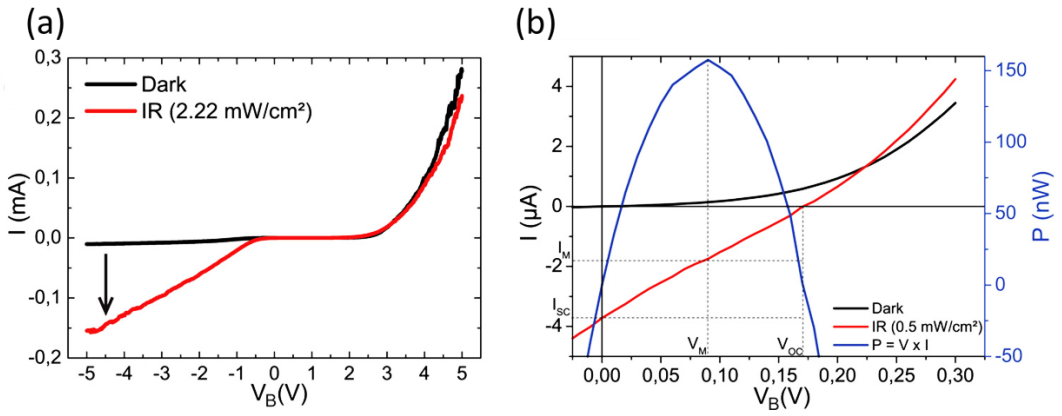

Figure 4-6. Current-Voltage characteristics in the dark (black line) and under infra-red illumination (red line) on the CNTs with an asymmetrical contact mode. (a) Electrical behavior in the range of -5V to 5V with an IR power density of $\rho = 2.22\ mW/cm^2$. (b) Magnified electrical behavior. The power is plotted (blue line) to obtain the V_M and I_M parameters.

Therefore these devices based on CS-CNTs Schottky diodes are found to exhibit potential benefits for photosensing and photovoltaic applications. In order to explore a further application in the photovoltaic field, the fill factor FF has been calculated, such value is a parameter which, in conjunction with V_{OC} and I_{SC}, determines the maximum power from a solar cell. The fill factor is given by the following expression:

$$FF = I_M V_M / I_{SC} V_0$$

Where I_M and V_M are the maximum current and maximum voltage respectively which leads to the maximum power generated by the photocurent. In figure 4-6 (b) the power curve is plotted and the fill factor parameters are indicated. The as-derived values of $V_M = 0.09\,V$ and $I_M = -1.75\,\mu A$ lead to a $FF = 25\%$. This value is slightly below the 33% measured for previously reported CNT Schottky diodes based on two-gates geometry [16].

In order to characterize the photoresponse performance of the device the responsivity factor R has been measured. The responsivity factor is given by the I_{Ph}/P_{in} with I_{Ph} as the photocurrent generated at a given bias voltage V_B with an incident power P_{in}. In figure 4-7 is plotted for various laser powers (x-axis), and for different forcing voltage ranged from 0 V to 5 V (vertical variation for each laser power). Different light sources with calibrated and focused light beam covering the visible range have been utilized. Each laser has a different laser incident power for instance $P_{in}^{458\,nm} = 2{,}8\,\mu W$, $P_{in}^{514\,nm} = 330\,\mu W$ and $P_{in}^{633\,nm} = 630\,\mu W$. The photonic response has been measured varying the P_{in} value decreasing the incident power as $P_{in}, P_{in}/2\,, P_{in}/5\,, P_{in}/10\,, P_{in}/10^2\,, P_{in}/10^3$ and $P_{in}/10^4$. The measured responsivity decreases with increasing laser power and increases with increasing forcing voltage. The plot exhibits a linear photoresponse as a function of the laser power following a unique slope for all three wavelengths at fixed bias, but slightly different for the different bias voltage at a fixed wavelength. This is indicative of a good calibration of our photodetector. The maximum responsivity R is measured at an extremely high value of $8{,}4 \times 10^4\ A/W$ at $V_B = 5V$ under a 458 nm light illumination and at a low excitation power $P_{in} = 0{,}28\,nW$. This leads to a measured external quantum efficiency (EQE) $\eta_m = 3{,}1 \times 10^5$. The external quantum efficiency gives us the ratio of the number of carriers collected by the photonic device to the number of photons of a given energy incident. The external quantum efficiency depends on the incident light wavelength and is given by:

$$\eta_m = \frac{R \times f \times h}{q}$$

Where f is the frequency of the laser, h is the Planck constant and q is the electron charge. This high level of EQE implies the presence of a high gain G leading to the

measurement of the intrinsic EQE η as $\eta = \eta_m/G$. In analogy to CNTs where EQE has been measured at a maximum η = 10% [17], we can assume here a minimum gain $G \sim 3{,}1 \times 10^6$ at 458 nm.

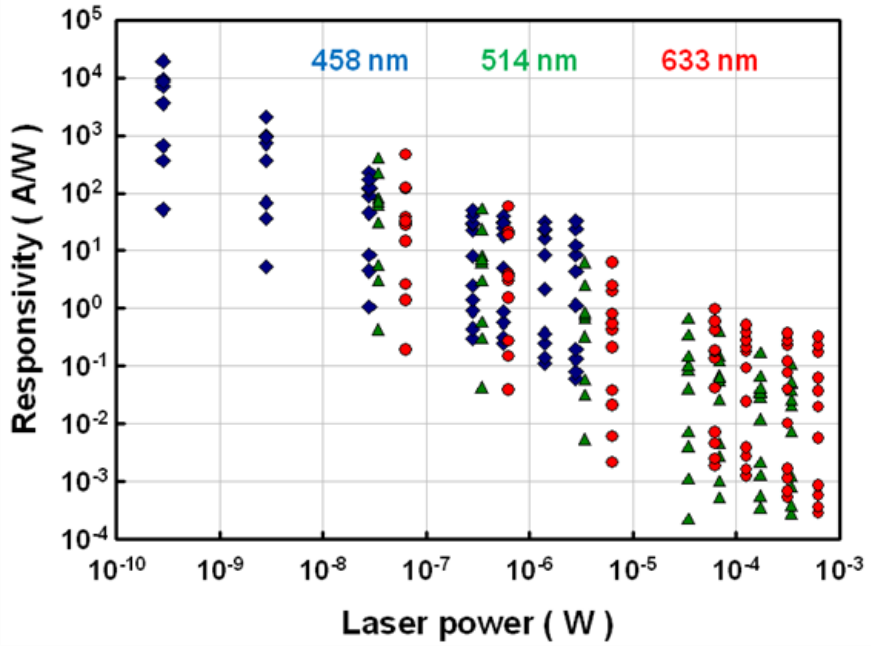

Figure 4-7. Responsivity as a function of laser power (λ = 458 nm,514 nm, and 633 nm) for different forcing voltage (ranged from 0 V to5 V). Each laser has different laser power (P_{in}^{458nm}= 2.8 µW, P_{in}^{514nm}= 330 µW,and P_{in}^{633nm} = 630 µW) at first, and photonic response was measured by decreasing laser power (P_{in} , $P_{in}/2$, $P_{in}/5$, $P_{in}/10$, $P_{in}/10^2$, $P_{in}/10^3$, and $P_{in}/10^4$).

In order to set the sights on the potential applications of such devices in telecommunications fields, time responsivity measurements have been performed in the infrared band at $\lambda = 1550\, nm$ using ultrafast Current-Voltage measurements as shown in figure 4-8.

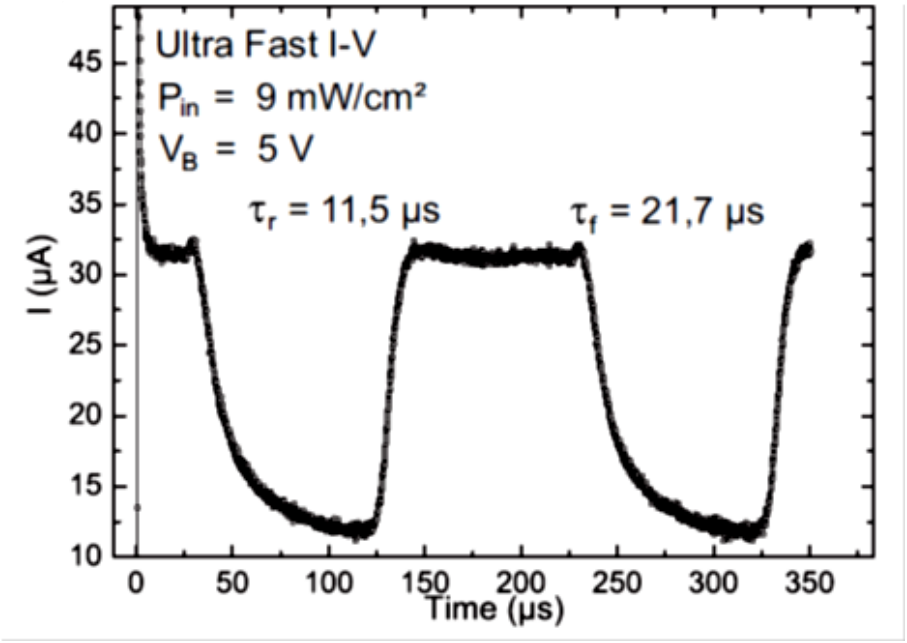

Figure 4-8. Ultrafast Current-Voltage characteristics of a CNT device upon infraredlight (λ = 1550 nm) set to 5 kHz at P in = 9 mW/cm ^{2} V $_{B}$ = 5 V. Rise and fall times are measured with the 10–90% method.

The device has been biased at $V_B = 5V$ and $\rho_{in} = 9\ mW/cm^2$. A mechanical chopper has been used to generate 5 kHz light pulses. For a reliable measurement of the rise and fall times, each current point has been measured every 100 ns during 20 ns to avoid parasitic device charging effects. Using the 10% – 90% method, the rise time has been determined at 11.5 µs and the fall time at 21.7 µs. Although modern telecommunication devices require picosecond time response, it is worth noting that these are the fastest time responses measured for CNTs based devices [18].

The characterization of Schottky diode devices based on cup-stacked carbon nanotubes arrays grown in lateral-PAA templates asymmetrically contacted reveals that such devices present a strong photonic response under light illumination opening the possibility for further photosensing and photovoltaic applications. This asymmetry connection arises from the smart use of the aluminum as a Schottky contact for holes carriers and the nickel catalyst ended tips as nanoscale electronic contacts. Due to the difference of the two contacts work functions, a built-in field is formed in the channel allowing charges photogeneration and separation under light illumination.

4.2.3 Metal decoration on devices without capping layer

The asymmetrical connection between the two device terminals is a necessary condition in order to have an electrical rectifier effect with photonic response under light illumination, albeit the metal work function responsible of asymmetrical connection has to be higher than the carbon nanotube work function. The figure 4-9 summarizes the different metals work functions highlighting candidates for the fabrication of a device with a photoresponse.

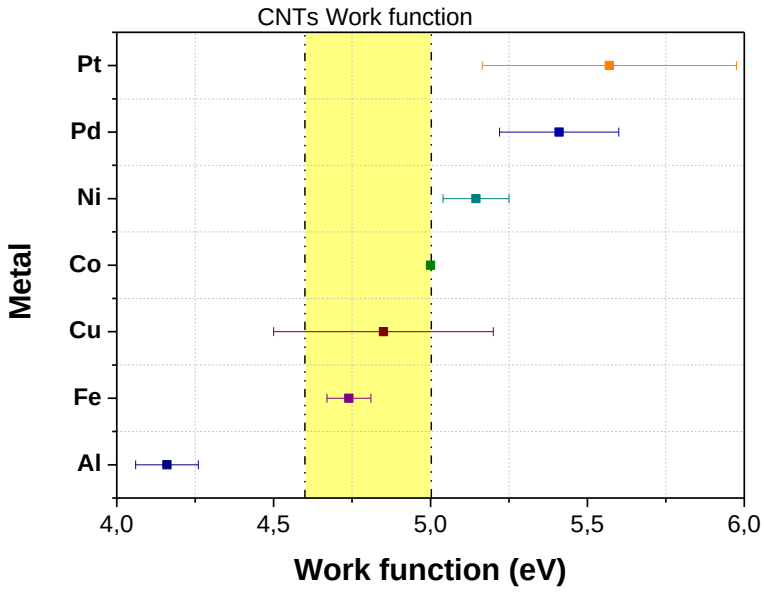

Figure 4-9. Work functions of carbon nanotubes and various metals which are possible to electrodeposite.

The metal decoration of the CNTs has been performed by an electrodeposition process. The decoration of the metal on the CNTs depends mainly on the structural quality of the CNTs. The electrodeposited mechanisms that can take place depends on the CNT quality, both situations are schematized in the figure 4-10. As it is previously mentioned the CNTs have higher electric conduction in the axial direction than in the radial direction. Therefore for zero defective nanotubes the electrical conduction will uniformly flow in such direction, leading to a current concentration at the catalyst nanoparticle located at the CNT

tip which implies that the decoration only takes place in the catalyst material. This phenomena has been corroborated when the electrodeposition process has been performed on SWCNTs with excellent structural properties [19]. On the contrary when CNTs have defect sites the electrodeposited metal are preferentially nucleated at these points on the side–walls [20], as well the current flow in the axial direction and the catalyst nanoparticle tip also acts as deposition site. In the present work, after the electrical characterization of devices with a capping layer, we concluded that the only explanation in order to obtain carbon nanotubes with a semiconducting behavior is that the structure of the resulting tubes has a cup-sacked configuration. Such structures possess graphene/graphitic edges that represent very effective potential sites for a salt reduction and subsequently for localized surface metal decoration through an electrodeposition process.

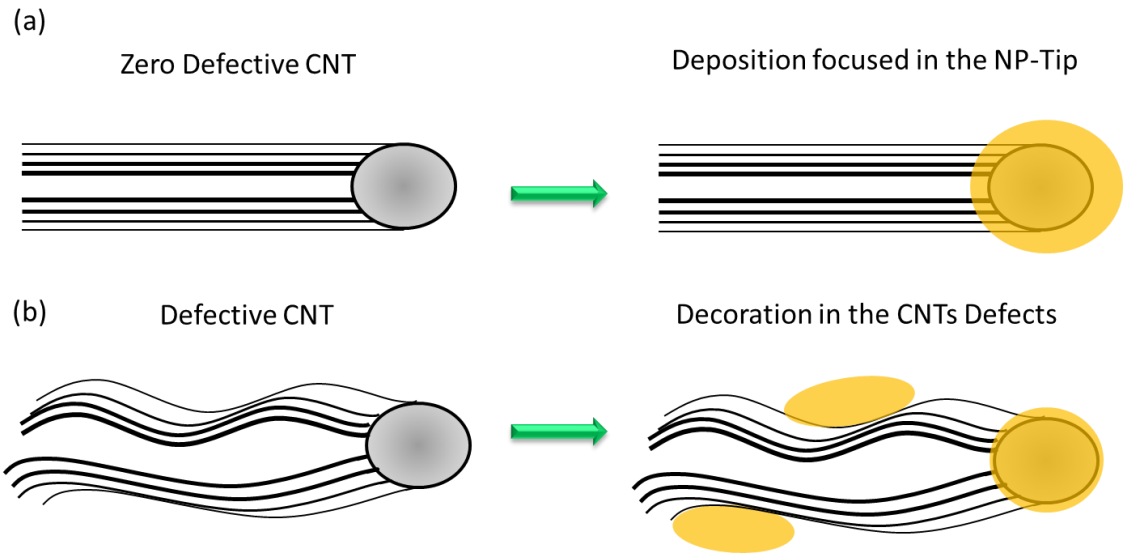

Figure 4-10 Schematic images of the possible deposition mechanism depending on the CNTs quality structure.

The electrical characterization of the lateral devices without a capping layer has been performed before and after the decoration process of various metals. The current-voltage curves are shown in figure 4-11. The contact mode of the devices without the capping layer is dominated by the side-wall mode. The main reason relies on the fact that it is most difficult to obtain a tip-contact mode in the top surface of the aluminum counter electrode. Therefore as is observed in figure 4-11 the electrical behavior for the devices with the

pristine CS-CNTs is completely symmetrical and a rectifier effect is not detected. On the contrary after metal decoration of nickel nanoparticles as indicated in the insight of the figure 4-11 (a), a significant current increase is measured, both in the reverse and the forward bias regimes, due to the newly formed contacts through nickel nanoparticles that increase the channel conductivity. However, asymmetrical behavior is observed in green line with a meaningfully higher current in the forward bias regime of almost two decades. Similar results are obtained when palladium has been decorated on the side-walls of the CS-CNTs as indicated in figure 4-11 (b). In both cases, upon exposure to infrared light with a wavelength of $\lambda = 850\, nm$ and a density power of $\rho = 2.22\ mW/cm^2$ the Ni and Pd decorated CS-CNTs devices exhibit a strong photonic response, as it is pointing out in figure 4-11 (a) and (b) respectively, and a photocurrent is generated. In order to confirm that the diode rectifier is also obtained due to the appropriate well matched work function of the metal decorated and the counter electrode, the metal decoration of iron with work function $q\varphi_{Fe} = 4{,}7\ eV$ and copper with a work function $q\varphi_{Cu} = 4{,}65\ eV$ has been performed in different devices. In figure 4-11 (c) and 12 (d) it is observed that after the electrodeposition into the CS-CNTs, the electrical current is increase respect the pristine devices however non rectifier effect and consequently there are not any photonic response. The increment in the current is again attributed due to the new contacts created between the two terminals.

Therefore the series of performed experiments reveals that the nature of the contact mode and the metal work function determines the electrical behavior of the device. The asymmetrically connection has to be achieved and the work functions have to satisfy the following relation:

$$\varphi_{Al} < \varphi_{CS-CNT} < \varphi_{Metal\ decorated}$$

The performances observed for high work function metal nanoparticles decorated devices are quite similar to one where the catalysts act as nanoplugs. Finally, the modulation of the band energy diagram at the interface is represented for different nanoparticles. It clearly supports the Schottky barrier model: nanoparticles work function higher than 5 eV allows the fabrication of ohmic contacts and thus an efficient rectifier, while those with work function lower than 5 eV let the device into symmetrical configuration with no rectifying effect.

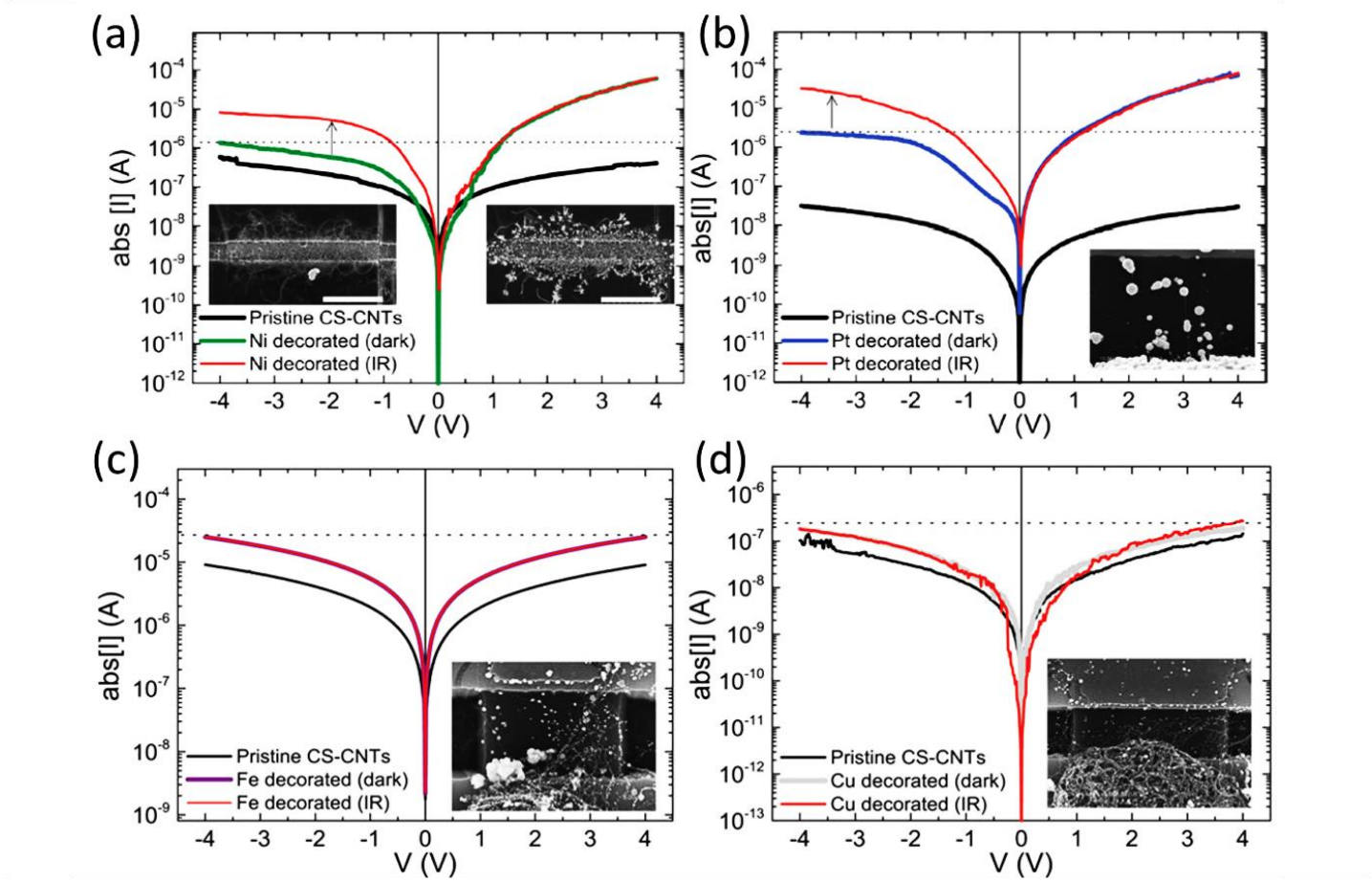

Figure 4-11 Current-Voltage of devices based on CS-CNTs grown inside lateral-PAA templates without a capping layer on top of the electrodes. (a) Current-Voltage characteristics of a CS-CNTs device before Ni decoration in the dark (black line), after Ni decoration in the dark (green line) and under IR illumination (red line). Left inset: SEM image before decoration. Right inset: SEM image after decoration. Scale bar: 20 µm. (b) I – V characteristics of a CS-CNTs device before Pt decoration in the dark (black line), after Pt decoration in the dark (purple line) and under IR illumination (red line). Right inset: SEM image after metal decoration by an electrodeposition process. Image size: 10 µm × 5 µm. (c) I – V characteristics of a CS-CNTs device before Fe decoration in the dark (black line), after Fe decoration in the dark (lilac line) and under IR illumination (red line). Right inset: SEM image after decoration by an electrodeposition process. Image size: 20 µm × 10 µm. (d) I – V characteristics of a CS-CNTs device before Cu decoration in the dark (black line), after Cu decoration in the dark (grey line) and under IR illumination (red line).

4.3 Vertical-PAA devices

The contact mode and the work function matching among the different component of the lateral-PAA based devices are key characteristics to control in these kinds device fabrication approach. Taking into account such evidences, the vertical-PAA devices based on CNTs have been fabricated while preserving the mentioned properties. The electrical characterization has been performed aiming to explore the potentialities of such devices as interconnects. Finally the device performance for the detection of water molecules has been performed targeting the possibility for a further application as gas sensing devices.

4.3.1 Electrical behavior

The electrical behaviors of the vertical-PAA templates have been performed depositing four different materials on the counter electrodes on top of the PAA surface. Figure 4-12 summarizes the current-voltage (I-V) curves for different voltage ranges and for different electrodes materials. In all cases a resistor behavior has been measured, reflecting the conducting nature of the CNTs grown inside the pores. The presence of a hysteresis phenomenon has been investigated: on the figures 4-12, the black lines correspond to the forward voltage sweeping and the red lines to the backward voltage sweeping. In the range of voltages studies there are no straightforward evidence of a hysteresis phenomenon.

The resistance in all cases varies between 5 Ω and 7 Ω, reflecting that in all cases approximately the same amounts of CNTs are contacted per electrode. The surface of each electrode is of 0.06 mm^2. A first order calculation of the resistivity of the individual CNTs can be performed. The total resistance R_{Total} of the measured system is given by:

$$R_{Total} = R_{Al} + R_{Electrode} + R_{CNT\,\|} \sim R_{CNT\,\|} = \frac{1}{\sum_i^N 1/R_{CNT(i)}}$$

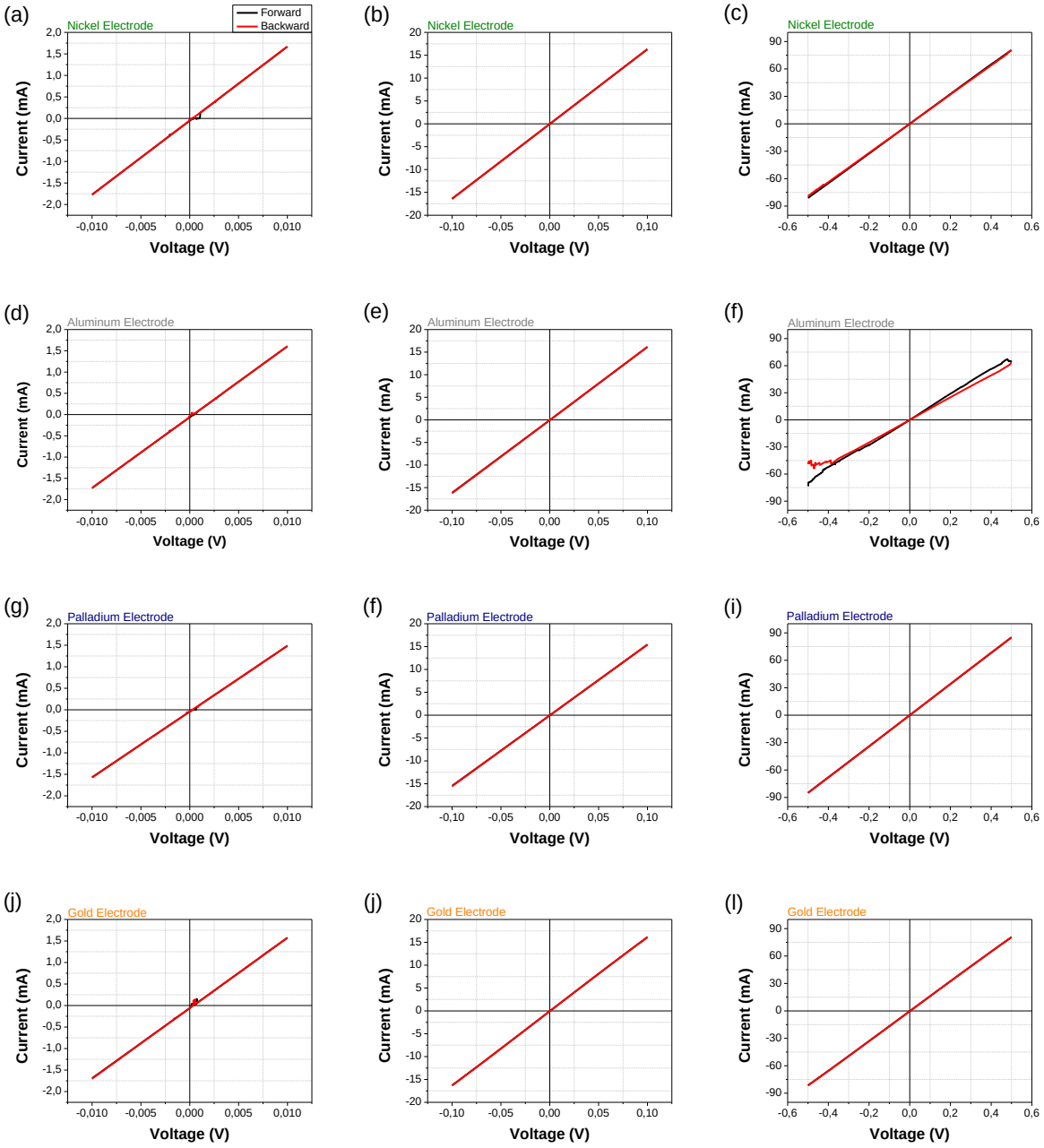

Figure 4-12. Current-Voltages curves for different applied voltages ranges in the dual sweep mode: 0.01 V, 0.1 V and 0.5 V. The red line indicates the forward voltage sweeping variation and the black line the voltage variation in the backward regime. Four different counter electrodes have been deposited: (a), (b) and (c) nickel, (d), (e) and (f) aluminum, (g), (h) and (i) palladium and (j), (k) and (l) gold.

Where R_{Al} is the resistance of the aluminum foil, $R_{Electrode}$ the resistance of the deposited metal electrode and $R_{CNT\,\|}$ is the resulting resistance of the CNTs connected in parallel between the aluminum and the counter electrode. Assuming that the resistance of the aluminum and the counter electrodes is of the order 10^{-8} Ω, such values are negligible in respect to the total measured resistance. On the other hand, considering that all the CNTs connected in parallel have the same resistance value, therefore if $R_{CNT(i)} = R_{CNT}$, and the total measured resistance is related to the resistance of the individual CNTs as:

$$N \cdot R_{Total} = R_{CNT}$$

The calculated R_{CNT} in all cases is of the order of 55 MΩ. In order to compare with other results we calculate the resistivity value that does not depend on the characteristics length of the transporting carrier element. In the literature it exists a wide range of CNTs resistivity values between $0.36\ m\Omega \cdot m$ to $117\ \Omega \cdot m$ [21, 22]. Such values strongly depend on the straightness of the tubes and their quality structure. In order to calculate the resistivity it is necessary to precise the characteristics lengths of the CNTs. Concerning the diameter, the tubes have an average diameter of 30 nm, on the other hand for the nanotube length we will approximate that the pores height are the same that CNTs length since the synthesis process has been stopped when the CNTs tips reached the top PAA surface. Therefore we assume that the average CNT length is 500 nm. Taking into account the mentioned considerations, in our case, the resistivity of the tubes is of the order of $\rho_{CNT} = 0{,}05\ \Omega \cdot m$ and the resistivity per electrode is of the order of $\rho_{Electrode} = 0{,}9\ \Omega \cdot m$. This last value is still high for interconnects applications comparing with the obtained value reported by Fiedler et al. [23] with a resistivity per via connection of $0{,}0004\ \Omega \cdot m$, however in such work lithography steps have been performed, the CNTs synthesis has been carried out at 600°C, and complicated post-treatments have been executed in order to improve the contact between the CNTs and the counter electrode. In our present work, the synthesis temperature is mainly limited by the aluminum foil which starts to degrade at 660°C. Consequently it is possible to achieve CNTs with a better structural quality which can lead to an improvement in conduction transport properties. Therefore further studies have to be performed to improve the conduction properties of the devices based on vertical-PAA templates that could open the possibility to applications in the interconnection

Concerning the individual resistivity of the CNTs, such value might still be overestimated. As it has been shown by cross-sectional TEM images (section 3.5.4) more than one CNT can grow per pore, however mostly just one tip is reaching the top surface. Therefore, in our calculation we are neglecting all the possible contacts that can take place inside the pores. In addition, the type of contact between the tubes can even be more dramatic for the resistivity inside the pore. Two types of contacts can occur (similarly as the contact mode between the CNTs and the counter electrode): the side-wall contact mode and the tip-contact mode, these contacts modes are schematized in the figure 4-13. When the side-wall contact mode takes place the contact resistance is much higher than tip mode, for instance Santini et al. [24] have reported a side-wall resistance of (45 ± 7) kΩ for nanotubes with diameters of (18 ± 3) nm. Therefore such kind of contact may increase even more the contribution to the resistance per pore leading to a more dramatic overestimation of the individual CNTs calculation.

In conclusion the measured resistance value gives a notion of the vertical device for the application as interconnect circuits, and on the other hand the transport deduced values of individual CNTs are overestimated by the introduced assumptions.

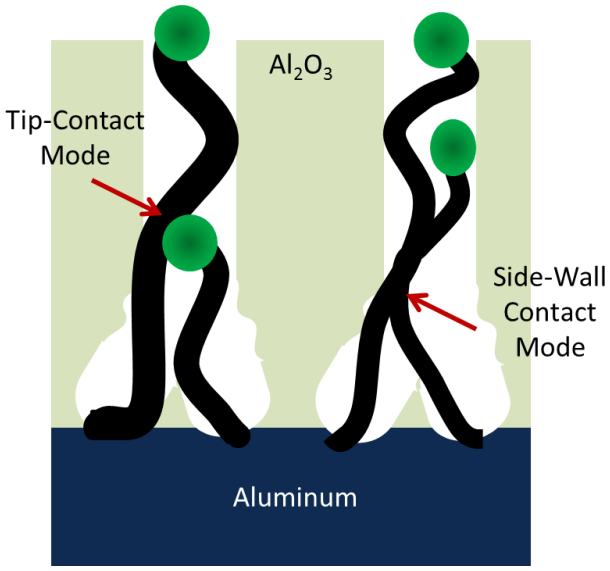

Figure 4-13. Schematized images of the possible contact modes between CNTs inside the pores of the PAA structure.

In all cases for the presented devices, the electrical behavior measured has been similar to a resistor type. For instance when aluminum has been deposited as counter electrode, the same connection architecture is obtained as the lateral-devices with capping layer. However there is no evidence of a semiconducting response of the CNTs. Two different reasons can explained the obtained electrical behavior in the devices based-on CNTs grown within vertical-PAA templates. Firstly, we can consider that a different tube formation is involved in the vertical-PAA templates than in lateral ones. Therefore the pores in the vertical direction can lead to the formation of carbon nanostructure mainly with conducting properties. Alternatively, in spite of the work functions, values have been preserved in both devices geometries: in the devices with the vertical templates the tip contact mode is not achieved between the metal electrode and the CNT tip. In such case, it is possible that part of deposited metal electrode can diffuse inside the pore and make the contact with the sidewall of the carbon nanostructure. Under the described situation, the tip contact mode is not preserved. Further studies have to be performed in order to clearly identify the constraints of the formation of a Schottky contact in vertical-PAA templates.

On the other hand, the same electrical characterization has been performed on device with a density of nanotubes of 60 CNTs/μm^2. The figure 4-14 (a) shows the current-voltage curve which presents a typical resistance. When the applying voltage is increased a non-linear behavior is obtained. This kind of behavior has been previously reported by Bockrath et al. [25] providing experimental evidence that the conductance in CNT bundles exhibits Luttinger liquid behavior, however these behaviors have been obtained at low temperatures [26]. More recently Kozlov [27] have revealed an abnormal zero bias at room temperature in a forest of CNTs. This phenomenon is attributed due to the tunneling of the charge carriers across the nanotube junctions which is enhanced by temperature gradients created by measuring currents and used for the characterization of the nanotube junction network [28]. Therefore such results are consistent with the cross-section TEM images, and evidence that the deduced CNT resistivity is overestimated since there are other contacts that are not considered. We attributed the apparition of the non-linear behavior at higher powers due to higher temperature gradient generated at higher voltages between nanotube junctions near the top PAA surface and inner aluminum which leads to an enhancement of nonlinearities in the sample properties [27]. This phenomenon is consistent with the greater

hysteresis effect in the reverse regime since more power is dissipated which emphasis the nonlinearities of the device. The nonlinear electron transport in CNT bundles upon exposure to chemical analytes have been recently started to be developed as sensing system [29].

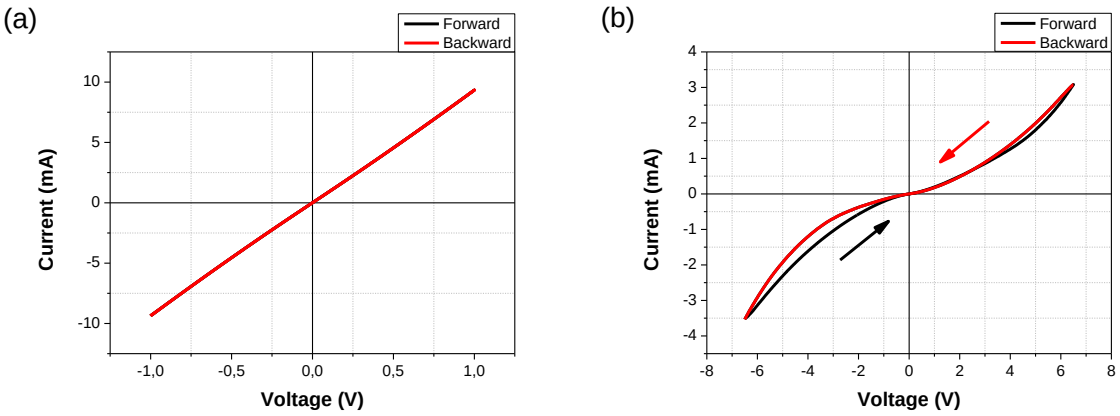

Figure 4-14. Current-Voltage curves in different sweeping voltage range for a sample with a density of CNTs of 60 CNTs/μm^2. (a) Resistor behavior in the range -1V to 1V. (b) Semiconducting behavior in the range -6 V to 6 V.

The fact that this kind of behavior has been detected in forest distributions indicates in our case that many CNTs are contacting at the bottom pores. This CNTs distribution is more pronounced in a sample with an anodization voltage of 30V, where more branches are created from a stem pore. Consequently the CNTs that reach the top surface have probably many CNTs contacting their surface along the pore.

4.3.2 Light Illumination

In order to test the photonic response of the vertical-PAA templates, the devices have been illuminated using a blue laser with a wavelength of 458 nm. The devices with the four deposited metal electrodes have been tested. However as is shown in figure 4-15 there is no evidence of a photocurrent generated due to light illumination. The present

measurements correspond to device with the palladium electrode, but similar results are obtained with the others counters electrodes. The non-response of the device under light illumination can be mainly attributed a two factors, firstly the light may not be able to interact with the CNTs due to the counter electrode material shadowing the majority of the photon flux. On the other hand, even if the light can enter to the pores it will mostly interact with the nanotube tip closer to the contact with the top electrode, whilst generally the maximum of the photocurrent amplitude is located in the channel regime between the two contacts [30, 31].

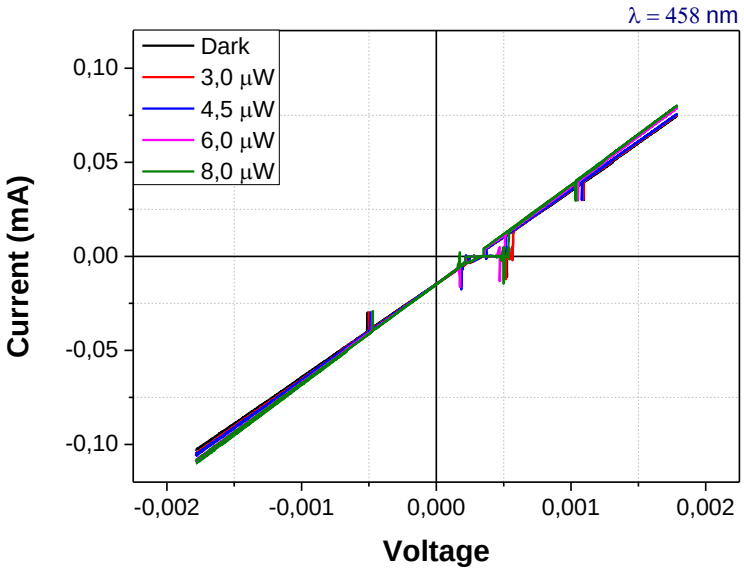

Figure 4-15. Current-Voltage curve of vertical-PAA device with Pd electrode deposited as counter electrode. Blue illuminations have been performed applying different powers.

4.3.3 Humidity Sensing

Several works have been focused on studying the electrical resistance variation of MWCNTs when exposed to various gas or vapor environments, including NH_3, NO_2, and CO [32, 33]. In particular gas sensors have been fabricated by Suresh Rajaputra et al. [34] using CNTs grown inside PAA templates, however in this case the aluminum has been removed in a chemical acid solution and the grown of CNTs was carried without catalyst, the resistivity

of the device being in the order of $100\ \Omega \cdot m$. Such designed devices present the advantage that gas can flow freely through the tubes due to the absence of the aluminum layer. Growing CNTs inside vertical-templates, Ding et al. [35] also performed H_2 sensing measurements by depositing a palladium top electrode.

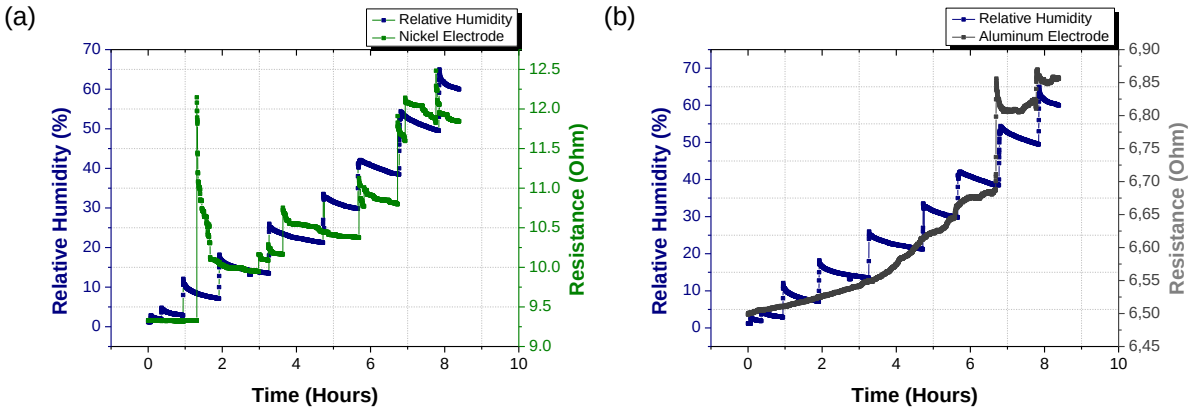

Figure 4-16. Resistance variations as results of humidity response of vertical device with different contact electrode: (a) nickel and (b) aluminum.

In the present work in order to perform humidity sensing measurement water vapor have been introduced in the chamber where the electrical device characterization is carried out. The tested devices have been the vertical devices with nickel and aluminum top electrodes. The relative humidity has been increased from 1% up to 65% at room temperature. Figure 4-16 shows the resistance variation with the change of the relative humidity inside the chamber. In both cases the resistance increases under the augmentation of the relative humidity. This response is consistent with the synthesis of highly defectives CNTs, as water vapor are preferentially absorbed on the polar oxygen-containing defects through the formation of hydrogen (H) bonds, which leads to a lowering of the induced p-type doping on the CNT and increasing the electrical resistance. With the nickel top electrode as is shown in figure 4-17(a), the device follows the trend of the humidity variation inside the chamber. However contact related effects also are detected, for instance in the relative humidity variation from 3% to 10% the gas flow injected has affected the probed contacting the counter electrode which explains the great drop in the resistance value. In

addition we observed that for relative humidity values lower than 40% the system requires 15 minutes approximately to detect the increment in the humidity. This fact indicates that the water molecules needs some time to penetrate the porous structure. On the other hand the device with the aluminum top electrode does not show a sensing response for humidity values lower than 50 % as is indicated in figure 4-17 (b). This device starts to detect the water molecules suddenly for values higher than 50%. In order to understand the huge difference in the sensing performance, the electrode surfaces have been observed by SEM as shown in the images in figure 4-17. In the case of the nickel electrodes, as it is clearly pointed out in figure 4-18(a) the pore structure is still easily recognized through the deposited metal, the insight reflects that CNTs tips are covered and after the metal electrode deposition and are still recognizable. In contrast, for the aluminum deposition most of the pores surface is covered as shown figure 4-17 (b), more likely by a uniform layer deposition, therefore in such device a higher amount of water molecules is required to interact with the active element of the device because the water molecules have to diffuse firstly through the metal electrode. This explains the two different sharped sensing behaviors observed in the device with deposited aluminum metal electrode. The resistance slowly increases in the range of 1% to 40% when the water molecules interact just with the counter electrode, and abruptly increases when the water molecules start to interact with the CNTs. The device begins to sense difference in the relative humidity.

The obtained results reveal that the deposited electrode plays a crucial role in these types of devices. Therefore the thickness of the metal electrode has to be optimized in order to improve the sensing behavior of the devices based on CNTs grown inside vertical-PAA templates(). Anyway, the introduced devices are quite promising for further gas sensing application.

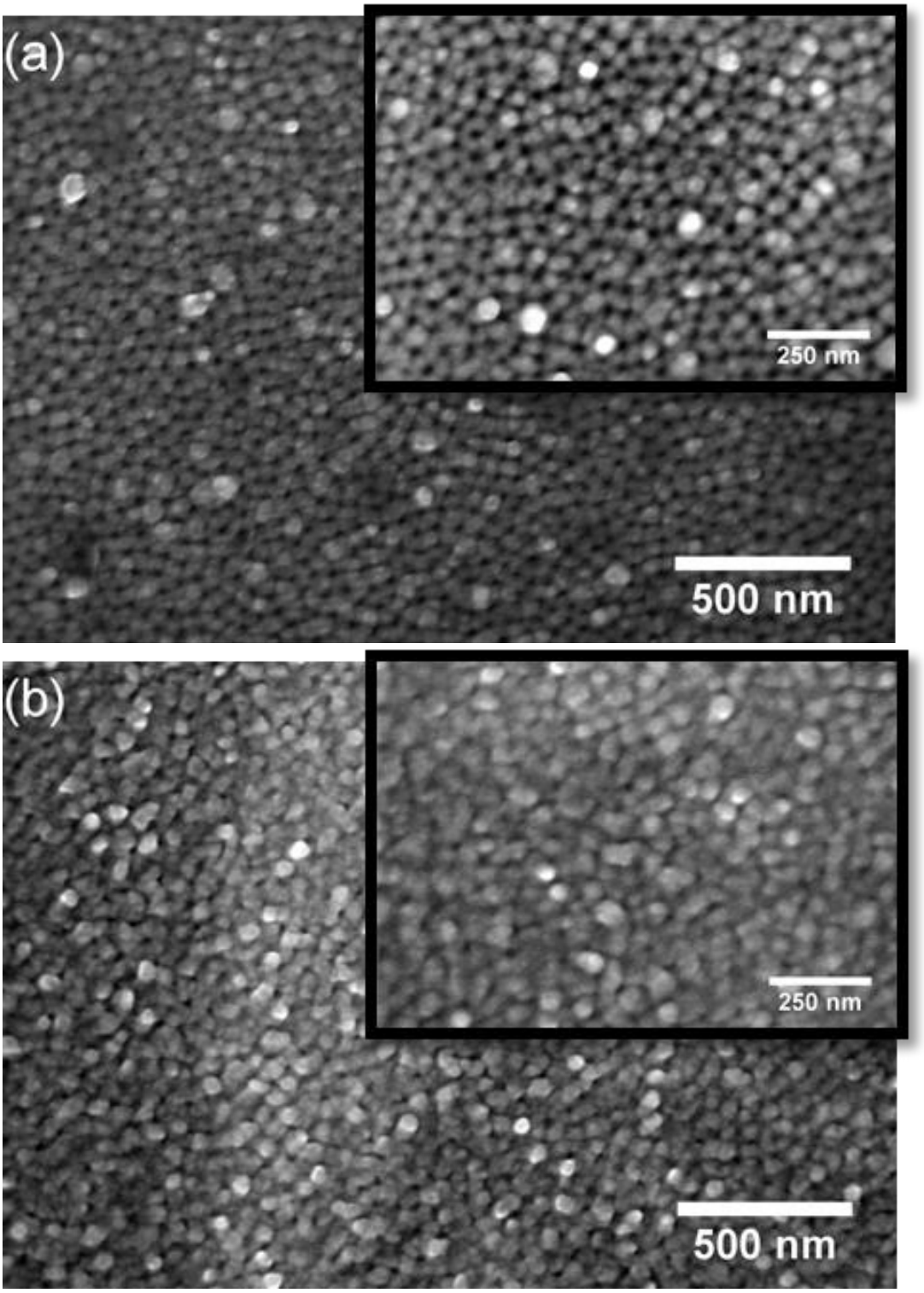

Figure 4-18. SEM top images of the metal electrodes deposited on top of the vertical templates. Two different metals have been deposited with a thickness of 30 nm. (a) Nickel and (b) Aluminum. Both images contain insights in higher magnifications.

4.4 Conclusions

The characterization of two different template approaches CNTs based devices has been performed. Both kinds of devices offer different application fields. In spite of both devices being based on arrays of CNTs, the inherent geometry determines the application domain.

For the lateral devices based on CNTs unequalled optoelectronic devices based on CNTs are presented for photovoltaic and photodetectors applications. These devices are based on asymmetrical contacted arrays of nanotubes leading to Schottky photodiodes. Lateral porous anodic alumina (LPAA) is used for the CVD synthesis of the organized nanotubes array and two methods are developed for engineering their Schottky contacts. Two different devices types have been fabricated in order to obtain such asymmetric contact. In one case the tip-contact mode has been promoted. The second procedure takes advantage of the defective zones of cup stacked-CNTs to perform a metal decoration process and modifies the nature of the side-contact mode between the CNTs and the counter electrodes. In order to obtain rectifier effect complementary to the asymmetrically device connection, the work functions have to be well matched, a clear relation between the values of the corresponding metal nanoparticle work functions and the measured rectifying effect has been established in a Schottky barrier model. Such work function differences lead to a built-in a field which is formed in the channel allowing charges photogeneration and separation under light illumination and a high sensitivity has been found within a broadband wavelength bandwidth (458 nm – 1550 nm). Photovoltaic parameters have been extracted and they evidenced fill factors quasi-independent of the wavelength at around 25%. The measured open circuit voltage is indicative of an intrinsic energy band gap of the as-growth CS-CNTs at around 0.17 eV. Finally, ultra-fast I – V measurements performed at λ = 1550 nm evidenced rise time measurements as fast as 11.5 μs which sets the actual state of the art for carbon nanotubes and carbon nanofibers. It is also worth mentioning at this point that , to the extent of our knowledge, these are the first ever reported functional devices based on lateral-PAA grown nanomaterials.

Chapter 4. The applications of devices based on CNTs growth inside PAA templates

For the fabrication of the vertical devices the contact mode and the relation between the metal work functions have been preserved. Four different counter electrodes have been deposited: nickel, aluminum, palladium and gold. Compared to the lateral-type devices, although the same connection configuration and contact mode are conserved, the electrical behavior of the device is a classical resistor. In order to establish the difference between the electrical behaviors, further studies are required to determine the structure of the synthetized in the vertical template, and additionally study the contact zone between the grown CNTs and the deposited metal electrode. The electrode resistivity has been calculated resulting of the order of 0.9 Ω·m, three orders of magnitude bigger than other reported optimized interconnects devices, however many strategies can furthermore be adopted in order to decrease this value. For instance, the synthesis temperature can be increased which will lead to CNTs with better structural properties. For devices with a low CNTs density a non-linear current-voltage behavior has been detected, equivalently to CNTs forest distribution. This phenomenon is attributed to the tunneling effect of charge carriers across the nanotube junctions enhanced by temperature gradients created by measuring applied currents and used for the characterization of the nanotube junction network. The present devices does not reflect a photonic response under light illumination, the problem could be associated with the fact that the CNT are inside the pore structure. Finally humidity sensing measurements has been performed and it has been verified that the sensing performance is quite sensible to the nature and uniformity of the deposited counter electrode.

The lateral devices exhibits electronic and optoelectronic responses that open new frontiers of the horizontal devices collectively organized arrays of one-dimensional nanomaterials. On the other the vertical devices based on CNTs can considerably contributes in the domain of interconnects and gas sensing.

References

[1] M. Gowtham*, et al.*, "Controlled fabrication of patterned lateral porous alumina membranes," *Nanotechnology,* vol. 19, p. 035303, 2008.

[2] M. Shiraishi and M. Ata, "Work function of carbon nanotubes," *Carbon,* vol. 39, pp. 1913-1917, 2001.

[3] C. Cordeiro*, et al.*, "Theoretical study of work function of conducting single-walled carbon nanotubes by a non-relativistic field theory approach," *Carbon,* vol. 47, pp. 690-695, 2009.

[4] N. de Jonge*, et al.*, "Characterization of the field emission properties of individual thin carbon nanotubes," *Applied Physics Letters,* vol. 85, pp. 1607-1609, 2004.

[5] S. J. Tans*, et al.*, "Room-temperature transistor based on a single carbon nanotube," *Nature,* vol. 393, pp. 49-52, 1998.

[6] R. Martel*, et al.*, "Single-and multi-wall carbon nanotube field-effect transistors," *Applied Physics Letters,* vol. 73, pp. 2447-2449, 1998.

[7] H. M. Manohara*, et al.*, "Carbon nanotube Schottky diodes using Ti-Schottky and Pt-Ohmic contacts for high frequency applications," *Nano letters,* vol. 5, pp. 1469-1474, 2005.

[8] Z. Chen*, et al.*, "The role of metal-nanotube contact in the performance of carbon nanotube field-effect transistors," *Nano letters,* vol. 5, pp. 1497-1502, 2005.

[9] Q. Liu*, et al.*, "Semiconducting properties of cup-stacked carbon nanotubes," *Carbon,* vol. 47, pp. 731-736, 2009.

[10] B. O. Boskovic*, et al.*, "Large-area synthesis of carbon nanofibres at room temperature," *Nature materials,* vol. 1, pp. 165-168, 2002.

[11] J. Vera-Agullo*, et al.*, "Evidence for growth mechanism and helix-spiral cone structure of stacked-cup carbon nanofibers," *Carbon,* vol. 45, pp. 2751-2758, 2007.

[12] T. Yamada*, et al.*, "Tunneling between carbon nanofiber and gold electrodes," *Journal of applied physics,* vol. 107, p. 044304, 2010.

[13] W. A. Harrison, *Electronic structure and the properties of solids: the physics of the chemical bond*: Courier Corporation, 2012.

[14] V. Robinson*, et al.*, "Work function reduction of graphitic nanofibers by potassium intercalation," *Applied Physics Letters,* vol. 87, p. 061501, 2005.

[15] S. M. Sze and K. K. Ng, *Physics of semiconductor devices*: John Wiley & Sons, 2006.

[16] J. U. Lee, "Photovoltaic effect in ideal carbon nanotube diodes," *Applied Physics Letters,* vol. 87, pp. 73101-73101, 2005.

[17] M. Freitag*, et al.*, "Photoconductivity of single carbon nanotubes," *Nano letters,* vol. 3, pp. 1067-1071, 2003.

[18] X. He*, et al.*, "Photothermoelectric p–n junction photodetector with intrinsic broadband polarimetry based on macroscopic carbon nanotube films," *ACS nano,* vol. 7, pp. 7271-7277, 2013.

[19] M. R. Maschmann*, et al.*, "Lithography-free in situ Pd contacts to templated single-walled carbon nanotubes," *Nano letters,* vol. 6, pp. 2712-2717, 2006.

[20] S. Arai*, et al.*, "Ni-deposited multi-walled carbon nanotubes by electrodeposition," *Carbon,* vol. 42, pp. 641-644, 2004.

[21] T. Hayashi*, et al.*, "A reversible strain-induced electrical conductivity in cup-stacked carbon nanotubes," *Nanoscale,* vol. 5, pp. 10212-10218, 2013.

[22] H. Dai*, et al.*, "Probing Electrical Transport in Nanomaterials: Conductivity of Individual Carbon Nanotubes," *Science,* vol. 272, pp. 523-526, April 26, 1996 1996.

[23] H. Fiedler*, et al.*, "Carbon nanotube based via interconnects: Performance estimation based on the resistance of individual carbon nanotubes," *Microelectronic Engineering,* vol. 120, pp. 210-215, 2014.

[24] C. A. Santini, *et al.*, "Carbon nanotube–carbon nanotube contacts as an alternative towards low resistance horizontal interconnects," *Carbon,* vol. 49, pp. 4004-4012, 2011.

[25] M. Bockrath, *et al.*, "Luttinger-liquid behaviour in carbon nanotubes," *Nature,* vol. 397, pp. 598-601, 1999.

[26] W. Y. Jang, *et al.*, "Electrical characterization of individual carbon nanotubes grown in nanoporous anodic alumina templates," *Applied Physics Letters,* vol. 84, pp. 1177-1179, 2004.

[27] M. E. Kozlov, "Nonlinear electrical properties of carbon nanotube forests," *Applied Physics Letters,* vol. 99, p. 133111, 2011.

[28] J. Park, *et al.*, "Electrical transport through crossed carbon nanotube junctions," *Journal of applied physics,* vol. 93, pp. 4191-4193, 2003.

[29] P. Gowda, *et al.*, "Chemical vapor detection using nonlinear electrical properties of carbon nanotube bundles," *Nanotechnology,* vol. 25, p. 025708, 2014.

[30] M. Engel, *et al.*, "Spatially resolved electrostatic potential and photocurrent generation in carbon nanotube array devices," *ACS nano,* vol. 6, pp. 7303-7310, 2012.

[31] M. Barkelid and V. Zwiller, "Photocurrent generation in semiconducting and metallic carbon nanotubes," *Nature Photonics,* vol. 8, pp. 47-51, 2014.

[32] L. Valentini, *et al.*, "Sensors for sub-ppm NO2 gas detection based on carbon nanotube thin films," *Applied Physics Letters,* vol. 82, pp. 961-963, 2003.

[33] C. Cantalini, *et al.*, "NO 2 gas sensitivity of carbon nanotubes obtained by plasma enhanced chemical vapor deposition," *Sensors and Actuators B: Chemical,* vol. 93, pp. 333-337, 2003.

[34] S. Rajaputra, *et al.*, "Multi-walled carbon nanotube arrays for gas sensing applications," *Nanotechnology,* vol. 19, p. 345502, 2008.

[35] D. Ding, *et al.*, "Hydrogen sensors based on aligned carbon nanotubes in an anodic aluminum oxide template with palladium as a top electrode," *Sensors and Actuators B: Chemical,* vol. 124, pp. 12-17, 2007.

Conclusions & Prospective

In the present work carbon nanotubes (CNTs) have been synthetized within porous anodic alumina (PAA) templates for their device applications. The devices have been based in two different templates approaches: the lateral-PAA and the vertical-templates. However in order to achieve the desire device configuration several hurdles have been overcome, therefore a deep understanding in the processes involved in each step of the fabrication were required, from the anodization process for the PAA fabrication until the synthesis of CNTs inside the pores. Once the devices have been fabricated, the mechanisms which take part in the device performance have been elucidated, allowing the enhancement of the specific function of the device or to obtain a notion of future improvements to realize.

The PAA templates have many advantages associated with their easy implantation and flexibility to control their geometrical features. In the present work, by investigating the anodization conditions, a fully characterization of the main pore properties have been performed, such as the pore diameter, interpore distance, porosity, circularity of the pores and the pore cell ordering. Such study provides useful information for a future precisely device characterization. In particular for lateral-templates the study of the impact of the anodization temperature has been realized. The obtained results reflect that the insulating layer deposited in order to execute the pore formation just in a determined direction, strongly affects the pore growth, and differently than the vertical pores where the temperature barely affects the pore configuration on the top surface, in the same temperature range, the lateral templates can leads to a pore merging phenomenon losing the pore array.

The catalyst nanoparticles have been deposited by pulse electrodeposition. The operational range depending on the anodization conditions has been studied. The catalyst deposition and the PAA fabrication are strictly related by the oxide barrier layer at the

bottom of the pores. The main constraint of the PAA relies on such barrier which introduces difficulties for a further metal nanoparticle deposition. In the present work, an exponential voltage decrease followed by a chemical wet etching has been applied in order to completely remove such barrier. By the application of such process a branched structure can be created at the bottom of the pores. The branched structures have been deduced comparing the pore density with the pattern of nanoparticles electrodeposited at the bottom of the pores, after the elimination of the PAA structure. This analysis allows the prediction of the best pore structure for further synthesis of carbon nanostructures.

The synthesis of carbon nanotubes through the HF-CVD technique has been successfully performed inside the PAA templates taking into account the geometrical constraints imposed by the porous structure. It has been evidenced that the branched structure at the bottom of the pores strongly affects the growth dynamics. For the very first time the CNT growth evolution at different synthesis times inside the PAA structure has been measured; such study provides meaningful information of the growth behavior within the pores. In spite of the fact that generally just one nanotube tip reaches the top PAA surface more than one CNT can grow in each pore and a competition is established inside the pore that can even block the CNT formation. The synthesis conditions and the pore structure have been conjointly adjusted to maximize the number of CNTs grown. In the vertical templates a density of 2×10^{10} CNTs/cm^2 has been achieved. Concerning the growth of CNTs inside the lateral templates, the synthesis temperatures have been study in order to obtain the most straight grown CNTs, which is a desirable characteristic for further device fabrication.

The characterization of two different templates approaches based devices has been performed and different applications domains have been established depending on their device designed configuration. Unequalled optoelectronic devices based on CNTs grown inside lateral-PAA templates are presented for photovoltaic and photodetectors applications. These devices are based on asymmetrical contacted arrays of nanotubes leading to Schottky photodiodes. The contacting mode between the CNTs and the counter electrode plays a crucial role in the electrical behavior. For instance a symmetrical behavior leads to a classical resistor behavior. On the other hand when the contact is between the nanoparticle tips of the CNT such symmetry is broken leading to Schottky contact. Under the lateral template, two different strategies have been implemented in order to achieve such

asymmetrical contact. In one case the insulating capping barrier deposited for the lateral anodization process is kept during the nanotubes growth in order to promote the tips contacts. On the other hand the insulating capping barrier is removed and a metal decoration process is executed to modify the nature of the previous side-wall contacts, adding a metal between the CNTs and the counter electrode, breaking the symmetrical contact. By this approach, it have been verified that the work function of the metals that contact with the aluminum electrode has to be higher than the CNTs work function. Therefore in order to obtain a Schottky contact, the asymmetrical contact has to be satisfied but in addition the work functions have to obey the following relation:

$$\varphi_{Al} < \varphi_{CNT} < \varphi_{Metal\ decorated}$$

The devices satisfying both conditions show a strong photonic response. The work function differences lead to a built-in field which is formed in the channel allowing charges photogeneration and separation under light illumination sensitivity has been found within a broadband wavelength bandwidth (458 nm – 1550 nm). Photovoltaic parameters have been extracted and evidenced fill factors which are quasi-independent of the wavelength at around 25%. Finally, ultra-fast current-voltage measurements performed at λ = 1550 nm evidenced rise time measurements as fast as 11.5 μs. It is also worth to mention at this point, that to the extent of our knowledge, they are the first ever reported functional devices based on lateral-PAA grown nanomaterials. Similarly for vertical devices the contact mode and the relation between the metal work functions have been preserved; however the linear behavior has been obtained, in principle we attributed this observation to a different carbon nanostructure growth in the different grown templates geometry or a diffusion of the material that acts as electrode inside the pores contacting the carbon nanostructure, leading to a symmetrical contact. Exploring the possible device application as interconnects circuits, the device resistivity has been calculated resulting of the order of 0.9 Ω·m, three orders of magnitude bigger than other interconnected devices, however several improvements can be done to decrease such value. Devices with a low CNTs density, due to more considerable branched structure shows a non-lineal current-voltage behavior, equivalently to CNTs forest distribution, revealing that many tubes are touching among then at the bottom pores. This phenomenon is attributed to the tunneling effect of charge carriers across the nanotube junctions enhanced by temperature gradients created by

measuring currents and used for the characterization of the nanotube junction network. Such non-linear behavior can act as a tracer to determine the structure at the bottom pores. The vertical devices do not reflect the photonic response under light illumination, this characteristic was expected because CNT are inside the pore structure and cannot fully interact with light. Finally humidity sensing measurements have been performed and it has been verified that the sensing performance is quiet sensible to the deposited counter electrode.

In the present work fundamental results associated to the growth of carbon nanostructures inside vertical PAA templates can serve as guidelines to extend the current frontiers for devices applications based on such nanotemplates fabrication approach. On the other hand, lateral-type PAA photosensing devices and vertical-type PAA gas sensing devices are presented with remarkable performances due to the adequate use of the Schottky contacts. Both results provide a considerable contribution in the field of nanodevices fabrication based on nanotemplates.

Regarding the future of the study topic, the introduced devices can been improved or slightly adapted in order to explore other applications area. For instance lateral-PAA based devices possess the great advantage that the grown CNTs are between two terminals. This configuration is very suitable for a further CNTs functionalization that expands the application fields as biosensing devices or gas sensors. Moreover such planar platform is very versatile for various applications as transistor based on CNTs. Concerning the vertical devices, still many improvements can be done to minimize the branched structure that will lead to bigger CNT yield. Under such conditions, considering interconnects application area, the number of contacted CNTs will be increased and the resistivity reduced. For the sensing applications, the thickness of the electrode deposited has to be investigated because it is the first element which interacts with the environment.